



UNIVERSITY OF
BIRMINGHAM

**ACOUSTIC AGITATION OF
DENSE CARBON DIOXIDE/WATER MIXTURES:
EMULSIFICATION, MASS TRANSFER, AND
REACTION ENGINEERING**

by

Steven Michael Cenci

A thesis submitted to
The University of Birmingham
for the degree of
DOCTOR OF PHILOSOPHY

School of Chemical Engineering
College of Engineering and Physical Sciences
The University of Birmingham
June 2014

UNIVERSITY OF
BIRMINGHAM

University of Birmingham Research Archive

e-theses repository

This unpublished thesis/dissertation is copyright of the author and/or third parties. The intellectual property rights of the author or third parties in respect of this work are as defined by The Copyright Designs and Patents Act 1988 or as modified by any successor legislation.

Any use made of information contained in this thesis/dissertation must be in accordance with that legislation and must be properly acknowledged. Further distribution or reproduction in any format is prohibited without the permission of the copyright holder.

UNIVERSITY OF BIRMINGHAM

University of Birmingham Research Archive

e-theses repository

This unpublished thesis/dissertation is copyright of the author and/or third parties. The intellectual property rights of the author or third parties in respect of this work are as defined by The Copyright Designs and Patents Act 1988 or as modified by any successor legislation.

Any use made of information contained in this thesis/dissertation must be in accordance with that legislation and must be properly acknowledged. Further distribution or reproduction in any format is prohibited without the permission of the copyright holder.

“Se getterai in un medesimo tempo due piccole pietre alquanto distanti l’una dall’altra sopra un pelago d’acqua senza moto, tu vedrai causare intorno alle dette due pietre due separate quantita’ di circoli, le quali quantita’ accrescendo, vengono a scontrarsi insieme... Avendo l’acqua tutte le sue parti di una medesima qualita’, e’ necessario che le parti attacchino esso tremore l’una l’altra senza mutarsi dal loro luogo.”

“If one drops two small stones simultaneously in a still body of water, each at a considerable distance from one another, you will notice about the two stones two distinct groups of circles forming, which, growing in intensity, will collide with each other... Since all the domains which constitute water remain of the same quality, it is necessary that each domain transfers such motion to the next without losing its position.”

Leonardo da Vinci, Del Moto e Misura dell’ Acqua.

*“prima moventur enim per se primordia rerum, inde ea quae parvo sunt corpora conciliatu et quasi proxima sunt ad viris principiorum, ictibus illorum caecis impulsa cientur, ipsaque porro paulo maiora lacesunt. sic a principiis ascendit motus et exit paulatim nostros ad sensus, ut moveantur illa quoque, in solis quae lumine cernere quimus nec quibus id faciant plagis apparet aperte.
...Nullam rem e nihilo gigni...”*

*“At first the atoms move of their own accord; then, those entities composed of small aggregates and possessing forces of almost equal magnitude to the first atoms, are themselves thrust into motion by the effect of invisible collisions, which gradually include aggregates of larger size. Thus, from the original atoms the motion grows, and is eventually revealed to our senses, in the same way that small floating particles may be observed against the sunlight, although the collisions responsible for this are not directly apparent.
...Nothing is generated from nothing...”*

Lucretius, De Rerum Natura.

*Dedicated to my father,
Renato Cenci Ariminensis*

Abstract

A biphasic mixture of dense carbon dioxide and water offers an important sustainable solvent system for reactions and separation of chemical compounds. The mixing and mass transfer effects in multiphase systems may be enhanced by agitation and increased interfacial areas, both of which are dependent upon the system selected. Therefore, the geometry and type of reactor will determine the efficiency of mass transfer and the overall reaction rates. In the present study, a 1 dm³ cylindrical, high-pressure reactor modified for ultrasound was characterised for its ability to emulsify carbon dioxide/water mixtures, and for mediating the physical and chemical effects required for the mass transfer, reaction and separation of organic compounds.

Acoustic agitation of the carbon dioxide/water mixture at 30 °C/80 bar led to the simultaneous formation of carbon dioxide/water (C/W) and water/carbon dioxide (W/C) emulsions, in which the dispersed phase occupied up to 10% of the volume depending on the conditions employed. These emulsions were stable for several minutes. On the other hand, inclusion of 1% of the non-ionic surfactant Tween 80 led to the generation of C/W emulsions which were stable for over 1 hour after ceasing sonication, and in which all of the carbon dioxide present in the system comprised the dispersed phase.

The mixing capacity of pulsed ultrasound was assessed by studying the mass transfer of the hydrophobic compound benzaldehyde across the carbon dioxide/water interface, and more importantly led to determination of the system mixing time, at which point the driving force for diffusive mass transfer reaches equilibrium. A model for mass transfer with a fast chemical reaction, namely the hydrolysis of benzoyl chloride, was used to separate the

mass transfer and kinetic effects, and to identify those reactions that would most significantly benefit from ultrasound-induced emulsification.

The Barbier synthesis, a synthetically important reaction, was studied as an example of a transformation occurring in a multiphase liquid/liquid/solid mixture. For the first time, this synthesis was shown to occur in a carbon dioxide/water mixture as solvent, leading to moderate to high yields. Moreover, it was possible to recover the homoallylic alcohol product directly from the carbon dioxide phase in which it was preferentially partitioned.

Acknowledgements

First and foremost I would like to thank my supervisors Dr. Gary Leeke for giving me this great opportunity and for providing moral support and valuable input throughout this study; and Dr. Liam Cox for his valuable collaboration and expert advice in matters of organic chemistry, and for providing access to the facilities at the School of Chemistry.

I would like to thank Dr. Tiejun Lu whose excellent practical expertise in high-pressure engineering have helped me through many situations, and for entertaining me with interesting conversations about China. I would also like to thank Dr. Alireza Bahari for his help during the first period of the PhD. A thank you also goes to my fellow student colleagues in the supercritical fluids group, especially Fabio, Ricardo, Fabricio, Luis and Luke. A big thank you also goes to Dan for the *philosophical* discussions and the coffee breaks.

It has been a real privilege carrying out research at the University of Birmingham and to benefit from all the facilities and excellent services offered. A thank you therefore must also go to the staff at the administrative office, in particular to Lynn Draper for providing all the essential assistance.

Finally, I would like to thank my family for all the support and encouragement that they have shown throughout this time.

Table of Contents

ABSTRACT	I
ACKNOWLEDGEMENTS.....	III
TABLE OF CONTENTS.....	IV
LIST OF FIGURES.....	IX
LIST OF TABLES	XIII
CHAPTER 1: INTRODUCTION	1
1.1 Background.....	2
1.2 Objectives	4
1.3 Thesis Layout.....	5
1.4 Publications Arising From this Work.....	7
1.5 International Conference Proceedings.....	7
CHAPTER 2: LITERATURE REVIEW	8
2.1 Introduction	9
2.2 Compressed Carbon Dioxide as a Solvent	10
2.2.1 Historical Perspective	10
2.2.2 Properties of Dense CO ₂	11
2.2.3 Reactions in Dense CO ₂	13
2.3 Biphasic Systems: CO ₂ /H ₂ O as a Green Alternative	16
2.4 Properties of Emulsion Systems	18
2.4.1 Emulsion Theory.....	18
2.4.1.1 Attractive Forces	20
2.4.1.2 Repulsive Forces.....	21
2.4.1.3 Mechanisms of Emulsion Breakdown	22
2.4.2 CO ₂ /H ₂ O Emulsions.....	22
2.4.3 Investigative Techniques for Characterisation of High-Pressure Emulsions	24
2.4.3.1 Droplet Size	25
2.4.3.2 Volume Fractions.....	28
2.4.3.3 Determination of Stability by Turbidity Measurements.....	28
2.5 Sound-Driven Processing.....	29
2.5.1 General Aspects of Ultrasound Theory	29

2.5.2 Cavitation: Bubble Inception, Growth and Implosion	30
2.5.3 Ultrasound-Induced Transformations: Chemical vs Physical Effects.....	32
2.5.3.1 Comparison of Ultrasound with Mechanical Stirring	36
2.5.3.2 Fluid Flow and Mixing in Acoustically-Agitated Systems.....	37
2.5.4 Cavitation in High-Pressure Fluids: the Blake Threshold.....	40
2.5.4.1 Cavitation in High-Pressure Water and High-Pressure CO ₂ Systems.....	41
2.6 Selection of Candidate Reactions for their Study in Dense CO ₂ /H ₂ O Systems	42
2.6.1 The Barbier Reaction.....	44
2.6.1.1 Green Aspects	47
2.7 Conclusions.....	49
CHAPTER 3: APPARATUS AND EXPERIMENTAL PROCEDURES	50
3.1 Reactor and Peripherals.....	51
3.1.1 The 1 dm ³ High-Pressure Ultrasound Vessel	51
3.1.2 Ultrasound Processor and Probe	53
3.1.3 Valves, Tubes, Pumps, Meters and Controls	55
3.1.4 Chemical Compounds and Solvents.....	56
3.1.5 Compound Addition to the Reactor	56
3.1.5.1 The 6-port Injection Valve	57
3.1.6 Sampling Sections.....	58
3.1.7 The 30 cm ³ High-Pressure View Cell	59
3.1.7.1 Main Functions of the 30 cm ³ High-Pressure View Cell.....	60
3.1.7.1.1 Observation of Single-Phase Behaviour.....	61
3.1.8 General Process Configuration.....	61
3.1.8.1 Selection of Operating Conditions.....	61
3.2 General Characterisation of the CO ₂ /H ₂ O/Ultrasound System	63
3.2.1 Ultrasound Power Calibration.....	63
3.2.2 Determination of the Presence of Cavitation in the Ultrasound Vessel.....	64
3.2.2.1 Aluminium Foil Erosion	65
3.2.2.2 Sonochemical Tests: The Weissler Reaction	65
3.2.3 CO ₂ /H ₂ O Emulsion Formation, Stability and Composition	67
3.2.3.1 Observation of Turbidity through the Pyrex Tube.....	67
3.2.3.2 Observation of Turbidity through the 30 cm ³ View Cell	69
3.2.3.2.1 Use of the Non-Ionic Surfactant Tween 80.....	70
3.2.3.3 Microscopic Visualisation of CO ₂ /H ₂ O Emulsions	70

3.2.3.3.1 Fused Silica Capillary Method.....	71
3.2.3.3.2 Microchannel Method.....	72
3.2.3.4 Emulsion Volume Fractions	75
3.2.3.4.1 Water Collection Experiments.....	76
3.2.3.4.2 CO ₂ Volume Fractions.....	77
3.2.3.4.3 Gas Chromatography	78
3.2.3.4.4 The Tracer Technique.....	78
3.3 Mass Transfer of Benzaldehyde in CO ₂ /H ₂ O: General Objectives	79
3.3.1 Solubility of Benzaldehyde in Compressed CO ₂ : The Chrastil Method	80
3.3.1.1 Experimental Quantification of Benzaldehyde Concentration in dense CO ₂	82
3.3.2 Benzaldehyde Partition Coefficient in CO ₂ /H ₂ O mixtures	84
3.3.3 Benzaldehyde Mass Transfer in CO ₂ /H ₂ O: The Two-Film Model	85
3.4 Kinetics of Benzoyl Chloride Hydrolysis in CO ₂ /H ₂ O: General Scope.....	86
3.4.1 Determination of Benzoyl Chloride Hydrolysis rates in CO ₂ /H ₂ O	88
3.4.2 Benzoyl Chloride Hydrolysis in the CO ₂ /H ₂ O/Tween 80 System	89
3.5 Damköhler Analysis for Mass Transfer and Reaction in CO ₂ /H ₂ O	91
3.6 Synthetic Applications in CO ₂ /H ₂ O: The Barbier Reaction	91
3.6.1 Particulate Filters.....	92
3.6.2 Method for the Zinc-Mediated Barbier Synthesis.....	92
3.6.3 Sampling and analysis	94
3.6.4 Zinc Particle Size Determination.....	96
3.6.5 Post-reaction Separation.....	96
CHAPTER 4: CHARACTERISATION OF THE CO₂/H₂O/ULTRASOUND SYSTEM	98
4.1 Introduction	99
4.2 Ultrasound Power Calibration.....	99
4.3 Cavitation Activity in High-Pressure Systems.....	102
4.3.1 Cavitation in Dense CO ₂	102
4.3.2 Cavitation in Water: The Sonochemical Test	108
4.4 Characterisation of CO ₂ /H ₂ O Emulsions: Emulsion Appearance	112
4.4.1 Macroscopic Observation of Ultrasound-Induced CO ₂ /H ₂ O Emulsions	113
4.4.1.1 Observation through the Pyrex Tube.....	113
4.4.1.2 Observations through the 30 cm ³ View Cell.....	115
4.4.1.3 Emulsion Stability by Time Lapse Recordings	116
4.4.1.4 Observation of Tween 80-Stabilised CO ₂ /H ₂ O Emulsions	118

4.4.2 Microscopic Visualisation of CO ₂ /H ₂ O Emulsions	120
4.4.2.1 Visualisation of CO ₂ /H ₂ O Droplets: The Capillary Method	120
4.4.2.2 The Microchannel Method.....	122
4.5 Characterisation of CO ₂ /H ₂ O Emulsions: Emulsion Volume Fractions.....	123
4.6 Conclusions.....	126
CHAPTER 5: MASS TRANSFER AND HYDROLYSIS RATES IN CO₂/H₂O	127
5.1 Introduction	128
5.2 Determination of Benzaldehyde Solubility in CO ₂ : The Chrastil Method.....	129
5.3 Experimental Quantification of Benzaldehyde in CO ₂	134
5.3.1 Effect of the Presence of Water in CO ₂ : Solubility Parameters	137
5.3.2 Benzaldehyde Partition Coefficient in CO ₂ /H ₂ O.....	143
5.4 Benzaldehyde Mass Transfer in CO ₂ /H ₂ O.....	146
5.4.1 Mass Transfer Coefficients for the Silent Case	149
5.4.2 Mass Transfer Coefficients for the Sonication Case	151
5.5 Benzoyl Chloride Hydrolysis Rates in CO ₂ /H ₂ O.....	161
5.5.1 Hydrolysis in the CO ₂ /H ₂ O/Tween 80 System	167
5.5.1.1 Effect of Pulse Rate.....	170
5.5.2 Comparison to the Literature	171
5.6 Damköhler Analysis for Mass Transport with Reaction.....	173
5.7 Mixing Efficiency and Choice of Reactor in Biphasic Chemical Reactions.....	177
5.8 Conclusions.....	178
CHAPTER 6: SYNTHETIC APPLICATIONS IN CO₂/H₂O: THE BARBIER REACTION	181
6.1 Introduction	182
6.2 Zinc-Mediated Barbier Synthesis in CO ₂ /H ₂ O	183
6.2.1 Investigation of Reaction Conditions on the Barbier Synthesis	187
6.2.2 Determination of Zinc Particle Size	191
6.2.3 Partitioning of Reagents and Products.....	196
6.2.4 Effect of Salts on the Allylation Reaction	198
6.2.4.1 Effect on the Chemoselectivity.....	198
6.2.4.2 Effect of Salt on Homoallylic Alcohol K _{CW}	201
6.4 Allylations Using Other Metals	203
6.5 Effect of Allylic Reagent Leaving Group	204
6.6 Effect of Aromatic Aldehyde Structure	205

6.7 The Barbier Synthesis in the CO ₂ /H ₂ O/Tween 80 System	206
6.8 Mass Transfer with Reaction in Liquid-Liquid-Solid Systems	208
6.8.1 Damköhler Analysis for the Barbier Reaction in CO ₂ /H ₂ O	212
6.9 Homoallylic Alcohol Product Separation.....	215
6.10 Conclusions.....	217
CHAPTER 7: GENERAL CONCLUSIONS AND FUTURE RECOMMENDATIONS	218
7.1 General Conclusions	219
7.2 Future Recommendations	223
CHAPTER 8: REFERENCES.....	226
APPENDIX	249
A1.1 UV Absorbance of Sonochemically-Generated Iodine.....	250
A1.2 Stability of Ultrasound-Generated CO ₂ /H ₂ O Emulsions	250
A1.3 Volume fractions of Emulsions Generated by Ultrasound.....	251
A1.3.1 Water Collection Experiments	251
A1.3.1.1 Estimation of Evaporative Water Loss by Sampling.....	252
A1.3.2 CO ₂ Volume Fraction Experiments.....	253
A2.1 Prediction of Benzaldehyde Solubility in CO ₂ : The Chrastil Method.....	254
A2.2 Experimental Evaluation of Benzaldehyde Concentration in CO ₂	255
A3 Benzaldehyde Mass Transfer from CO ₂ to Water	257
A4.1 Benzoyl Chloride Hydrolysis Rates in CO ₂ /H ₂ O.....	261
A4.2 Benzoyl Chloride Hydrolysis in the CO ₂ /H ₂ O/Tween 80 System.....	263
A5 Damköhler Analysis for Hydrolysis of Benzoyl Halides in CO ₂ /H ₂ O.....	264
A6.1 Representative Data for the Barbier Synthesis in CO ₂ /H ₂ O at 30 °C/80 bar.....	265
A6.2 Barbier Synthesis in the CO ₂ /H ₂ O/Tween 80 System.....	268
A6.3 Barbier Synthesis in CO ₂ /H ₂ O with Substituted Aromatic Aldehydes	268
A6.4 NMR Spectral Data.....	269
A6.5 Damköhler Analysis for the Barbier Synthesis in CO ₂ /H ₂ O	277

List of Figures

Figure 2–1 Energy profile of two interacting droplets as a function of interdroplet distance	20
Figure 2–2 Structure of the non-ionic surfactant Tween 80.....	24
Figure 2–3 Photograph showing the quartz capillary used by Raber et al. [2006].....	25
Figure 2–4 Microscopic visualisation of carbon dioxide/water emulsions (C/W): (a) generated by ultrasound [Murphy et al., 2007]; (b) generated by passing through a sand pack and stabilised by 1 wt.% Tween 80 [Torino et al., 2010]	26
Figure 2–5 Schematic representation of the main events occurring during a cavitation cycle.....	31
Figure 2–6 Flow field map generated from LDA data by Kumar et al. [2006], showing the mean velocities ($m\ s^{-1}$) as a result of acoustic streaming in a 2 L vessel; the horizontal lines represent boundary condition locations	38
Figure 2–7 Velocity pattern arising following ultrasonic horn vibration determined by PIV [Dahlem et al., 1999].....	39
Figure 2–8 Representation of the various fluid conditions in relation to the Blake threshold in the presence of acoustic energy.....	41
Figure 2–9 The Barbier reaction.....	44
Figure 2–10 Proposed mechanism for the allylation reaction, reproduced from Dam et al. [2008].....	45
Figure 3–1(a) Schematic diagram showing the main components of the 1 dm ³ ultrasound reactor used throughout this thesis; (b) photograph of the reactor in its standard configuration, before modification of the head to include the ultrasound probe	52
Figure 3–2 The 6-Port valve used for injection of compounds in the CO ₂ phase. In the LOAD position, CO ₂ flows from ports 2–3, bypassing the standard volume loop 1–4; in the INJECT position, flow is diverted through the loop to occupy the volume between positions 2–1–4–3 (5 and 6 are the waste ports).....	57
Figure 3–3 The sampling section, L1, used for evaluation of sample composition from the top CO ₂ fraction of the vessel; (1) vessel CO ₂ outlet; (2) ball valve; (3) 1/16" tube; (4) 20 mL glass vial for sample collection; (5) circulation pump; (6) line to the vessel; a similar configuration was adopted for the sampling section L2	58
Figure 3–4 Drawing of the 30 cm ³ view cell	60
Figure 3–5 Process flow diagram showing the general process configuration adopted for the studies described in this thesis. (1) CO ₂ cylinder; (2) CO ₂ pump P1; (3) automatic back-pressure regulator; (4) heat exchanger; (5) 6-port valve for injection of compounds; (6) pump P2 for secondary H ₂ O addition; (7) 1 dm ³ ultrasound vessel; (8) CO ₂ phase sample from collection line L1; (9) water phase sample from collection line L2; (10) circulation pump P3; (11) 30 cm ³ view cell; (12) in studies of product recovery, V8 provided the vent to the view cell	62
Figure 3–6 The pyrex tube utilised for macroscopic visualisation of CO ₂ /H ₂ O mixtures during sonication in the ultrasound vessel	68
Figure 3–7 Drawing showing the microchannel, silicon wafer, and hole dimensions (see text for description); all measurements in mm.....	73
Figure 3–8 Top view photograph showing the pyrex/silicon device. (a) Black silicon wafer; (b) drilled hole in silicon wafer connecting underside opening to upside channel; (c) etched channel; a transparent pyrex wafer is bonded on top of the silicon wafer	73
Figure 3–9 Photograph showing the underside of the microfluidic device with Nanoport connections. (a) Silicon wafer; (b) adhesive bond; (c) Nanoport; (d) nut; (e) 1/32" PEEK tube.....	73

Figure 3–10 Algorithm used for the calculation of the solubility of benzaldehyde; from Chrastil method [1982].....	82
Figure 3–11 Figure 3–11 Benzoyl chloride hydrolysis in CO ₂ /H ₂ O	87
Figure 4–1 Effect of power amplitude on the temperature rise of the vessel contents following pulsed ultrasound at 20 kHz; ultrasound was stopped after 180 s. Conditions: CO ₂ /H ₂ O 35% v/v, 80 bar, 30 °C initial T	100
Figure 4–2 Plot of the electric power draw and acoustic power absorbed by CO ₂ /H ₂ O calculated using ΔT from Figure 4–1 according to Eq. 3.1. Conditions: 3 min pulsed ultrasound at 20 kHz, CO ₂ /H ₂ O 35% v/v, 30 °C (initial T)/80 bar	101
Figure 4–3 Graph showing the Blake threshold and vapour pressure lines for initiation of cavitation in CO ₂ and water at different temperatures. $P_B = P_H - P_V$; P_B (Blake pressure), P_H (system pressure), P_V (vapour pressure). In order to initiate cavitation an acoustic pressure greater than the Blake threshold must be applied. Reproduced from Kuijpers et al. [2002]	104
Figure 4–4 Figure 4–4 (Left): image of aluminium foil erosion following 1 min sonication in CO ₂ /H ₂ O. Four layers of foil were wrapped around a stainless steel plate positioned 1 cm below the probe. Conditions: CO ₂ /H ₂ O 50% v/v, 30 °C/80 bar, 70% amplitude, 25% pulse rate. (Right): pitting of the horn as a result of cavitation following approx. 1 year of high-pressure operation	106
Figure 4–5 Visualisation of aluminium foil following ultrasound treatment in CO ₂ –H ₂ O at 30 °C/ 80 bar: (a) photograph showing the flat strips of aluminium foil before (left) and after ultrasound treatment in the reactor; (b) and (c) after ultrasound treatment for 20 minutes with CO ₂ /H ₂ O 50 v/v%, 30 °C/80 bar, 70% amplitude; (b= $\times 20$, c= $\times 40$, objective); images were viewed with an Olympus CH2 light microscope and recorded with a Leica DFC259 camera	107
Figure 4–6 Iodine formation from potassium iodide using pulsed ultrasound (80% amplitude). A head pressure was applied to a 800 mL aqueous solution by using nitrogen at 1 or 70 bar and 30 °C. Error < 4%, see Appendix A1.1	110
Figure 4–7 Macroscopic observation of turbidity in the circulating water fraction from the ultrasound vessel observed through the pyrex tube, following sonication (70% amplitude, 25% pulse rate) of CO ₂ /H ₂ O mixtures using 660 cm ³ of water (a, b, and c), or 670 cm ³ of water (all the rest); (a) 27 °C/62 bar (CO ₂ =vapour); (b) 27 °C/70 bar (CO ₂ =liquid/subcritical); 60 s after starting sonication; (c) same as (b), 25 s after stopping sonication; (d) 27 °C/75 bar (CO ₂ =liquid/subcritical); (e) 35 °C/100 bar (CO ₂ =supercritical), 30 s after starting sonication; (f)-same as (e); 50 s after starting sonication	114
Figure 4–8 Observation of the lower water fraction from CO ₂ /H ₂ O mixtures in the ultrasound vessel using the 30 mL view cell; (a) circulation, no sonication; (b) 10 min following the start of sonication; (c) 5 min after stopping sonication and circulation; (d) CO ₂ droplets collecting on the inside edge of the window after stopping sonication and circulation (arrow). Conditions: 30 °C/80 bar, 70% amplitude, CO ₂ /H ₂ O 35% v/v	115
Figure 4–9 Images of the emulsion passing through the view cell from the top CO ₂ fraction of the ultrasound vessel, recorded with the Photron camera; (a) only circulation; (b) after 3 min of sonication with circulation, an insoluble (water-containing) emulsion appears; (c) after 10 min of sonication with circulation, the light is completely blocked by the opacity of the emulsion filling the cell; (d) after 5 min since stopping sonication, light transmittance is partly restored. Conditions: 30 °C/80 bar, 70% amplitude, 25% pulse rate, CO ₂ /H ₂ O 35% v/v	117
Figure 4–10 Stability of CO ₂ /H ₂ O emulsions generated by ultrasound measured as the increase in light intensity through the view cell after stopping sonication and circulation; (♦) turbidity at 0.05 W cm ⁻³ associated with unstable macro-sized droplets formed by interfacial waves; (■) turbidity at 0.55 W cm ⁻³ associated with micro-sized emulsions; both sets were obtained at 30 °C/75 bar, CO ₂ /H ₂ O 50% v/v. (▲) Stability data obtained in the present work: 30 °C/80 bar, 0.2 W cm ⁻³ (75% amplitude), CO ₂ /H ₂ O 35% v/v. Both lines representing stable dispersions fit a second-order polynomial, whereas the low-stability dispersion followed a power relationship (all with $r^2 > 0.99$). See Appendix A1.2.....	117
Figure 4–11 Photograph showing the appearance of the Tween 80 (1%) -stabilised CO ₂ /H ₂ O emulsions through the view cell, following 10 min pulsed ultrasound in the sonic vessel. Conditions: 30 °C/80 bar, 75% amplitude, CO ₂ /H ₂ O 35% v/v	119

Figure 4–12 Observation of spherical droplets approximately 10 μm in diameter generated by pulsed ultrasound of $\text{CO}_2/\text{H}_2\text{O}$. Conditions: 30 $^\circ\text{C}$ /80 bar, $\text{CO}_2/\text{H}_2\text{O}$ 45% v/v, 70% amplitude, 3 min sonication (work undertaken by Dr. Alireza Bahari).....	121
Figure 4–13 Image depicting the failure point as a fracture originating at the channel inlet and progressing downwards towards the chip edge (arrow); water with a head pressure of CO_2 at 60 bar was passed from the reactor through the PEEK/steel connections	122
Figure 4–14 Volume fraction ($V\phi$) of CO_2 dispersed in the water phase following sonication of the $\text{CO}_2/\text{H}_2\text{O}$ mixture at 70% amplitude; the standoff distance (SD) signifies the position of the biphasic line with respect to the probe; the negative values denote conditions in which the biphasic line was above the probe surface (i.e. probe immersed in water). SD was varied by changing the initial water volume in the reactor, which was (from left to right): 800, 700, 650, 630, 600 and 580 cm^3 of water. Conditions: 30 $^\circ\text{C}$ /80 bar, 70% amplitude, 25% pulse rate, see Appendix A1.3.2.....	124
Figure 5–1 Solubility data for benzaldehyde in scCO_2 over a range of temperatures and pressures; experimental data was compiled by Walther and Maurer [1992].....	129
Figure 5–2 Log-log plot of the benzaldehyde solubility (S) vs density (ρ) for the determination of the association constant k from the experimental data reported by Walther and Maurer [1992]; see Appendix A2.1.....	131
Figure 5–3 Plot of $(\ln S - k \cdot \ln \rho)$ vs $1/T$ with $k = 3.259$ (see Appendix A2.1). The values ‘ a ’ (slope) and ‘ b ’ (intercept) were then inserted into Eq. 5.1	131
Figure 5–4 Correlation of experimental data for benzaldehyde, obtained from Walther and Maurer [1992], and the Chrastil predictions using $k = 3.259$, for temperatures of 40 $^\circ\text{C}$ and 80 $^\circ\text{C}$	132
Figure 5–5 Correlation of experimental data for benzaldehyde, obtained from Walther and Maurer [1992], and the Chrastil predictions using $k = 3.259$, for 60 $^\circ\text{C}$	133
Figure 5–6 Correlation of experimental data for benzaldehyde, obtained from Walther and Maurer [1992], and the Chrastil predictions using $k = 3.259$, for 100 $^\circ\text{C}$	133
Figure 5–7 Benzaldehyde concentration appearing in the CO_2 phase following sonication of the $\text{CO}_2/\text{H}_2\text{O}$ mixture. Benzaldehyde (0.061 mol) was directly added to the water phase prior to sealing and pressurisation of the reactor (line of best fit to show when the maximum concentration was attained). Conditions: 30 $^\circ\text{C}$ /80 bar, 70% amplitude, $\text{CO}_2/\text{H}_2\text{O}$ 35 v/v%. See Appendix A2.2.....	135
Figure 5–8 Dependency of pressure on the mole fraction of water in the vapour phase for the $\text{CO}_2/\text{H}_2\text{O}$ system at 50 $^\circ\text{C}$. Adapted from King et al. [1992].....	137
Figure 5–9 Concentration profiles for benzaldehyde appearing in the water phase following 1 mL injection into the CO_2 phase, in the presence of only circulation or under acoustic agitation. Conditions: 30 $^\circ\text{C}$ /80 bar, pulsed ultrasound at 70% amplitude, $\text{CO}_2/\text{H}_2\text{O}$ (35% v/v), see Appendix A3.....	147
Figure 5–10 Plot of the left-hand term in Eq. 5.9, α , against time for benzaldehyde mass transfer for silent conditions (based on mean values shown in Figure 5–9).....	148
Figure 5–11 Plot of the logarithmic mass transfer term ‘ α ’ from Eq. 5.9 (K_{mtCO_2}) and Eq. 5.22 ($K_{\text{mtH}_2\text{O}}$) against time for benzaldehyde in the presence of ultrasound; concentrations and conditions were based on those presented in Figure 5–10; lines are best-fit to the data points. See Appendix A3.....	153
Figure 5–12 Pseudo first-order plots for the hydrolysis of benzoyl chloride in $\text{CO}_2/\text{H}_2\text{O}$, under silent conditions or in the presence of acoustic agitation at different amplitude settings; each value in the legend represents the amplitude setting; the lines are best-fit to the data ($r^2 \geq 0.96$) and the slopes are numerically equal to the observed reaction rate constant, k_{obs} ; see Appendix A4.1. Conditions: 30 $^\circ\text{C}$ /80 bar, $\text{CO}_2/\text{H}_2\text{O}$ (35% v/v).....	161
Figure 5–13 Effect of acoustic power on the apparent rate constant for the hydrolysis of benzoyl chloride, using the data and conditions from Figure 5–12.....	162

Figure 5–14 Scheme showing two hypothetical scenarios for the concentration profile of solutes travelling through two films with simultaneous mass transfer and reaction. C_{Ac} = concentration of species A in the bulk CO_2 phase, C_{Acint} = concentration of species A at the interface on the CO_2 side, C_{Awint} = concentration of species A at the interface on the water side, C_{Bw} = concentration of species B in the bulk water phase, C_{Aw} = concentration of species A in the bulk water phase	165
Figure 5–15 Hydrolysis rates of benzoyl chloride in CO_2/H_2O at 30 °C/80 bar, in the presence and absence of Tween 80 and under various operating conditions; the lines are best-fit to the data, see Appendix A4.1 and A4.2.....	169
Figure 5–16 Observed rate constants (k_{obs})/intrinsic rate constants (k_{rxn}) as a function of the Damköhler number (Da) for the hydrolysis of several benzoyl halides in CO_2/H_2O from the present work and from the results of Timko et al. [2006b]. For silent conditions $2D_{Aw}/d_{32}$ was replaced by kw . Vertical error bars are experimental uncertainties (not shown for literature data). Vertical line represents point when $Da = 1$; horizontal line represents the predicted well-mixed limit. See Appendix A5	176
Figure 6.1 Reaction scheme for the Barbier synthesis, forming homoallylic alcohol.....	182
Figure 6–2 Formation of homoallylic alcohol (1) and benzyl alcohol (2)	185
Figure 6–3 Possible electron-transfer pathway leading to the reduction of aldehyde.....	186
Figure 6–4 Time course of the allylation reaction in CO_2/H_2O . $x:y:z$ represent initial molar ratios (zinc/allyl bromide/aldehyde), while “%” values represent the ultrasound amplitude setting. (- - -) Benzyl alcohol product; (—) homoallylic alcohol product; lines are best-fit to the data. Conditions: $CO_2/H_2O = 42\%$ v/v, 30 °C/ 80 bar, 25% pulse rate	190
Figure 6–5 Particle size of untreated zinc, before and after ambient sonication with a 500 W sonifier at ambient conditions (described in Section 3.6.4).....	192
Figure 6–6 Zinc particle size following sonication of zinc (0.2 mol L^{-1}) in N_2/H_2O for 1 hour at 30 °C/70 bar. Run 1 and run 2 signify repeats of the same experiment (solid lines); samples from runs 1 and 2 after ambient sonication for 2 minutes (dashed line)	193
Figure 6–7 Zinc particle size following sonication in CO_2/H_2O for 1 hour at 30 °C/80 bar; the two data series represent repeats of the same experiment	194
Figure 6–8 Effect of various salts on allylation kinetics (dashed line represents reaction without salt). Conditions: $CO_2/aq. = 40 \text{ v/v}\%$, 30 °C/ 80 bar, ultrasound amplitude 80%.....	200
Figure 6–9 Effect of salt concentration on homoallylic alcohol K_{CW}	202
Figure 6–10 Time course for the formation of the homoallylic alcohol product in the presence and absence of 1% Tween 80. Conditions: 30 °C/ 80 bar, $CO_2/H_2O = 42\%$, v/v, pulsed ultrasound at 80% amplitude, zinc/allyl bromide/benzaldehyde 2:2:1	207
Figure 6–11 Simplified model for the mass transfer of allyl bromide with reaction on the metal particle ..	209
Figure 6–12 Possible transport/reaction pathways experienced by various species during the zinc-mediated Barbier synthesis in CO_2/H_2O mixtures; RX = allyl bromide, R^I = benzaldehyde, ROH = benzyl alcohol, $RZnX$ =organozinc intermediate, $R-R^I$ =homoallylic alcohol product, shown are successive reaction steps of allylzinc formation (1), and homoallylic alcohol formation (2),dashed arrows=mass transfer, solid arrows=reaction.....	210
Figure 6–13 Figure 6–13 Comparison of observed rate constants k_{obs} and intrinsic rate constants k_{rxn} as a function of the Damköhler number Da , for the zinc-mediated Barbier reaction. The vertical error bars are associated with the uncertainties in k_{rxn} ; the horizontal error bars are associated with uncertainties in droplet diameters. Conditions: 30 °C/ 80 bar, CO_2/H_2O (42% v/v), zinc/allyl bromide/benzaldehyde 2:2:1 (based on 0.061 mol of benzaldehyde), 2 hours pulsed ultrasound at 80% amplitude	213
Figure A6 First-order plots for the reaction of benzaldehyde in the Barbier synthesis; k_{obs} (Tween 80) = $4.43 \times 10^{-4} \text{ s}^{-1}$; k_{obs} (without Tween 80) = $1.45 \times 10^{-4} \text{ s}^{-1}$; ($r^2 \geq 0.94$). Conditions: CO_2/H_2O 42% v/v, 30 °C/80 bar, pulsed ultrasound at 80% amplitude	268

List of Tables

<i>Table 2–1 Main properties of Water and Compressed CO₂; modified from Van Iersel et al. [2007]</i>	12
<i>Table 2–2 Pioneering Reactions in dense CO₂</i>	15
<i>Table 5–1 Solubility of benzaldehyde in CO₂ predicted by the Chrastil method</i>	134
<i>Table 5–2 Comparison between the initial benzaldehyde injected in the CO₂ phase (C_{c0} = initial concentration, n_{c0} = initial mols) and the benzaldehyde (C_c, n_c) measured in CO₂ after 40 minutes pulsed ultrasound at 70% amplitude, 30 °C/80 bar, CO₂/H₂O (35% v/v); values in parentheses indicate the concentration assessed 30 minutes after stopping sonication</i>	136
<i>Table 5–3 Solubility Parameters for Various Substances</i>	141
<i>Table 5–4 Comparison of KCW and KOW for Various Compounds</i>	144
<i>Table 5–5 Main physical properties of CO₂ and water at 30 °C/80 bar</i>	155
<i>Table 5–6 Mass transfer coefficients for benzaldehyde under silent conditions and acoustic agitation at 30 °C/80 bar</i>	158
<i>Table 5–7 Comparison of the effective mass transfer coefficient and specific interfacial area obtained with a range of contacting devices</i>	159
<i>Table 5–8 Benzoyl Chloride Hydrolysis Rates in Various Emulsion Systems</i>	171
<i>Table 5–9 Various parameters used for the separation of kinetic and mass transfer properties for the hydrolysis of benzoyl halides in the CO₂/H₂O/ultrasound system reported by Timko et al. [2006b]</i>	174
<i>Table 6–1 Zinc-promoted allylation of benzaldehyde by allyl bromide. Conditions: 2 hours pulsed ultrasound at 80% amplitude, and CO₂/H₂O (42% v/v) unless stated otherwise</i>	184
<i>Table 6–2 Comparison of the zinc-mediated allylation in the presence of ultrasound and pressurised water (by either CO₂ or N₂), or under stirring at ambient conditions in a sealed bottle. Yield/selectivity after 4 hours was unchanged</i>	191
<i>Table 6–3 Effect of salt on the chemoselectivity of the allylation reaction. Conditions: 30 °C/ 80 bar, 2 hours pulsed ultrasound, 80% amplitude, CO₂/H₂O (42% v/v)</i>	199
<i>Table 6–4 Effect of changing the metal mediator on allylations; M/allyl bromide/benzaldehyde 1:1:1 (based on 61 mmol of benzaldehyde); Conditions: CO₂/H₂O (42% v/v), 2 hours pulsed ultrasound 80% amplitude</i>	203
<i>Table 6–5 Allylation reactions with various allylic compounds. Allylic reagent/benzaldehyde 2:1 (based on 61 mmol of benzaldehyde). Conditions: CO₂/H₂O (42% v/v), 2 hours pulsed ultrasound 80% amp. X = leaving group in allylic reagent</i>	204
<i>Table 6–6 Allylation reactions with substituted aromatic aldehydes. Conditions: 30 °C/80 bar, CO₂/H₂O (42% v/v), 2 hours pulsed ultrasound 80% amplitude, zinc/allyl bromide/aldehyde 2:2:1, satd. NaCl where applicable</i>	206
<i>Table A1–1 Sonolytic iodine formation</i>	250
<i>Table A1–2 Integrated density values calculated by ImageJ for stability of CO₂/H₂O emulsions</i>	250
<i>Table A1–3 Water volume fractions ($V_w\phi$) in dispersions generated by ultrasound</i>	251
<i>Table A1–4 CO₂ volume fractions ($V_c\phi$) from emulsions generated by ultrasound</i>	253
<i>Table A2–1 Calculated Chrastil parameters for the prediction of the solubility of benzaldehyde in CO₂ using $k = 3.259$</i>	254
<i>Table A2–2 GC Data for evaluation of benzaldehyde concentration in CO₂</i>	255

<i>Table A3–1</i>	<i>Concentration of benzaldehyde appearing in the water phase following injection in the CO₂ phase.....</i>	<i>259</i>
<i>Table A3–2</i>	<i>Log-time values for benzaldehyde mass transfer with circulation.....</i>	<i>260</i>
<i>Table A3–3</i>	<i>Log-time values for evaluation of the mass transfer coefficients on the CO₂ K_{mtCO_2} and on the water side (by the Laplace method, K_{mtH_2O}) during sonication.....</i>	<i>260</i>
<i>Table A4–1</i>	<i>Benzoyl chloride hydrolysis rates in CO₂/H₂O</i>	<i>261</i>
<i>Table A4–2</i>	<i>Benzoyl chloride hydrolysis in the presence of Tween 80.....</i>	<i>263</i>
<i>Table A4–3</i>	<i>Rate constant for benzoyl chloride hydrolysis in the presence of Tween 80.....</i>	<i>263</i>
<i>Table A5</i>	<i>Parameters for the Damköhler analysis of the hydrolysis of benzoyl halides.....</i>	<i>264</i>
<i>Table A6–1</i>	<i>Data for the zinc-mediated Barbier reaction between benzaldehyde and allyl bromide in CO₂/H₂O.....</i>	<i>265</i>
<i>Table A6–2</i>	<i>GC retention times of reagents and products employed in the Barbier synthesis.....</i>	<i>268</i>
<i>Table A6–3</i>	<i>Damköhler parameters for the Barbier synthesis</i>	<i>277</i>

Chapter 1

INTRODUCTION

1.1 Background

Biphasic systems play an important role in the chemical, petrochemical and food industries. They are traditionally symbolised by gas-liquid operations, in which solutes transfer to either the gas or liquid phase depending on the specific requirements. In this way, chemical species may be preferentially *trapped* in one phase while being separated from the counter-phase. In many cases, the transfer of the chemical species is coupled to a reaction which has the purpose of either depleting the reactant to form an innocuous product, such as in applications for the removal of hazardous pollutants, or to generate a product of desirable commercial value. In both cases, the first step of the process involves the mass transfer of the solute across the interface. In this respect, homogeneity of the system may be characterised by more efficient mixing between the phases and increased mass transfer effects. Interfacial areas and turbulent flow may both control mixing on the small and large scales. Therefore, for novel reactor designs, evaluation of the effects of mixing on the hydrodynamic and mass transfer properties is important for selecting those reactions that will experience the greatest enhancements.

Liquid-liquid systems are less commonly encountered than gas-liquid systems, although with the increase in the use of dense carbon dioxide as a high-density, low-viscosity solvent, the number of applications employing carbon dioxide as a benign counter-phase have also increased, and include the use of carbon dioxide/water, and carbon dioxide/ionic liquid biphasic systems. Pioneering work by the Johnston group in the field of carbon dioxide/water emulsions has shown great capabilities for their use in many applications including reactions and separations [Da Rocha *et al.*, 1999]. These systems rely on the use of surfactants that, depending on their chemical nature, stabilise either carbon dioxide or water droplets as the dispersed phase. The main advantage of these systems is that high

interfacial areas may be achieved potentially leading to enhanced mass transfer rates. However, the use of surfactants may not always be advantageous in applications that require separation of the phases, due to difficulties inherent with emulsion breakdown. High surface areas through multiphase dispersions may also be achieved by contacting devices such as high-shear mixers and ultrasonic mixers. High power ($> 1 \text{ W cm}^{-2}$ of irradiating surface), low frequency ($< 100 \text{ kHz}$) ultrasound may offer distinct advantages compared to conventional emulsifying devices including effects arising from cavitation, such as erosion of soft surfaces, formation of micro-sized emulsions, increased turbulence through acoustic streaming (physical effects), as well as enhanced kinetic rates due to sonochemical activity (chemical effects). Recently, an ultrasound reactor was designed and used by the Tester group at MIT for the generation of carbon dioxide/water emulsions and the acceleration of chemical reactions through mass transfer enhancements [Timko *et al.*, 2006b]. Progress in this field would be highly desirable, especially for advancing the understanding of high-pressure biphasic systems, and for aiding their translation into industry.

Therefore, the central objective of the work described in this thesis is to characterise dense carbon dioxide/water mixtures, which are acoustically-agitated using a novel reactor design, namely a 1 dm^3 high-pressure cylinder modified for ultrasound operating in the 20 kHz region.

1.2 Objectives

The objectives of this study are:

- General characterisation of the carbon dioxide/water/ultrasound system, including quantification of the power dissipated through the fluid due to ultrasound, the resulting energy efficiency, and evaluation of the capability of the high-pressure system to mediate sonochemical reactions.
- Characterisation of ultrasound-induced carbon-dioxide emulsions, using both macroscopic and microscopic analysis. A method employing time-lapse recordings has been employed to assess the stability of carbon-dioxide/water emulsions based on macroscopic observations. Two methodologies for microscopic visualisation of carbon-dioxide/water emulsions have been tested. Experiments have assessed the volume fraction of the dispersed phase using a combination of water collection and tracer techniques. For comparative purposes, carbon dioxide/water emulsions stabilised by the non-ionic surfactant Tween 80 has also been studied.
- Based on experimental data, a mass transfer analysis for the transport of a hydrophobic solute (benzaldehyde) from the carbon dioxide to the water phase has been performed using the two-film model in order to quantify the mixing efficiency of the system under conditions of pulsed ultrasound. Experiments have identified the main mass transfer and hydrodynamic parameters involved in acoustic agitation of carbon dioxide/water mixtures.
- The mass transfer model has been extended to include a fast reaction, namely the hydrolysis of benzoyl chloride, in order to separate the mass transfer and kinetic effects and to understand the potential implications of employing high-pressure acoustic agitation for achieving mixing in the presence of a chemical reaction.

➤ Finally, the system has been deployed as a novel methodology for the generation of synthetically important chemical compounds. The Barbier synthesis has been investigated as an example of a multiphase reaction in which the liquid/liquid/solid system experiences dispersion by ultrasound. The effects of the carbon dioxide/water/ultrasound system on the product yield and selectivity have been assessed relative to the same reaction performed under ambient conditions. The system has also been tested for its ability to allow selective partitioning and recovery of the product.

1.3 Thesis Layout

Following this introductory Section, Chapter 2 presents an extensive review detailing the main body of the work undertaken to date in biphasic carbon dioxide/water systems, especially in terms of carbon dioxide/water emulsions and the primary methods available for their study and characterisation. A description of the theory behind ultrasonic processing in relation to both its physical and chemical effects, and the background and rationale behind the Barbier synthesis can be found in Chapter 2.

Chapter 3 summarises all the apparatus and experimental procedures utilised in the present work, including a detailed description of the high-pressure equipment used including vessels, pumps, pipes, fittings, and valves. Here the general methodology for the injection, study, sampling and analysis of organic compounds in carbon dioxide/water will be given.

Chapter 4 contains the results relevant to the general characterisation of the carbon dioxide/water/ultrasound system. The power calibration using a calorimetric technique is described for evaluation of the acoustic power transferred to the fluid. Here the results of cavitation-dependent effects are discussed in relation to the dependence on system pressure. Chapter 4 also contains the results of stability studies of the carbon dioxide/water

emulsion using time-lapse recordings, and results of the study of dispersed-phase volume fractions generated by ultrasound.

The solubility of benzaldehyde in carbon dioxide and water-saturated carbon dioxide, and the partition coefficient of benzaldehyde in the carbon dioxide/water biphasic system are described in Chapter 5 and used to justify the use of benzaldehyde as the model hydrophobic compound to study its transport across the carbon dioxide/water interface. Chapter 5 also presents the use of the two-film model for evaluating the mass transfer coefficients in the presence and absence of pulsed ultrasound, and more importantly, to gain a value for the system mixing time, under which emulsification of the carbon dioxide/water biphasic system results in diffusive equilibrium. Here, the hydrolysis of benzoyl chloride is investigated as a model for mass transfer in the presence of a fast reaction.

Chapter 6 presents results related to the study of the Barbier synthesis in the carbon dioxide/water/ultrasound system, and ways to improve the yield, selectivity and recovery of the homoallylic alcohol product.

Chapter 7 contains the overall conclusions of the work undertaken in the present study, including an insight into the main advantages and limitations of the carbon dioxide/water/ultrasound system, and recommendations on alternative reactor designs and classes of reactions that could benefit from future exploration.

Due to the large number of symbols utilised in Chapter 5, a Notation Section has been included at the end of the Chapter. References have been grouped at the end of the thesis.

1.4 Publications Arising From this Work

- Cenci, S. M., Cox, L. R. and Leeke, G. A. (2012). Recent advances in catalysis for efficient process chemistry. *Recent Pat. Catal.*, **1**, (1) 2-12.
- Cenci, S. M., Cox, L. R. and Leeke, G. A. (2014). Ultrasound-induced emulsification of subcritical carbon dioxide/water with and without surfactant as a strategy for enhanced mass transport. *Ultrason. Sonochem.*, **21**, (1) 401-408.
- Cenci, S. M., Cox, L. R. and Leeke, G. A. (2014). Ultrasound-induced CO₂/H₂O emulsions as a medium for clean product formation and separation: The Barbier reaction as a synthetic example. *ACS Sustainable Chem. Eng.*, **2**, (5) 1280-1288.

1.5 International Conference Proceedings

- Cenci, S. M., Bahari, A. and Leeke G. A. (2010). Carbon–carbon coupling in a biphasic system of water and supercritical CO₂. *AIChE Annual Meeting*, Salt Lake City, UT, November 7–12.

Chapter 2

LITERATURE REVIEW

2.1 Introduction

Due to current economic, social and environmental challenges, the manufacture of chemicals requires increased innovation at the chemistry/engineering interface [Tucker, 2006; Federsel, 2009; Davies and Welch, 2009]. As a consequence, the development of novel synthetic procedures that focus on the use of inexpensive raw materials, higher energy efficiency, and improved separation and recovery of products, have become increasingly important [Cooper *et al.*, 2010]. While the bulk chemical industry has progressively evolved to undertake safer and cleaner processes, the fine chemicals industry still suffers from a lack of alternative, more sustainable methods [Sheldon, 1997]. The manufacture of chemicals and pharmaceuticals therefore requires the development of novel synthetic procedures whose overall life-cycle benefits from higher energy efficiency. Only in recent years have the major pharmaceutical and chemical companies endeavoured to apply green chemistry ethics to the manufacture of chemicals. In this respect, the right choice of solvents plays a crucial aspect for the development of safer and cheaper processes, with properties such as melting and boiling points, flammability, toxicity, and recyclability comprising only a few of the key selection parameters involved [Henderson *et al.*, 2011].

This review presents the most recent advances in the fields of organic synthetic applications using compressed carbon dioxide and carbon dioxide/water mixtures as solvents, with particular emphasis on emulsion systems. The theory of ultrasound is introduced, in the context of its use as an alternative form of energy able to induce chemical and physical changes in the irradiated fluid. Finally, the Barbier reaction is discussed as a potential example for studying synthetically useful transformations in carbon dioxide/water systems.

2.2 Compressed Carbon Dioxide as a Solvent

Compressed carbon dioxide shows solvent properties similar to those of a non-polar liquid, making it the compound of choice for many industrial applications, including extractions and purifications, preparation of coatings, and chemical synthesis. For this reason, its use as a replacement solvent in synthetic industrial processes is rapidly increasing, and has become an integral part of Green Chemistry research. Compressed gases, and especially Supercritical Fluids (SCFs), have been extensively investigated and employed for their capacities to act as solvents in a range of transformations [Leitner and Jessop, 1999]. Most SCFs are low molecular weight substances with relatively low critical temperatures, making them ideal solvents for operations that ultimately require the recovery of thermally-labile compounds. Depressurisation of the SCF will finally leave any previously-dissolved species free from solvent residues. Other advantages of SCFs include the capacity to tune the solvent power by altering the pressure and temperature (and hence density), and the combination of gas-like diffusivities (faster reaction rates) with liquid-like solubilities.

2.2.1 Historical Perspective

Studies regarding the solubility of substances in supercritical fluids were first undertaken 50 years after the discovery of the critical point of substances in 1822 by Cagniard de la Tour [McHugh and Krukonis, 1994]. Subsequently, Thomas Andrews (Queen's College, Belfast) undertook extensive investigations on the phase behaviour of carbon dioxide (CO_2). However, due to technical and social barriers, and a rising demand for cheaper energy, the first commercial supercritical CO_2 (scCO_2) fluid technology for food

applications was not developed until 1978, when the first plant for the decaffeination of coffee beans by HAG AG (Bremen, Germany) was constructed [Saito, 1996].

2.2.2 Properties of Dense CO₂

Owing to its low critical point (31 °C/73.8 bar), non-toxic, inert nature, and ease of separation upon depressurisation, liquid or scCO₂ is often the preferred choice out of other commonly used compressed fluids. Supercritical solvents that are usually employed for a range of applications include: scH₂O (potentially corrosive), scC₂H₄ (flammable), scC₃H₈ (flammable), and scXe (expensive) [Darr and Poliakoff, 1999]. The main physicochemical properties of CO₂ and water are summarised in Table 2–1, modified from Van Iersel *et al.*, [2007].

Although the use of dense CO₂ as a solvent has attracted much attention as an alternative to organic solvents, its behaviour at the molecular level is still poorly understood. The extremely low polarisability which is lower than for alkanes, coupled to its low relative permittivity, has led researchers to traditionally classify CO₂ as an extremely non-polar solvent with properties which are opposite those of water. However, initial observations revealed that the physicochemical properties of CO₂ varied from those of hydrocarbons, resulting in significant differences when comparing the solubility of many compounds [Raveendran *et al.*, 2005]. The solubility of a substance is often proportional to the vapour pressure of the substance; on the other hand, in compressible fluids at higher pressures, intermolecular forces become more dominant with higher fluid densities, so that for higher molecular weight compounds solubility increases with pressure.

Property	H ₂ O (20 °C/1 bar)	Liquid CO ₂ (15 °C/52 bar)	scCO ₂ (> 31 °C/74 bar)
Density, ρ (kg m ⁻³)	998	825	400-985
Viscosity, μ (Pa s)	1×10^{-3}	7×10^{-5}	4×10^{-5} - 1×10^{-4}
Diffusivity (cm ² s ⁻¹) ^(a)	$\sim 10^{-5}$	$\sim 10^{-4}$	$> 10^{-3}$
Speed of sound, C (m s ⁻¹)	1483	394	171-746
Saturated vapour pressure, (N m ⁻²)	2×10^3	51×10^5	varies with T and P
Surface (single phase), or interfacial (between phase and respective counter- phase) tension, σ (mN m ⁻¹) ^(b)	72 30-50 (H ₂ O/alkanes)	2 < 20 (CO ₂ /H ₂ O)	<i>n.a.</i>
Kamlet-Taft polarisability, π^*	1.09	<i>n.a.</i>	-0.1 (alkanes = 0)
Polarity ^(c) E_T^N	1	0.096-0.117 (24 °C)	9.25×10^{-3} - 7.09×10^{-2} (alkanes $\approx 9 \times 10^{-3}$)
Relative permittivity ^(d) , ϵ_r	80	1.5	1.1-1.5

Table 2–1 Main properties of Water and Compressed CO₂; modified from Van Iersel et al. [2007]^(a)[McHugh and Krukonis, 1994].^(b)[Jacobson et al., 1999a].^(c)[Jessop et al., 2012; Jessop et al., 1995].^(d)[Beckman, 2004].

However, early studies by Consani and Smith [1990] highlighted that this was not the case for many compounds, and that the presence of certain functional groups affected the solubility of compounds possessing long hydrocarbon chains. One class of compounds showing specific solute-solvent interactions with CO₂ are perfluorinated hydrocarbons [DeSimone *et al.*, 1992; Dardin *et al.*, 1998]. It is generally accepted that fluorocarbons are highly soluble in CO₂ and that fluorine substitution in otherwise insoluble organic compounds renders them more CO₂-philic [Raveendran and Wallen, 2003].

Although CO₂ has a dipole moment of zero, it differs from hydrocarbons due to its quadrupole moment, which is a result of static charges present on individual atoms. The quadrupole moment of CO₂ is indeed responsible for the dipole-quadrupole interactions with water [Tassaing *et al.*, 2005]. The specific interaction between CO₂ and water will be examined in more detail in Section 5.3.1, when the presence of water in dense CO₂ will be discussed in relation to its effect on the solubility of organic compounds.

Early interpretation of the fluid properties of dense CO₂ led to the realisation that significant rate enhancements in the mass transfer and diffusivity of solutes occurs near the critical region, as a consequence of natural convection phenomena arising from high buoyant effects at low kinematic viscosities [Debenedetti and Reid, 1986], further highlighting the beneficial properties of CO₂ compared to traditional organic solvents.

2.2.3 Reactions in Dense CO₂

Interest in SCFs stemmed not only from their advantageous physical properties but also from their chemical properties. The initial findings that near their critical points and conditions of maximum compressibility, SCFs showed augmented density-dependent accelerations in reaction rates and increased selectivities, provided a scope for further

investigations in this area [Eckert and Knutson, 1993]. The Noyori group first demonstrated the beneficial roles of scCO₂ as a green chemistry solvent for carrying out hydrogenation reactions [Jessop *et al.*, 1994; Noyori, 2005]. The view was that the high miscibility of CO₂ with H₂ (the concentration of H₂ in CO₂ at 50 °C/120 bar was eight times higher than in THF under the same conditions) combined with low generation of volatile organic compounds, would render this type of reaction attractive for large-scale industrial applications [Jessop *et al.*, 1996].

Rate enhancements of up to an order of magnitude have been observed for various transformations near the critical point of solvents including: the decomposition of organic compounds [Johnston and Haynes, 1987], Diels-Alder reactions [Paulaitis and Alexander, 1987], and esterifications [Eckert and Chandler, 1998]. Solvophobic rate enhancements have been documented with decreasing scCO₂ densities for Diels-Alder reactions [Qian *et al.*, 2004].

In recent years, the number and type of reactions explored in dense CO₂ has significantly increased, and include those performed using chemical or biological catalysts (Table 2–2). Various ligands and catalysts have been specifically designed to suit a particular class of reaction. Due to the high solubility of fluorinated compounds in CO₂, perfluorinated ligands have been developed for homogeneous catalysis in CO₂, including hydroformylation [Kainz *et al.*, 1997], Diels-Alder [Oakes *et al.*, 1999] and C–C coupling [Shezad *et al.*, 2002] reactions. The potential for these systems to be employed in an industrial setting has been demonstrated by exploration of their capabilities under continuous flow, at both the laboratory and commercial scale. Licence *et al.* [2003] showed that the production capacity of the palladium-catalysed hydrogenation of isophorone could be scaled-up by a factor of 400 (up to 100 kg h⁻¹) by employing a fixed bed reactor.

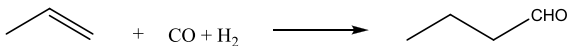
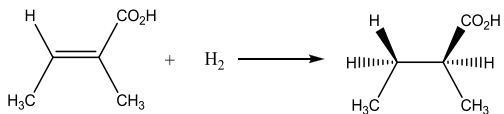
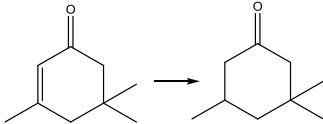
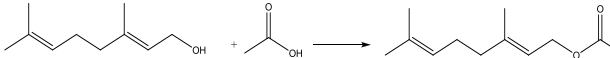
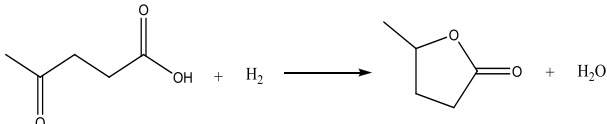
Reference	Conditions	Reaction
[Randolph <i>et al.</i> , 1988]	Cholesterol oxidase/ scCO ₂ 35 °C/100 bar	Cholesterol oxygenation
[Rathke <i>et al.</i> , 1991]	Co ₂ (CO) ₈ scCO ₂ 80 °C/82 bar	
[Xiao <i>et al.</i> , 1996]	Ru catalyst scCO ₂ 50 °C/180 bar	
Thomas Swann Process [Licence <i>et al.</i> , 2003]	Pd/support scCO ₂ /H ₂ 104–116 °C/ 100–300 bar	
[Peres <i>et al.</i> , 2003]	Novozym 435 scCO ₂ 40 °C/100 bar	
[Bourne <i>et al.</i> , 2007]	Ru catalyst scCO ₂ /H ₂ O 200 °C/100 bar	

Table 2–2 Pioneering Reactions in dense CO₂

Lee *et al.* [2005] successfully carried out the Suzuki cross-coupling of bromobenzene and *p*-tolylboronic acid in scCO₂ using palladium(II) microencapsulated in polyurea (PdEncatTM). Subsequently, the Suzuki-Miyaura reaction was extended to continuous-flow mode using the same microencapsulated palladium(II) catalyst in scCO₂ in the presence of methanol as a co-solvent, which showed improved conversions compared to reactions employing toluene/methanol as the solvent [Leeke *et al.*, 2007]. The ability to successfully translate these reactions to a continuous-flow process using CO₂ as the solvent has also led to the synthesis of diaryl ethers and diaryl sulfides using polymer-supported phosphonium fluoride in a fixed-bed reactor [Lee *et al.*, 2008]. These examples demonstrate the wide

scope and success of CO₂ as a solvent, and its wide applicability as a tool for the development of novel synthetic routes in process chemistry.

2.3 Biphasic Systems: CO₂/H₂O as a Green Alternative

One of the limitations of CO₂ is that its solvating power is confined to small, relatively non-polar compounds, which limits its potential use as a renewable solvent for compounds containing hydrophilic groups. One solution is to include a second aqueous phase, such as water, which can greatly increase the accessibility of hydrophilic species (such as salts), that are commonly employed in many organic chemistry reactions. An additional advantage is presented by the reaction of CO₂ with water which leads to the formation of carbonic acid, providing an intrinsic proton source (pH 3–4) [Holmes *et al.*, 1999; Beckman, 2004; Roosen *et al.*, 2007].

The renewable nature of CO₂ and water also makes this solvent mixture particularly attractive for green chemistry applications. Most biphasic systems employ an organic-aqueous biphasic system, and are considered useful strategies for improving product and catalyst separation following a reaction [Cornils *et al.*, 1997; Yoshida and Itami, 2002]. Aqueous biphasic catalysis is a two-phase process in which a catalyst (usually homogeneous) is present in a different liquid phase to that in which reactants and products are dissolved [Cornils, 1999]. The system is most conveniently adopted for reactions such as hydrogenations, hydroformylations, and C–C couplings that rely on expensive transition metal-based catalysts (Pd, Pt, Ru, Rh). At reaction completion, the two phases may be separated: the product is recovered from one phase while the catalyst solution may be recycled. The first catalysts to be employed in biphasic solvents used sulfated phosphine ligands (TPPTS), which are to date still used in industry for the rhodium-catalysed

hydroformylation of propene [Herrmann *et al.*, 1995]. The unreacted liquefied propene and the reaction products are easily separated from the homogeneous aqueous catalyst mixture without resorting to energy-consuming procedures. Due to their versatility, the use of TPPTS ligands has been successfully extended to CO₂/H₂O systems. For example, Heck reactions have been carried out in biphasic CO₂/H₂O using Pd(OAc)₂ as the catalyst and TPPTS as the ligand [Bhanage *et al.*, 1999]. The flexibility of the CO₂/TPPTS strategy in industrial processing has also been exploited by Hallett *et al.* [2008], who performed the hydroformylation of 1-octene using a rhodium catalyst in a THF/water mixture, which was subsequently separated by using CO₂ as a ‘*solubility switch*’ solvent for product and catalyst recovery. Biphasic CO₂/H₂O has also been employed for the sequential hydrogenation/dehydration of levulinic acid in a flow process using a tubular reactor, followed by separation of the product-rich CO₂ phase [Bourne *et al.*, 2007]. Indeed, the mutual solubility of CO₂ and water is low, with mole fractions of water in CO₂ and CO₂ in water being 3.1×10^{-3} and 2.4×10^{-2} respectively, at 25 °C/76 bar [King *et al.*, 1992]. The preferential partitioning of hydrophobic and hydrophilic species at the interface therefore makes CO₂/H₂O systems particularly suited to separation procedures.

However, the addition of a second liquid phase increases the resistance to mass transfer of solutes, and therefore an appropriate strategy should be employed in order to optimise mass transfer rates. Mixing in multiphase systems may be achieved by a wide range of equipment each designed specifically to obtain a particular process outcome. Emulsions result from the mixing of two otherwise immiscible liquid phases, achieving greater interfacial areas, and will be discussed next. The use of ultrasound as a method for achieving both increased surface areas and increased agitation will be introduced in Section 2.5.

2.4 Properties of Emulsion Systems

Mass transfer between the hydrophobic and the aqueous phase may be enhanced by increasing the interfacial area. Emulsions achieve this through the dispersion of one phase into the other by the formation and stabilisation of small droplets.

2.4.1 Emulsion Theory

Typically, emulsions are classed according to their droplet size [McClements, 2011; McClements, 2012]:

- emulsions (or macro-emulsions), with a range of 100 nm–100 µm
- nanoemulsions, with a range of 10–100 nm
- microemulsions^(e), with a range of 2–50 nm.

Emulsions and nanoemulsions are thermodynamically unstable [Taylor, 1998], according to Eq. 2.1:

$$\Delta G_f = A\gamma - T\Delta S \quad (2.1)$$

where ΔG_f is the free energy of formation, $A\gamma$ is the interfacial free energy term of the droplets (A being the total surface area, and γ the surface tension), and $-T\Delta S$ is the entropic term. The entropic term is always negative as the number of possible configurations accessible to an emulsified system is greater than that accessible to any single phase [McClements, 2012]. It follows that for emulsions and nanoemulsions ΔS is low, due to the small number of droplets formed. For these systems, $A\gamma$ outweighs $-T\Delta S$, and ΔG_f is greater than zero. Although thermodynamically unstable, emulsions and nanoemulsions are kinetically stable. The kinetic stability depends on the magnitude of the energy barrier present between the dispersed and the separated states which, for this particular range of

^(e)The contradiction in the terminology bears a historical reason.

sizes (nano- and micrometre), is dependent on a range of hydrodynamic phenomena (or fluid flow factors), namely interface mobility and presence of surfactants [Petsev, 2004]. In essence, due to the viscosity of the two fluids, motion in one fluid will be transferred through the boundary onto the other fluid. It is generally accepted therefore, that the rate of approach of two droplets is proportional to the rate of thinning of the film between them. The kinetic stability may therefore be prolonged in these systems by controlling the particle size distribution and by including stabilisers (emulsifiers, texture modifiers, weighting agents or ripening modifiers).

Microemulsions, on the other hand, are thermodynamically stable systems. In this case, $\Delta G_f < 0$ due to ΔS being the dominant term when large numbers of smaller droplets are formed compared to conventional emulsion systems. For microemulsions, and nanoemulsions of size < 90 nm, kinetic stability tends to increase as the gravitational forces leading to separation (creaming and settling) are outweighed by Brownian motion due to smaller droplet sizes.

The thermodynamic and kinetic theories of emulsion formation and stability may incorporate factors that arise due to the presence of surfactants. The most important observation of emulsion behaviour in the presence of surfactants is summed in the Bancroft rule: “*the phase in which the surfactant is the most soluble, will be the continuous phase*”. The oil/aqueous/surfactant system is a dynamic one, where surfactant molecules continuously diffuse through the continuous phase to the droplet surface and vice versa.

The forces governing emulsion stability are attractive and repulsive. Droplet-droplet interactions at relatively large separations (10^{-8} m $< d < 10^{-7}$ m), are described by the Derjaguin, Landau, Verwey, and Overbeek (DLVO) theory [Verwey and Overbeek, 1948;

Derjaguin *et al.*, 1954], in which the Van der Waals attractive potential is balanced by the repulsive potential (Figure 2–1).

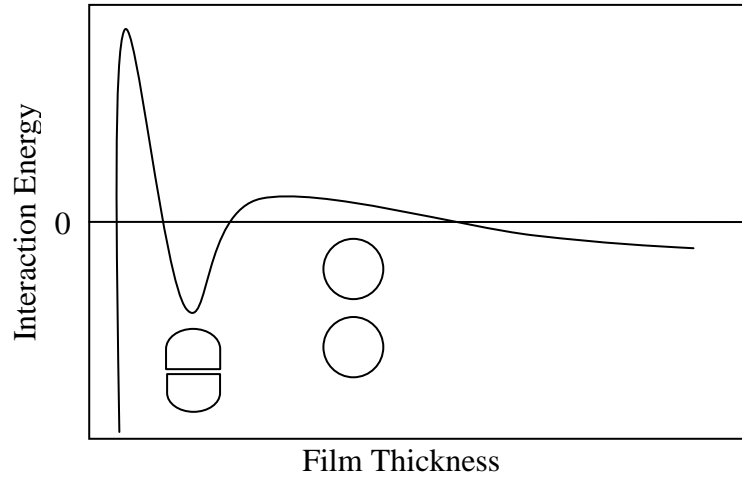


Figure 2–1 Energy profile of two interacting droplets as a function of interdroplet distance [Petsev, 2004]

2.4.1.1 Attractive Forces

The potential of attraction (V_a) between two droplets of radii r_1 and r_2 is given by Eq. 2.2:

$$V_a = -\frac{A_H}{12} \left[\frac{y}{x^2 + xy + x} + \frac{y}{x^2 + xy + x + y} + 2 \ln \left(\frac{x^2 + xy + x}{x^2 + xy + x + y} \right) \right] \quad (2.2)$$

Where $x = d/2r_1$, $y = r_2/r_1$, and d is the shortest distance between the droplets. The energy of attraction is limited by A_H , also known as the Hamaker constant (Eq. 2.3):

$$A_H = \pi^2 (\rho N_A / MW)^2 \beta_1 \quad (2.3)$$

Where ρ is the density of the material in the particles, N_A is Avogadro's number, MW is the molecular weight of the material, and β_1 is the interaction of a pair of the molecules that make up the particles. As can be inferred from Eq. 2.2, when d decreases, the potential for attraction increases in magnitude until it reaches infinity upon contact.

2.4.1.2 Repulsive Forces

The repulsive potential is generally the result of adsorption of surfactant molecules, although it can also be induced by the adsorption of hydroxyl ions or protons [Pashley, 1981]. Furthermore, the presence of other charged species and impurities may also play a role in electrostatic repulsion, V_r (Eq. 2.4):

$$V_r = 2\pi\epsilon_0\epsilon r\varphi^2 \ln\{1 - \exp[-\kappa d]\} \quad (2.4)$$

Where ϵ_0 is the permittivity of a vacuum, ϵ is the relative permittivity of the continuous phase relative to vacuum, φ is the surface potential, and κ is the inverse of the Debye screening length. To date, φ has been conventionally substituted by the zeta potential (ζ), which may be quantified by measuring droplet velocity in an electric field. ϵ is important when considering solvents of different polarities ($\epsilon = 78.54$ and $\epsilon = 2$ for ambient water and compressed CO₂, respectively, [Beckman, 2004]). With decreasing ϵ , collisions are more frequent, and a higher surface potential is required for electrostatic repulsion. This is usually achieved by using ionic surfactants.

Combining Eq. 2.2 and Eq. 2.4 allows evaluation of the total interaction potential. It has been found that droplets require a minimum value for ζ of 30 mV for stable emulsions to persist for periods of days or longer. The ideal situation is encountered when the total interaction potential is zero. Due to the balancing forces between droplets of μm -size, the relation of ζ confirms the thermodynamically unstable nature of emulsions, since the lowest energy configuration attainable is that of coagulated droplets when the total interaction potential reaches infinite negative values.

2.4.1.3 Mechanisms of Emulsion Breakdown

Emulsions gradually decrease in stability via several mechanisms:

Flocculation and Coalescence. Flocculation is the aggregation of emulsions without complete coalescence; a thin film of continuous phase exists between the droplets in the floc. Coalescence is the agglomeration and fusion of droplets into larger ones, with no continuous phase present between the droplets. The film that was separating the droplets has drained or ruptured due mainly to hydrodynamic phenomena.

Settling/Creaming. The droplets will fall or rise depending on density differences between the dispersed and continuous phases. Settling rates are related to droplet size, as defined by Stokes' Law (Eq. 2.5):

$$U = \frac{(2gr^2)(\rho_d - \rho)}{9\mu} \quad (2.5)$$

Where g is the gravitational constant, r is the droplet radius, ρ_d is the droplet density, and ρ and μ are, respectively, the density and the viscosity of the continuous phase. Substituting $U=h/t$ into Eq. 2.5 and rearranging, allows calculation of the settling half-life for a vessel of height h , through Eq. 2.6:

$$t_{1/2} = \frac{9\mu h}{4gr^2(\rho_d - \rho)} \quad (2.6)$$

2.4.2 CO₂/H₂O Emulsions

Work in the fields of surfactant-stabilised water in carbon dioxide (W/C) and carbon dioxide in water (C/W) microemulsions and emulsions began over two decades ago by various groups [Hoeftling *et al.*, 1991; Harrison *et al.*, 1994]. Unlike oil/water emulsions, C/W emulsions may be formed with only 0.1–2 wt.% surfactant due to the lower interfacial

tension between CO₂ and water ($< 20 \text{ mN m}^{-1}$) compared to that between alkanes/water ($30\text{--}50 \text{ mN m}^{-1}$) [Jacobson *et al.*, 1999a]. The interfacial tension between CO₂ and water decreases with increasing pressure [Banerjee *et al.*, 2013] as a consequence of the electrophilicity and significant quadrupole moment of CO₂ leading to partial miscibility with water.

The first type of emulsions of interest were W/C, the principle being that small water droplets in emulsions with high surface areas would mimic the properties of bulk water and form an ideal environment for protein chemistry, separation and environmental science [Johnston *et al.*, 1996]. The first surfactants were non-ionic, and were synthesised from fluorocarbon–hydrocarbon hybrids, due to the inability of CO₂ to solubilise regular hydrocarbon surfactants with ionic headgroups. The higher quadrupole moment of CO₂ compared to other compressed gases such as C₂H₄, impeded sufficient solvation of unmodified hydrophobic tails, leading to increased free energy associated with the transfer of the ionic headgroup [Harrison *et al.*, 1994]. On the other hand, the high solubility of fluorinated compounds in dense CO₂ [Consani and Smith, 1990], which initially found successful application in the synthesis of fluoropolymers [DeSimone *et al.*, 1992], led the way for the development of fluorinated surfactants.

Subsequently, W/C emulsions [Jacobson *et al.*, 1999a] and microemulsions [Jacobson *et al.*, 1999b] were employed for carrying out various reactions, including the hydrolysis of benzyl halides and the hydrogenation of styrene [Jacobson *et al.*, 1999c]. These emulsions were optically transparent, with droplet diameters of $2\text{--}50 \text{ }\mu\text{m}$. Later, C/W emulsions with droplet diameters of $2\text{--}4 \text{ }\mu\text{m}$ were generated by including non-ionic alkylene oxide surfactants [Da Rocha *et al.*, 2001]. These type of emulsions may be formed due to the low solubility of the alkylene oxide chains in CO₂, with water being the continuous phase.

Even if poor correlation to the Bancroft rule was observed, additional effects such as mass and momentum transfer could be taken into account for the mechanisms relevant to emulsion formation and stability. Phase inversion from C/W to W/C could be demonstrated upon increasing the temperature, by conductivity experiments using electrodes placed inside the high-pressure cell [Psathas *et al.*, 2000]. Recently, C/W and W/C emulsions were generated by passing a CO₂/H₂O mixture through a sand pack in the presence of Tween 80, a bio-compatible, water-miscible, non-ionic surfactant, the structure of which is depicted in Figure 2–2 [Torino *et al.*, 2010].

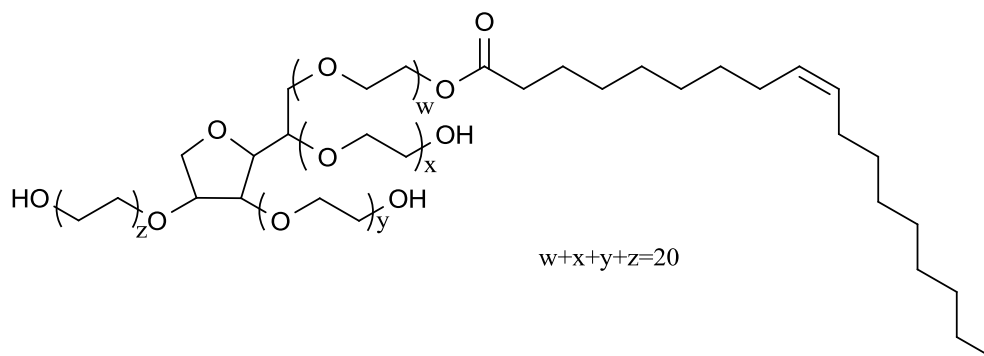


Figure 2–2 Structure of the non-ionic surfactant Tween 80

2.4.3 Investigative Techniques for Characterisation of High-Pressure Emulsions

One of the drawbacks of working with high-pressure fluids is the limited availability of the techniques required for characterising the physical properties of such fluids, compared to those available for systems at ambient conditions. However, a few examples exist where obtaining the physical parameters of high-pressure multiphase systems was possible. More specifically, with respect to high-pressure emulsions, methods that rely on optical measurements have proven to be the most successful.

2.4.3.1 Droplet Size

The most important characteristic for understanding emulsion stability and predicting the transfer and reaction of compounds across the interface is the droplet size. By far the most direct technique for gaining information on size of droplets with diameters $> 1\ \mu\text{m}$ is light microscopy, as it provides information in a model-independent manner. However, investigation of high-pressure emulsions requires specially-constructed chambers, able to withstand the conditions. The most cost-effective way of achieving microscopic visualisation of high-pressure systems is by constructing chambers from thin-walled capillary tubes. The critical aspect of these devices resides in the high-pressure connection. Lee *et al.* [1999] used a fused silica capillary tube ($360\ \mu\text{m OD} \times 100\ \mu\text{m ID}$) with each end placed in PEEK tubing (no indication is provided for the type of seal) connected to 1/16" valves, to characterise W/C emulsions stabilised with ionomeric surfactants up to 350 bar. High-pressure chambers have been developed for a wide range of studies. Early investigations for the characterisation of supercritical fluids containing solubilised proteins relied on specialised high-pressure flow chambers designed for high-pressure Raman and IR spectroscopy [Poliakoff *et al.*, 1995; Leitner and Jessop, 1999]. Raber *et al.* [2006] fabricated a high-pressure capillary to carry out fluorescence microscopy studies of ethanol/water mixtures up to 1000 bar. The high-pressure connection to the quartz capillary was made by employing a high-strength epoxy resin (Figure 2–3).



Figure 2–3 Photograph showing the quartz capillary used by Raber *et al.* [2006]

A further, albeit more expensive approach, is to create channels embedded in small silicon wafers. Recently, the Jensen group fabricated a microchip device by anodically bonding a pair of pyrex and silicon wafers, with the latter containing an etched microchannel; the pressure connections were then formed by soldering the inlet holes of the silicon wafer to 1/16" stainless steel tubes through electron beam evaporation [Murphy *et al.*, 2007].

Both microchannel and capillary techniques have been proven to be successful strategies for characterisation of C/W emulsions. For example, ultrasound-generated C/W emulsions were shown to consist of droplets with diameters of $15 \pm 3 \mu\text{m}$, Figure 2–4 (a), whereas Tween 80-stabilised C/W emulsions were shown to be significantly smaller, with droplet diameters being in the range 0.5–5.4 μm depending on the flow rates through a sand pack, Figure 2–4 (b).

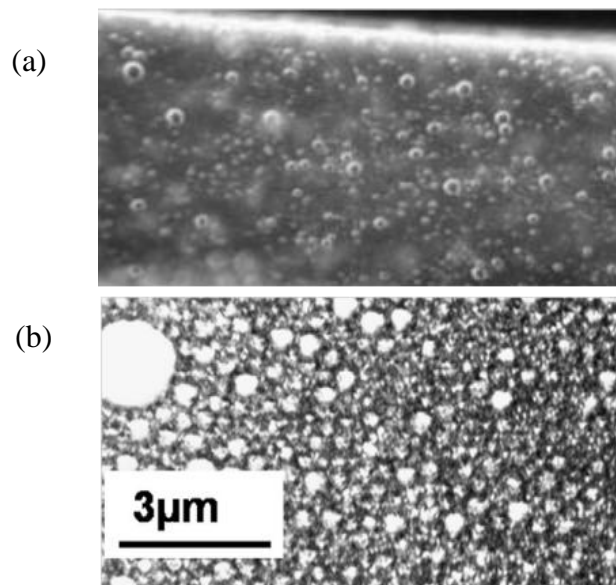


Figure 2–4 Microscopic visualisation of carbon dioxide/water emulsions (C/W): (a) generated by ultrasound [Murphy *et al.*, 2007]; (b) generated by passing through a sand pack and stabilised by 1 wt.% Tween 80 [Torino *et al.*, 2010]

Other optical investigative techniques include the use of instruments that measure the distribution of particles by determining the intensity of scattered light [McClements, 1999].

If the emulsion is unstable, the measurement will detect the change in the particle size

distribution. Dynamic light scattering does not measure the total light scattered but the dynamics over short periods of time [Alexander and Dalgleish, 2006]. Only dilute colloidal systems are suitable for this investigation, as the correlation is based on the assumption that each photon is only scattered once. The light reaching the detector will be a diffraction pattern at a given angle, fluctuating in intensity due to the Brownian motion of the particles. The majority of light scattering instruments are designed for ambient conditions and high-pressure measurements remain problematic. However, specialised devices have been assembled for high-pressure measurements. For example, a laser light-scattering apparatus was designed by Nishikido *et al.* [1980,1981] for determining the size of micelles of ionic and non-ionic surfactants in aqueous solutions up to 1000 bar. Alargova *et al.* [2001] designed and fabricated a high-pressure flow cell equipped with optical windows to determine the size and distribution of polystyrene latex particles suspended in near and critical water by dynamic light scattering. The size of flocculated acrylate polymers in scCO₂ [Yates *et al.*, 1997], and the size of core shell silica in liquid CO₂ [Dickson *et al.*, 2006] were investigated using a high pressure DLS apparatus, finding the colloidal dispersions to be in the order of 100 nm in diameter.

Other, non-invasive techniques have been developed to obtain droplet size measurements without the need to alter the sample. For example, low-intensity ultrasound has been proposed by McClements and Povey [1989] as a method for obtaining thermophysical data of liquids or liquid mixtures. The foundation for resolving droplet size and characteristics lies in ultrasonic scattering theory, which allows extensive emulsion properties to be identified by measuring the attenuation and velocity of sound waves through the emulsion [Friberg *et al.*, 2004]. Low-frequency acoustic techniques may also be employed for probing the critical properties of supercritical fluid binary mixtures [Kordikowski *et al.*,

1996]. Another, non-invasive technique involves the use of pulsed field gradient nuclear magnetic resonance (PFG NMR) spectroscopy, which relies on the measurement of molecular self-diffusion for evaluation of droplets size [Hollingsworth *et al.*, 2004].

2.4.3.2 Volume Fractions

The second most important characteristic which defines emulsions is the volume fraction. In surfactant-stabilised emulsions (such as oil in water emulsions), this is commonly defined as the ratio of the initial volume of the phase to be dispersed as a fraction of the total volume. On the other hand, in systems that do not utilise surfactants, not all of the initial phase to be dispersed may be emulsified, and may form a second phase. Knowledge of these two properties, namely emulsion size and volume fraction, will allow for an estimation of the emulsion surface area. The surface area is important for evaluating mass transport rates and for the prediction of overall reaction kinetics in scale-up operations.

2.4.3.3 Determination of Stability by Turbidity Measurements

The stability of an emulsion is related to the constancy of the interfacial area. The Mie theory of light scattering predicts that there exists a relationship between the turbidity of an emulsion and the interfacial area [Pearce and Kinsella, 1978]. Turbidity measurements can be made with a spectrophotometer, knowing the absorbance and the path length. The stability of dispersions of poly(2-ethylhexyl acrylate) in scCO₂ was assessed by O'Neill *et al.* [1997], who measured the change in turbidity over time, with a high-pressure UV spectrophotometer.

Emulsions and in more general terms dispersions, improve the contact of fluids in multiphase systems. Some form of agitation is usually required to initiate the dispersive process. Ultrasound irradiation of multiphase systems induces important chemical and physical changes, which will be addressed in the following Section.

2.5 Sound-Driven Processing

While the effects of sonochemistry have been studied for more than 80 years, many aspects surrounding ultrasound processing remain elusive and their understanding continues to evolve. Throughout the last few decades, significant advances have been made in the fields of ultrasound processing, which started from the pioneering work undertaken by Mason's group at Coventry University. Ultrasound is widely employed in industrial applications for its ability to act as an alternative energy source to classic stirring and heating [Mason and Lorimer, 2002].

2.5.1 General Aspects of Ultrasound Theory

When a mechanical oscillator (such as a sonic probe) vibrates, the oscillations are transmitted through the medium in contact, in the form of pressure waves. For longitudinally-directed oscillations, the pressure wave is oriented in the same direction as the oscillations [Chen *et al.*, 2012]. Complex patterns arise, whereby the acoustic radiation force propagates with Langevin dynamics, its intensity being affected by the motion of the molecules in its path [Torr, 1984]. As a consequence, the molecules that make up the medium will experience compression, and due to the intrinsic nature of the fluid, restorative forces will result in dilations. Due to the intimate packing of molecules in a fluid, each compression-dilation cycle will affect neighbouring molecules, therefore

allowing the wave to propagate. Part of the wave energy is lost through micro-scattering (heat by friction) and absorption (attenuation) through the material. The product of the density of the medium and speed of sound constitutes the impedance, and both factors affect the propagation through the medium. When vibrations lie above the human threshold for hearing (18 kHz), the sound spectrum enters the ultrasound region, which finds most applications in chemistry and processing as it coincides with frequencies able to excite the medium and induce enhancements in molecular motion. In heterogeneous systems, the radiation force will be directed towards the medium with the highest impedance and therefore lowest energy density. In the case of vapour-liquid systems this will be the liquid. For liquid-liquid systems, the governing factors will be the physical properties of the fluid, such as liquid and vapour densities, viscosity, and surface tension [Issenmann *et al.*, 2011]. In this respect, CO₂ exhibits distinct patterns in high-pressure ultrasound when compared to sonication of ambient liquids [Van Iersel *et al.*, 2010]. For example, interfacial disruption is several orders of magnitude greater in wavelength compared to ambient systems, improving the micromixing and dispersive capacity of these systems compared to ambient conditions.

2.5.2 Cavitation: Bubble Inception, Growth and Implosion

In the majority of applications, the positive effects of ultrasound may be ascribed to the actions of cavitation. Cavitation is the formation of gas-filled bubbles, originating as a consequence of a decrease in the local pressure below the saturated vapour pressure of a liquid (rarefaction). A subsequent high-pressure stage, originating from the compression of the ultrasound wave, forces the bubble to collapse. The time scale of ultrasound-induced cavitation ranges from a few microseconds to a few hundred microseconds and has been

shown to depend on the physical properties of the fluid, such as vapour pressure, surface tension, viscosity and the conditions of the system [Tzanakis *et al.*, 2011].

Figure 2–5 presents a possible scenario that may develop in CO₂/H₂O biphasic systems irradiated with ultrasound energy. Cavity inception occurs preferentially near a surface during the low-pressure stage of the cycle and is characterised by formation of a vapour bubble. Increased mass transfer effects ensure high flow rates of gas across the interface. Surface tension forces prevail and rapid expansion leads to the generation of bubbles of bigger diameters which, during the high-pressure stage, implode, forming a distinctive micro-jet. In the presence of a surface, a counter-jet is formed, leading to a powerful shockwave that breaks any other surrounding bubbles (*'splashing effect'*).

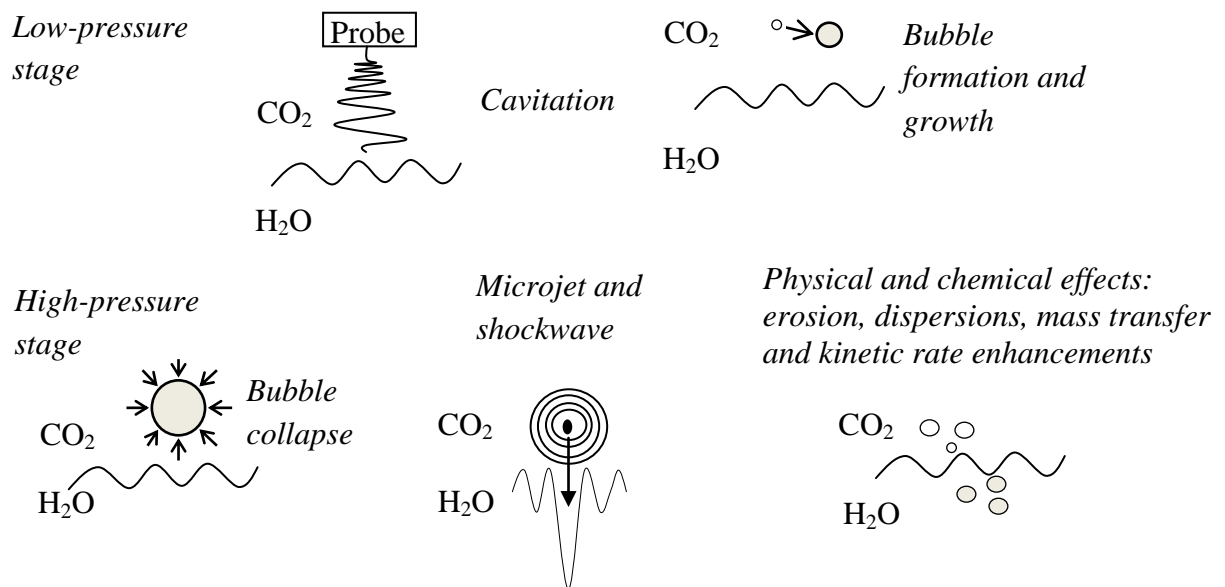


Figure 2–5 Schematic representation of the main events occurring during a cavitation cycle

Destructive high-velocity, high-pressure collisions form increased numbers of micro-bubbles. Depending on the fluid properties, if a powerful jet streaming event occurs,

foaming may develop in the surrounding implosion zone, creating a ‘*cushioning*’ effect. Tension and viscous forces usually counteract each other, so that liquids with high surface tension/viscosity ratios tend to form larger bubbles which are less prone to both collapsing and micro-jetting [Tzanakis *et al.*, 2011]. Surfactants, by lowering surface tension and acting as barriers for mass transfer at the gas–liquid interface, may also affect bubble growth [Leong *et al.*, 2011]. However, the effects of surfactants are complex as they may (i) alter the coalescence between bubbles through adsorption, (ii) increase micro-streaming due to a no-slip condition at the solid boundary [Keswani *et al.*, 2013].

Although cavitation is extremely complex to quantify, several techniques have been utilised in order to gain an understanding of its properties [Sutkar and Gogate, 2009]. The most common include sonoluminescence [Suslick *et al.*, 1990; Suslick and Flannigan, 2008], chronoamperometry [Keswani *et al.*, 2013], surface erosion [Iwai and Li, 2003; Hutli *et al.*, 2008], direct pressure measurements [Campos-Pozuelo *et al.*, 2005], polymer degradation [Price and Smith, 1993], and measurement of the effects of redox reactions [Feng *et al.*, 2002]. Unlike for low-frequency applications, high-frequency (megahertz) ultrasound used in diagnostic applications does not rely on the effects of cavitation and is therefore non-destructive. In these cases the frequencies at which the pressure wave is generated is too high for the successive rarefaction-compression stages of cavitation.

2.5.3 Ultrasound-Induced Transformations: Chemical vs Physical Effects

Ultrasound has successfully been employed for enhancing the rate, yield and selectivity of many reactions [Thompson and Doraiswamy, 1999]. The ‘*hot spot*’ theory of ultrasound predicts that organic compounds with sufficiently high vapour pressures are able to diffuse into rapidly expanding cavitation bubbles, which upon collapsing, induce the sonolytic

reactions that are responsible for great rate accelerations [Kardos and Luche, 2001]. High transient temperatures (5000 °C) and pressures (2000 bar) which originate as a result of localised bubble collapse lead to thermal kinetic enhancements. Often thermal dissociation (sonolysis) of covalent bonds occurs and is responsible for the generation of free radical species that initiate extremely fast reactions on discrete molecules in solution (termed ‘*true sonochemistry*’) [Luche *et al.*, 1990; Flannigan and Suslick, 2005; Pflieger *et al.*, 2010]. Free radicals such as OH• and H• have been detected in solution by various techniques following the application of ultrasound, including electron spin resonance (ESR) and spin trapping [Riesz and Kondo, 1992], and fluorescence dosimetry [Mason *et al.*, 1994; D'Auzay *et al.*, 2010]. Examples where the reaction rates experience an enhancement due to ultrasound-induced free-radical formation have been reported [Cains *et al.*, 1998; Dharmarathne *et al.*, 2012]. Traditionally, ultrasound found extensive applications in the fields of surface cleaning and degradation of organic matter thanks to the presence in many volatile organic pollutants of thermally-labile bonds which readily undergo cleavage upon ultrasonic treatment, thus facilitating oxidation reactions. For example, one recent study investigated the effect of ultrasound frequency on the catalytic degradation of azo dyes using CCl₄, Cu(0) or TiO₂ as the additives [Eren and Ince, 2010]. The authors found that low frequency (20 kHz) ultrasound was more effective than high frequency (1.1 MHz) ultrasound for decomposing the azo dyes when insoluble additives were included, whereas high frequency ultrasound was more effective in the absence of additives due to more efficient release of OH radicals into the bulk solution. An increase in CCl₄ degradation with increasing ultrasound frequency was observed by Petrier and Francony [1997], who postulated that only during conditions (i.e. an optimal frequency of 200 kHz) in which the radicals could escape the collapsing bubble (and avoid recombination), could rate

accelerations take place. Secondary phenomena arising as a result of the primary cavitation event and which are distinct from those related to thermal activation are termed ‘*false sonochemistry*’ [Suslick *et al.*, 1997], or mechanochemistry. Rather than mediating the sonolytic effect as a direct consequence of the hot spots generated during cavitation collapse, the physical effects are the result of hydrodynamic forces arising from a strong extensional flow field in the fluid surrounding the collapsing bubble [Crum, 1995; Kuijpers *et al.*, 2004], and they involve non-volatile substrates which are unlikely to undergo molecular fragmentation. The physical effects of ultrasound may be exploited for treatment of metals, nucleation, and crystal engineering, as well as polymer synthesis [Cravotto and Cintas, 2012; Cravotto *et al.*, 2013]. The use of ultrasonic treatment has been particularly useful for mediating mechanochemical effects on metal-based catalysts via thermally-disfavoured pathways. For example, Tennyson *et al.* [2010] performed C–C coupling reactions and anionic polymerisations in acetonitrile by ultrasound-induced mechanical scission of a Pd(II) macromolecular complex, liberating the active catalyst. Additionally, polymer backbones experience high tensile strain in proximity of hydrodynamic forces induced by ultrasound. Tabata *et al.* [1981] found that the polymeric β -D-glucan drug Schizophyllan could be degraded by ultrasonic treatment, and its high viscosity decreased while retaining the same biological activity.

Research in the use of ultrasound as a means to mediate the enhancement of organic synthetic reactions covers many examples. These processes often involve both heterogeneous species (such as metal catalysts) and discrete organic compounds and therefore the exact mechanism controlling the rate enhancement may not strictly belong to the chemical or the physical type, but may overlap [Cravotto and Cintas, 2007]. In some cases, the effect of ultrasound not only induces a rate enhancement, but also a change in

the distribution of the products [Ando *et al.*, 1984]. Several C–C coupling reactions have shown to undergo rate enhancements compared to conventional heating. Zhang *et al.* [2008] have shown that the reaction time of Suzuki couplings between phenylboronic acid and arylhalides was significantly decreased when ultrasonic treatment was employed compared to conventional heating and stirring. Rajagopal *et al.* [2002] found that the ligand-free Suzuki cross-coupling of arylhalides with phenylboronic acid could be greatly accelerated when performed in ionic liquids under ultrasound irradiation, due to accelerated formation of the active metal complex *in situ*, and possible generation of Pd(0) from a cavitation-induced single electron transfer mechanism. Many other transformations have been performed in the presence of ultrasonic irradiation including C–N and C–O bond-forming reactions, esterifications, etherifications, and C–alkylations/acylations, and have been extensively reviewed in Chen *et al.* [2012]. The presence of high-intensity ultrasound has also been employed to aid in the preparation of a wide range of nanostructured materials [Bang and Suslick, 2010].

Finally, ultrasound has found its way as an emerging technology in the energy industries, especially for the treatment of fuel. Indeed, ultrasound-assisted oxidative desulfurization has been developed as an alternative to high-pressure hydrotreatment for the selective oxidation of sulfur in common thiophenes in diesel to sulfur oxides, using metal [Mei *et al.*, 2003] or activated carbon catalysts [Gonzalez *et al.*, 2012]. In many cases, specialised flow sonoreactors have been tested and proven to be successful even at the commercial scale [Wu and Ondruschka, 2010].

One consistent problem with ultrasonic probes is the increasing erosion of the irradiating surface due to the formation of microjets associated with cavitation, commonly referred to as ‘pitting’. Although improvements in the composition of ultrasonic probes may increase

the resistance to chemical and cavitation attack, it may be important to take into consideration the effects of leached metal species on the performance of reactions, as often catalysis may require extremely low concentrations of active species, as low as in the ppm or ppb range.

Other mechanical effects of ultrasound exist which are unrelated to cavitation, such as acoustic streaming, which is the appearance of a body force due to absorption of energy by the fluid near the ultrasound probe, and interfacial waves, which occur at the interface of fluids of different density following oscillation by the sound wave. These phenomena may contribute to the macromixing capacity of ultrasound, and influence the mass transfer of solutes in fluids. Therefore, the applications for power ultrasound are wide and varied although any potential beneficial role must be determined within a specific set of conditions under which the system operates.

2.5.3.1 Comparison of Ultrasound with Mechanical Stirring

Ultrasound may confer distinct advantages compared to mechanical agitation in multiphase systems due to mass transfer effects at the solid/liquid and liquid/liquid interface.

Hagenson and Doraiswamy [1998] found that for a solid-liquid reaction that did not undergo sonolytic activation, at similar power, ultrasound increased the intrinsic mass transfer coefficient ~2-fold and the effective diffusivity ~3-fold with respect to mechanical stirring. Similarly, the rate of an oxidation reaction was shown to be ~9-times higher under ultrasound-mixing compared to mechanical stirring, due to an apparent reduction in the diffusion layer thickness [Worsley and Mills, 1996]. In these systems, the solid-liquid interface may benefit from advantages due to cavitation of the liquid layer surrounding the solid surface, leading to convection-dependent mass transfer enhancements. Ultrasound

may also induce significant changes in particle aggregation and surface properties due to high velocity collisions and/or erosion of metal surfaces, which are not possible under mechanical stirring [Lindley, 1992].

On the other hand, the advantages of ultrasound may be more subtle for liquid/liquid systems, where cavitation-induced convective phenomena are more pronounced in regions close to the ultrasound probe, and may become irrelevant in reactors of larger dimensions. For these systems, ultrasound may be superior to mechanical agitation as long as the presence of the emulsion provides an advantage to mass transfer (due to increased mass transfer coefficient and increased surface areas). Appropriate reactions (or processes) must be selected in order to highlight any potential beneficial effects of ultrasound. A more detailed analysis will be the scope of Chapter 5, when the mixing properties of ultrasound will be assessed for its capacity to increase the rate of chemical reactions.

2.5.3.2 Fluid Flow and Mixing in Acoustically-Agitated Systems

Heat and mass transfer in multiphase systems is determined by the efficiency of mixing. Mixing is defined as the increase in homogeneity between phases required to achieve a particular process outcome. In multiphase fluids, acoustic irradiation generates mixing through formation of dispersions. However, formation of a fast dispersion is not the only factor affecting mixing efficiency, and the degree of diversification of the flow also plays an essential role [Guida *et al.*, 2010]. Therefore, for novel reactor geometries and fluid systems, the hydrodynamic flow behaviour should be understood in order for mixing to be optimised. In laminar flow systems, the fluid streams flow parallel to each other and the velocity at any point remains constant over time. These conditions permit any convective mass transfer to occur only in the direction of flow and therefore mass transfer mostly

occurs through molecular diffusion. On the other hand, turbulent flow allows separation of the fluid into small domains, therefore significantly reducing the mixing path, and convective mass transfer occurs randomly in all directions. A turbulent flow regime therefore constitutes the most appropriate condition for achieving effective mixing.

The work describing fluid flow in acoustically-agitated systems under a range of ultrasound frequencies, and their study using particle image velocimetry (PIV) and laser Doppler anemometry (LDA) techniques has been recently reviewed [Gogate *et al.*, 2011]. For example, Kumar *et al.* [2006] used LDA (Figure 2–6) to measure mean flow and turbulence parameters in an ultrasonic horn reactor at power densities of 0.015–0.035 W cm⁻³. The authors found that liquid circulation velocities (with axial velocity being much higher than radial and tangential velocities) were higher close to the irradiating source, and significantly lower at the walls and bottom of the reactor, and that most of the turbulence kinetic energy and dissipation rate was occurring in 2% of the total liquid volume below the horn.

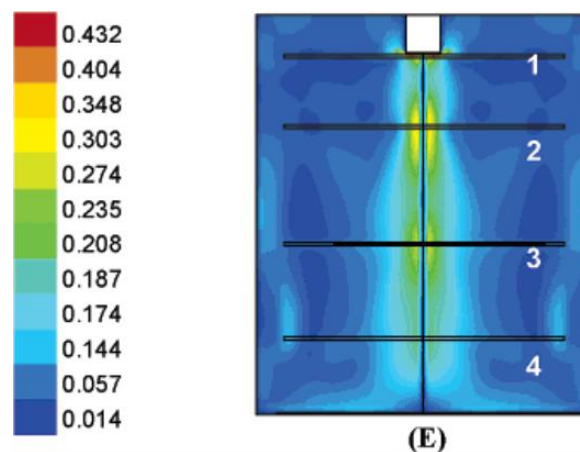


Figure 2–6 Flow field map generated from LDA data by Kumar *et al.* [2006], showing the mean velocities (m s⁻¹) as a result of acoustic streaming in a 2 L vessel; the horizontal lines represent boundary condition locations

Using PIV experiments, Mandroyan *et al.* [2009] measured maximum velocities of 1.1 m s^{-1} in a 537 cm^3 vessel. Most notably, the authors found an inversely proportional relationship between axial velocity and probe diameter, which was the result of the intensity of cavitation bubbles affecting fluid flow. The ability to map the fluid flows originating from acoustic streaming have permitted better understanding of the developing pattern, which is consistent with the generation of two contra-rotating vortices similar to the secondary flow motions observed in mechanically-stirred reactors (Figure 2–7). These optical techniques are however limited by the necessity to visualise tracers through transparent fluids, and the use of glass reactors is usually essential. This becomes a challenge in the case of multiphase fluids, where the generation of dispersions results in the mixture being opaque. Furthermore, although valuable, these methods only describe the Eulerian character of the flow, preventing a full description of the mixing phenomena, which may on the other hand be obtained from Lagrangian information [Ottino, 1989].

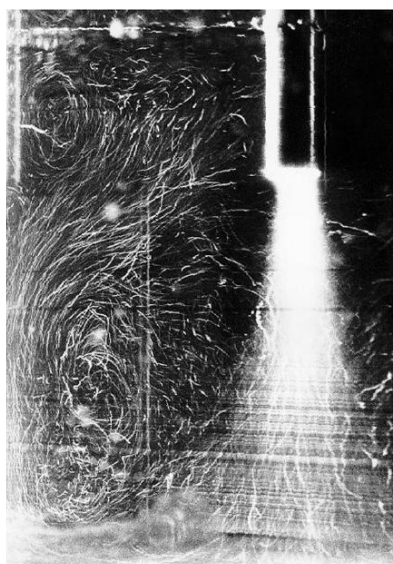


Figure 2–7 Velocity pattern arising following ultrasonic horn vibration determined by PIV
[Dahlem *et al.*, 1999]

An example of a Lagrangian tracking technique is positron emission particle tracking (PEPT), whereby γ -rays released from electron-positron annihilation are captured by two position-sensitive detectors [Barigou, 2004]. A quantitative image of a positron-emitting tracer may be constructed under different conditions of fluid flow, allowing three-dimensional flow fields to be obtained from multiphase agitated systems [Guida *et al.*, 2012]. The PEPT technique has been thus successfully employed for tracking the flow of complex mixtures, where the opacity of the fluid may limit direct optical measurements, and for a diverse range of reactor systems, including for example mapping the flow in a high-pressure fluidized bed [Leadbeater *et al.*, 2012].

The majority of studies examining fluid flow behaviour in ultrasonic systems have concentrated on the application of continuous rather than pulsed irradiation, as the most complex flow patterns are thought to arise during the former. However, pulsed ultrasound may offer distinct advantages compared to continuous ultrasound when mass transport is present in combination with a chemical reaction, and therefore the effect of pulsed versus continuous ultrasound should take into account all aspects of fluid flow in relation to both mass transport and reaction. Indeed, it has been demonstrated that the rate of a fast chemical reaction may depend on the pulse rate, due to an increase in the spatial reactive sites and residual pressure amplitude during the ‘*off*’ stage of the cycle [Tuziuti *et al.*, 2008; Gonzalez *et al.*, 2012].

2.5.4 Cavitation in High-Pressure Fluids: the Blake Threshold

Ultrasound-induced cavitation in high-pressure systems differs significantly from that occurring under ambient conditions, as the vapour pressure of the fluid is a factor of the static pressure of the system. Cavitation occurs at or above the Blake threshold (Figure

2–8), defined as the difference between the hydrostatic pressure (P_H) and the vapour pressure of a fluid (P_V).

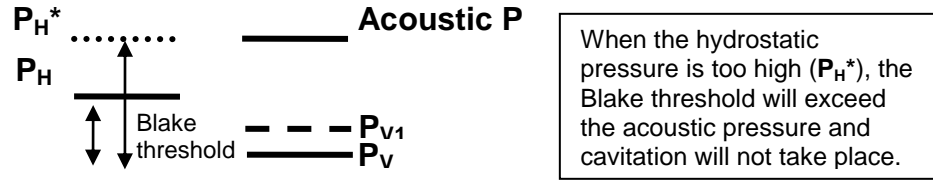


Figure 2–8 Representation of the various fluid conditions in relation to the Blake threshold in the presence of acoustic energy

In high-pressure fluids, initiation of cavitation is dependent on two variables, the static pressure of the system and the vapour pressure of the fluid. For example at $P_H^* = 70$ bar and a temperature of 28 °C, water ($P_V = 0.025$ bar) will experience far less cavitation than CO_2 ($P_V = 65$ bar), due to their respective Blake thresholds of 70 and 5 bar.

Fluid composition may also affect cavitation in high-pressure systems. For example, bubble inception and growth in water strongly depends on the presence of impurities and dissolved gas [Yanagida, 2008; Rooze *et al.*, 2013]. Gas molecules disrupt the ordered structure of water, lowering the surface tension, with the primary result of promoting bubble inception via increased nucleation sites. As discussed previously however, lower surface tensions also contribute to lower shape stability and bubble growth.

2.5.4.1 Cavitation in High-Pressure Water and High-Pressure CO_2 Systems

Few studies exist on the cavitation of water at static pressures above atmospheric. Goldfarb *et al.* [1998] measured the acoustic threshold required for the cavitation-dependent reduction of $\text{Ru}(\text{NH}_3)_6^{3+}$ by a cathodic current response, under a head pressure of either argon or CO_2 . However, the study demonstrated that at higher pressures, the effects observed in the presence of CO_2 were most likely due to cavitation of CO_2 itself rather than

water. Indeed, the relative power required to induce cavitation at 20 °C/10 bar, was lower for CO₂ than for argon, and at pressures of 30–50 bar, the threshold for cavitation under CO₂ gradually decreased to zero, while that for argon rose exponentially. The lower threshold required for cavitation in the presence of CO₂ was ascribed to formation of a transient CO₂ liquid phase and a lower CO₂/H₂O interfacial tension, γ (γ decreased from 70.1 to 14.5 mN m⁻¹ when going from 5 to 51 bar). As a result of the decrease in the pressure amplitude during the rarefaction stage of ultrasound, the condensed CO₂ was able to experience cavitation in water at pressures of 35–50 bar.

Unlike for ultrasound in high-pressure water, a number of applications that rely on the cavitation-induced effects of ultrasound in liquid or supercritical CO₂ have been reported [Matsuyama and Mishima, 2010; Balachandran *et al.*, 2006; Sanganwar and Gupta, 2009; Matsuyama *et al.*, 2011]. For example, Kuijpers *et al.* [2002] demonstrated that cavitation was possible in CO₂-expanded methyl methacrylate (MMA), and that free-radical reactions could be induced for the formation of poly-MMA in a CO₂/MMA mixture but not in pure MMA.

2.6 Selection of Candidate Reactions for their Study in Dense CO₂/H₂O Systems

The number of transformations that have been studied using dense CO₂ as a solvent has greatly expanded in the past few decades and covers a wide range of reactions, including carbonation (CO₂ may act both as a carbon source and as the solvent), alkylation, polymerisation, Diels-Alder, epoxidation, C–C coupling, hydroformylation, hydrogenation and oxidation reactions, in the presence of either homogeneous or heterogeneous catalysts. A recent review by Jessop [2006] provides a comprehensive description of homogeneous organic reactions effected in supercritical fluids. The flexibility of processes using CO₂

furthermore resides in the ability to alter the solvent properties by employing co-solvents which are able to increase the solubility of a variety of compounds, including aromatics, as demonstrated by Xiao *et al.* [1996], who observed an increase in the conversion and selectivity in hydrogenation reactions when fluorinated alcohols were included as co-solvents. Moreover, CO₂ may not exclusively be employed as a solvent for reactions, and its use may be extended as a solvent for carrying out separations and facilitated recovery of catalysts and/or products. In this respect, CO₂ has been successfully employed as an expanding fluid for the organic phase, which may be separated from the aqueous phase following reactions [Hintermair *et al.*, 2011].

Therefore, keeping in mind the wide range of reactions available, together with the processing potential offered by dense CO₂, a selection criterion was adopted for identifying those reactions that could mostly benefit from the presence of a CO₂/H₂O biphasic mixture, while also potentially allowing extending the existing knowledge regarding synthetic applications in green solvents. Most common base-mediated and Pd-catalysed C–C coupling reactions (*i.e.* Suzuki-, Heck-, Sonogashira-, and Stille-couplings), were instinctively ruled out due to the low pH in the presence of carbonic acid. Moreover, the high cost of transition metal catalysts would limit the viability of initial exploratory experiments at the litre scale. The type of reaction would therefore have to fill the following conditions:

- Tolerance to an aqueous environment
- Tolerance to an acidic environment
- Proven beneficial role of a co-solvent
- Presence of multiple immiscible phases that would benefit from ultrasound-promoted dispersion (*i.e.* CO₂/H₂O/solid mediator)

- Ability to recover most of the product by CO₂/H₂O phase separation *in situ*
- Wide catalyst and substrate availability and scope

2.6.1 The Barbier Reaction

Organic reactions in aqueous media have attracted increasing attention due to the benign nature of water as a solvent, and now encompass a wide variety of transformations [Li, 2005]. The branch of organometallic chemistry that includes the study of allylmetals has been significantly developed in the past few decades [Yamamoto and Asao, 1993; Roy and Roy, 2010]. Allylmetal–carbonyl additions offer a particularly important example, as a new C–C bond is formed with the potential for high diastereo- and enantioselectivities [Denmark and Fu, 2003]. The Barbier synthesis is one such important C–C bond-forming reaction, which constitutes a powerful methodology for formation of synthetically valuable homoallylic alcohols, through the one step addition of an electrophilic reagent (the carbonyl) to an allylic reagent, by a metal mediator (Figure 2–9) [Li, 1996].

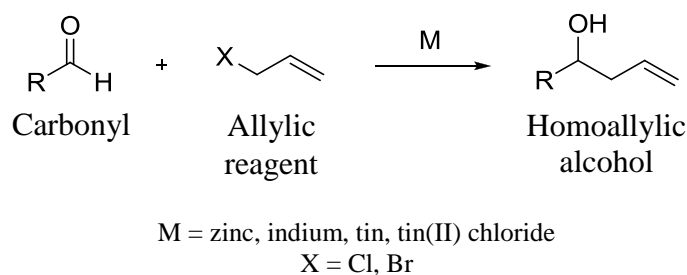


Figure 2–9 The Barbier reaction

The generalised accepted mechanism for many *in situ*-derived allyl metals involves insertion of the metal across the C–X bond of the allyl halide, and formation of a nucleophile allyl metal species which undergoes reaction with the carbonyl via a cyclic,

Zimmerman Traxler-like transition state to provide the corresponding homoallylic alcohol product (Figure 2–10).

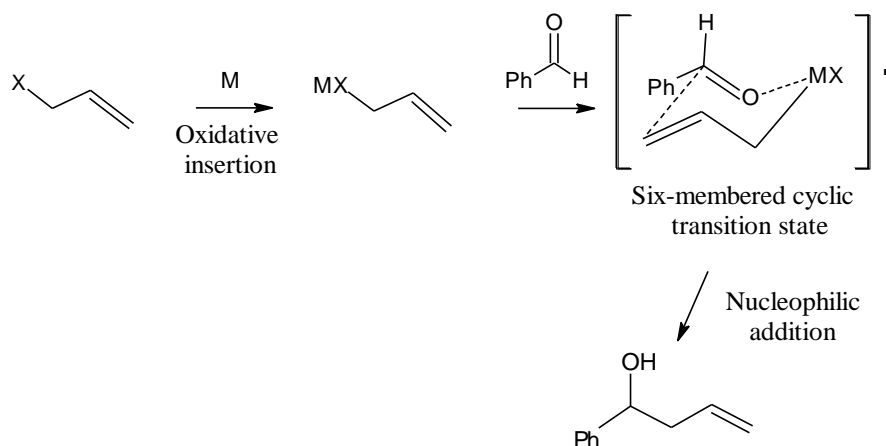


Figure 2–10 Proposed mechanism for the allylation reaction, reproduced from Dam *et al.* [2008]

The use of metal mediators such as zinc and indium greatly increases the environmental performance of these reactions as they are non-toxic and may be employed in the presence of an aqueous environment. Many factors affect the outcome of the reaction, such as activation of the carbonyl, solubilisation of the reagents, and stabilisation of the transition state. Various conditions may thus improve yields, selectivities and rates. They include the use of Lewis acids and bases, Brønsted acids, salts, surfactants, co-solvents and co-catalysts.

The beneficial effect of an aqueous environment may originate from water's ability to stabilise the transition state, or by simply providing a source of H^+ and OH^- ions for final dissociation of the product from the mediator. Early reports by Nokami *et al.* [1983] clearly demonstrated the beneficial role of water in tin-mediated Barbier allylations, which proceeded faster when water was employed as a co-solvent with diethyl ether. In some cases, the presence of water in the biphasic mixture was necessary to dissolve transition metal salts such as SnCl_2 [Ito *et al.*, 2000].

The ability of Brønsted and Lewis acids to act as co-promoters in allylation reactions has also been documented in various reports. Yanagisawa *et al.* [1993] reported that the allylation of carbonyl compounds by tetraallyltin showed exclusive chemoselectivity towards aldehydes when undertaken in a hydrochloric acid/THF mixture. However, no explanation was provided for the observed results. Similarly, the allylation of aldehydes by allyltributyltin in an aqueous acid/THF solvent has been reported [Yanagisawa *et al.*, 1997]. Loh and Xu [1999] subsequently demonstrated the good performance of trifluoromethylsulfonic acid as a catalyst for the allylation of carbonyls with allyltributyltin. This reaction was also efficiently carried out in the presence of carboxylic acids in various solvents [Li and Zhao, 2005]. Furthermore, the regioselectivity of the crotylation could be tuned by varying the acidity of the carboxylic acid solution (highest yields observed with $pK_a < 3.66$). The use of organic proton donors has also been described by Park *et al.* [2008], who describe the use of acetic acid as a proton source in allylation reactions for construction of natural products.

Lewis acids have also been employed as co-promoters for improving allylation reactions. Traditionally, Lewis acids such as $FeCl_3$ have been identified as efficient catalysts for allylation reactions involving allyltrimethylsilane reagents [Watahiki and Oriyama, 2002], although the reactions must be carried out in organic solvents due to the decomposition of $FeCl_3$ in water. Subsequently, lanthanum triflate was shown to catalyse the allylation of aldehydes by stannane reagents with low catalyst loadings [Aspinall *et al.*, 2002]. Recently, lanthanide-surfactant catalysts were developed for the allylation of benzaldehyde with tetraallyltin in water [Deleersnyder *et al.*, 2008]. Finally, formation of the organometallic compound *in situ* may also contribute to additional Lewis acidity due to the formation of metal salts. Although the numerous examples demonstrate the well-accepted

beneficial role of such promoters, the exact mechanism by which Brønsted and Lewis acids mediate an improvement in the allylation reaction has not been elucidated, although activation of the carbonyl oxygen, and activation of the metal surface may be possible effects.

Finally, sonochemical activation has also been demonstrated to influence the efficiency of allylations. Luche and Damiano [1980] first showed the ability of ultrasound to enhance the formation of organolithium and organomagnesium reagents in an organic solvent. Subsequently, the allylation reaction was shown to proceed successfully in an aqueous environment using zinc (the generated organometallic being more water-tolerant than those of Mg or Li) [Petrier and Luche, 1985]. The effect of high intensity ultrasound on metal surfaces is difficult to assess, although it most probably involves activation of the surface by removal of the protective oxide layer and exposure of reactive sites (see Section 6.2.2). Durant *et al.* [1995] reported an increased yield in the allylation of carbonyl compounds by using zinc powder formed via a sonoelectrochemical technique.

2.6.1.1 Green Aspects

Given the appeal of allylation reactions, efforts have been made to improve their industrial aspects, including the use of ionic liquids as solvents [Gordon and Ritchie, 2002], continuous flow [Kopach *et al.*, 2012], or solvent-free conditions [Andrews *et al.*, 2001]. Although Grignard reagents were traditionally employed for allylations of carbonyl compounds, flammability concerns inspired the development of nucleophilic allylating reagents that were stable in aqueous media, allowing allylations to be carried out in water. In this respect, organotin reagents and tin salts were increasingly employed for allylation reactions [Mandai *et al.*, 1984; Boldrini *et al.*, 1987]. However, the toxicity of

allylstannane intermediates has encouraged the search for more benign reagents. As a consequence, indium and zinc were both identified as efficient metals able to carry out allylations in aqueous media. The European Medicines Agency guidelines on the presence of impurities in drug formulations, classify zinc within the group of metals with low inherent toxicity, whereas no guidelines are currently available for indium. Indium is more expensive than zinc and generally requires acid treatment in a quenching step for final release of the homoallylic alcohol product.

Zinc is a cheap and versatile metal which, due to its high water-tolerance, may be found in a number of aqueous synthetic examples. Indeed, zinc has been employed as a mediator in palladium(0)-catalysed coupling reactions, whereby hydrogen formation through the reaction between zinc and water regenerated the Pd catalyst [Mukhopadhyay *et al.*, 2000]. Jessop *et al.* [2002] attempted the addition of diethylzinc reagent to aromatic aldehydes in scCO₂ followed by quenching with an aqueous salt solution to form phenylpropanolol, although the chemo- and enantioselectivities were drastically lower than for other supercritical solvents. The reductive capacity of zinc has also been demonstrated in CO₂/H₂O biphasic mixtures, where the low pH promoted the selective reduction of nitroarenes to *N*-arylhydroxylamines [Liu *et al.*, 2009]. Allylations in only CO₂ have been previously attempted with indium. For example, the indium-mediated allylation of benzaldehyde was carried out in liquid CO₂ in a 10 cm³ reactor (82% yield under vigorous stirring for 48 hours) [Haberman *et al.*, 1999]. However, a quenching step had to be performed on the residue with conc. hydrochloric acid *ex situ*, following depressurisation, limiting the environmental performance of such methodology.

2.7 Conclusions

In this Chapter the most relevant background to this Thesis has been presented, including examples from the literature describing the deployment of dense carbon dioxide/water systems as non-conventional solvents for mediating sustainable synthetic and separation procedures. In this context, CO₂/H₂O emulsions increase the contact between the phases through the stabilisation of µm-sized droplets. The most relevant literature describing the use of ionic and non-ionic surfactants which have been developed based on their solubilities in CO₂ has also been presented. Ultrasound processing has been introduced as an alternative method to mechanical agitation, able to induce physical and chemical effects in the irradiated fluid. Finally, the Barbier reaction is introduced as a potential model for studying synthetically useful transformations in carbon dioxide/water.

In the forthcoming Chapters, the aspects relating to the study of CO₂/H₂O systems in the presence of acoustic agitation using a 1 dm³ high-pressure cylindrical reactor modified for ultrasound, will be given. Due to the novelty of the reactor geometry and dimensions, the results obtained for evaluation of the sonochemical activity, the emulsification capacity, and the mass transfer and kinetic properties will be discussed. Finally, the synthetic and separation capabilities of the CO₂/H₂O system will be determined using the Barbier reaction as an example.

Chapter 3

APPARATUS AND EXPERIMENTAL PROCEDURES

3.1 Reactor and Peripherals

Section 3.1 describes the apparatus employed in the high-pressure studies, including the custom-built ultrasound vessel, the pumps, connections and valves.

3.1.1 The 1 dm³ High-Pressure Ultrasound Vessel

The reactor used for all of the high-pressure ultrasound studies consisted of a cylindrical stainless steel-616 vessel (Parr series 4680, MO, IL), (Figure 3–1). The inside diameter and inside depth were 9.5 cm and 15.8 cm, respectively, and the internal volume of the cylinder was 1.13 dm³. However, the presence of several additional components attached to the vessel head, including the internal cooling loop and the ultrasound probe described in more detail in Section 3.1.3, resulted in the final volume being 1 dm³ (specified by the manufacturer). The vessel had a maximum working pressure of 200 bar at 350 °C. A split ring closure with eight screws (steel A4140, torque 33 Nm) enabled pressure-tight sealing. A PTFE gasket provided the pressure seal. The position of the rupture disk was changed so that it was placed in-line with the pressure gauge and the CO₂ inlet, as shown in Figure 3–1 (a). This resulted in the connector which originally supplied the rupture disk, to now serve as the CO₂ outlet. The remaining opening consisted of a 14 cm, 1/4" OD stainless steel dip tube for sampling from the aqueous fraction present in the lower section of the vessel. The head was modified to accommodate an ultrasonic horn, secured in place with a retainer fitted with screw caps (item 1932HC, steel-4140, with a maximum torque of 13 Nm). These screw caps failed a total of three times during three years of operation either due to the unavailability of an appropriate torque key, making it impossible to control the tightening, or due to wear and tear. The screws failed cross-sectionally, and when this occurred, the bottom half had to be drilled out.

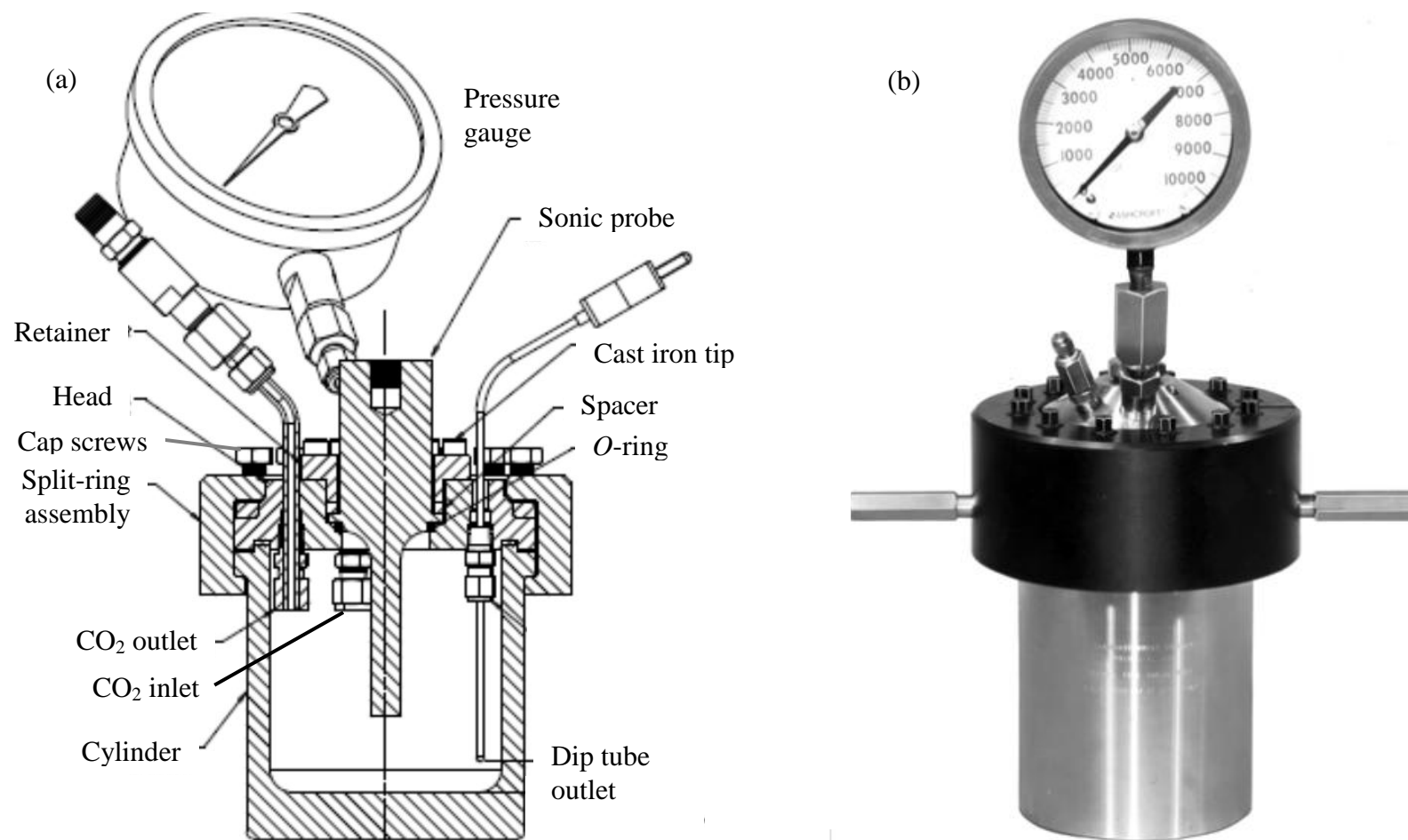


Figure 3-1 (a) Schematic diagram showing the main components of the 1 dm³ ultrasound reactor used throughout this thesis; (b) photograph of the reactor in its standard configuration, before modification of the head to include the ultrasound probe

A flange prevented direct contact between the ultrasound probe and vessel head by creating isolation through an *O*-ring (1.359" internal diameter \times 0.139" width), which becomes compressed when the flange is bolted down. For compressed CO₂ applications, the *O*-ring may either be manufactured from NBR or Kevlar. Wear and tear or excessive compression spuriously resulted in damage to the *O*-ring leading to the reactor leaking through the space between the probe and the vessel head, with parts of the *O*-ring appearing in the vessel following operation.

3.1.2 Ultrasound Processor and Probe

The ultrasonic processor (20 kHz VCX-1500 W, Sonics & Materials, CT, USA) converts 50–60 Hz voltage to high-frequency electrical energy. The alternating voltage reaches the most sensitive component in the ultrasonic processing equipment, namely, a ceramic piezoelectric crystal housed within the converter. Each change in polarity will rapidly contract and expand the crystals leading to transformation of electrical energy into mechanical energy. The high-frequency longitudinal vibrations are amplified by the probe, which, depending on its characteristics, will vibrate at constant amplitude throughout each cycle, thus transferring ultrasound energy through the medium. During the probe's operation, while in contact with the medium, a sensory feedback system relays information on pressure variations (detected as resistance to probe vibration) and adjusts the electrical power draw in order to maintain a constant probe amplitude. A standard probe of tip diameter 1.9 cm (surface area of 2.83 cm²) was used, and consisted of a 90%Ti-6%Al-4%V alloy, which is commonly employed due to its good acoustic properties, high tensile strength, low toxicity, and high resistance to cavitation erosion. The probe further comprised a threaded stud at the top for connection to the converter. The maximum ideal

amplitude of vibration specified by the manufacturer was 75 μm . The amplitude may be controlled by the operator to reach values of 20–100%. Pulsed ultrasound presents a more energy-efficient alternative to continuous sonication. It is often desirable to employ pulsed ultrasound for applications that are temperature-sensitive or require specific types of mixing, as advantageous physical and chemical phenomena (such as settling of the dispersion) are permitted during each *off* stage of the cycle. Pulse rate determines the time during which the probe is conveying energy to the fluid during each cycle and may be varied between values of 1–59 s. For example, a 25% pulse rate signifies that the sonic burst will be *on* for 1 second, and *off* for 3 seconds (unless otherwise specified, 25% pulse rate was used for all the studies described in this thesis). The sonic processor is equipped with a digital display which confers information such as sonication time, power draw (watts), energy (joules) and temperature, allowing the operator to manually preset a range of sonication conditions if desired. The greater the viscosity of the fluid, the greater is the resistance detected, and the processor will respond by increasing the power supply. Small drifts in the resonant frequencies due to resistance will result in the processor stalling. An ‘*overload*’ error message will then be displayed on the unit, shutting down the instrument. This occurred several times, mostly when the fluid pressure was high relative to the temperature. For example, ‘*overload*’ occurred when a $\text{CO}_2/\text{H}_2\text{O}$ liquid mixture was sonicated at 30 °C/100 bar, but not at 50 °C/100 bar or at 30 °C/80 bar, and when $\text{N}_2/\text{H}_2\text{O}$ was sonicated at 30 °C/80 bar, but not at 30 °C/70 bar. Although presently unclear, the occurrence of the *overload* signal could originate from a sudden rise in the acoustic impedance of the fluid. Acoustic impedance is the resistance to wave propagation and is a factor of both the fluid density and the speed of sound through the fluid, so that fluctuations in these properties could result in the processor stalling. Aside from varying the system

temperature and pressure, this impeding problem could also be resolved by decreasing the amplitude setting.

3.1.3 Valves, Tubes, Pumps, Meters and Controls

All valves, tubes and fittings were made from stainless steel and were purchased from Swagelok unless otherwise stated. The openings positioned in the reactor head consisted of drilled holes through which 1/4" tubes could pass and form the relative inlet and outlet pipes. Each tube and opening was sealed via 1/4" NPT bore-through male connectors fitted from the inner side of the reactor head. The outlet originating from the dip tube was controlled by a 1/4" NPT ball valve (Parr item A143VB), whereas the CO₂ outlet was controlled by a 1/8" needle valve. The tube from the remaining opening was connected to the pressure gauge, bursting disc and CO₂ inlet via a 1/4" union cross. The CO₂ inlet was also controlled by a 1/4" needle valve. Two further openings in the vessel head served to house a cooling coil made from 1/4" tube, allowing cold water to be circulated through the reactor contents by a peristaltic pump (Watson-Marlow), and isothermal conditions to be maintained during operation. Heating of the reactor was provided by an electric heating jacket insulated by ceramic fibre inside a work surface. Heating was controlled by a temperature controller (Parr 4838) connected to a J-type thermocouple placed in a thermowell which was immersed in the vessel. CO₂ was delivered to the vessel via a dual piston high-pressure pump (Thar Instruments), electronically connected to a PC. Delivery could be controlled by either setting a desired pressure or flow rate. The amount of CO₂ entering the reactor was recorded via a mass flow meter (Rheonik, Rhe08) positioned in-line before the pump. In all the studies that employed a CO₂/H₂O biphasic, the typical mass of CO₂ fed to the reactor was between 250 and 300 g, depending on the volume of aqueous

fraction utilised. Recirculation of the vessel contents was achieved by 1/8" and 1/16" tube connections from the vessel to a dual piston HPLC pump (Jasco, PU-2087).

3.1.4 Chemical Compounds and Solvents

Benzaldehyde [100-52-7], benzoyl chloride [98-88-4], benzoic acid [65-85-0], *n*-octane [111-65-9], polysorbate (Tween 80) [9005-65-6], allyl bromide [106-95-6], allyl chloride [107-05-1], allyl alcohol [107-18-6], 1-phenyl-3-buten-1-ol (97%) [936-58-3], 2-4-methylbenzaldehyde [104-87-0], chlorobenzaldehyde [89-98-5], 4-methoxybenzaldehyde [123-11-5], (*E*)-3-phenylprop-2-enal [104-55-2], *n*-decane [124-18-5], diethyl ether [60-29-7], zinc dust (<10 μm) [7440-66-6], tin powder (<100 μm) [7440-31-5], bismuth powder (100 mesh) [7440-69-9], tin(II) chloride dihydrate [10025-69-1], KI, NaCl, NaBr, NH_4Cl , NaH_2PO_4 , KH_2PO_4 , and iodine solution (from 0.05 M concentrate) were purchased from Sigma-Aldrich in > 98% purity (unless otherwise stated) and used as received. Liquid CO_2 (for liquid withdrawal) and compressed nitrogen (oxygen-free) were supplied by BOC U.K., CP grade, with a given purity of 99.995%. Distilled water was used in all experiments. All valves, fittings, and tubes were purchased from Swagelok unless stated otherwise.

3.1.5 Compound Addition to the Reactor

A method had to be devised for the introduction of organic compounds to the reactor. Initial studies would involve the use of small hydrophobic reagents, preferably at concentrations below their solubility limits in liquid CO_2 . More specifically, the study of the mass transfer from CO_2 to water necessitated the solute to be dissolved in the CO_2 phase. In reaction studies, kinetic data could be misinterpreted if any reaction occurred

during vessel sealing and pressurisation. Ideally, therefore, compounds had to be added to the top CO₂ phase following pressurisation and equilibration of the solvent mixture. One option involved adding compounds via a pump connected in-line with the CO₂ inlet. However this may have resulted in sources of error when dealing with small quantities of reagent. Therefore, for greater precision, a six-port valve was employed.

3.1.5.1 The 6-port Injection Valve

An injection 6-port valve (Rheodyne 7125) was employed for injection of hydrophobic compounds into the compressed CO₂ phase (Figure 3–2). Standard bypass loops, with volumes from 20 μ L to 16 mL (volumes certified by Valco), were used to construct bypass lines for injection of known volumes of compound.

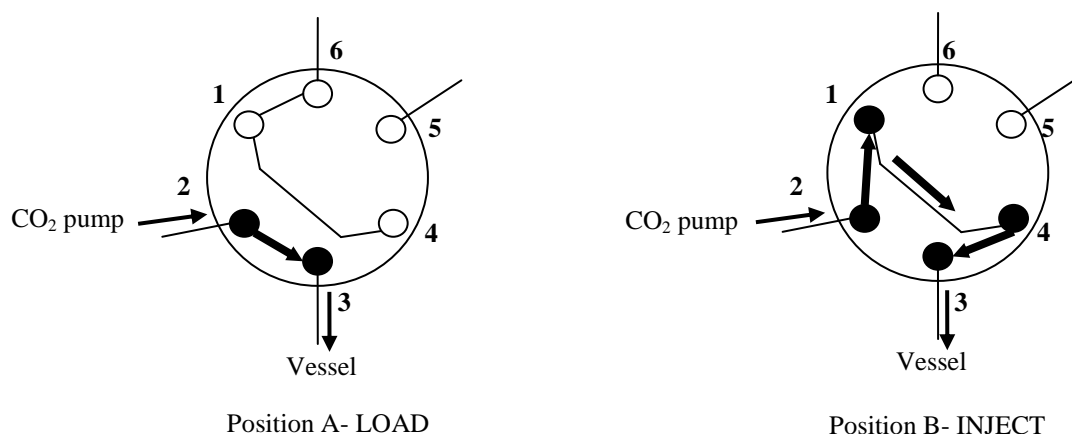


Figure 3–2 The 6-Port valve used for injection of compounds in the CO₂ phase. In the LOAD position, CO₂ flows from ports 2–3, bypassing the standard volume loop 1–4; in the INJECT position, flow is diverted through the loop to occupy the volume between positions 2–1–4–3 (5 and 6 are the waste ports)

The valve was positioned in-line with the CO₂ feed. This allowed all CO₂-soluble compounds to enter the top section of the vessel and dissolve in the CO₂ phase (provided that they were at or below their solubility limits at the operating pressure and temperature). The direct connections to the valve were made by 1/16" stainless steel tubing and

connected via reducers to the 1/4" union cross. The volume was flushed twice with compound through the waste port prior to injection in order to achieve better precision.

3.1.6 Sampling Sections

In studies that required sampling of the reactor contents, 1/8" stainless steel tube sections were connected to the CO₂ (L1) and water (L2) outlet valves. The outlet of each section was controlled by a 1/8" 3-way valve so that flow could either be directed to the recirculation pump or diverted to a sample collection section into a 20 mL capped glass vial. The cap of the vial contained a small puncture to prevent build-up of gas upon CO₂ expansion. The sampling section L1 originating from the top CO₂ phase is shown in Figure 3–3.

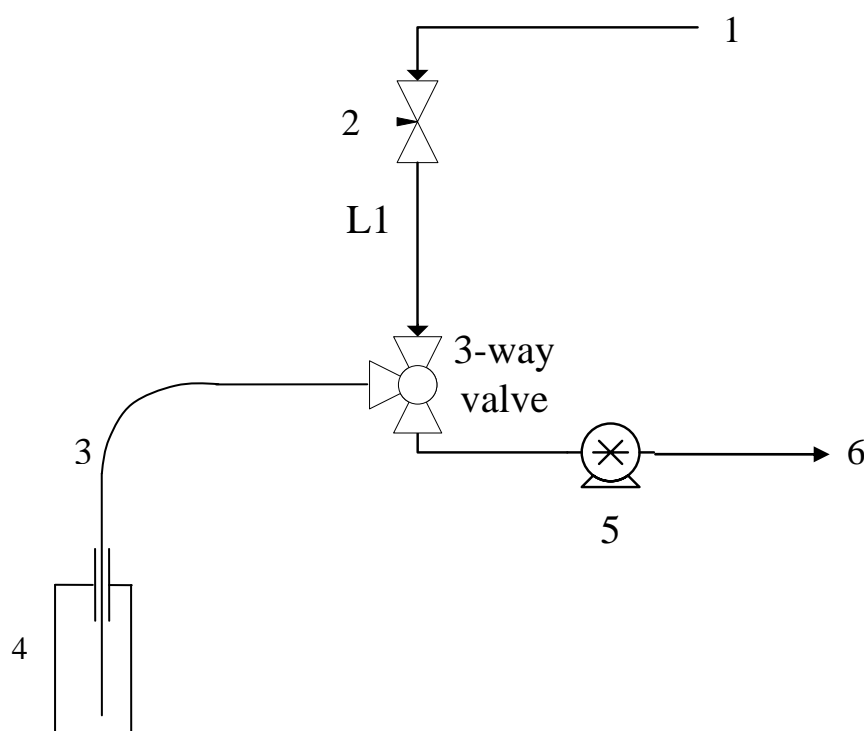


Figure 3–3 The sampling section, L1, used for evaluation of sample composition from the top CO₂ fraction of the vessel; (1) vessel CO₂ outlet; (2) ball valve; (3) 1/16" tube; (4) 20 mL glass vial for sample collection; (5) circulation pump; (6) line to the vessel; a similar configuration was adopted for the sampling section L2

In studies where the quantity of dissolved compound had to be determined in the CO₂ phase, the volume of each sampling section had to be determined. For evaluation of the internal volume, the section comprising L1, ball valve and 3-way valve, was filled with water by submerging in a water bath. The valves were closed and the section was dried, removing any water collected in the free openings of the valves with a syringe. The section was then secured by clamps and the contents emptied into a pre-weighed glass vial by opening the 3-way valve. Any water remaining in the section was expelled with a gentle stream of dry nitrogen. The resulting volumes were 2.5 and 2.1 mL for the sections originating from the CO₂ (L1) and water (L2) sections of the vessel, respectively. The calculated error after six trials was < 3%.

The effect of sampling position inside the ultrasound vessel was assessed by extending the dip tube with a silicone tube section secured to the cooling tube, resulting in the sampling position being 3.7 cm below the probe rather than 8.2 cm for the dip tube alone.

3.1.7 The 30 cm³ High-Pressure View Cell

A second high-pressure vessel (Parr series 4790, MO, USA) was employed in combination with the ultrasound reactor (Figure 3–4). It consisted of a stainless steel cylinder of internal volume 30 cm³ (internal diameter 2.5 cm and internal depth 5.7 cm), fitted with two screw-in sapphire windows 1.5 cm in diameter (maximum operating pressure, 344 bar at 200 °C). The head comprised five openings: one was fitted with an internal 5 cm dip tube to serve as an inlet, one led to an external 1/8" tube to serve as an outlet, and the remaining openings served to direct to a pressure gauge, rupture disc, and a bore-through fitting for insertion of a J-type thermocouple for temperature recording. Heating was provided by two electric heating plates connected to a dedicated controller (BTC-404) and was monitored via the

thermocouple by a Pico-Log Recorder. The seal was provided by PTFE and the head was secured to the vessel cylinder by a split ring closure secured by six screws.

3.1.7.1 Main Functions of the 30 cm³ High-Pressure View Cell

The primary purpose of this vessel was:

- allow observation of the contents of the ultrasound vessel following sonication as a stand-alone observation vessel;
- allow collection/separation of desired fractions following sonication in the ultrasound vessel.

Visualisation experiments were often configured to position the view cell in-line between the ultrasound vessel and the circulation pump by appropriately connecting each outlet and inlet through 1/16" and 1/8" stainless steel tubing.

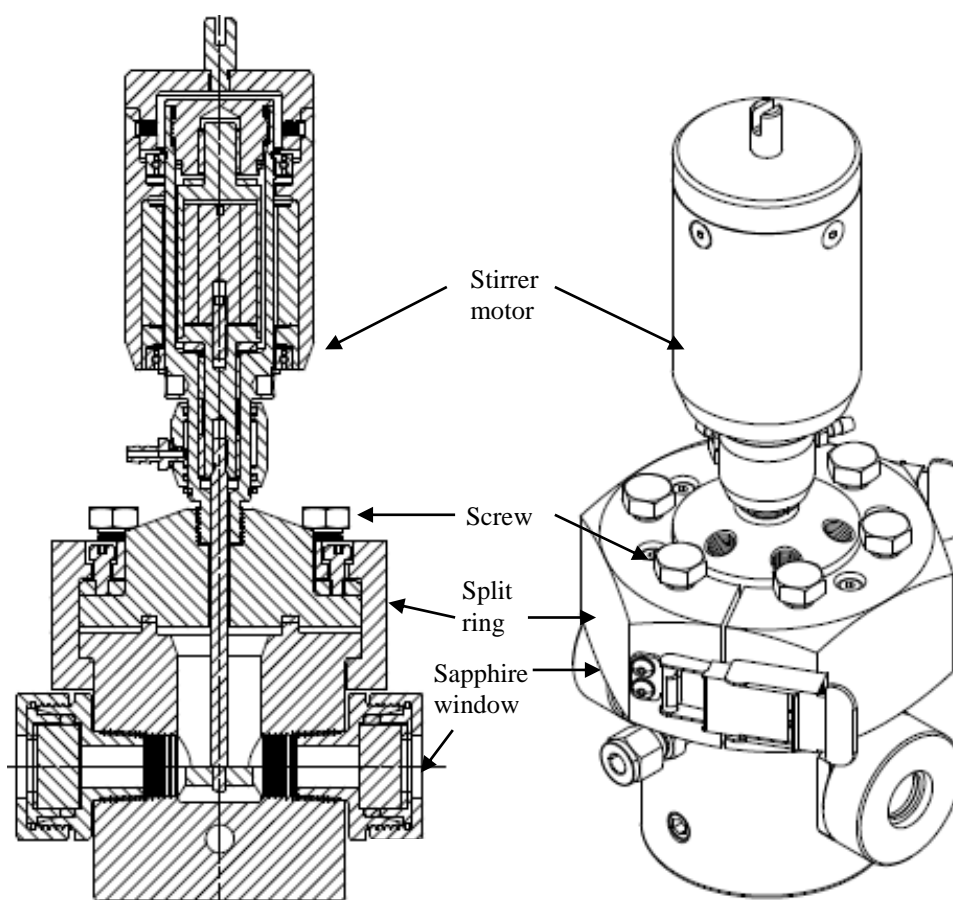


Figure 3–4 Drawing of the 30 cm³ view cell

3.1.7.1.1 Observation of Single-Phase Behaviour

For qualitative assessment of compound solubility, the view cell was connected to the 6-port valve so that visual inspection could be carried out to evaluate the possibility of formation of a second phase following compound injection. Illumination was provided by a Visilight I-LED spotlight (VWR, U.K.), and the window was observed by a camera connected to a monitor. This analogue camera and monitor did not allow any recordings to be made. However, a reasonable level of magnification was achieved by the lens, allowing clear observation of the view cell interior and cell lower base. In case of two-phase behaviour, small droplets were seen collecting at the bottom of the cell.

3.1.8 General Process Configuration

The general process configuration is shown in Figure 3–5. The dashed line represents an additional bypass line for employing the 30 cm³ high-pressure view cell to visualise the ultrasound vessel contents, or to recover large samples of product. Small samples on the other hand were collected with a 20 mL capped glass vial from lines L1 and L2 (see Section 3.1.6) originating from the CO₂ and water fractions, respectively.

3.1.8.1 Selection of Operating Conditions

Given the tuneable nature of CO₂ density, it may be of significant interest to study the CO₂/H₂O system across a range of temperatures and pressures. However, due to a necessity to validate the data under comparable conditions, initial investigations would need to stand against the available benchmarks. In particular, one study describing a smaller vessel of different geometry and smaller size [Timko, 2004], offered the possibility for comparison between the two systems. Furthermore, it became evident that in order for

the present technology to maintain a fairly sustainable character, the operating conditions would have to be kept relatively mild. Indeed, the use of high temperatures and pressures may be perceived as introducing safety concerns in industrial applications. CO₂ reaches an optimal liquid-like density (0.7 g cm⁻³) at the subcritical state (30 °C/80 bar), and may be an ideal solvent for carrying out preliminary investigations with small organic compounds. Therefore, this temperature and pressure was chosen and will constitute the conditions for the majority of the subsequent investigations presented in this thesis, although higher pressures (up to 140 bar) and temperature ranges (up to 60 °C) were used.

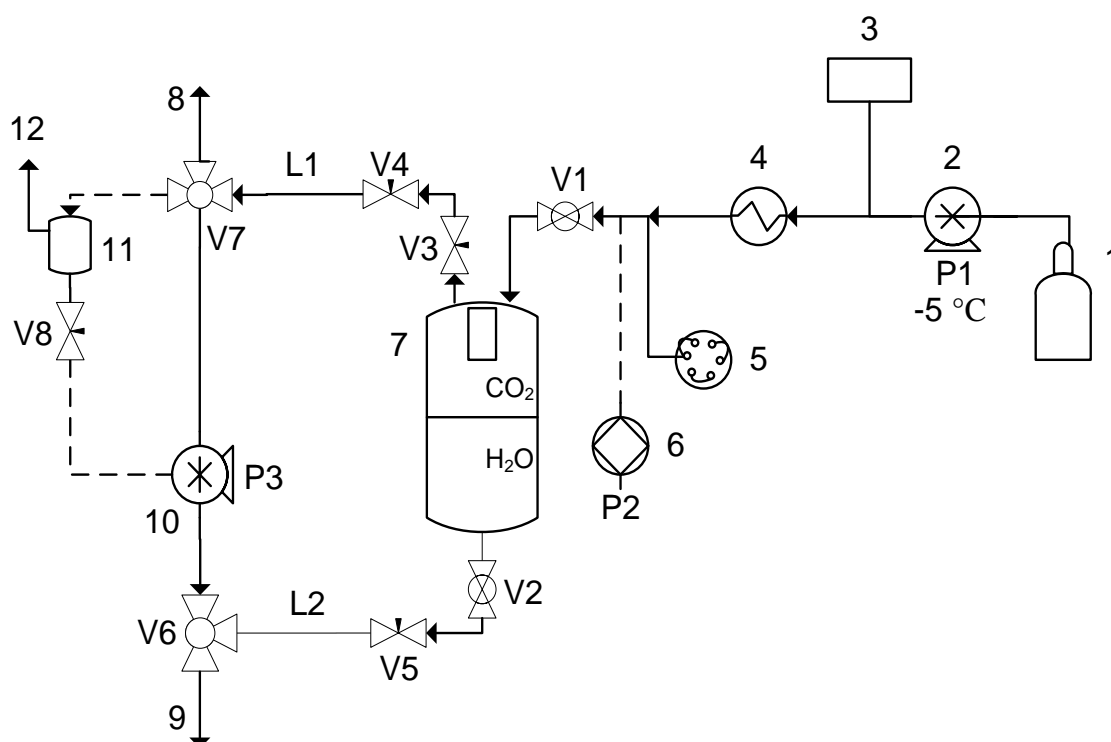


Figure 3–5 Process flow diagram showing the general configuration adopted for the studies described in this thesis. (1) CO₂ cylinder; (2) CO₂ pump P1; (3) automatic back-pressure regulator; (4) heat exchanger; (5) 6-port valve for injection of compounds; (6) pump P2 for secondary H₂O addition; (7) 1 dm³ ultrasound vessel; (8) CO₂ phase sample from collection line L1; (9) water phase sample from collection line L2; (10) circulation pump P3; (11) 30 cm³ view cell; (12) in studies of product recovery, V8 provided the vent to the view cell

3.2 General Characterisation of the CO₂/H₂O/Ultrasound System

In terms of its geometry and size, the 1 dm³ ultrasound vessel was unique amongst its kind and therefore had to be characterised in terms of its sonochemical and emulsion-forming properties. Sonochemical activity pertains to the ability to mediate the sonolytic reactions known to enhance the rates of organic reactions. Emulsion formation is an important physical phenomenon arising in heterogeneous mixtures, which may contribute to the enhanced mass transfer of solutes.

3.2.1 Ultrasound Power Calibration

Ultrasonic irradiation transmits energy through the medium, through the reactor walls and to the surroundings. For sonochemical processes, it is common to evaluate the acoustic energy entering the fluid as this will ultimately be responsible for any effects observed. In order to draw a correlation between the electric power supplied and the amount of acoustic power absorbed by the medium, a power calibration was undertaken following a standard calorimetric method [Mason, 1991]. Electric power was noted from the digital watt metre on the processor display, whereas the dissipated power was calculated by Eq. 3.1:

$$P_{acou} = \frac{\Delta T}{\Delta t} \times (C_p M) \quad (3.1)$$

Where $\Delta T/\Delta t$ is the temperature rise over a given time interval, and C_p and M are the specific heat capacity (J kg⁻¹ °C⁻¹) and mass (kg) of the fluid, respectively. Dissipation to the surroundings in the form of heat was a main concern for the present system due to the size of the reactor. Therefore, following heating to 30 °C with 650 cm³ of distilled water, the reactor was sealed and insulated with two layers of Rockwool Flexi material (with a thermal conductivity of 0.035 W m⁻¹ °C⁻¹, cut from 1.4 m × 0.4 m × 0.05 m slabs, Pencoed

Bridgend, U.K.). The system was pressurised with CO₂ to reach a final pressure of 80 bar. Temperature recordings were taken every second by a Pico-Log recorder connected to a K-type thermocouple, positioned inside the thermowell of the vessel. The recordings were automatically transferred to a PC. Under these conditions, the heat loss was measured as $9.6 \times 10^{-4} \text{ }^{\circ}\text{C s}^{-1}$, at which almost adiabatic conditions could be assumed. The contents were sonicated for 180 s at specific amplitude settings in the range of 20–80% and 25% pulse rate, while the temperature rise was continuously recorded. During this sonication period the pressure rise was < 5 bar. After ceasing sonication, temperature recordings were continued for approximately 30 minutes. Insertion of the mass of CO₂ (0.3 kg), water (0.65 kg), reactor (20 kg), sealing rings (7.38 kg), and specific heat capacities of CO₂ (5221.4 J kg⁻¹ °C⁻¹), water (4180 J kg⁻¹ °C⁻¹), stainless steel 616 (502 J kg⁻¹ °C⁻¹), and steel A4140 (460 J kg⁻¹ °C⁻¹), respectively, yielded the power values in watts, which were plotted together with electric power values against the respective amplitude settings.

3.2.2 Determination of the Presence of Cavitation in the Ultrasound Vessel

An important aspect of novel sonochemical vessels is their ability to induce the cavitation-dependent physical and chemical changes (see Section 2.5.3) that mediate the mass transfer and kinetic enhancements observed in many applications. This Section details the experimental procedures used for determination of the presence of cavitation in the CO₂/H₂O system under pulsed ultrasound. The results obtained will be presented in Section 4.3 along with a thorough discussion regarding the importance of operating conditions and vessel geometry on cavitation-induced effects.

3.2.2.1 Aluminium Foil Erosion

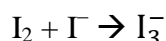
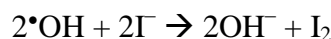
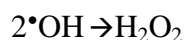
A quick and simple qualitative test for the presence of cavitation is aluminium foil erosion [Saez *et al.*, 2005]. A 4 cm × 4 cm × 0.2 cm stainless plate was wrapped four times with aluminium foil and placed ~1 cm below the ultrasound probe. The plate was secured with thin copper wires passing through holes drilled at each of its four corners and held in position by wrapping around the cooling tube. Pulsed ultrasound was carried out for 1 minute in CO₂/H₂O at 30 °C/80 bar with 50 v/v% of CO₂. Photographs were taken following depressurisation and compared with a control experiment that did not involve ultrasound.

3.2.2.2 Sonochemical Tests: The Weissler Reaction

True sonochemical reactions are thought to be mediated by the free-radical species which are generated during the forceful collapse of cavitation bubbles. In this respect, probe surface area, distance of the probe from the reactor walls, and the reactor geometry may all influence the cavitation distribution through the fluid [Gogate *et al.*, 2011].

Since the occurrence of cavitation may not necessarily imply the presence of sonolytic effects that lead to the free radical reactions normally associated with high localised temperatures and pressures, several chemical dosimetry techniques have been developed for evaluation of the sonochemical efficiency in ultrasonic reactors. The most commonly employed methods include: monitoring the oxidation of Fe²⁺ to Fe³⁺ [Nomura *et al.*, 1996], fluorescence [Mason *et al.*, 1994], phenolphthalein decomposition [Rong *et al.*, 2001], and generation of luminescence [Price *et al.*, 2010]. Another commonly used standard test employed for confirmation of the presence of free radicals is the oxidation of potassium iodide (KI) to iodine (I₂) [Sutkar and Gogate, 2009; Hart and Henglein, 1985], referred to

as the Weissler reaction, as progress of the reaction depends on the formation of H_2O_2 as the oxidizing agent. The key reactions are thought to be as follows [Morison and Hutchinson, 2009]:



Therefore, based on the lack of knowledge regarding the presence of cavitation in high-pressure multiphase systems, the Weissler reaction was used as a test in order to assess the sonochemical activity in the high-pressure ultrasound reactor in the presence of water pressurised with either CO_2 or N_2 .

An aqueous solution of 12 wt.% potassium iodide (final volume 800 cm^3) was loaded in the reactor and heated to 30°C . The water volume ensured that the probe was immersed by a few centimetres, and that sonication was occurring in the aqueous phase. The reactor was sealed and the contents were purged of air by flushing with N_2 (oxygen-free) and then the reactor was pressurised with either N_2 (to 1 bar using a low-pressure regulator, or to 70 bar with a high-pressure regulator), or with CO_2 to 80 bar. The maximum N_2 pressure possible under these conditions was 70 bar as above this pressure, the ultrasound processor produced an ‘*overload*’ error (see Section 3.1.2). Ultrasound was started with 80% amplitude under isothermal conditions by employing the peristaltic pump for water cooling. Samples of 5–10 mL were taken by opening valve V6 originating from the dip tube outlet (see Figure 3–5) at regular 2–5 min intervals, and analysed with an Aquarius Cecil CE 7500 Spectrophotometer (School of Biochemical Engineering, University of Birmingham). The maximum absorbance for I_2 was found at a wavelength of 354 nm. The

concentration in each sample was obtained by a standard calibration for I_2 (from a 0.05 M concentrate).

3.2.3 CO_2/H_2O Emulsion Formation, Stability and Composition

As described in the following Sections, emulsion formation, stability and composition were assessed for CO_2/H_2O mixtures by employing various techniques. Due to the novel geometry, size and ‘*black box*’ nature of the ultrasound vessel, visualisation of the vessel contents presented an initial challenge. Verification that some form of dispersion was being formed in the presence of ultrasound had to be undertaken. The ability of ultrasound to emulsify the CO_2/H_2O mixture was also assessed in the presence of the non-ionic surfactant Tween 80. This surfactant was chosen due to an existing in-depth knowledge of its CO_2/H_2O emulsion properties from the literature [Torino *et al.*, 2010]. An additional advantage of this surfactant is that it is bio-compatible within the limits imposed by the FDA regulation CFR 172.840, and is widely utilised in the food industry.

3.2.3.1 Observation of Turbidity through the Pyrex Tube

The first approach was to prepare a tube by pulling the fused ends of a standard pyrex tube (OD = 0.8 cm, $L \approx 10$ cm) so that the middle section was of a larger volume than the two openings at either ends. Polyether ether ketone tubing (PEEK, 1/16” OD \times 0.025” ID, VWR) was used to form the high-pressure connections. PEEK is an inert material that withstands high pressures (rated at 240 bar), and has been previously employed in high-pressure investigations [Murphy *et al.*, 2007; Trachsel *et al.*, 2009]. Sections of PEEK were inserted in either opening of the pyrex tube, and the space between the pyrex and the PEEK was sealed with high-strength Araldite® epoxy resin. The free ends of the PEEK tube were

connected to the ultrasound reactor and the circulation pump via 1/16" stainless steel tubes through PEEK ferrules and unions, as shown in Figure 3–6.

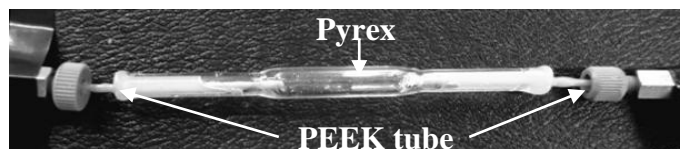


Figure 3–6 The pyrex tube utilised for macroscopic visualisation of CO₂/H₂O mixtures during sonication in the ultrasound vessel

The first prototype allowed visual observation of the contents of the vessel during sonication. During each experiment, the vessel was heated to 30 °C. Water (600–700 cm³) was introduced and the vessel was sealed and charged with CO₂ to 60–100 bar, depending on the conditions tested. Circulation pump P3 was started so that the fluid would flow at a rate of 20 cm³ min^{−1}. The vessel contents were circulated from the lower water section to flow through the pyrex tube and return to the top CO₂ section. Ultrasound was commenced at 70% amplitude and 25% pulse rate and carried on for 3 minutes, after which time sonication was stopped while circulation was kept going. Images were taken with a Sony digital camera. Since the fluid was drawn from the water phase via the 1/4" 14 cm dip tube, a potential time delay existed between emulsion formation and its appearance in the pyrex tube. The highest pump flow rate (20 cm³ min^{−1}) was therefore selected in order to view the ultrasound vessel contents as quickly as possible. Based on the volume of the circulating fluid and the flow rate the time delay was estimated as 13 s. This enabled identification of the time required for steady-state conditions of emulsion formation to be reached (the time at which emulsion formation equals emulsion breakdown). Following several trials, the pyrex tube experienced failure (see Section 4.4.1.1 for further details), and therefore an alternative method for visualisation had to be devised.

3.2.3.2 Observation of Turbidity Through the 30 cm³ View Cell

As discussed in Section 3.1.7.1 and shown in Figure 3–5, a special configuration was adopted that employed the 30 cm³ view cell for the visualisation of CO₂/H₂O emulsions originating from the ultrasound vessel. During visualisation of the lower water phase, a desired volume of water was added to the ultrasound vessel (500–700 cm³), whereas the view cell was filled with 30 cm³ of water. During visualisation of the top CO₂ phase, water was added only to the ultrasound vessel, as the view cell would be filled by the circulating top CO₂ phase. Both vessels were sealed and CO₂ was introduced by the CO₂ pump.

Emulsion stability was assessed by measuring the time required for turbidity to completely disappear, which was related to the amount of light passing through the view cell from a Visilight I-LED spotlight. The equipment necessary for measuring light intensity directly (such as an optical power meter) was not available, therefore the amount of light passing through the view cell was correlated to the sum of the grayscale pixel values (integrated density) in images of the view cell windows, using ImageJ (free image-processing program). The program assigns each pixel a specific value based on the intensity within the grayscale range. Time-lapse recordings were obtained with a Photron high-resolution camera at 10 s intervals, and the digital image was transferred to a PC using the Photron software. The light transmitted over time was evaluated by dividing the integrated density at a given time point by the maximum density recorded in the absence of turbidity before commencing ultrasound. Typically, an area equivalent to $\sim 5 \times 10^5$ pixels was analysed in each frame, and approximately 250 frames were analysed. In each experiment, the water or CO₂ phase was circulated via pump P3 through the view cell for 30 min at a flow rate of 20 cm³ min⁻¹, until the temperature difference between the ultrasound vessel and the view cell was < 2 °C. The CO₂/H₂O mixture was then sonicated for 20 minutes with pulsed

ultrasound at 70% amplitude, during which time the view cell became completely turbid. Sonication was stopped and the view cell was then quickly isolated by closing valves V7 and V8 and the time-lapse recordings were immediately commenced. Experiments were also performed at 50 °C/140 bar (same density as 30 °C/80 bar but above the CO₂ supercritical point).

3.2.3.2.1 Use of the Non-Ionic Surfactant Tween 80

In separate experiments, emulsion stability was also assessed for the CO₂/H₂O/Tween 80 system. Above the critical micelle concentration (CMC), non-ionic surfactants such as Tween 80 exist in water in the form of micelles as aggregates of 50–100 molecules [Kerwin, 2008]. In experiments using Tween 80, solutions were prepared by stirring either 0.5 or 1 wt.% Tween 80 in water at 40 °C. The solution was then cooled to 30 °C and added to the vessel as the aqueous phase. The vessel was subsequently sealed and pressurised with CO₂ as previously described.

3.2.3.3 Microscopic Visualisation of CO₂/H₂O Emulsions

As described in Section 2.4.3.1, droplet size is one of the most defining characteristics influencing emulsion stability, and a number of investigative techniques exist for obtaining droplet diameters. Direct observation is the most reliable method although for high-pressure systems this task is complicated by requirement of specialised devices able to sustain the operating conditions. Ideally the wall of the channel should be a few hundred µm and never above 1 mm in order to take into account the microscope lens depth of field at higher magnifications.

3.2.3.3.1 Fused Silica Capillary Method

The first approach was to make a channel out of a length of fused silica capillary (10 cm L x 0.363 mm OD x 0.1 mm ID, CM Scientific, Shipley, U.K.) as described in the literature [Lee *et al.*, 1999]. An opaque polyimide coating surrounds the capillary to confer structural support; this must be burned off in order to expose the transparent capillary, although the procedure also removes the flexibility conferred by the polyimide layer, increasing the fragility of the capillary. Each end of the capillary was placed inside 1/16" PEEK tubing, which was melted to form a seal around the capillary. Parts of the PEEK tube were glued to a microscope slide in order to provide additional structural support. One end of the 1/16" PEEK tube was connected to the opening originating from the lower section of the ultrasound vessel via unions and 1/16" stainless steel tubing. The outlet PEEK tube opening was connected to the circulation pump for return of the contents to the reactor. The capillary unit was secured on the stage of an Olympus CH2 microscope equipped with a Dolphin camera (Allied Vision Tehnologies, U.K.).

Work undertaken by Dr. Alireza Bahari (School of Chemical Engineering, University of Birmingham) using one of such capillary units resulted in microscopic visualisation of CO₂/H₂O emulsions. Briefly, the CO₂/H₂O mixture (45% v/v) was sonicated at 70% amplitude, 25% pulse rate for 3 minutes at 30 °C/80 bar. Sonication was stopped and circulation by the pump was immediately commenced allowing the emulsion to pass through the capillary for visualisation under the microscope. Images of the passing emulsion were captured at ×100 magnification using the oil objective. Unfortunately, only one set of experiments could be carried out using this methodology as although the capillary showed good strength to hydrostatic pressures up to 80 bar, its strength towards tensile and bending forces during the building, handling and connection stages was

extremely low. Alternative methodologies were therefore explored for microscopic visualisation of emulsions.

3.2.3.3.2 Microchannel Method

One of the most utilised techniques for fabricating high-pressure microfluidic channels relies on anodic bonding between silicon and pyrex wafers [Marre *et al.*, 2012]. Recently a microfluidic device was fabricated using this technique for visualising CO₂/H₂O emulsions under a light microscope [Murphy *et al.*, 2007]. The innovative aspect of the devices reported by Murphy *et al.* [2007] was the tube-silicon connection, which was formed by solder-based metal deposition. Since this technique is quite expensive and requires knowledge of hand-held micro-soldering techniques, a more viable option had to be devised. A collaboration with Dr David Cheneler (School of Mechanical Engineering, University of Birmingham), led to the design of a more economical microfluidic device which utilised commercially-available high-pressure connections (Figures 3–7 to 3–9). The connections were formed using Nanoport™ Assemblies (Upchurch Scientific), which included nuts and ports made of PEEK, ferrules and gaskets made of Perlast perfluorelastomer, and adhesive rings used for sealing made of polyamide epoxy resin. This type of epoxy resin is highly suitable for these applications and came with a pressure specification of 103 bar. Other advantageous properties included good water, alkali, and acid resistance, and excellent adherence to silicon, quartz, glass and polymers.

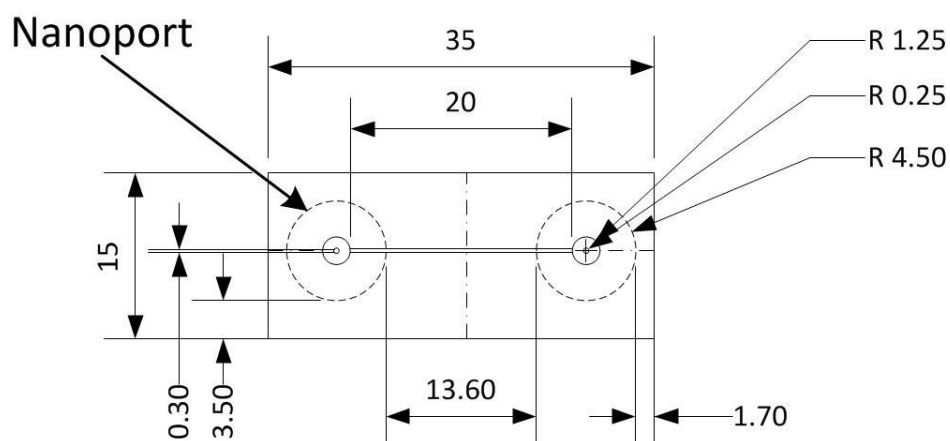


Figure 3–7 Drawing showing the microchannel, silicon wafer, and hole dimensions (see text for description); all measurements are in mm

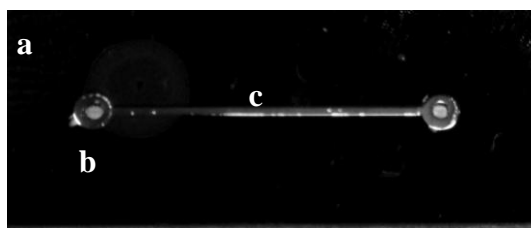


Figure 3–8 Top view photograph showing the pyrex/silicon device. (a) Black silicon wafer; (b) drilled hole in silicon wafer connecting underside opening to upside channel; (c) etched channel; a transparent pyrex wafer is bonded on top of the silicon wafer

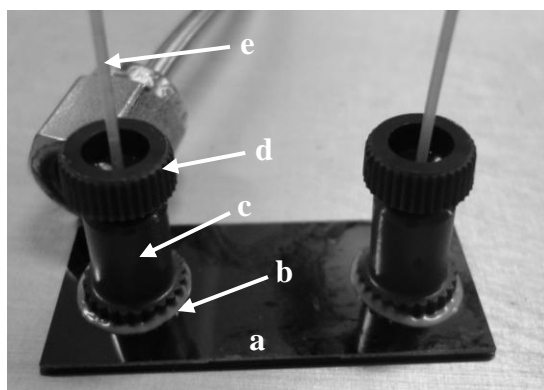


Figure 3–9 Photograph showing the underside of the microfluidic device with Nanoport connections. (a) Silicon wafer; (b) adhesive bond; (c) Nanoport; (d) nut; (e) 1/32" PEEK tube

The chosen connections were for tubing with OD 1/32" which had a pressure rating of 103 bar (Nanoport™ Assembly items N-126S, 6-32 coned, Upchurch Scientific), since the 1/16" connections had a specified maximum operating pressure of only 35 bar. The corresponding port had a diameter of 8.4 mm and after taking into account the adhesive ring forming the bond, these could be used to seal chip holes of diameter up to 1.6 mm. The adhesive ring must undergo curing which may involve one or more heating stages (specific methods are provided by the manufacturer, and depend on the type of adhesive used). A channel (300 µm diameter × 250 µm depth × 20 mm length) was etched in a silicon wafer (35 mm length × 15 mm width × 500 µm thickness) using a hydrofluoric acid etch technique. Etching is a microfabrication technique that removes layers of a surface by chemically reacting with the surface and its passive oxide layers [Monk *et al.*, 1993]. Two holes (2.5 mm in diameter) were drilled on the underside of the wafer so as to provide an inlet/outlet connection to both ends of the channel. A glass wafer (Pyrex 7740) of the same dimensions was subsequently anodically bonded to the silicon wafer (Applied Microengineering LTD, Oxford). Once the ports were bonded, connections to the vessel were made, via the nut included in the assembly unit, with PEEK tubing (1/32" OD × 500 µm ID, VWR), and 1/16"-1/32" stainless steel reducing unions (500 µm bore, VWR). The lowest opening diameter of 500 µm along the connecting lines ensured the passage of emulsions with diameters of a few micrometres. The whole unit would be mounted on a small stage for microscope viewing. Testing of the device was achieved in the following manner: one end of the microchannel was connected to section L2 of the ultrasound vessel, which was under a hydrostatic pressure of 60 bar, while the other end of the microchannel was left opened to prevent any back-pressure. Valve V6 was then gradually opened. Due to the time required for the search and fabrication of the microfluidic device, only one

prototype could be tested. The discussion related to the testing of the device is presented in Section 4.4.2.2 along with the information obtained from the literature regarding the use of similar devices and the most common failure points associated with them.

3.2.3.4 Emulsion Volume Fractions

Although emulsion stability and droplet size may provide important information, the total interfacial area is also determined by the volume fraction, or the volume of a particular phase (oil or water) dispersed in the continuous phase (water or oil). For oil/water systems stabilised by surfactants, this simply depends on the initial volumes included in the system, as all the oil will be dispersed in the water phase. On the other hand, emulsions that are not stabilised by a surfactant would be less stable, and the volume of each phase dispersed in the other will not be simply the initial volumes introduced in the system. Volume fractions therefore provide valuable information on the amount of each phase dispersed in the other and may be useful when interpreting time-dependent effects such as changes in mass transfer and reaction rates of solutes.

The general procedures employed for charging the vessel and for sonication were analogous to those described in Section 3.2.3.1. All experiments were carried out at 30 °C/80 bar, in the presence of ultrasound at 70% amplitude and 25% pulse rate. In order to assess the composition of the emulsion, different techniques were carried out depending on the fraction to be examined. As described in the following Sections, water collection experiments were carried out in order to assess the amount of water present in the dispersion, whereas a tracer technique was used to evaluate the fraction of dispersed CO₂.

3.2.3.4.1 Water Collection Experiments

The measurements for determination of the volume fraction of water dispersed in CO₂ relied on the collection of water using the standard sampling tube L1 described in Section 3.1.6. The expansion of CO₂ during sample collection could result in water losses to the atmosphere due to evaporation. A common method for limiting such losses involves trapping of the condensing water in a pre-weighed glass collector placed in a low temperature bath at –80 °C, while the mass of expanding CO₂ is measured by a wet test meter [Leeke, 2000]. However, such methods are usually employed to measure low quantities of water, as for example when water is present in CO₂ up to its saturation concentration. Indeed, the solubility of water in liquid CO₂ at 30 °C/80 bar is 0.05 mol L^{–1} [King *et al.*, 1992], and therefore evaporative losses would constitute a significant source of error for small sample sizes. However, preliminary investigations revealed that the quantity of water present in the ultrasound-induced dispersions was much greater than that present due to its solubility in CO₂, and that therefore collection at 20 °C would offer a satisfactory method for obtaining approximate values of the water fractions. Furthermore, samples originating from the top section of the vessel had a higher quantity of CO₂ than samples from the lower section of the reactor, which mostly consisted of water. This suggested that even in the presence of pulsed ultrasound, two simultaneous environments existed in the top and bottom sections of the vessel, which had to be further investigated. The error associated with evaporation losses of water was estimated using an appropriate method (see Appendix A1.3.1.1).

It should be noted that although not available for the present study, other techniques may be employed for the quantification of water in samples. For example, one method would

involve the use of an ionic tracer which dissolves exclusively in water (such as NO_3^- from KNO_3), and which may be quantified by ion chromatography [Timko, 2004].

Following pulsed ultrasound of the $\text{CO}_2/\text{H}_2\text{O}$ mixture (35% v/v) for 20 minutes in the presence of circulation, circulation was stopped and section L1 was isolated by closing valves V4 and V7, and the contents were allowed to slowly discharge in the pre-weighed glass vial (described in Section 3.1.6) by slowly opening valve V7. Line L1 was then carefully removed from the connections to the vessel by firstly closing valve V3, and the remaining water deposited on the post expansion side of the valve was slowly flushed out with dry nitrogen over 1–2 minutes. The experiment was repeated several times and the water fraction was calculated by dividing the mass of water collected by the total volume of the sampling section L1. Water collection experiments were also carried out following sonication of the $\text{CO}_2/\text{H}_2\text{O}/1\%$ Tween 80 system.

3.2.3.4.2 CO_2 Volume Fractions

CO_2 volume fractions were measured by a tracer technique. The assumption was that if a tracer partitions preferentially (>99.9%) in CO_2 , it may be expected that its presence in samples originating from the water-continuous phase may be the result of CO_2 droplets acting as carriers. Octane was chosen as the tracer as it is highly soluble in dense CO_2 [Schneide.G *et al.*, 1967], it possesses a $\text{CO}_2/\text{H}_2\text{O}$ partition coefficient greater than 100000 [Timko *et al.*, 2004], and has previously been successfully employed as a tracer for the CO_2 phase [Timko, 2004].

3.2.3.4.3 Gas Chromatography

All gas chromatographic analysis undertaken throughout this PhD was carried out using a Shimadzu GC-2010 equipped with a DB-5 column and a Flame Ionization Detector, combined with autosampler and injector AOC-20 (School of Chemistry, University of Birmingham). Specific details regarding the heating programme and injection volumes will be found in the appropriate Appendix Section, to which the reader will be referred from the relevant description appearing in the text.

3.2.3.4.4 The Tracer Technique

The volume fraction of dispersed CO₂ was measured with different water loadings in order to assess the effect of the position of the biphasic line from the ultrasound probe (termed as standoff distance, see Appendix A1.3.2 for further details).

Following loading with an appropriate volume of water, the vessel was pressurised with CO₂ to 70 bar at 40 g min⁻¹ using pump P1, and octane (1 mL) was injected into the top CO₂ phase via the 6-port valve during final pressurisation to 80 bar at 10 g min⁻¹. This procedure was followed for the injection of all hydrophobic compounds into the CO₂ phase described henceforth. The quantity of compound injected into the vessel was controlled by deploying the appropriate standard volume loops connected in series.

For experiments involving octane, the contents originating from the lower section of the vessel were circulated through pump P3 at 20 cm³ min⁻¹. Pulsed ultrasound was then commenced at 70% amplitude and carried on for 20 minutes, after which sonication was stopped. In order to exclude collection of larger bubbles originating from acoustic streaming, a period of 1 minute was allowed to pass between termination of sonication and sample collection. This time was allowed to pass by assuming that the larger bubbles

generated during ultrasound would return back to the CO₂ phase a few seconds after stopping ultrasound, whereas emulsion droplets would persist for several minutes.

Sample line L2 containing the circulating water phase was isolated by closing valves V5 and V6, and the sample was collected by bubbling through acetone in the capped glass vial on ice. Observations conducted during preliminary water collection experiments performed on this sample line (Section 3.2.3.4.1), revealed that the fraction originating from this section of the vessel consisted mostly of water, the volume of which was noted for appropriate dilution in acetone. The volume fraction was calculated using Eq. 3.2:

$$\text{Volume fraction (\%)} = \frac{C_c}{C_{c0}} \times \frac{V_{dil}}{V_s} \times 100 \quad (3.2)$$

Where, C_c is the concentration of octane in the dispersed phase measured by gas chromatography (see Appendix A1.3.2), C_{c0} is the initial concentration of octane in CO₂, and V_{dil} and V_s are the volumes of the diluted sample and of the sample collected, respectively ($V_{dil}/V_s = 6$). CO₂ volume fractions were also assessed following sonication of mixtures which included 1 wt.% of the non-ionic surfactant Tween 80, under the same conditions employed in experiments that did not include Tween 80. This concentration of surfactant was employed as preliminary macroscopic observations following the experiments detailed in Section 3.2.3.2 revealed that stable emulsions were generated under these conditions.

3.3 Mass Transfer of Benzaldehyde in CO₂/H₂O: General Objectives

Since the synthesis of the majority of chemical and pharmaceutical compounds starts from small organic hydrophobic molecules, benzaldehyde was selected as the CO₂-soluble compound to model the transfer of solutes from the CO₂ to the water phase. Benzaldehyde also contains an important functional group for organic chemistry, namely the carbonyl

group. No impurities were present in the benzaldehyde stock following 1 month of storage, and no other compounds were detected during the mass transfer experiments as confirmed by GC analysis, indicating that benzaldehyde was a suitable model compound for the mass transfer studies. It was anticipated that for small organic hydrophobic molecules, the majority of the mass transfer resistance resided in water, and therefore evaluation of the mass transfer coefficients would be important for understanding and predicting the behaviour of such compounds in CO₂/H₂O biphasic mixtures. Furthermore, the objective was to obtain valuable information on the mixing capacity of ultrasound in the present vessel geometry, and to compare the results with other systems reported in the literature. The following Sections will provide a description of the methods employed for evaluation of mass transfer in CO₂/H₂O mixtures in the absence and presence of ultrasound. Chapter 5 presents the results and discussion related to these experiments.

3.3.1 Solubility of Benzaldehyde in Compressed CO₂: The Chrastil Method

The study of the mass transfer of compounds in biphasic systems relies on the condition that the solute or reagent is initially freely soluble in the solvent. Indeed, any undissolved solute forming an additional liquid phase would complicate interpretation of the data. With the view of studying the mass transfer of benzaldehyde in CO₂/H₂O, and with the possibility of further employing benzaldehyde as a CO₂-soluble reagent in synthetic studies, it was therefore desirable to gain knowledge of the solubility of benzaldehyde in dense CO₂. As described in Section 3.1.8.1 the conditions of temperature and pressure for the majority of the studies described in this thesis would be 30 °C/80 bar, and therefore the solubility of benzaldehyde was determined at these conditions.

The solubility of benzaldehyde in CO₂ was assessed both theoretically and validated experimentally. The theoretical solubility of benzaldehyde in dense CO₂ was predicted using the Chrastil method (Eq. 3.3), by extrapolation from the data compiled by Walther and Maurer [1992] over the range of 40–120 °C and 66–223.4 bar. It is found that in compressible fluids, the solubility of a solute may be related to the density of the solvent [Chrastil, 1982], by:

$$\ln S = k \ln(\rho) + \frac{a}{T} + b \quad (3.3)$$

Where S is the solubility of the solute in CO₂ (g L⁻¹), ρ is the CO₂ density (g L⁻¹), T is the temperature (K), k is the association constant, which is specific for the particular solvent and is independent of both pressure and temperature, a is a constant dependent on the heat of solvation and vaporisation of the solute, and b is a constant dependent on the molecular masses of the solvent and solute and on the melting points of the solute. Since it is customary in the literature describing the Chrastil method to express both units of solubility and density in g L⁻¹, this unit will be used exclusively for evaluation of the solubility of benzaldehyde. Similarly, determination of the physical parameters appearing in Eq. 3.3 requires the temperature to be expressed in Kelvin, therefore for all other aspects not directly related to the Chrastil method, and for the purpose of clarity, the temperature will be expressed in degrees Celsius. The constants k , a , and b are not directly quantifiable, although they may be determined experimentally through the Chrastil method by following a simple algorithm (Figure 3–10). Indeed, it has been shown that a logarithmic plot of S (determined experimentally) against ρ for isothermal conditions generates a straight line with slope k [Sparks *et al.*, 2008]. The term $\ln S - k \ln(\rho)$ may then be calculated using k , and plotted against $1/T$ to obtain the slope a and intercept b , and allow prediction of S .

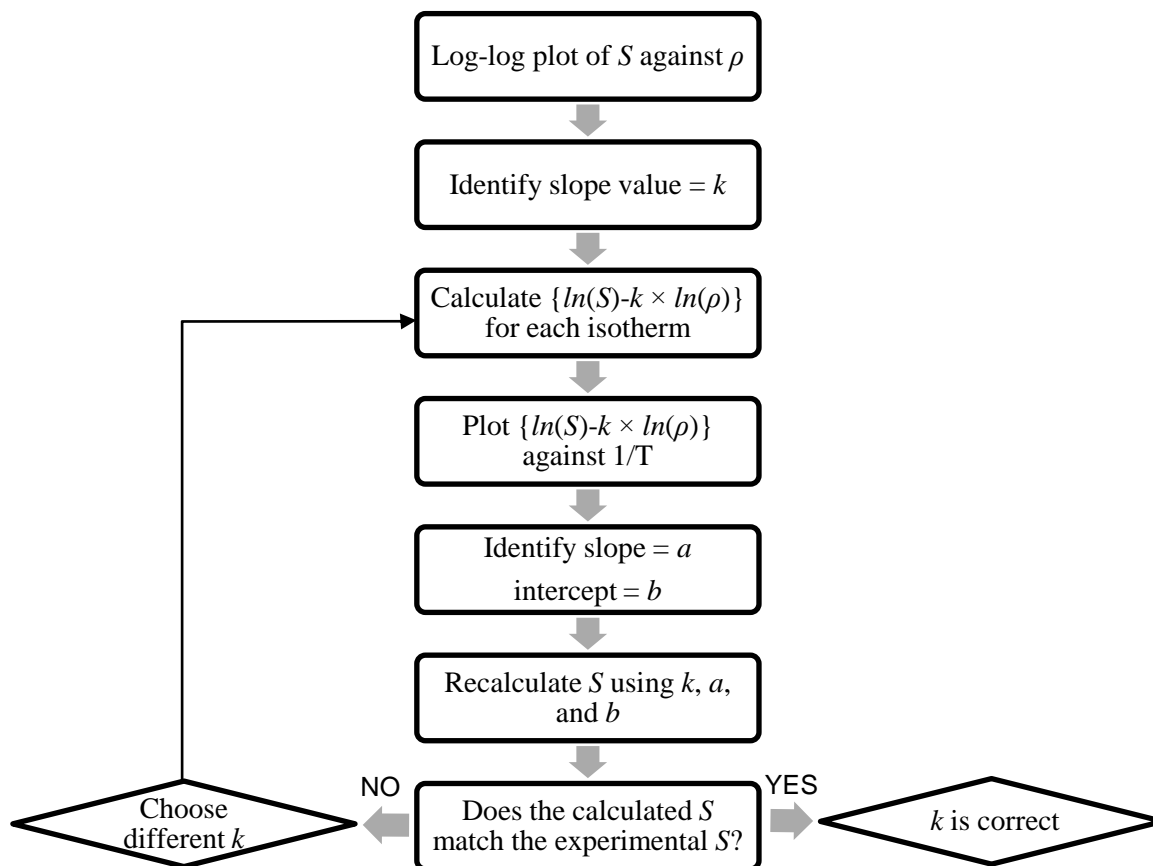


Figure 3–10 Algorithm used for the calculation of the solubility of benzaldehyde; from the Chrastil [1982] method

3.3.1.1 Experimental Quantification of Benzaldehyde Concentration in dense CO₂

In order to test the validity of the theoretical solubility of benzaldehyde obtained through the Chrastil method, an equivalent amount of benzaldehyde, based on 350 cm³ of CO₂ was loaded in the reactor filled with CO₂/H₂O and the concentration measured in both fractions following acoustic agitation. This Section presents the methodology employed for experimental quantification of benzaldehyde concentration.

In order to simplify sample collection and analysis from the CO₂ phase, quantification of solutes was accomplished by deploying an internal standard. The use of internal standard also provided a preliminary evaluation of its capability for being employed to monitor yields in future studies involving synthetic reactions. The concentration of solute may be quantified provided that the internal standard concentration was much lower with respect to the solute, and that the CO₂/H₂O partition coefficient of the internal standard was > 99.9%. *n*-Decane was chosen as the internal standard due to its high solubility in liquid CO₂ [Reamer and Sage, 1965; Pando *et al.*, 1983], chemically inert nature, and density (0.73 g cm⁻³) which approximates that of CO₂ at 30 °C/80 bar. The reactor was heated to 30 °C and subsequently water (650 cm³) and *n*-decane (2.5 mmol) were added. Benzaldehyde (61 mmol) was either added directly with the *n*-decane, or injected into the flowing CO₂ stream using the 6-port valve following sealing and pressurisation of the reactor, until a final pressure of 80 bar was reached. Pulsed ultrasound was commenced at 70% amplitude. Samples were taken every 20 minutes over a total time of 90 minutes from the CO₂ phase by isolating sample line L1 and allowing the contents to slowly bubble in acetone on ice. The concentration of benzaldehyde in CO₂ was assessed relative to the internal standard by GC (see Appendix A2.2). Samples were also taken 30 minutes after stopping sonication, in order to allow separation of the phases and to provide a comparison with samples obtained during sonication. The water-soluble fraction was analysed by isolating sample line L2 and collecting 2–5 mL samples. An aliquot was taken and measured by GC without further dilution. Finally, since the presence of water in the CO₂/H₂O biphasic system would lead to water-saturation of the CO₂ phase, the solubility of benzaldehyde in CO₂ was discussed in relation to solute structure and water-solute interactions.

3.3.2 Benzaldehyde Partition Coefficient in CO₂/H₂O mixtures

The benzaldehyde partition coefficient between CO₂ and water, K_{CW} , was calculated at 30 °C/80 bar by measuring the concentration at equilibrium according to Eq. 3.4:

$$K_{CW} = \frac{C_c}{C_w} \quad (3.4)$$

where C_c and C_w are the respective concentrations in carbon dioxide and water. The mole fraction partition coefficient may be obtained from K_{CW} by Eq. 3.5:

$$K_{CW}^X = K_{CW} \frac{\rho_w}{\rho_c} \frac{MW_c}{MW_w} \quad (3.5)$$

where ρ_w , ρ_c , MW_w and MW_c , are the densities and molecular weights of water and CO₂, respectively. For the majority of the studies presented in this thesis, ρ_c was 0.7 g cm⁻³. The equilibrium value was taken as that after approximately 5 hours when no considerable change in the partition coefficient could be observed. The 6-port injection valve was deployed coupled to the 1 mL standard volume loop to ensure that the injection volume was well below the solubility of benzaldehyde in CO₂ as evaluated from the experiments described in Section 3.3.1.1. The lower water section of the vessel was recirculated at 20 cm³ min⁻¹ for 5 hours, and sample lines L1 and L2 were isolated for determination of the concentration of benzaldehyde in the water and CO₂ fractions, respectively. The CO₂ concentration was assessed in the same manner as described for octane in Section 3.2.3.4.4. Concentrations appearing in the water phase from the lower section of the vessel were evaluated by taking 2 mL aliquots at regular time intervals by isolating line L1. To avoid removing liquid volumes that would affect the operating conditions, no more than 4 or 5 aliquots were taken over the course of each experiment at different time points. For the same set of conditions, experiments were repeated three times and the errors calculated. The aliquots were analysed immediately by gas chromatography without further dilution

due to the relatively high solubility of benzaldehyde in water at 30 °C (7 g L⁻¹), which resulted in detectable quantities for GC analysis.

3.3.3 Benzaldehyde Mass Transfer in CO₂/H₂O: The Two-Film Model

Various models exist describing the mass transfer of solutes in biphasic systems, including the penetration model, in which the diffusion of a substance is dependent on a finite contact time along the interface [Toor and Marchello, 1958], the surface renewal model, in which it is assumed that the regions surrounding the interface are constantly being replaced with fresh fluid [Danckwerts, 1951], and the two-film model, which assumes that mass transfer proceeds via molecular diffusion through stagnant films on either side of the interface [Lewis and Whitman, 1924]. The two-film theory is more widely used and is relatively simpler compared to the other models, and was therefore adopted for evaluation of the mass transfer of benzaldehyde from CO₂ to water. In general terms, the rate of change in the concentration of a solute, C , in a given bulk phase is dependent on the mass transfer coefficient, k , the interfacial area, a , the volume of the bulk phase, V , and the driving force between the concentrations in the bulk and the equilibrium concentration at the interface, C^* as described in Eq. 3.6:

$$\frac{dC}{dt} = k \frac{a}{V} (C - C^*) \quad (3.6)$$

Solving in terms of benzaldehyde disappearance from the CO₂ phase (see Appendix A3), and integrating leads to the final expression shown in Eq. 3.7:

$$\ln \left| \frac{C_{c0} - \left(\frac{V_w}{V_c} + K_{CW} \right) C_w}{C_{c0}} \right| = -K_{mtCO_2} \frac{a}{V_c} \left(\frac{V_w}{V_c} + K_{CW} \right) t \quad (3.7)$$

where C_{c0} is the initial concentration of benzaldehyde in the CO_2 phase and C_w is the concentration of benzaldehyde appearing in the water phase, K_{CW} is the $\text{CO}_2/\text{H}_2\text{O}$ partition coefficient of benzaldehyde, and V_c and V_w are the respective bulk volumes of CO_2 and water. A plot of the left-hand term against time yields the slope which may be used for evaluation of the overall mass transfer coefficient on the CO_2 side ($K_{m\text{CO}_2}$) using the known quantities. A more in-depth description of the mass transfer coefficients will be provided in Section 5.4, when the results will be used for comparison with other systems reported in the literature.

The mass transfer of benzaldehyde was assessed following its injection (1 mL) into the CO_2 phase at 30 °C/80 bar, under conditions of silent agitation using the circulation pump at $20 \text{ cm}^3 \text{ min}^{-1}$, or under acoustic agitation at 70% amplitude, 25% pulse rate. The mass transfer of benzaldehyde was assessed by monitoring its concentration by GC appearing in the water phase over time (see Appendix A3).

3.4 Kinetics of Benzoyl Chloride Hydrolysis in $\text{CO}_2/\text{H}_2\text{O}$: General Scope

Reactions in multiphase systems are affected by both mass transfer of the reactants to the reaction site, and by the intrinsic rate of reaction. The reactant usually encounters most of the mass transfer resistance in the phase in which it is less soluble, which will accordingly influence the observed rate constant by a factor dependent on the partition coefficient of the reactant. Following on the model for mass transfer of small hydrophobic compounds from CO_2 to water, reactions occurring in water would be expected to be much slower in $\text{CO}_2/\text{H}_2\text{O}$ systems compared to ones occurring in pure solvents, if the reactant preferentially partitions in CO_2 . The intrinsic rate of reaction will also impact on the observed rate constant, as extremely fast reactions are expected to enhance diffusion of

reactant across the interface. Therefore, by deploying a fast reaction, valuable information may be gathered regarding the interdependence between mass transfer and kinetics, since for increasingly fast reactions the mass transfer may become the limiting factor, and the observed reaction rate may approximate the mass transfer rate.

The hydrolysis of benzoyl halides represents a well known model for studying the kinetics in multiphase systems containing an aqueous environment, in which a hydrophobic species (the acid chloride) must cross the interface, meet the hydrophilic species (water), and react irreversibly. Benzoyl chloride (Figure 3–11) was chosen as the reactant, as it is cheap and readily available compared to other benzoyl halides, and its rate constant measured in pure water is fast (1.2 s^{-1}) [Song and Jencks, 1989].

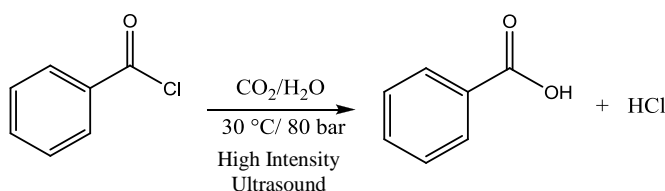


Figure 3–11 Benzoyl chloride hydrolysis in $\text{CO}_2/\text{H}_2\text{O}$

Its simplicity further resides in the fact that in the presence of excess water, it follows pseudo first-order kinetics [Jacobson *et al.*, 1999b; Timko *et al.*, 2003], according to Eq. 3.8:

$$k_{\text{obs}} = k'[\text{H}_2\text{O}] \quad (3.8)$$

where k_{obs} is the observed rate constant, which is pseudo first-order (s^{-1}) in benzoyl chloride (Eq. 3.9):

$$\ln \frac{C_c}{C_{c0}} = -k_{\text{obs}} t \quad (3.9)$$

where C_{c0} is the initial concentration of benzoyl chloride in CO_2 , and C_c is the concentration of benzoyl chloride in CO_2 to be determined. A plot of the left-hand term against time yields a straight line with a slope which is numerically equal to the rate constant k_{obs} . The benzoic acid product is highly soluble in water ($\sim 3 \text{ g L}^{-1}$) and therefore its measured concentration appearing in the water phase over time was related to the amount of benzoyl chloride depleted in the CO_2 phase by the following mass balance:

$$C_c = C_{c0} - \frac{V_w}{V_c} C_w \quad (3.10)$$

Some benzoic acid partitioning occurred into the CO_2 phase, however, due to the low $\text{CO}_2/\text{H}_2\text{O}$ partition coefficient of benzoic acid ($K_{\text{CW}} = 0.37$) [Brudi *et al.*, 1996], and the short time of reaction ($\leq 30 \text{ min}$), the concentration of benzoic acid in the CO_2 phase was found to be insignificant compared to that found in the water phase and was therefore omitted from the above mass balance.

3.4.1 Determination of Benzoyl Chloride Hydrolysis rates in $\text{CO}_2/\text{H}_2\text{O}$

The solubility of benzoyl chloride in dense CO_2 has never been assessed experimentally, although it may be assumed that due to its much higher octanol/water partition coefficient ($K_{\text{OW}} = 162$), it would be much more soluble than benzaldehyde ($K_{\text{OW}} = 43$). As a qualitative check, the visualisation method described in Section 3.1.7.1.1 was used to observe any two-phase behaviour. Briefly, the 30 cm^3 view cell was heated to 30°C and filled with CO_2 up to 80 bar. The analogue camera was pointed so as to obtain a clear magnified view of the bottom of the view cell, which was illuminated by the Visilight spotlight. Benzoyl chloride was injected in the port valve using the $100 \mu\text{L}$ standard volume loop, providing a CO_2 concentration of 0.028 mol L^{-1} . Since no droplets were observed to collect on the bottom inside surface of the cell, complete solubilisation of

benzoyl chloride was assumed to take place in CO₂ at values below this concentration. Therefore, the 1 mL standard volume loop was employed, providing an initial benzoyl chloride concentration in 0.35 L of CO₂ of 0.0245 mol L⁻¹, below that permissible according to the visual test.

Following heating of the ultrasound vessel to 30 °C and charging with water (0.65 L) and CO₂, benzoyl chloride (0.0086 mol) was injected into the reactor and its conversion monitored over time under either circulation or acoustic agitation by pulsed ultrasound (25%) with amplitude settings of 20–70%. Aliquots (2–3 mL) were collected from the circulating water fraction originating from the lower section of the vessel, and analysed for the presence of benzoic acid by GC without further dilution (see Appendix A4.1). The resulting values of k_{obs} were used for the separation of the mass transfer and kinetic effects, and for evaluating the mixing efficiency of ultrasound, as discussed in further detail in Sections 5.6 and 5.7.

3.4.2 Benzoyl Chloride Hydrolysis in the CO₂/H₂O/Tween 80 System

Since the presence of non-ionic surfactants was expected to affect the emulsion composition and therefore mass transfer rates, any changes observed in the rate of the hydrolysis of benzoyl chloride in the presence of Tween 80 would provide information on any effects on the mass transfer. The hydrolysis of benzoyl chloride was therefore also studied in the presence of Tween 80. The procedure was identical as that described for the hydrolysis in Section 3.4.1, other than that 1% Tween 80 was dissolved in water prior to charging of the aqueous phase in the reactor. Following the start of pulsed ultrasound, samples were taken at regular intervals from the top and lower sections of the reactor, and

quenched by trapping the organic acid in acetone on ice. Benzoyl chloride was never detected in samples, signifying either that:

- CO₂ droplets were completely depleted of reactant by the time they reached the sampling point.
- Since emulsions stabilised by Tween 80 could theoretically be more concentrated than emulsions without surfactant, there was a possibility that they carried a greater concentration of reactant, and that this quickly reacted during sample depressurisation, possibly overestimating the value of the rate constant.

In order to exclude the latter hypothesis, an experiment was carried out with the view cell positioned in-line to the ultrasound vessel as a visual aid of emulsion stability. Following injection of benzoyl chloride and sonication of the CO₂/H₂O/Tween 80 mixture for one minute, ultrasound was stopped and the contents originating from the lower section of the vessel were circulated until the emulsion was seen to fully break and a transparent aqueous phase was observed in the view cell. The aqueous phase was thus sampled for determination of the concentration of the benzoic acid product, and was found to match the concentration in samples collected at one minute of sonication when the emulsion was still present. This observation confirmed that CO₂ droplets were most probably depleted of reactant by the time they had reached the sampling point, and that benzoyl chloride did not quickly react upon breaking of the emulsion, with a possibility of overestimating the observed reaction rate.

The value for the theoretical yield of benzoic acid was evaluated by measuring the concentration of benzoic acid appearing in samples following sonication of an amount which was equivalent to the 100% yield of benzoic acid. Benzoic acid (1 g, 8.6 mmol) was sonicated in the CO₂/H₂O/Tween 80 mixture, and samples were taken and analysed by GC

at 20 minute intervals over one hour. The theoretical yield of benzoic acid thus determined was $0.01 \pm 0.005 \text{ mol L}^{-1}$.

3.5 Damköhler Analysis for Mass Transfer and Reaction in CO₂/H₂O

In order to obtain a clearer understanding of the mass transfer and kinetic effects governing the observed rate constant in the ultrasound-induced CO₂/H₂O emulsion, the results for the hydrolysis of benzoyl chloride were analysed in relation to the Damköhler number, Da , which is defined as the ratio of the transport time to reaction time. Identification of Da , in combination with the observed sonic enhancements with respect to silent conditions, and data from mass transfer studies, allowed an in-depth characterisation of the CO₂/H₂O/ultrasound system and prediction of the conditions that would lead to the well-mixed limit, beyond which no further mass transfer enhancements may be achieved for chemical reactions.

3.6 Synthetic Applications in CO₂/H₂O: The Barbier Reaction

Following the general characterisation of the CO₂/H₂O/ultrasound system, and the studies on the mass transfer of benzaldehyde and hydrolysis of benzoyl chloride, the attention turned next towards the possibility of exploiting the ultrasound reactor for exploration of applications that would be synthetically useful to the chemical and pharmaceutical industry. As discussed briefly in Sections 2.6 and 2.6.1, the Barbier synthesis was carefully chosen from a number of potential candidate reactions due to its simplicity of operation and tolerance to a moderately acidic aqueous environment. Evaluation of the observed rate constant in the presence of ultrasound would provide information on the mass transfer and kinetic effects and allow direct comparison with the results obtained in Chapter 5.

Typically, the Barbier synthesis involves the reaction between the allylating agent (usually an allyl halide) and a carbonyl compound in the presence of a metal mediator, to afford the homoallylic alcohol product. A more in-depth discussion regarding the chemistry of the reaction will be presented in Section 6.2 together with the observed results. The procedures described in the following Sections employed benzaldehyde as the primary carbonyl reagent, further extending the scope of the mass transfer studies which employed benzaldehyde as the model compound.

3.6.1 Particulate Filters

Since metal powders were employed, the presence of a particulate solid species would necessitate the use of some form of filtration method for sample collection of the reactor contents. Therefore, two types of filtration devices were used. The first consisted of three layers of stainless steel sheet (325 mesh) secured around each outlet opening inside the reactor. In the second, two in-line sintered filters (Swagelok, 0.5 μm pore size) were connected respectively before the L1 and L2 sampling sections. In this way, powder-free samples were obtained and potential blocking of the sampling tubes would be avoided.

3.6.2 Method for the Zinc-Mediated Barbier Synthesis

The choice of reactant concentration was based on the findings from Chapter 5 regarding the solubility of benzaldehyde (the limiting reagent in the Barbier synthesis) in CO_2 , which was evaluated as 0.174 mol L^{-1} . A standard loop of appropriate volume therefore ensured that the concentration of benzaldehyde in the CO_2 phase following injection was below its solubility limit. A typical experiment involved the use of molar ratios of zinc/allyl bromide/benzaldehyde of 2:2:1. Experiments were also carried out to study the effect of

varying the reagent mole ratios, and when this was the case, it will be specified in the appropriate Section (see also Appendix A6.1). It was anticipated that due to the hydrophobic character of the reagents and the homoallylic product, a significant portion of these species would preferentially partition in the CO₂ phase. Therefore, it was decided that for simplicity the CO₂ fraction would be monitored by the same internal standard method employed for experiments studying the solubility of benzaldehyde. Since *n*-decane proved to be a good hydrophobic internal standard for evaluation of the concentration of benzaldehyde dissolved in CO₂, it was also employed in the Barbier synthesis.

In a typical experiment, the reactor was heated until the desired temperature was reached. Zinc dust (8 g, 122 mmol), allyl bromide (10.6 mL, 122 mmol), *n*-decane (as the internal standard, 0.5 mL, 2.5 mmol), and water (580 mL) were added to the reactor. In experiments involving salts, water was replaced with a salt-containing aqueous phase with salt concentrations ranging from 1.3 to 6 mol L⁻¹. The salts NaCl, NaBr, NH₄Cl, NaH₂PO₄, and KH₂PO₄ were all tested for their capacity to improve the performance of the Barbier reaction. In other experiments, water was replaced with an aqueous solution containing 1% Tween 80, which was prepared in the same manner as that described in Section 3.2.3.2.1. In other experiments, the effect of metal was assessed by including either tin (< 100 µm) or bismuth (100 mesh) as the mediators instead of zinc [Petrier *et al.*, 1985b; Wada and Akiba, 1985]. In order to extend the scope of the Barbier reaction in CO₂/H₂O, the allylation of several substituted aromatic aldehydes was also investigated. 2-chlorobenzaldehyde, 4-methylbenzaldehyde, 4-methoxybenzaldehyde, (*E*)-3-phenylprop-2-enal were used with each having an initial CO₂-phase concentration of 0.145 mol L⁻¹.

The aqueous phase, reagent, metal and internal standard were loaded in the reactor, which was quickly sealed and charged with CO₂ at 40 g min⁻¹ via the high-pressure pump P1 (see

Figure 3–5), up to a pressure which was 10 bar below the required final pressure. The CO₂ flow rate was then decreased to 10 g min⁻¹ for injection of benzaldehyde (61 mmol) via the six-port valve fitted with a bypass tube of known volume (for benzaldehyde this was 6.22 mL or 16.8 mL when both reagents were co-injected). For the majority of the experiments the conditions were kept at 30 °C/80 bar. In a separate set of experiments, the effect of temperature and pressure was investigated by performing the reactions at 60 °C/120 bar. Once the desired pressure was reached, ultrasound was commenced at 80% amplitude and 25% pulse rate, and the contents were sonicated for the required time.

3.6.3 Sampling and analysis

Samples were taken at regular intervals from both the CO₂ and water fractions of the reactor, during which time, ultrasound was momentarily stopped. Samples originating from the CO₂ fraction were slowly bubbled through cold acetone by isolating sampling section L1. Samples from the water fraction were taken by isolating sampling line L2. The pressure was kept constant between each sampling by topping the reactor with fresh CO₂. Aliquots (2–3 mL) from each fraction were analysed by GC. Samples originating from the water fraction were analysed without further dilution, since the solution was transparent and no immiscible phases were observed. The yield of the homoallylic alcohol product arising from benzaldehyde was calculated using GC calibrations and the internal standard method (for CO₂ fraction samples), due to commercial availability of the product 1-Phenyl-3-buten-1-ol (see Appendix A6.1). However, due to unavailability of the standards for the corresponding substituted benzaldehydes and to time restrictions that prevented purification from the reaction mixture, a GC calibration could not be performed for these compounds and therefore the yield was estimated by measuring the ratio of GC peak area

of homoallylic alcohol relative to the sum of the peaks of unreacted aldehyde and products. Further identification of the homoallylic alcohol product was obtained by concentrating the enriched fractions *in vacuo* and analyzing samples by ^1H NMR at 300 MHz and ^{13}C NMR spectroscopy at 100 MHz (School of Chemistry, University of Birmingham).

Upon completion of the reaction at 60 °C/120 bar, the CO_2 density (0.43 g cm^{-3}) was increased by quickly cooling the reactor with cold water to 30 °C/80 bar (0.7 g cm^{-3}) and continuing sonication for 1 hour, in order to maintain constant CO_2 solvation during the separation stage, and therefore remove bias due to differences in solubility. Following experiments with salts, the aqueous fraction was extracted twice with diethyl ether (10–20 mL) and the organic fraction analysed by GC.

For comparative purposes, reactions were also performed in the ultrasound reactor pressurised with 70 bar N_2 rather than CO_2 , and under ambient stirring in sealed 100 mL glass bottles. For reactions using N_2 as the pressurising gas, the lack of a compressed fluid surrounding the ultrasound probe would potentially affect acoustic agitation of the water phase. Therefore, the volume of water was adjusted to 700 mL rather than 580 mL to ensure that the probe was at least partially immersed in the water phase. Following sonication for 1 hour the water phase was collected and $2 \times 50 \text{ mL}$ samples were taken, extracted each with $2 \times 50 \text{ mL}$ diethyl ether, and aliquots analysed by GC. For reactions at ambient conditions, zinc (6 mmol), allyl bromide (6 mmol), benzaldehyde (3 mmol) and *n*-decane (0.26 mmol) were added to water (50 mL) in sealed 100 mL glass bottles positioned on a hot plate at 30 °C and agitated using a magnetic stir bar. Following termination of the reaction, the mixture was Buchner filtered and the powder was washed with diethyl ether, whereas the filtrate was extracted with diethyl ether ($2 \times 50 \text{ mL}$). The combined organic fractions were then analysed by GC.

3.6.4 Zinc Particle Size Determination

In order to investigate any potential effects of ultrasound on zinc particles (such as changes in particle size due to erosion or aggregation), samples were analysed in a mastersizer following sonication in the ultrasound reactor for 1 hour in CO₂/H₂O (at 30 °C/80 bar) or in N₂/H₂O (at 30 °C/70 bar). The results were compared with those of untreated samples containing an equivalent concentration of zinc in distilled water under ambient conditions. Since solid particles may normally experience aggregation via electrostatic interactions, aliquots from each sample were also treated at ambient conditions with 95% amplitude continuous ultrasound for 2 min using a 20 kHz, 500 W sonifier (model VC505, Sonics & Materials, CT, USA). For evaluation of particle sizes, a Malvern Mastersizer (HYDRO 2000SM, Malvern, U.K.) was used. This relies on a laser diffraction technique to determine particle size in dilute dispersions. The pattern of diffraction is related to particle size via the Mie theory model. The refractive index of zinc (RI = 1.467) was used for analysis of the samples. The stirrer speed in the sample cell was set to 1000 rpm, and the suspension was added by pipette until the laser obscuration reached ~10 % of its total value. Three readings were taken for each sample and the mean calculated by the mastersizer. The values plotted on the ordinate axes represent the population of particles analysed as determined by obscuration of the laser. The results obtained are presented in Section 6.2.2 and are discussed in relation to the effects of ultrasound on solid particles reported in the literature.

3.6.5 Post-Reaction Separation

Since one of the major advantages of biphasic systems lies in the ability to separate species by exploiting the solute preferential partitioning in either phase, recovery of the homoallylic alcohol product was assessed by passing the CO₂ fraction through the 30 cm³

high-pressure view cell, which was employed as a post-reaction separation vessel. The cell was kept between 20–30 °C. In order to ensure removal of any water present in the CO₂ phase and to facilitate separation of the phases, 50 mL of water was slowly collected by opening valves V2 and V5, while the reactor pressure was maintained between 80–100 bar via pump P1. The pressure of the view cell was controlled below 30 bar with valves V7 and V8 to ensure that the CO₂ in the view cell was in gaseous form and did not carry any product when vented from the outlet. Two valves were positioned in line in order to control the CO₂ flowing into and venting out of the cell. Each cycle may be summarised as follows: the valve before the cell (V7) was carefully opened so that the pressure in the cell would not exceed 30 bar; the resulting pressure drop in the ultrasound vessel (≤ 5 bar) was rectified by topping up with CO₂; the valve after the cell was carefully opened to vent CO₂ gas while the product mixture, which was condensing in the view cell, was monitored by observing the position of the meniscus through the windows. Following ~2–3 hours of separation cycles, the product was collected and any residues remaining in the view cell were recovered by dissolving in acetone. The fractions were combined, concentrated *in vacuo* and the product was weighed in a pre-weighed glass vial. An aliquot was dissolved in acetone and analysed by GC. The results are presented in Section 6.9, along with any recommendations for optimisation of this separation procedure.

Chapter 4

CHARACTERISATION OF THE CO₂/H₂O/ULTRASOUND SYSTEM

4.1 Introduction

Ultrasonic irradiation of multiphase systems may lead to both chemical and physical effects which are related to the generation of cavitation. Chemical effects are mostly associated with observation of enhanced kinetics due to the initiation of free-radical reactions, while the physical effects may comprise a wide range of phenomena, including the generation of dispersions and agitation which may be responsible for mixing and enhanced mass transfer. Due to the novelty of the system in terms of its vessel geometry and ultrasound power, it was important to evaluate the sonochemical activity in pressurised systems. While the mixing efficiency and mass transfer rates will be the subjects of discussion of Chapter 5, the present Chapter will also assess the emulsifying capacity of ultrasound for CO₂/H₂O mixtures, and determine the volume fractions of dispersed phase under ultrasound irradiation. Due to the ‘*black box*’ nature of the reactor, both macroscopic and microscopic methods were devised for visualisation of the sonicated vessel contents. The overall findings would provide information for comparison of the results with those obtained for other similar systems found in the literature, and help to evolve the current understanding of the effects induced by ultrasound in high-pressure multiphase systems.

4.2 Ultrasound Power Calibration

The sonochemical effects of ultrasound strongly depend on the supplied power density, although they do not increase monotonically with supplied power. Not all of the electric power is converted to heat, and loss of efficiency must therefore be quantified. Loss in electric efficiency may be the result of several factors, including heat loss to the surroundings (although this is thought to be minimal when proper insulation is employed), loss to other forms of energy (*e.g.* vibration and sound), and loss related to transducer efficiency due to piezoelectric, dielectric, and elastic effects [Mezheritsky, 2004].

Sonochemical reactors equipped with transducers of higher frequencies display higher efficiencies [Asakura *et al.*, 2008]. Indeed, the highest frequency transducers are associated with a higher conversion efficiency, from 60% at frequencies < 100 kHz to over 80% at frequencies > 1 MHz. Quantification of the ultrasound power absorbed by the fluid is related to the heat generated during sonication [Koda *et al.*, 2003], which is dependent on the physical properties of the fluid through which the ultrasound energy is transferred (in this case CO₂, water, and reactor material). Aside from providing information regarding acoustic power, knowledge of the temperature profile may also be beneficial when considering synthetic and food applications [Fryer and Robbins, 2005], where heat and hydrodynamic factors are crucial for obtaining process homogeneity in batch reactors [Trujillo and Knoerzer, 2011]. Therefore, a calorimetric calibration was carried out for the present reactor filled with CO₂/H₂O. The temperature rise due to pulsed ultrasound was evaluated under different electric power (Figure 4–1).

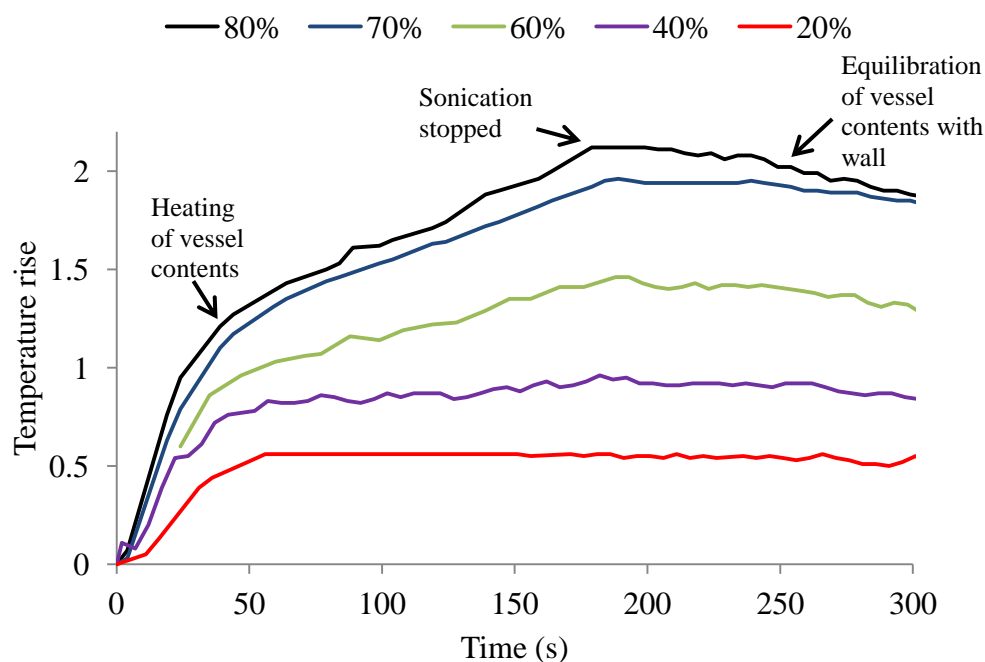


Figure 4–1 Effect of power amplitude on the temperature rise of the vessel contents following pulsed ultrasound at 20 kHz; ultrasound was stopped after 180 s. Conditions: CO₂/H₂O 35% v/v, 80 bar, 30 °C initial T

Analysis of the temperature rise revealed a distinct pattern which was observed irrespective of the electric power draw, and which was attributable to different stages of the reactor and its contents. From the temperature rise, the absorbed acoustic power could be evaluated (see Section 3.2.1) and plotted as a function of the amplitude setting (Figure 4–2). The energy efficiency was thus estimated as 70% at higher electric power. Comparison of the efficiency with that of a smaller vessel with a volume of 87 cm³ [Timko, 2004], revealed that electric efficiency was lower in the present case (70% compared to 78%), highlighting a possible effect of vessel geometry on acoustic efficiency.

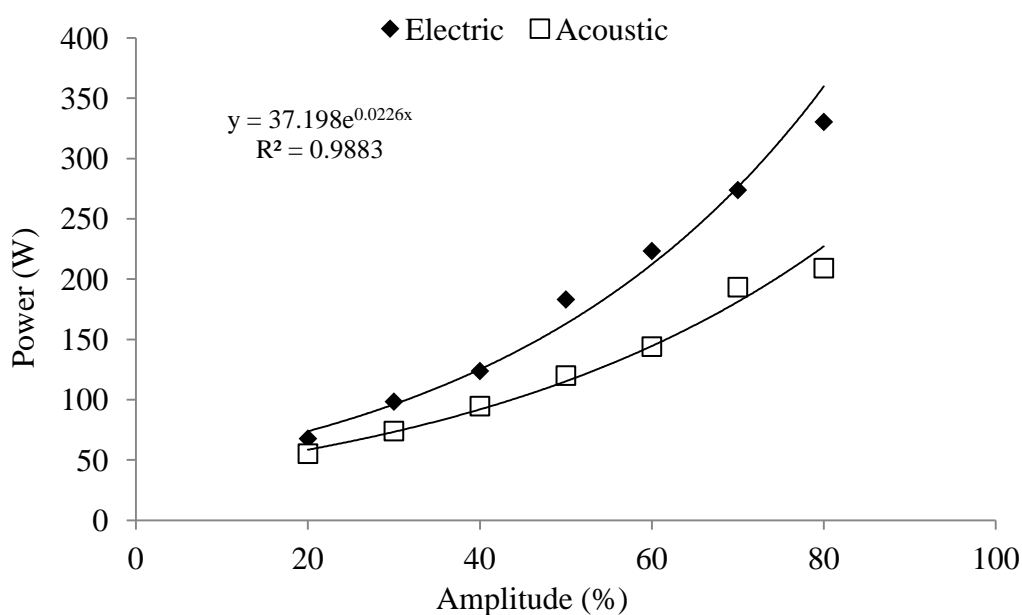


Figure 4–2 Plot of the electric power draw and acoustic power absorbed by CO₂/H₂O calculated using ΔT from Figure 4–1 according to Eq. 3.1. Conditions: 3 min pulsed ultrasound at 20 kHz, CO₂/H₂O 35% v/v, 30 °C (initial T)/80 bar

The results showed that the conversion efficiency of the present reactor was within that for other commonly-employed sonochemical devices. Absorbed power in the form of power density (power delivered to the vessel divided by vessel volume) and power intensity (power delivered to the vessel divided by the probe cross section), may be thus used as

reference values when comparing the effects of ultrasound with those reported for other systems.

4.3 Cavitation Activity in High-Pressure Systems

Scale-up of highly cavitation-dependent processes (*i.e.* sonochemical reactions) is usually problematic due to the dependence on localised cavitation events (immediately below the irradiating probe), and wide differences in the energy dissipation in the bulk volume, which shows a variation of 100-400% as the distance from the probe is increased in larger reactors [Kumar *et al.*, 2007]. The reactor design in terms of the ratio of reactor diameter to probe diameter, distance of the probe from the reactor walls, and liquid height all play a role on the cavitation activity distribution [Gogate *et al.*, 2011]. The physical properties of the fluids and the system conditions are also important aspects affecting the presence of cavitation, especially for high-pressure systems. Therefore, it was important to assess the cavitation activity for the present reactor geometry in the CO₂/H₂O system.

4.3.1 Cavitation in Dense CO₂

The possibility to achieve high-intensity cavitation activity in compressed CO₂ (or any high-pressure fluid) is a matter of ongoing debate, and erroneous interpretation of the data for many multiphase systems may lead to confusion regarding which phase experiences cavitation. Ultrasonically-induced cavitation in the presence of CO₂ has been demonstrated in several recent cases. For example, Kuijpers *et al.* [2005] studied radical polymerisations in CO₂-expanded methyl methacrylate under pressures of up to 10 bar. In radical polymerisations, initiation of the chain reaction normally requires the use of an initiator. However, in the work of Kuijpers *et al.* [2005], this additive was not required, as the application of ultrasound was sufficient to initiate the polymerisation. Furthermore,

because cavitation also induced polymer chain scission, the molecular weight was controlled to remain below the limit over which negative viscosity effects would ensue. Although the presence of cavitation was not directly examined, the authors suggested that bubbling CO₂ through methyl methacrylate served for inception and growth of the cavities. A similar interpretation was provided by Kruus *et al.* [1990], who studied the polymerisation of styrene in the presence of CO₂ at 1 bar under ultrasonic irradiation. These studies suggest that CO₂ was not the cavitating fluid, since it was present as a gas. Moreover, it has been argued that fluids with a high vapour pressure experience a subsequent ‘softer’ implosion due to facilitated vapour transfer and a higher number of gas molecules residing inside the expanding cavitation bubbles [Rooze *et al.*, 2013; Van Iersel *et al.*, 2007]. For the same reasons, cavitation should be facilitated for fluids with a higher vapour pressure, as long as the Blake threshold does not exceed the maximum applied acoustic pressure (see Section 2.5.4 and Figure 4–3).^(a)

Indeed, visual observation of cavitation streams appearing beneath the ultrasonic probe during sonication in CO₂ up to 75 bar provided proof that cavitation was possible in CO₂ at subcritical pressures [Kuijpers *et al.*, 2002]. A recent study by Balachandran *et al.* [2006] demonstrated that ultrasound-induced physical changes could take place in scCO₂. They observed pronounced cell damage in the extraction of essential oils from plant materials when using ultrasound at 40 °C/160 bar. They also found that strips of aluminium foil placed below the irradiating source showed significant pitting under the same conditions. Matsuyama *et al.* [2011] studied the formation of porous glass via the mechanofusion of core/shell structures in subcritical CO₂.

^(a)The vapour pressure of water increases from 0.006 bar at 0 °C to 0.04 bar at 30 °C.

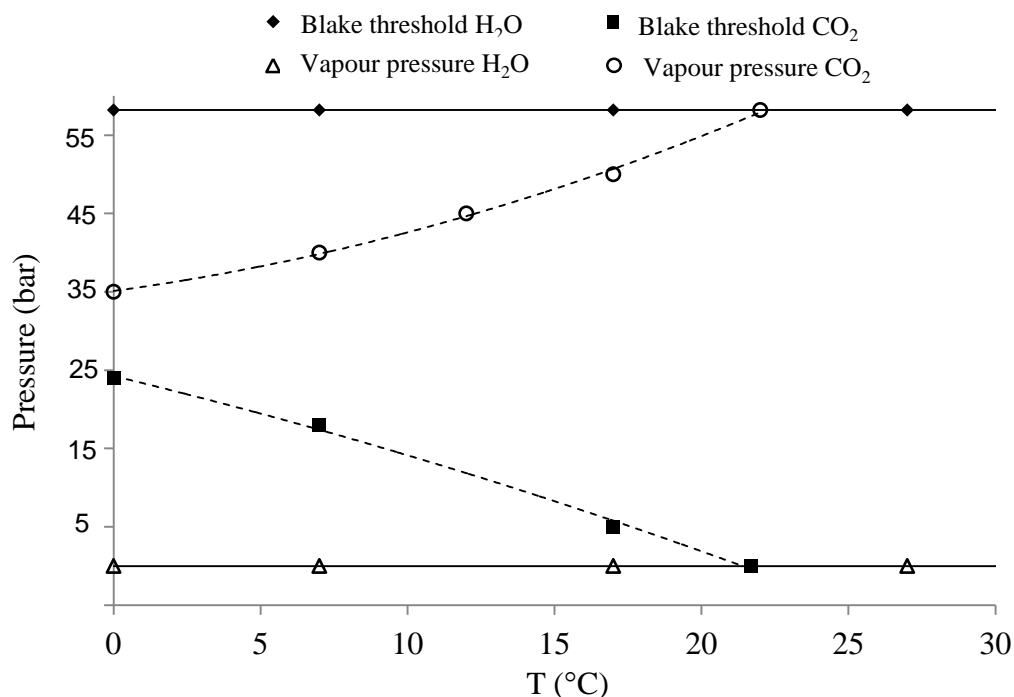


Figure 4–3 Graph showing the Blake threshold and vapour pressure lines for initiation of cavitation in CO₂ and water at different temperatures. $P_B = P_H - P_V$; P_B (Blake pressure), P_H (system pressure), P_V (vapour pressure). In order to initiate cavitation an acoustic pressure greater than the Blake threshold must be applied. Reproduced from Kuijpers et al. [2002]

The authors reported that sonication was responsible for the high-impact forces generated between the template (poly-methyl methacrylate) and guest (glass) particles, leading to attachment or embedding of the particles. Cavitation was observed through a view cell and proposed to be the primary mechanism of microparticle formation.

Ultrasound has also been frequently employed as a means of activating metal surfaces towards reactions. The activation has been ascribed to various mechanisms, each depending on the metal being considered. Although an indirect role by an increase in surface area has generally been postulated to account for observed increased reaction rates, tribological theory is now more widely accepted, by which ultrasound induces morphological surface changes that lead to localised chemical effects [Suslick, 1990]. Erosion of the metal surface was proposed as the primary mechanism for effecting metal

activation, largely as a result of investigations detailing the ultrasound-induced erosion and pit-formation on various metals [Vyas and Preece, 1977; Hansson and Morch, 1980]. A direct consequence of surface erosion is breakage of the passivating surface layer and an increase in the number of activated pits [Lucbe, 1994]. The reactive surface then becomes more accessible to reagents, which is of significance in synthetic applications. Regardless of any erosion taking place, ultrasonic breakage can also occur as long as the energy is sufficient to overcome the self-cohesion of the passivating layer (mostly a mixture of carbonates and oxides) and the cohesion between this surface layer and the underlying metal, which is certainly true for magnesium, zinc, and aluminium, all of which have been employed in sonochemical reactions [Pasha and Jayashankara, 2005; Reddy *et al.*, 2013; Petrier *et al.*, 1985a; Lucbe and Damiano, 1980; Horst *et al.*, 1999]. The common feature for these metals is the presence of a soft metal layer, as even if the oxide layer is hard (as for aluminium), plastic deformations are able to disrupt this sufficiently to lead to activation [Lenderink *et al.*, 1993]. The surface of cubic-face-centered metals (Al, Ag, Cu) undergoes more pronounced micrometric roughness changes than hexagonal lattice (Zn) metals. The increase in roughness is accompanied by structural changes along the crystalline structure, as evidenced by Scanning Electron Micrographs and X-Ray powder Diffraction techniques, respectively [Verdan *et al.*, 2003]. Usually, passive layers covering the surface of metals are extremely thin (a few nm) and are amorphous, unless they are subjected to conditions in which the layer thickens, rendering it crystalline. In any case, it is expected that ultrasound treatment removes this passive layer by tearing off the more weakly bounded grains from the surface of the metal.

The presence of cavitation in CO₂ was investigated by irradiating aluminium foil wrapped around a stainless steel plate which was positioned 1 cm below the ultrasound probe in

CO₂/H₂O. In order to rule out any effect induced by pressure, controls were carried out by subjecting the foil to a sequential pressurisation/depressurisation procedure in the absence of ultrasound. In the presence of ultrasound, a distinct circular hole of a size consistent with the probe diameter was formed (Figure 4–4, left). This result demonstrated that the damage was most likely induced by a vertical cavitation stream and did not occur due to a random reaction which would have rather affected all parts of the foil similarly. The steel plate was positioned 1 cm below the probe, so that the results were valid at least for the top CO₂ environment.

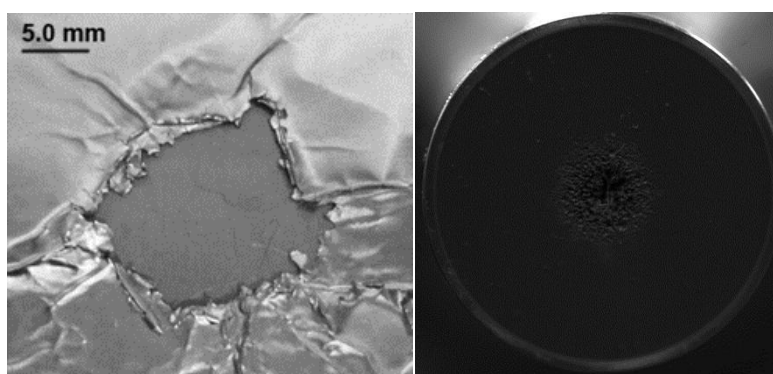


Figure 4–4 (Left): image of aluminium foil erosion following 1 min sonication in CO₂/H₂O. Four layers of foil were wrapped around a stainless steel plate positioned 1 cm below the probe. Conditions: CO₂/H₂O 50% v/v, 30 °C/80 bar, 70% amplitude, 25% pulse rate. (Right): pitting of the horn as a result of cavitation following approx. 1 year of high-pressure operation

Further demonstration of the presence of cavitation came from the observation of ‘pitting’ sites at the centre of the ultrasonic horn (Figure 4–4, right), indicating that cavitation was forceful enough to create microjets and physical damage at the solid metal surface.

In order to investigate whether this effect could be reproduced in the water phase, flat strips of aluminium foil were placed at the bottom of the water phase and subjected to pulsed ultrasonic irradiation for 20 minutes at 70% amplitude following pressurisation with CO₂. After ultrasonic treatment, the aluminium foil gradually degraded from cm to μm-size (Figure 4–5).

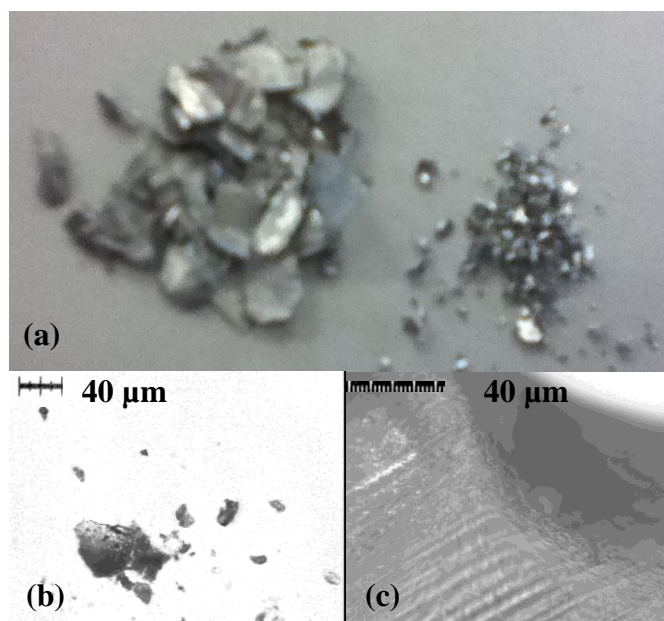


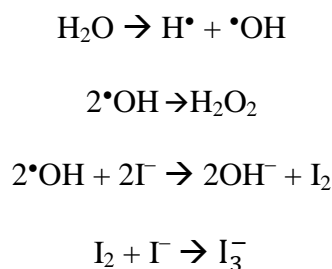
Figure 4–5 Visualisation of aluminium foil following ultrasound treatment in CO₂/H₂O at 30 °C/ 80 bar: (a) photograph showing the flat strips of aluminium foil before (left) and after ultrasound treatment in the reactor; (b) and (c) after ultrasound treatment for 20 minutes with CO₂/H₂O 50 v/v%, 30 °C/80 bar, 70% amplitude; (b= $\times 20$, c= $\times 40$, objective); images were viewed with an Olympus CH2 light microscope and recorded with a Leica DFC259 camera

Macro- and microscopic visualisation of these particles revealed distinct features that were not present in the absence of sonication. First, the smallest visible particles were below 10 µm in diameter, Figure 4–5 (a) and (b), and second, the shape of the particles changed from flat to highly deformed three-dimensional structures, with deep ridges consistent with the result of mechanical forces acting on the metal surface, Figure 4–5 (c). These results, combined with the literature data, demonstrated that aluminium undergoes significant morphological changes when irradiated by ultrasound in a CO₂/H₂O environment. Moreover, the changes were consistent with a cavitation stream originating from beneath the probe. It is, however, difficult to assess the magnitude of the cavitation forces generated, which could be significantly lower than those required to mediate sonolytic reactions, as the cohesive forces holding the passive oxide/carbonate layer and metal together are much weaker than those of covalent bonds. Cavitation in the water phase was

next assessed by monitoring the sonochemical activity in the presence of a head pressure of gas.

4.3.2 Cavitation in Water: The Sonochemical Test

Early reports demonstrated that the intensity of the effects of ultrasound may be significantly reduced in water under high hydrostatic pressures [Dezhkunov *et al.*, 1997]. In order to investigate whether *true* sonolytic reactions (frequently encountered in sonochemical applications) could take place in the present system, the Weissler reaction was employed as a standard chemical dosimetry test for sonochemical efficiency (see Section 3.2.2.2), and the evolution of iodine species was monitored under different conditions. Progress of the transformation is determined by the reaction of the iodide anion from potassium iodide with free-radical species that originate from the breaking of the H–OH bond and therefore may not occur in the absence of water [Morison and Hutchinson, 2009] (Scheme 4–1).

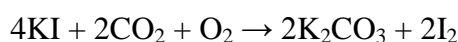


Scheme 4–1 Proposed sonolytic reactions occurring in the presence of iodide, water, and high intensity ultrasound

The type of gas dissolved and the hydrostatic pressure applied are important factors affecting the intensity of the effects of ultrasound. The presence of gases or impurities increases the bubble nucleation rate (the more soluble the gas, the lower the interfacial tension), but may also decrease the intensity of the cavitation effects [Rooze *et al.*, 2013]. Furthermore, the presence of sonochemical effects may be determined by the physical

properties of the gas, and the conditions under which the system is operated. For example, Goldfarb *et al.* [1998] demonstrated that with increasing pressures, cavitation in water was more likely to occur under a head pressure of CO₂ than of argon. Therefore, in an effort to gain further understanding of the sonochemical effects of ultrasound in high-pressure systems, the evolution of iodide species was monitored in water with a head pressure of either nitrogen or CO₂ at different pressures.

Preliminary investigations revealed that it was not possible to use CO₂ as the gas for the potassium iodide test, as considerable reaction was observed to occur even in the absence of ultrasound by simple contact of aqueous potassium iodide with an atmosphere of CO₂. The effect observed in the presence of CO₂ may be a consequence of oxidation to potassium carbonate occurring during sample collection (Scheme 4–2):



Scheme 4–2 Oxidation of iodide species occurring in the presence of CO₂ and O₂

This result was unexpected, since it was a replication of an experiment carried out by Timko [2004], who had observed low and no iodine production by sonication of aqueous potassium iodide in the presence of a head pressure of CO₂ at 1 and 80 bar, respectively. Although no sonochemical effects were possible at higher pressures in his study, the presence of cavitation in water was observed through a quartz window. This cavitation was however assumed to derive from dissolved CO₂ in water acting as nucleation sites.

In the present case, progress of the Weissler reaction under a head pressure of N₂ was observed at 1 bar but not at 70 bar (Figure 4–6).

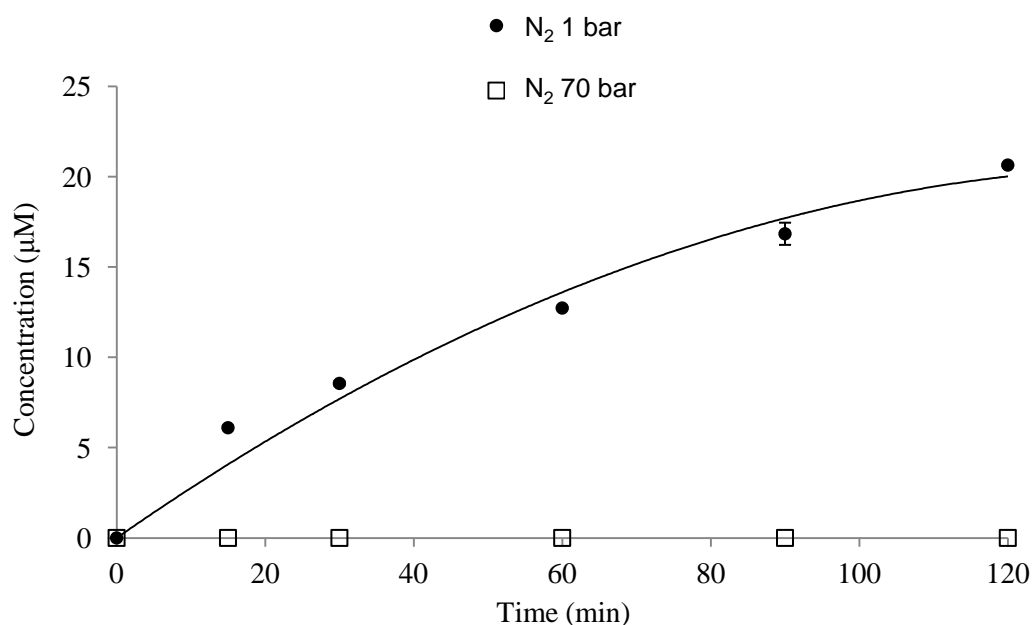


Figure 4-6 Iodine formation from potassium iodide using pulsed ultrasound (80% amplitude). A head pressure was applied to a 800 mL aqueous solution by using nitrogen at 1 or 70 bar and 30 °C. Error < 4%, see Appendix A1.1

Iodine production increased fairly linearly and the production rate was $1.7 \times 10^{-7} \text{ mol h}^{-1} \text{ W}^{-1}$. This value was however approximately 30 times lower than those reported for standard glass sonochemical reactors ($\sim 5 \times 10^{-6} \text{ mol h}^{-1} \text{ W}^{-1}$) operating at ambient conditions [Seymour *et al.*, 1997], further supporting the view that sonolytic rate enhancements are not likely to occur in water under high pressures with this reactor geometry.

Cavitation may occur in both high-pressure CO₂ and in water pressurised with CO₂, although the true nature of the cavitating phase is difficult to assess, and in both cases inception of CO₂ bubbles may constitute the primary event. In the first case, implosion of the CO₂ bubbles in a CO₂ phase may generate the forces responsible for effects such as damage to soft metal surfaces, whereas in the second case, implosion of CO₂ bubbles in a water phase may generate the forces responsible for splitting of water molecules leading to

sonochemical reactions. However, the presence of hot spots seems improbable in a water phase pressurised with CO_2 . This is supported by Henglein and Gutierrez [1988], who found that ultrasonic irradiation in the presence of CO_2 could mediate polyacrylamide degradation but not sonolytic reactions such as the formation of hydrogen peroxide and the oxidation of iodide. The authors suggested that although the degradation of polymers is of a mechanical nature, and dependent on the presence of hydrodynamic shear forces, sonolytic reactions rely on high temperatures arising during the adiabatic compression of cavitation bubbles. High temperatures were favoured for mono- and diatomic gases, due to their high ratio of specific heats, γ (the ratio of heat capacities at constant volume and at constant pressure), but not for polyatomic gases, such as CO_2 .

4.4 Characterisation of CO₂/H₂O Emulsions: Emulsion Appearance

Ultrasound in high-pressure (and especially near-critical fluids) displays distinct advantages compared to sonication of fluids under ambient conditions, including ‘soft’ cavitation [Goldfarb *et al.*, 1998], and increased biphasic interfacial disruption with better dispersive and micromixing capacity due to the low surface tension, high vapour density and low liquid density of CO₂ [Van Iersel *et al.*, 2010]. In the vicinity of a heterogeneous surface, the acoustic wave leads to the generation of physical and mechanical phenomena which may be beneficial regardless of any sonochemical effect taking place [Kumar *et al.*, 2007; Shchukin *et al.*, 2011]. As a consequence, two immiscible liquids will generate an emulsion, which may not be solely localised beneath the irradiating surface once formed, but as in the present case, should occupy larger fractions of the vessel volume. Other factors governing ultrasound efficiency for heterogeneous systems include distance of the biphasic line from the probe (here with a water phase volume of 650 cm³, this was 1 cm below the ultrasound probe), probe surface area, and vessel geometry. The capability of ultrasound to generate CO₂/H₂O emulsions in the reactor vessel was therefore next assessed. Information relating to the apparatus and experimental procedures used for macroscopic and microscopic visualisation of emulsions can be found in Section 3.2.3. Section 4.4.1 provides a description and discussion of the results relating to macroscopic observation of emulsions using various techniques, and more specifically the observation of the persistence of opacity as a measure of emulsion stability following acoustic agitation of the CO₂/H₂O mixture. On the other hand, Section 4.4.2 discusses the findings following the investigations carried out for the determination of the size of emulsion droplets.

4.4.1 Macroscopic Observation of Ultrasound-Induced CO₂/H₂O Emulsions

In general, macroscopic inspection may offer both qualitative and quantitative information regarding the appearance and stability of emulsions. A change in the opacity may be indicative of the presence of μm -sized droplets which originates from light scattering phenomena. For example, Psathas *et al.* [2002] observed that surfactant-stabilised CO₂/H₂O emulsions appeared milky white. However, the macroscopic appearance of the emulsion should not be used as an indication of droplet size, but only as a gross indication of the presence of an emulsified system.

4.4.1.1 Observation Through the Pyrex Tube

Due to an absence of windows in the ultrasound vessel, a strategy was devised whereby its contents could be visualised by circulation through a pyrex tube following pulsed ultrasound. One end of the pyrex tube was connected to the outlet of the vessel that originated from the lower water fraction of the biphasic, while the other end was connected to the circulation pump allowing the contents to be fed back to the vessel via the top opening with a flow rate of $20\text{ cm}^3\text{ min}^{-1}$ (full experimental details are provided in Section 3.2.3.1). The appearance of opacity through the pyrex tube at 27 °C was pressure-dependent, and was observed when the CO₂ was in the liquid^(b) region but not when the CO₂ was vapour (Figure 4–7). During conditions when CO₂ was vapour only mm-sized gas bubbles could be observed in the water phase, Figure 4–7 (a). The emulsion appeared as a fine turbid cloud entering the tube a few seconds following the start of sonication, and quickly filling the remaining volume of the tube. After 3 minutes of sonication, this opacity persisted for several minutes when sonication was stopped. Based on an estimated time

^(b)From NIST: <http://webbook.nist.gov/chemistry/fluid/>.

delay for emulsion appearance of 13 s (see Section 3.2.3.1), the time to reach steady-state conditions for emulsion formation was evaluated as approximately 30 s. Between the time of first observation of the emulsion and the time to reach steady state, the appearance of turbidity in the pyrex tube was intermittent, and coincided with each acoustic burst. This stage may be marked by faster droplet breaking rates, and conditions in which droplet breaking and droplet forming rates are not yet at equilibrium.

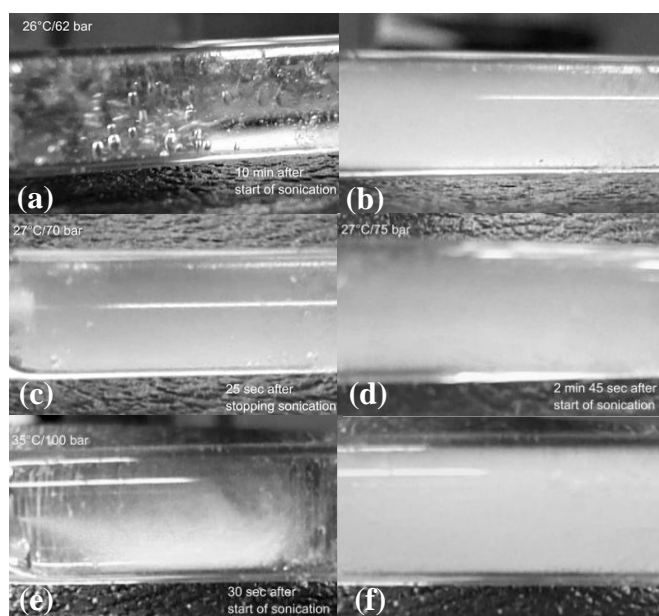


Figure 4–7 Macroscopic observation of turbidity in the circulating water fraction from the ultrasound vessel observed through the pyrex tube, following sonication (70% amplitude, 25% pulse rate) of CO₂/H₂O mixtures using 660 cm³ of water (a, b, and c), or 670 cm³ of water (all the rest); (a) 27 °C/62 bar (CO₂=vapour); (b) 27 °C/70 bar (CO₂=liquid/subcritical); 60 s after starting sonication; (c) same as (b), 25 s after stopping sonication; (d) 27 °C/75 bar (CO₂=liquid/subcritical); (e) 35 °C/100 bar (CO₂=supercritical), 30 s after starting sonication; (f)-same as (e); 50 s after starting sonication

Further experiments were not possible owing to leaking at the pyrex/PEEK connection. The pyrex tube was prepared by fusing and manually pulling the ends of a standard rod, so that the resulting wall thickness could not be determined. The high-strength Araldite® epoxy resin adhesive has long-term (several months) resistance to various inorganic acids,

and a tensile shear strength which depends on the curing conditions. However, no curing conditions were undertaken, and failure tests assessing the effect of curing temperature and time on leaking at high pressure should be carried out.

Nonetheless, these observations allowed initial inspection of the vessel contents, revealing the presence of dispersions of dense CO₂/H₂O and providing the incentive for carrying out further investigations into their appearance and stability using a more reliable methodology.

4.4.1.2 Observations through the 30 cm³ View Cell

Application of ultrasound to the biphasic coincided with increased turbidity in the view cell, which lasted approximately 15-20 minutes after stopping ultrasound (Figure 4–8). Decreased stability produced a characteristic upwardly-moving front line, resulting in the view cell becoming transparent again. The same pattern was observed during sonication at 40 °C/110 bar and at 50 °C/140 bar. Further support for the presence of the emulsion was provided by the increasing number and size of droplets collecting on the top inside of the window after stopping ultrasound, an indication that CO₂ coalescence was taking place, Figure 4–8 (d).

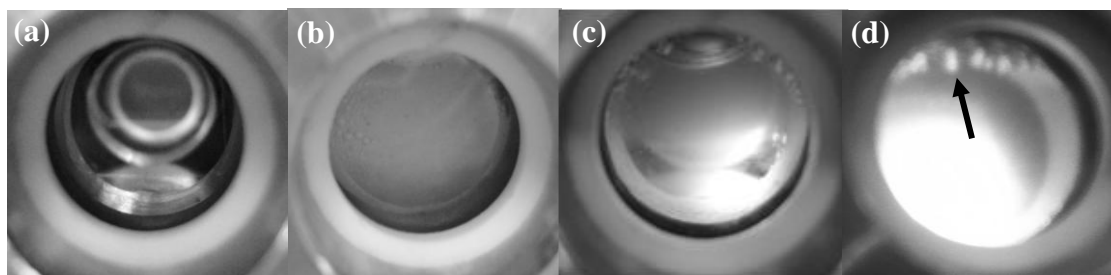


Figure 4–8 Observation of the lower water fraction from CO₂/H₂O mixtures in the ultrasound vessel using the 30 mL view cell; (a) circulation, no sonication; (b) 10 min following the start of sonication; (c) 5 min after stopping sonication and circulation; (d) CO₂ droplets collecting on the inside edge of the window after stopping sonication and circulation (arrow). Conditions: 30 °C/80 bar, 70% amplitude, CO₂/H₂O 35% v/v

If the top CO₂ phase was passed from the ultrasound vessel through the view cell (Figure 4–9), sonication resulted in a gradually rising phase, signifying that water appeared as the dispersed phase in the top CO₂-continuous phase of the reactor. Therefore, these observations demonstrated the utility of the view cell for exploration of the contents of the ultrasound vessel and provided the scope for carrying out experiments to assess the emulsion stability.

4.4.1.3 Emulsion Stability by Time Lapse Recordings

Emulsion stability is an important property affecting the efficiency of reaction and separation procedures. Factors such as droplet life-time and the variation of droplet diameter over time (due to coalescence) influence the hydrodynamic and mass transfer properties of the system, and this becomes particularly important in emulsion systems which are not stabilised with surfactants. For example, droplet size may be estimated by turbidimetry and Mie theory, where turbidity is given by $\tau(\lambda) = 1/l \ln(I_0/I)$, where l is the path length, and I_0 and I are the intensities of the incident and transmitted light, respectively [Dickson *et al.*, 2003]. Although the apparatus for carrying out turbidity studies was not available, emulsion stability was evaluated by recording the time required for the emulsion to revert back to the biphasic after stopping sonication, which was directly proportional to the amount of light passing through the view cell over time (Figures 4–9 and 4–10). Images were captured with a Photron camera and analysed using the ImageJ algorithm for assigning greyscale values to each pixel (see Section 3.2.3.2 for further details).

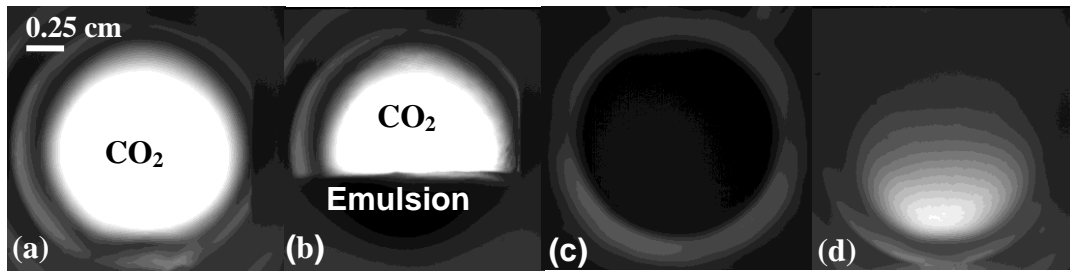


Figure 4–9 Images of the emulsion passing through the view cell from the top CO₂ fraction of the ultrasound vessel, recorded with the Photron camera; (a) only circulation; (b) after 3 min of sonication with circulation, an insoluble (water-containing) emulsion appears; (c) after 10 min of sonication with circulation, the light is completely blocked by the opacity of the emulsion filling the cell; (d) after 5 min since stopping sonication, light transmittance is partly restored. Conditions: 30 °C/80 bar, 70% amplitude, 25% pulse rate, CO₂/H₂O 35% v/v

The increase in light intensity resulting from an increase in transparency through the view cell as the CO₂/H₂O mixture reverted back to biphasic conditions following cessation of ultrasound is shown in Figure 4–10.

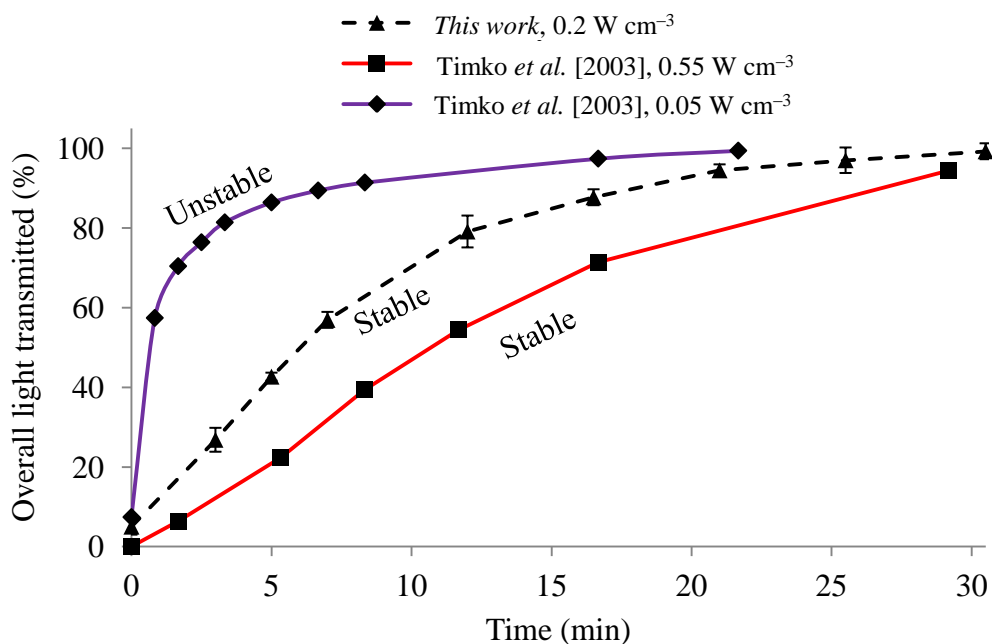


Figure 4–10 Stability of CO₂/H₂O emulsions generated by ultrasound measured as the increase in light intensity through the view cell after stopping sonication and circulation; (♦) turbidity at 0.05 W cm⁻³ associated with unstable macro-sized droplets formed by interfacial waves; (■) turbidity at 0.55 W cm⁻³ associated with micro-sized emulsions; both sets were obtained at 30 °C/75 bar, CO₂/H₂O 50% v/v. (▲) Stability data obtained in the present work: 30 °C/80 bar, 0.2 W cm⁻³ (75% amplitude), CO₂/H₂O 35% v/v. Both lines representing stable dispersions fit a second-order polynomial, whereas the low-stability dispersion followed a power relationship (all with $r^2 > 0.99$). See Appendix A1.2

The plot also shows superimposed data reproduced from turbidity studies of ultrasound-induced CO₂/H₂O emulsions from the literature [Timko *et al.*, 2003]. The authors associated the observation of a greater stability with the persistence of a turbidity lasting for several minutes, representing smaller droplets in the μm -range (as confirmed by microscopic visualisation), whereas turbidity lasting only a few seconds was associated with larger droplets ($> 100 \mu\text{m}$, generated by the lowest power amplitude specified by the ultrasound processor), and non-cavitation dependent interfacial mixing.

The sonic processor utilised in the present work displayed a lowest power setting of 20% amplitude, which was still able to generate dispersions that lasted for several minutes, therefore the lowest-stability dispersions could not be replicated. The trend obtained at a power density of 0.2 W cm^{-3} in the present system was quite distinct from that expected for unstable dispersions, which are obtained by the action of interfacial waves, as the half-life of emulsion stability was > 5 minutes compared to only a few seconds for unstable dispersions. Since most of the CO₂/H₂O applications make use of surfactant molecules as stabilisers, the view cell was next employed for observation of ultrasound-generated emulsions in the presence of the non-ionic surfactant Tween 80.

4.4.1.4 Observation of Tween 80-Stabilised CO₂/H₂O Emulsions

The use of a surfactant may be beneficial for increasing the surface area and stability of an emulsion. Processes that experience mass transfer limitations may show reduced process times, greater homogeneity and selectivity. A number of research groups have studied the use of surfactants for stabilising CO₂/H₂O emulsions. Tween 80 is a biocompatible (restricted use, mostly for foods, see Section 3.2.3), non-toxic compound that is suitable for food and medical applications. Due to its amphiphilic, non-ionic nature, Tween 80 has been shown to stabilise either C/W (where CO₂ is dispersed in the water-continuous phase)

or W/C (where water is dispersed in the CO₂-continuous phase) emulsions, depending on the system pressure and temperature [Torino *et al.*, 2010]. Conditions for which C/W emulsions were generated required that the hydrophobic tail–tail interactions were stronger than the tail–CO₂ interactions, and the interface bends around CO₂. These C/W emulsions were observed by Torino *et al.* [2010] across a range of conditions up to 60 °C/500 bar, above which coexistence of the emulsion with a CO₂ and a water phase was observed. In their study, highly concentrated C/W emulsions could be stabilised (even with 90 wt % CO₂) with mean droplet diameters of 0.5–5.4 µm depending on the flow rates through a sand pack. Other non-ionic surfactants have been reported for stabilising CO₂/H₂O emulsions. For example, Da Rocha *et al.* [2001] observed white concentrated CO₂/H₂O emulsions in the 2–4 µm size range, when including amphiphilic ethylene oxide-containing polymeric surfactants. Therefore, in order to assess the capability of ultrasound to generate stable emulsions, a 1 wt% Tween 80 solution was sonicated in the presence of CO₂ at 30 °C/80 bar. Fractions from both the top and lower sections of the vessel formed a milky white emulsion after a few seconds of commencing sonication, as observed through the view cell (Figure 4–11).

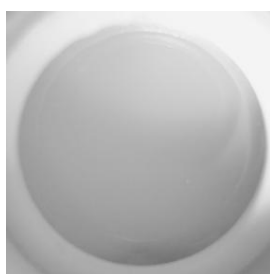


Figure 4–11 Photograph showing the appearance of the Tween 80 (1%) -stabilised CO₂/H₂O emulsions through the view cell, following 10 min pulsed ultrasound in the sonic vessel. Conditions: 30 °C/80 bar, 75% amplitude, CO₂/H₂O 35% v/v

As for the emulsions described in Section 4.4.1.2, Tween 80-stabilised emulsions broke down by coalescence of CO₂, showing a characteristic rising demulsification front after stopping sonication which reverted back to the biphasic in ~ 1 hour, as observed through the view cell. This demonstrated the greater stability of emulsions containing Tween 80 compared to emulsions that were generated in its absence, which lasted for 20–25 minutes. Since the macroscopic appearance and stability of CO₂/H₂O emulsions generated by ultrasound had been determined, the attention was next directed towards microscopic inspection of the droplets in these systems.

4.4.2 Microscopic Visualisation of CO₂/H₂O Emulsions

The search next progressed towards identifying a suitable method for obtaining an estimate of droplet size. Various techniques exist for evaluation of droplet size as described in Section 2.4.3.1, although high-pressure systems presented several challenges. Since a proper device for microscopic characterisation was not available, attempts were made for fabrication of a suitable prototype.

4.4.2.1 Visualisation of CO₂/H₂O Droplets: The Capillary Method

Ultrasound-generated emulsions were observed under the microscope by passing the contents from the bottom section of the ultrasound vessel through a fused pyrex capillary tube, as described in Section 3.2.3.3.1. Spherical droplets approximately 10 µm in diameter were observed, as pictured in Figure 4–12 (work undertaken by Dr. Alireza Bahari).

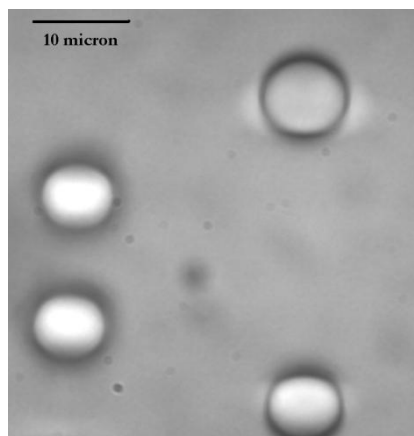


Figure 4–12 Observation of spherical droplets approximately 10 μm in diameter generated by pulsed ultrasound of CO₂/H₂O. Conditions: 30 °C/80 bar, CO₂/H₂O 45% v/v, 70% amplitude, 3 min sonication (work undertaken by Dr. Alireza Bahari)

Unfortunately, the capillary broke soon after, preventing further characterisation using this technique. Failure of the pyrex capillary resulted from tensile and bending forces during its making, handling, and connection to the ultrasound reactor. On the other hand, the capillary did not fail once in operation and was able to sustain hydrostatic pressures of up to 80 bar. Therefore, due to its fragility, only one capillary unit was successfully assembled and used for visualisation of CO₂/H₂O emulsions.

Although Figure 4–12 provides good evidence of the presence of spherical μm -sized droplets following sonication in the ultrasound vessel, it should not be used as an indication of the mean droplet diameter. An accurate value of mean droplet diameter and diameter distribution would ideally require analysing thousands of droplets, which was not possible in the present case using the capillary method.

4.4.2.2 The Microchannel Method

The use of a microchannel as replacement of the pyrex tube was attempted for characterisation of the emulsion droplets. Due to the limited demand for such specialised equipment, and the high cost of the units that are rarely described in the literature, the microchannel was custom-built. All the materials and methods for fabrication and testing can be found in Section 3.2.3.3.2. Application of a hydrostatic pressure of 60 bar resulted in failure at the channel inlet (Figure 4–13). Failure was not observed at the nanoport connection, proving the feasibility of such devices in high-pressure applications.

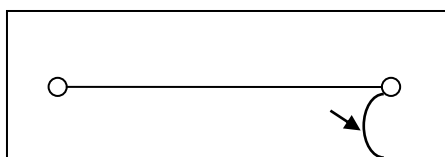


Figure 4–13 Image depicting the failure point as a fracture originating at the channel inlet and progressing downwards towards the chip edge (arrow); water with a head pressure of CO₂ at 60 bar was passed from the reactor through the PEEK/steel connections

Some possible explanations may be found in the literature. The Rudolf von Rohr group at ETH developed a similar microfluidic device for carrying out hydrogenation reactions in scCO₂ [Trachsel 2008; Trachsel *et al.*, 2009]. Following mechanical tests, the authors identified fracture of the silicon/glass as the most unpredictable type of failure, due to the brittleness of glass and variability in the strength of the bond between silicon and glass [Trachsel *et al.*, 2008]. Studies carried out by Blom *et al.* [2001] described the mechanical strength of the bond by the beam theory, where the square of the beam (in this case the channel) width is inversely proportional to the maximum applicable pressure. They concluded that a maximum 515 μm channel width allowed for an applied pressure of 150 bar. A similar device fabricated by the Jensen group at MIT was utilised for visualisation of CO₂/H₂O emulsions [Timko, 2004; Murphy *et al.*, 2007]. The pyrex was anodically bonded to patterned silicon wafers as in the present case, and the device was able to

withstand pressures of up to 200 bar. The pressure was lower (80 bar) while the channel width was smaller (300 μm) in the present case. Bond energy is highly dependent on annealing temperature and surface roughness, and may pose a significant limiting factor in the robustness of microfluidic devices. Surface roughness determines the bonding distance between the two surfaces, and a high value may lead to an increase in nucleation sites for fractures. However, annealing temperature was not provided, and surface cleaning, roughness measurements, and tensile strength tests were not carried out by the manufacturer, highlighting bond strength as a possible limiting factor.

Due to the time invested in the search for a suitable, relatively cheap design, final assembly and testing of the unit was not possible until the later stages of this PhD. Therefore, the remaining two units fabricated were not tested. Nonetheless, information gathered from these investigations may provide a scope for future improvements.

4.5 Characterisation of CO₂/H₂O Emulsions: Emulsion Volume Fractions

Another important property of emulsions is the fraction of dispersed phase present in the continuous phase, as it will ultimately determine the overall interfacial area and contact between the phases. Such information could be useful when considering emulsion-dependent mass transfer phenomena. Preliminary investigations revealed that during acoustic agitation, two distinct environments were generated in the ultrasound vessel, a water-continuous environment existing below the probe, and a CO₂-continuous environment existing above the probe in the upper region of the vessel (as confirmed by the presence of small amounts of water in samples). The procedures for assessing the volume fraction of CO₂/H₂O emulsions are described in Section 3.2.3.4. Measurement of the water mass in samples originating from the top CO₂-continuous fraction were used to

determine the volume fraction of water in CO₂ (W/C) emulsions. The results revealed that the volume fraction of water in these emulsions was $6.5 \pm 0.3\%$ (see Appendix A1.3.1).

Evaluation of the volume fractions of CO₂ in water (C/W) during sonication were assessed by measuring the concentration of octane, a hydrophobic tracer which partitions $> 99.9\%$ in CO₂, in samples originating from the lower section of the vessel. GC analysis (see Appendix A1.3.2) revealed that the fraction of CO₂ dispersed in the water phase was between 1% and $\sim 6.7\%$, depending on the standoff distance (SD) of the biphasic line from the probe (Figure 4–14).

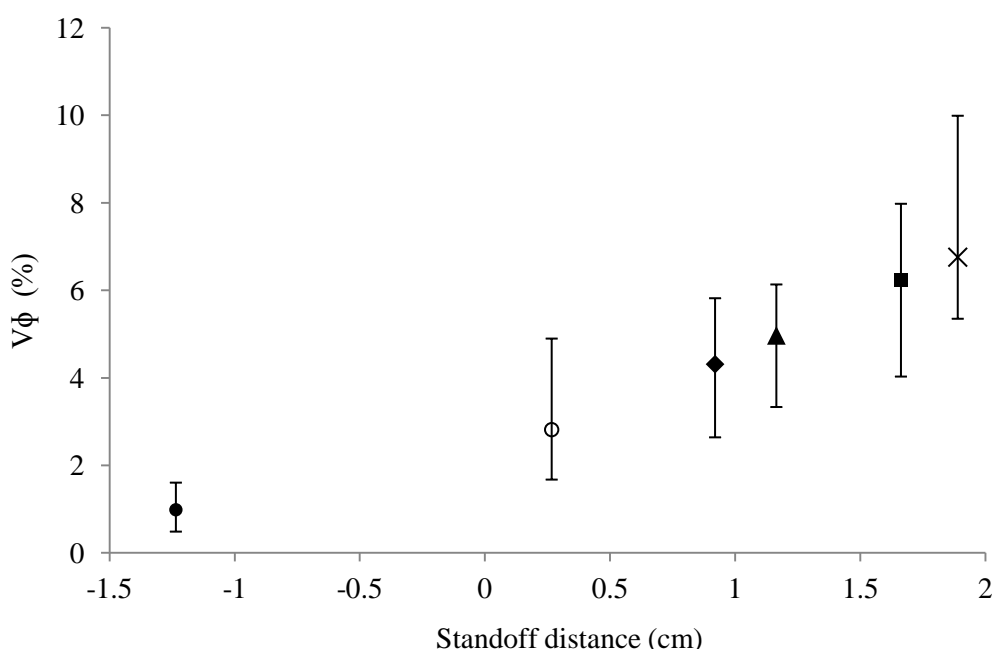


Figure 4–14 Volume fraction ($V\phi$) of CO₂ dispersed in the water phase following sonication of the CO₂/H₂O mixture at 70% amplitude; the standoff distance (SD) signifies the position of the biphasic line with respect to the probe; the negative values denote conditions in which the biphasic line was above the probe surface (i.e. probe immersed in water). SD was varied by changing the initial water volume in the reactor, which was (from left to right): 800, 700, 650, 630, 600 and 580 cm³ of water. Conditions: 30 °C/80 bar, 70% amplitude, 25% pulse rate, see Appendix A1.3.2

The large errors in these measurements were most probably associated with the heterogeneous nature of the emulsion at the sampling point, which may be variable due to the possible presence of turbulence generated by acoustic streaming. Moving the sampling

point slightly higher from the bottom of the vessel by extending the dip tube through the use of a silicone tube resulted in only octane-containing CO₂ being collected, indicative of the presence of interfacial waves. The outlet position is an important variable in the study for optimisation of the conditions, and should therefore constitute the scope of further investigations for this vessel geometry. Regardless of the magnitude of the errors, the results provided a general guide to the composition of the emulsion, which consisted of volume fractions that were always < 10%, and which differed in their nature in the top and lower sections of the reactor.

The low volume fractions encountered in the absence of stabilisers may be the result of the necessity of the system to maintain a low free energy in the form of a dilute emulsion, as higher droplet numbers would lead to increased coalescence due to attractive forces.

On the other hand, in the presence of Tween 80, water collection and octane tracer experiments from the top and lower sections of the vessel showed that water was the continuous phase throughout. The C/W volume fraction in the presence of Tween 80 was $35 \pm 2\%$, indicating that all of the CO₂ was dispersed in the water-continuous phase.

4.6 Conclusions

This Chapter described the general characterisation of the CO₂/H₂O/ultrasound system. Approximately 70% of the electric energy was absorbed by the CO₂/H₂O mixture in the form of acoustic energy. Measurement of the ultrasound-induced cavitation activity confirmed the presence of cavitation during high-pressure operation, although this was not consistent with the presence of high-energy bubble collapse, as evidenced by the lack of sonochemical activity. Ultrasound coincided with the appearance of a turbid emulsion which was stable for several minutes after stopping ultrasound, and which displayed volume fractions of the dispersed phase of 6.5% and 6.7%, in CO₂-continuous and water-continuous emulsions, respectively. Fabrication of a pyrex capillary tube allowed microscopic visualisation of the emulsion droplets, which were in the 10 µm range. However, further characterisation of the emulsion droplets was not possible due to the perishable nature of the devices. Inclusion of Tween 80 in the sonicated CO₂/H₂O mixture resulted in emulsions which were stable for over 1 hour, and in which all of the CO₂ present in the system was dispersed in the water-continuous phase. Once these general properties had been evaluated, the mass transfer properties and reaction kinetics in the CO₂/H₂O/ultrasound system were investigated by deploying small organic compounds.

Chapter 5

MASS TRANSFER AND HYDROLYSIS RATES IN CO₂/H₂O

5.1 Introduction

The rate of many biphasic reactions is influenced by the presence of the liquid-liquid or gas-liquid interface. The driving force for mass transfer is typically the difference in chemical potential, which is dependent on the concentration of the solute present in each phase. Since most organic reactions involve the use of small hydrophobic reagents, a suitable model for the study of mass transfer in liquid-liquid systems would involve the transfer of a hydrophobic compound from the dense CO_2 phase to the water phase. Benzaldehyde was selected as the compound of choice as it contains the important carbonyl group (found in many organic reactions) and has been studied previously for similar systems, allowing direct comparison with the literature and further understanding of the implications of scale-up. Since solubility and partitioning may be significant factors controlling mass transfer phenomena, evaluation of the solubility of benzaldehyde and its partition coefficient in dense $\text{CO}_2/\text{H}_2\text{O}$ mixtures is described. Mass transfer rates for benzaldehyde from CO_2 to water were evaluated for both silent conditions (only recirculation), and in the presence of acoustic agitation, in terms of the overall mass transfer, effective mass transfer, and film mass transfer coefficients. Finally, the rates for the hydrolysis of benzoyl chloride were evaluated and the mixing efficiency of ultrasound is discussed in terms of its ability to reduce the mass transfer limitations in biphasic reactions. Due to the number of symbols used, a notation Section is presented at the end of this Chapter.

5.2 Determination of Benzaldehyde Solubility in CO₂: The Chrastil Method

In the present study, evaluation of the solubility of benzaldehyde in CO₂ was an important aspect since it would provide the limit below which benzaldehyde would freely diffuse in the CO₂ phase for the study of mass transfer. The importance of obtaining accurate solubility data also lies in the ability to predict the maximum amount of solute that may be recovered from the CO₂ phase in separation procedures. Indeed, the solvating power of CO₂ may be tuned by manipulating the temperature and the pressure. One direct consequence of this is a remarkable increase in the solubility of benzaldehyde from 0.29 g L⁻¹ to 80 g L⁻¹ (a factor of ~280) when increasing conditions from 40 °C/60 bar to 120 °C/223.4 bar. Solubility data for benzaldehyde in CO₂ were compiled by Walther and Maurer in 1992 and are presented in Figure 5–1.

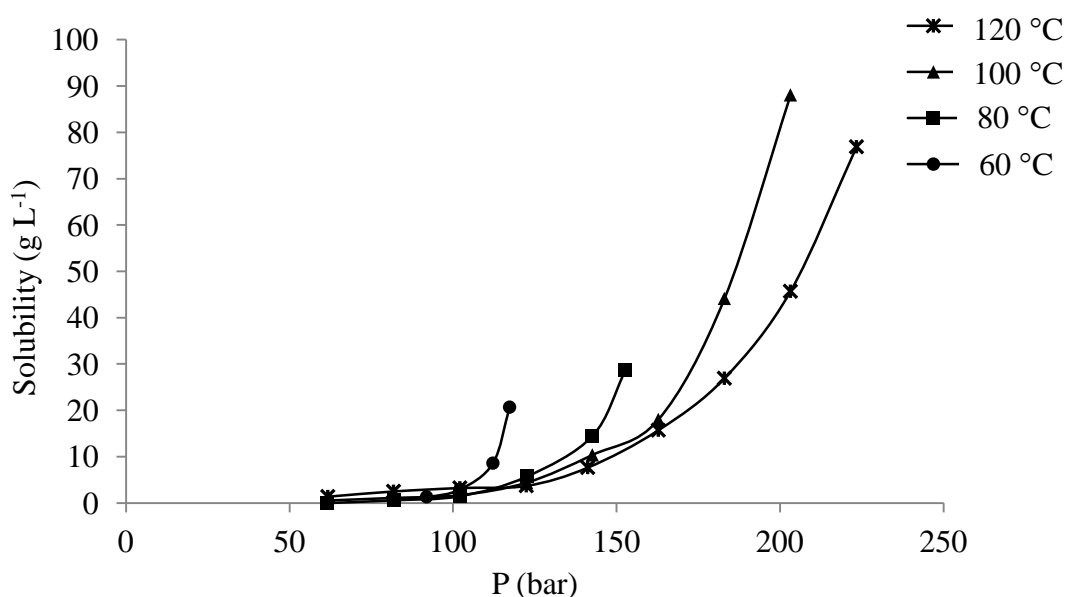


Figure 5–1 Solubility data for benzaldehyde in scCO₂ over a range of temperatures and pressures; experimental data was compiled by Walther and Maurer [1992]

The solubility of benzaldehyde at 30 °C/80 bar was predicted using the Chrastil relationship, Eq. 5.1:

$$\ln S = k \ln(\rho) + \frac{a}{T} + b \quad (5.1)$$

Where S is the solubility of the compound in CO₂, ρ is the CO₂ density, T is the temperature, k is an association constant which is characteristic for a given gas and solvent and ‘ a ’ and ‘ b ’ are physical parameters. It is customary for the Chrastil method to express both units of solubility and density with the units g L⁻¹, and this unit will therefore only be used in the present Section. Equally, determination of the physical parameters appearing in Eq. 5.1 requires the temperature to be expressed in Kelvin, therefore for all other aspects not directly related to the Chrastil method, and for the purpose of clarity, the temperature will be expressed in degrees Celsius.

Logarithmic isothermal plots of benzaldehyde solubility, obtained from Walther and Maurer [1992], against ρ , obtained from NIST^(a), generated straight lines (Figure 5–2) with slopes k (Eq. 5.2) and intercepts equal to $a/T+b$, as expected according to the Chrastil method [Chrastil, 1982; Sparks *et al.*, 2008].

$$\text{slope} = k ; \text{intercept} = \frac{a}{T} + b \quad (5.2)$$

The isothermal plots at different temperatures were parallel to each other and remained linear over the full range of available data. The association constants generated by each isothermal line were then used to obtain suitable values for ‘ a ’ and ‘ b ’ (see Appendix A2.1), and further adjusted to fit Eq. 5.1 to allow prediction of the solubility of benzaldehyde at 30 °C/80 bar (Figure 5–3). It was found that good agreement existed between the solubility data reported by Walther and Maurer [1992] and the predictions

^(a)Thermophysical Properties of Fluid Systems: <http://webbook.nist.gov/chemistry/fluid/>.

calculated by the Chrastil method for pressures ≤ 130 bar using $k = 3.259$ (Figures 5–4 to 5–6). For pressures > 130 bar the solubility was underpredicted by up to 35%.

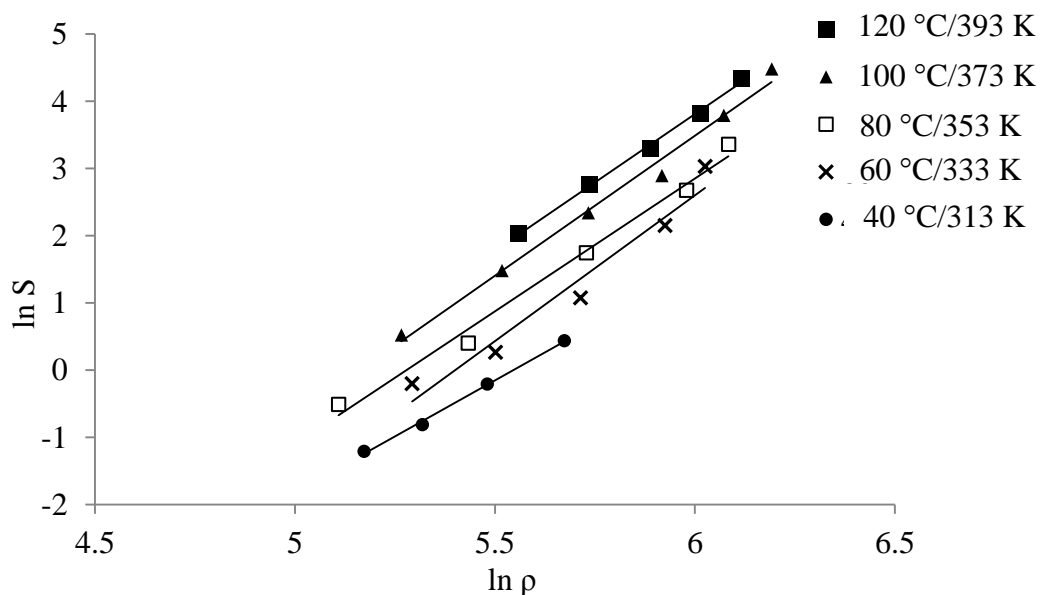


Figure 5–2 Log-log plot of the benzaldehyde solubility (S) vs density (ρ) for the determination of the association constant k from the experimental data reported by Walther and Maurer [1992]; see Appendix A2.1

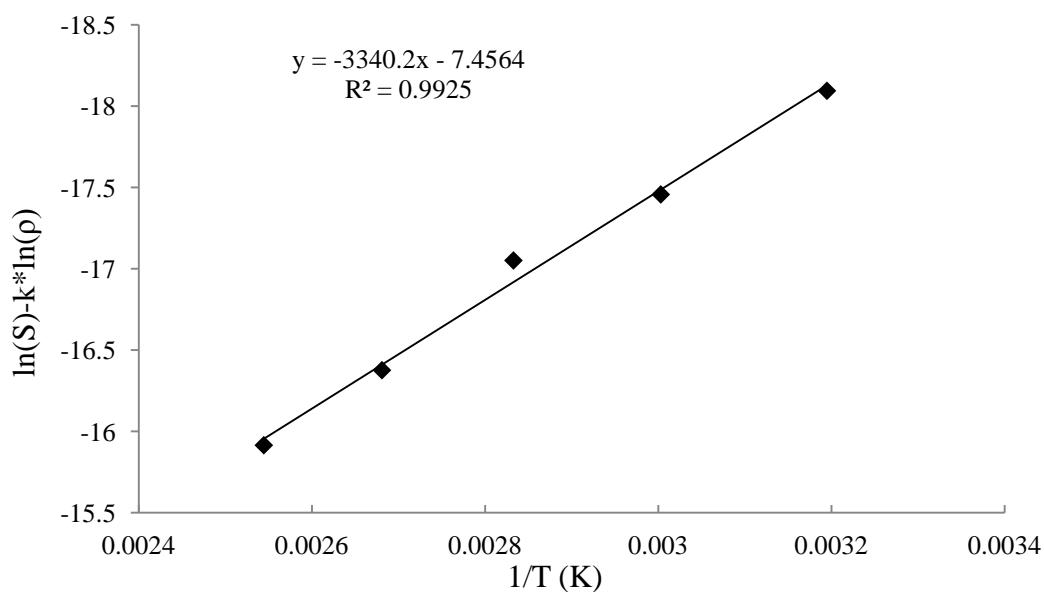


Figure 5–3 Plot of $(\ln S - k \cdot \ln \rho)$ vs $1/T$ with $k = 3.259$ (see Appendix A2.1). The values 'a' (slope) and 'b' (intercept) were then inserted into Eq. 5.1

The solubility of solutes in supercritical fluids is controlled by the competing effects of solute vapour pressure and solvent density. The solubility of benzaldehyde increased with pressure and therefore was dependent on the CO₂ density. How well the predicted solubilities correlate with the experimental values is determined by the range of pressures studied and is indeed a factor of the competing solute vapour pressure and solvent density, which are balanced at the crossover pressure [Leeke *et al.*, 2004]. Due to the high density of CO₂ at 30 °C/80 bar (700 g L⁻¹), the model may be expected to provide a reasonable method for calculation of the solubility of benzaldehyde at conditions where the solvent density shows the predominant effect (Table 5–1).

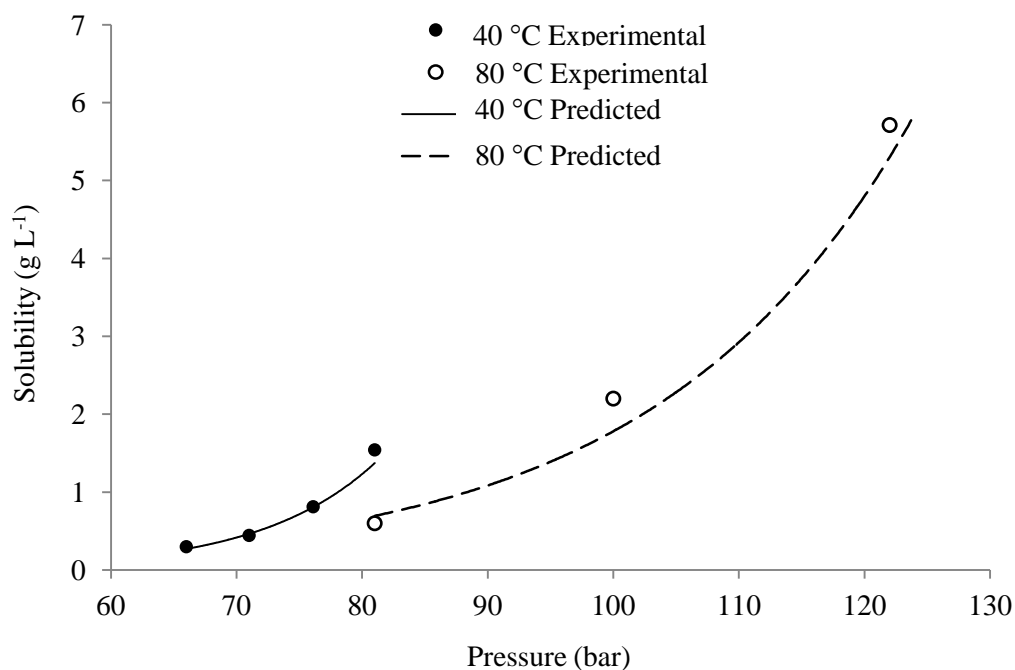


Figure 5–4 Correlation of experimental data for benzaldehyde, obtained from Walther and Maurer [1992], and the Chrastil predictions using $k = 3.259$, for temperatures of 40 °C and 80 °C

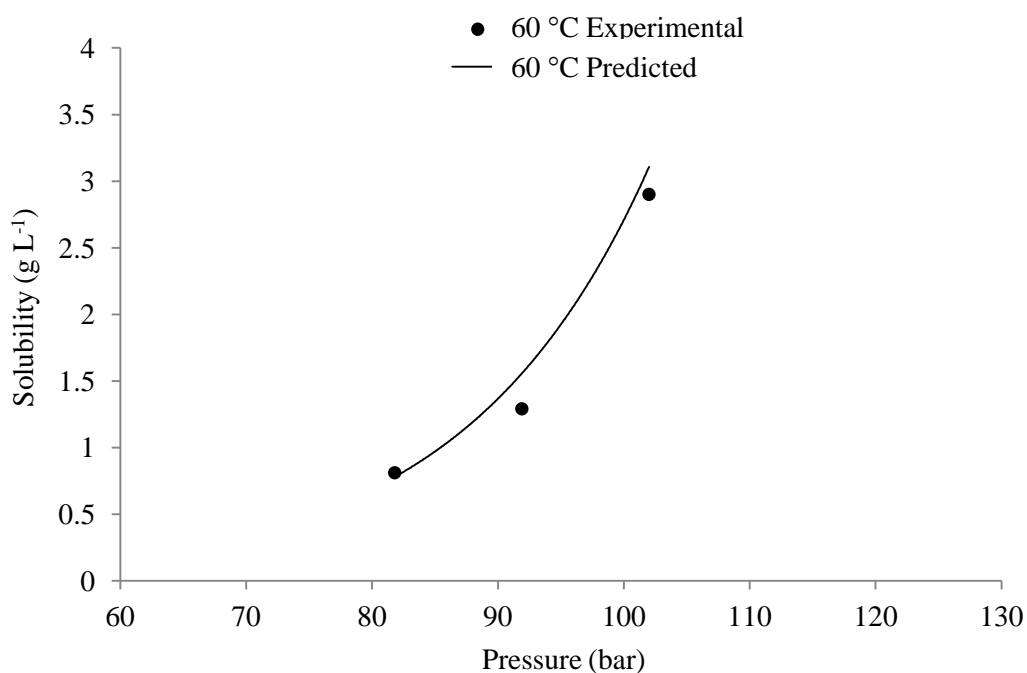


Figure 5–5 Correlation of experimental data for benzaldehyde, obtained from Walther and Maurer [1992], and the Chrastil predictions using $k = 3.259$, for 60 °C

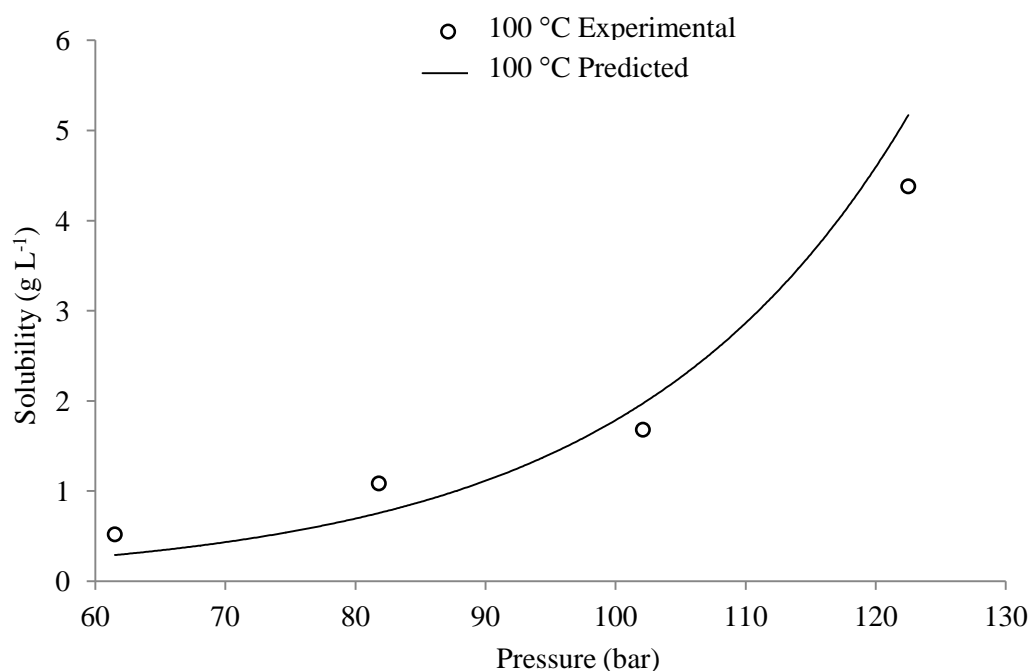


Figure 5–6 Correlation of experimental data for benzaldehyde, obtained from Walther and Maurer [1992], and the Chrastil predictions using $k = 3.259$, for 100 °C

<i>k</i>	<i>a</i>	<i>b</i>	Predicted <i>S</i> 30 °C/80 bar (g L ⁻¹) ^(b)	Average deviation %
3.259	-3340.2	-7.456	17.77	7

Table 5-1 Solubility of benzaldehyde in CO₂ predicted by the Chrastil method

5.3 Experimental Quantification of Benzaldehyde in CO₂

Since the conventional experimental determination of the concentration of solutes in compressed gases can offer some practical challenges, the concentration of benzaldehyde in the CO₂ phase was assessed using *n*-decane as the internal standard. A quantity of benzaldehyde approximately equivalent to the maximum solubility in 350 cm³ of CO₂ (predicted by Eq. 5.1) was loaded in the vessel in the presence of the CO₂/H₂O biphasic (35% v/v). The concentration appearing in the CO₂ phase was subsequently measured under conditions of acoustic agitation. Benzaldehyde was either injected in the top CO₂ phase with the 6-port valve by exploiting the standard 1/16" tubes connected in series (amounting to a total internal volume of 6.22 mL), or placed directly in the water phase of the vessel before sealing and pressurising. Due to its density (1.04 g cm⁻³) benzaldehyde fell to the bottom of the water phase when placed directly in the vessel. Therefore the latter method also provided a quick check of the ability of ultrasound to recover benzaldehyde from the lower water fraction for dissolution into the top CO₂ phase.

Analysis of CO₂ samples during sonication showed a gradual increase in the concentration of benzaldehyde in the CO₂ phase (Figure 5-7).

^(b)Final predictions of benzaldehyde solubility using the Chrastil relationship.

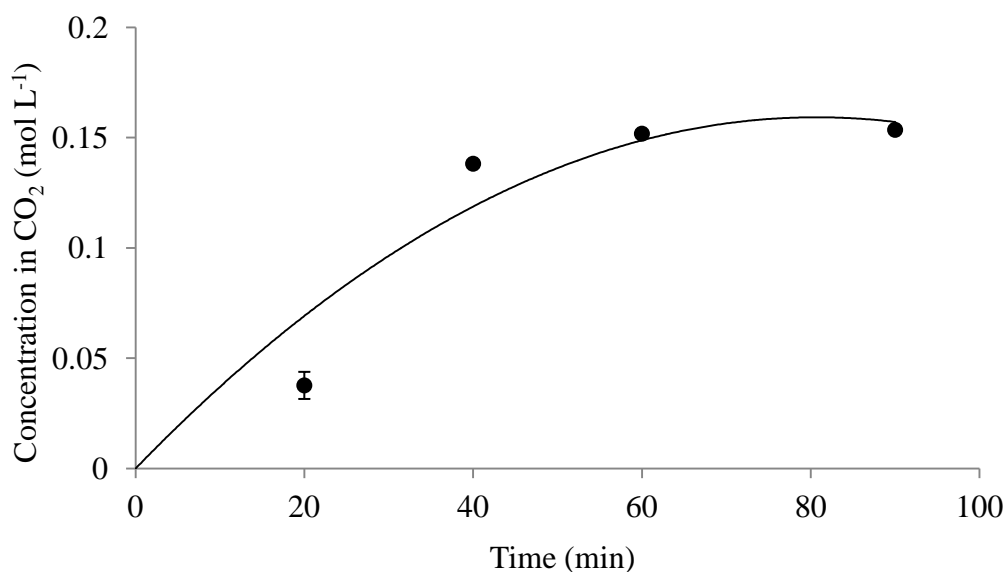


Figure 5–7 Benzaldehyde concentration appearing in the CO_2 phase following sonication of the $\text{CO}_2/\text{H}_2\text{O}$ mixture. Benzaldehyde (0.061 mol) was directly added to the water phase prior to sealing and pressurisation of the reactor (line of best fit to show when the maximum concentration was attained). Conditions: 30 °C/80 bar, 70% amplitude, $\text{CO}_2/\text{H}_2\text{O}$ 35 v/v%. See Appendix A2.2

The time required to reach equilibrium was approximately 40 minutes, after which a maximum benzaldehyde CO_2 concentration of $0.153 \pm 0.002 \text{ mol L}^{-1}$ was reached. The concentration values of benzaldehyde in CO_2 varied by < 1% between the two methods of benzaldehyde addition, demonstrating the capacity of ultrasound to mix the phases and allow hydrophobic compounds residing at the bottom of the vessel to be recovered and dissolved into the top CO_2 phase. The measured concentration of benzaldehyde in the CO_2 phase after sonication was below the initial concentration injected (Table 5–2).

Indeed, analysis of the water fraction revealed a considerable presence in this phase, signifying that partitioning was occurring between the phases.

Parameter	Value ^(c)
C_{c0} (mol L ⁻¹)	0.174
C_c (mol L ⁻¹)	0.153 (0.157)
n_{c0} (mol)	0.061
n_c (mol)	0.053 (0.055)

Table 5–2 Comparison between the initial benzaldehyde injected in the CO₂ phase (C_{c0} = initial concentration, n_{c0} = initial mols) and the benzaldehyde (C_c , n_c) measured in CO₂ after 40 minutes pulsed ultrasound at 70% amplitude, 30 °C/80 bar, CO₂/H₂O (35% v/v); values in brackets indicate the concentration assessed 30 minutes after stopping sonication

These observations revealed that benzaldehyde could be used in subsequent studies with an initial CO₂-phase concentration of up to 0.174 mol L⁻¹ and that the respective quantity of benzaldehyde introduced in the system would be freely soluble across the CO₂/H₂O biphasic without formation of a third insoluble phase. In terms of the solubility of organic compounds, CO₂/H₂O systems may differ with respect to CO₂ systems. Therefore, in order to gain further understanding on how the physicochemical properties of the CO₂/H₂O system may affect the solubility of organic compounds, two factors were next considered:

- (1) The effect of the presence of water on the solubility of organic compounds in water-saturated CO₂.
- (2) The effect of the structure of organic compounds on the CO₂/H₂O partition coefficient, and comparison with the octanol/water partition coefficient commonly employed in applications under ambient conditions.

^(c)The water concentration was $1.3\text{--}1.4 \times 10^{-2}$ mol L⁻¹ allowing closure of the mass balance with an error of 0.0025 mol (4%).

5.3.1 Effect of the Presence of Water in CO_2 : Solubility Parameters

The presence of water in dense CO_2 up to its saturation point has been shown to have a significant effect on the properties of CO_2 with many important implications. In accordance with reported values, no measurable differences exist between the density of water-saturated CO_2 and pure CO_2 in the range of 10-300 bar and 11-59 °C within the experimental uncertainty [Hebach *et al.*, 2004; King *et al.*, 1992]. This factor may be attributed to the low solubility of water in CO_2 , which is ~ 0.003 based on mole fraction at 30 °C/80 bar [Pappa *et al.*, 2009]. This value merely doubles at 50 °C/200 bar, Figure 5–8. However, the presence of water has been shown to affect the solubility of solutes in CO_2 . Iwai *et al.* [2004] reported an increase in the solubility of palmitic acid in water-saturated scCO_2 by 16%, compared to scCO_2 .

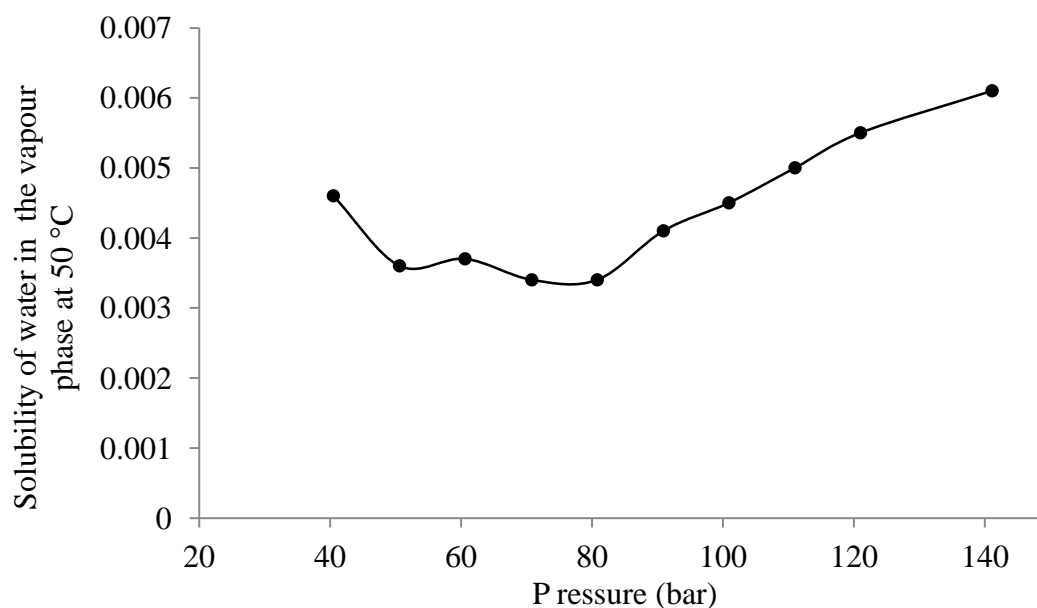


Figure 5–8 Dependency of pressure on the mole fraction of water in the vapour phase for the $\text{CO}_2/\text{H}_2\text{O}$ system at 50 °C. Adapted from King *et al.* [1992]

The solubility of palmitic acid in CO_2 increased even further when water was switched with ethanol, due to increased availability of H-bond sites [Iwai *et al.*, 2002]. Indeed, the self-association of water may limit the number of free H-bond sites. Similarly, the solubility of caffeine was observed to increase by up to 22% when scCO_2 was saturated with water [Iwai *et al.*, 2006]. The type and intensity of forces between water and the supercritical fluid are responsible for interactions with solutes, affecting their solubility [Gupta *et al.*, 1992]. The nature of the association of water in dense CO_2 has attracted fervent interest recently due to emerging technologies involving the injection of scCO_2 in geological reservoirs (such as oil or deep ocean reservoirs). *Ab initio* theoretic studies, combined with infrared spectroscopy measurements, initially pointed to dipole-quadrupole interactions as the main forces responsible for stabilisation of the solvation sphere of water in scCO_2 [Tassaing *et al.*, 2005; Glezakou *et al.*, 2010]. Recently, it has been demonstrated with good computational agreement that up to seven CO_2 molecules form the first solvation shell around one water molecule via electrostatic interactions and hydrogen bonds [Thanthiriwatte *et al.*, 2012]. The association of water with supercritical fluids may lead to local density augmentation in regions where the densities are found to be higher than the bulk density of the solvent, although these effects are difficult to quantify [Tucker, 1999]. Furthermore, the nature of the solute is a determining factor in affecting the forces responsible for solute-solute and solute-solvent interactions. Macnaughton and Foster [1994] found up to 90% enhancement in the solubility of 2,4 dichloro-(phenoxy)-acetic acid but minimal change in the solubility of DDT (possessing no H-bonding groups) when scCO_2 was saturated with water.

The Hildebrand parameter, δ , is one example of a model which may be used as a prediction of solubility. It is equivalent to the square root of the cohesive energy density [Gurdial *et al.*, 1993], defined by Eq. 5.3 as:

$$\delta = \sqrt{\frac{\Delta H_v - RT}{V_m}} \quad (5.3)$$

where ΔH_v is the enthalpy of vaporisation (50300 J mol⁻¹ for benzaldehyde), R is the gas constant (8.31 J K⁻¹ mol⁻¹), and V_m is the molar volume (m³ mol⁻¹). The partial molar volumes of solutes measured in supercritical solvents depend on the system conditions and the structure of the solute [Eckert *et al.*, 1986], and are in general negative. The molar volume of benzaldehyde in dense CO₂ has been evaluated at 41.8 °C and pressures up to 150 bar [Foster *et al.*, 1989], and was found to range over the values -2.5×10^{-4} m³ mol⁻¹ and -25×10^{-4} m³ mol⁻¹. Insertion of the values into Eq. 5.3 and the molar volume of pure benzaldehyde (1.02×10^{-4} m³ mol⁻¹ at 20 °C/1 bar), yields $\delta = 21.6$ MPa^{0.5}.

The cohesive energy theory may offer an explanation regarding the solute solubility trends in compressed CO₂ discussed in Section 5.2. As the temperature is increased, the cohesive forces holding the liquid or solid solute together become weaker, allowing single molecules to exist within a solvation shell. Further increases in pressure and density then decrease the intermolecular distances between solute and solvent, increasing the attractive forces between like-like molecules. It is well established that the electron-deficient carbon atom in CO₂ can participate in interactions with electron-donating groups [Raveendran *et al.*, 2005]. For example, the specific interaction of CO₂ with polymers containing electron-donating carbonyl groups has been demonstrated by Fourier Transform IR spectroscopy [Kazarian *et al.*, 1996]. Raman spectroscopic studies using acetaldehyde have further demonstrated the existence of co-operative hydrogen bonds between the oxygen in CO₂

and the electron-deficient hydrogen atom on the carbonyl carbon or the α -carbon atoms [Blatchford *et al.*, 2002].

However, the Hildebrand model is only valid for solutions of weakly interacting components, and therefore other models have been developed. One of these, the Hansen solubility model, takes into account the effects of nonpolar (dispersive, δ_d), polar (dipole-dipole, δ_p), and hydrogen bonding (δ_h) interactions [Williams *et al.*, 2004], according to:

$$\delta^2 = \delta_d^2 + \delta_p^2 + \delta_h^2 \quad (5.4)$$

Table 5–3 presents some of the parameters for benzaldehyde, water, CO₂, and cyclohexane (for comparative purposes) used for the correlation of solute solubility.

Parameter	Benzaldehyde	Water	CO ₂	Cyclohexane
Permanent dipole, μ_D (D)	2.37–3.0 ^(d)	1.87	0.0	0.0
Kamlet-Taft parameters ^(e)				
α (acidity)	0.0	1.17–1.23	0.0	0.0
β (basicity)	0.39	0.14–0.49	0.01	0.0
π (polarisability)	1.0	1.09–1.14	–0.109 ^(f)	0.1
Hansen solubility parameter (MPa ^{0.5}) ^(g)				
δ_d	19.4	15.6	13.6 ^(h)	16.8
δ_p	7.4	16	4.5 ^(h)	0.0
δ_h	5.3	42.3	5.2 ^(h)	0.2

Table 5–3 Solubility Parameters for Various Substances

^(d)[Gore *et al.*, 1971; Desyatnyk *et al.*, 2005].

^(e)[Jessop *et al.*, 2012].

^(f) $\pi^* = 0.173(\rho_c/\rho_c^{cr}) - 0.37$, ρ_c^{cr} = critical density of CO₂, 0.467 g cm^{–3} [Smith *et al.*, 1987].

^(g)25 °C [Hansen, 2007].

^(h)Estimated at 30 °C/80 bar from [Williams *et al.*, 2004].

The α and β parameters relate to the hydrogen bonding acidity and basicity of the solute respectively, whereas π^* is a measure of the dipolar solute interaction with the solvent. Although the dipole moment provides guidance for the separation of charge in a molecule, it offers no information regarding the interactions with a solvent. Benzaldehyde has a dipole moment greater than water, but displays low solubility in water. Equally, the Hansen dispersive parameter would seem to have a limited effect on the solubility of benzaldehyde, as δ_d is similar across the range of molecules presented.

The parameter δ_h on the other hand, may have a strong effect on the solubility of compounds. For example, the partition coefficient of a wide range of compounds has been shown to be primarily related to their H-bonding character [Timko *et al.*, 2004]. Caffeine (6 H-bond acceptor sites), 2,4 dichlorophenoxyacetic acid (3 H-bond acceptor sites and 1 H-bond donor site), and benzoic acid (2 H-bond acceptor sites and 1 H-bond donor site) were found to have low K_{CW} values ($K_{\text{CW}} = 0.04, 0.03$, and 0.37 , respectively) due to their strong interactions with water, and preferential partitioning in the water phase. Benzaldehyde, on the other hand, only possesses one H-bond acceptor site, and the low acidity of the carbonyl hydrogen in water ($\text{p}K_{\text{a}} = 14.9$) would be a major contributor to its poor interaction with water. The H-bond parameter, δ_h , shows the greatest variability, with water displaying exceptionally high H-bonding capacity. In this respect, the H-bonding character of benzaldehyde is much more similar to that of CO_2 than it is for water. Therefore, it is expected that the difference in the H-bonding character between benzaldehyde and water would result in benzaldehyde partitioning preferentially in the CO_2 phase.

However, the H-bonding character of solutes is not the only property affecting their solubility in water-saturated CO_2 . In the study by Macnaughton and Foster [1994], 2,4

dichlorophenoxyacetic acid ($\delta_p=8.6$, $\delta_h=10.7^{(i)}$), experienced a 90% solubility enhancement in water-saturated CO₂, while Leeke [2000] observed a decrease in the solubility of carvacrol ($\delta_p=1.741$, $\delta_h=11.25$) and limonene ($\delta_p=0.6$, $\delta_h=0.0$) of up to 55% and 85%, respectively, in water-saturated CO₂ compared to water-free CO₂ [Leeke, 2000]. Since carvacrol and 2,4 dichlorophenoxyacetic acid have similar δ_h values but differ greatly in their solubilities in water-saturated CO₂, dipolarity, δ_p , is also likely to play a strong influence on the interactions of these compounds with water. This suggests that although benzaldehyde does not participate in strong H-bond interactions with water, its moderately high dipole-dipole character could allow for some interaction with water. Although the solubility of benzaldehyde is not expected to decrease in water-saturated CO₂ relative to water-free CO₂ due to the compensatory effects imparted by δ_p , solubility tests should be carried out in the future to assess the validity of this hypothesis.

5.3.2 Benzaldehyde Partition Coefficient in CO₂/H₂O

The partition coefficient in biphasic mixtures is an important parameter that may be relevant to the reaction, separation and release of organic compounds often encountered in chemistry, food, agricultural and pharmaceutical applications. The partition coefficient of solutes in CO₂/H₂O mixtures, K_{CW} , will be briefly addressed, and compared to the corresponding partition coefficient in octanol/water, K_{OW} , for selected compounds. The partition coefficient was quantified according to the experimental procedure described in Section 3.3.2, and calculated by:

$$K_{CW} = \frac{C_c}{C_w} \quad (5.5)$$

⁽ⁱ⁾From Yamamoto [2013].

where C_c and C_w are the respective concentrations in carbon dioxide and water. The mole fraction partition coefficient, K_{CW}^X , may be obtained from K_{CW} by:

$$K_{CW}^X = K_{CW} \frac{\rho_w}{\rho_c} \frac{MW_c}{MW_w} \quad (5.6)$$

where ρ_w , ρ_c , MW_w and MW_c , are the densities and molecular weights of water and CO₂, respectively. For the majority of the studies presented in this thesis, ρ_c was 0.7 g cm⁻³. After 5 hours of circulation, K_{CW}^X was measured as 41.8 ± 3.2 at 30 °C/80 bar (with CO₂/H₂O 35% v/v), which was very similar to that reported in the literature ($K_{CW}^x = 39.1 \pm 3.7$ [Timko *et al.*, 2004], and $K_{CW}^X = 39$ [Wagner *et al.*, 1999]), indicating that partitioning was approximately complete during this time. The value for the partition coefficient based on molar concentrations, $K_{CW} = 12$, will be used for benzaldehyde throughout the remainder of this thesis.

Various groups have undertaken studies for the assessment and prediction of the partition of a wide range of compounds in CO₂/H₂O mixtures. In the studies by Abraham *et al.* [1994] and Lagalante and Bruno [1998], the linear solvation energy relationship (LSER) was used for the prediction of the mole fraction partition coefficient, K_{CW}^X for several compounds. Using a seven-parameter relationship, the LSER was:

$$\log K_{CW}^X = 2.175 - 1.578R_2 + 0.6323\pi_2^H - 2.254\alpha_2^H - 1.986\beta_2^H + 0.9221V_2 + 2.343\pi_1 \quad (5.7)$$

where R_2 is the excess index of refraction, π_2^H is the dipolarity/polarisability, α_2^H is the effective hydrogen bond acidity, β_2^H is the effective hydrogen bond basicity, V_2 is a measure of the molar volume [Abraham and McGowan, 1987], and π_1 is the solvent dipolarity/polarisability of CO₂ (Table 5–3) [Smith *et al.*, 1987]. The subscripts 1 and 2

denote the descriptors for the solvent and solute, respectively. The partition coefficient based on molar concentration, K_{CW} , may then be obtained using Eq. 5.6. The LSER relationship may be used to fit the experimental K_{CW} of a wide number and range of compounds with good agreement [Timko *et al.*, 2004]. On the other hand, a quick comparison between K_{CW} and K_{OW} revealed that for many compounds these values differed significantly (Table 5–4).

Compound	$K_{CW}^{(j)}$	$K_{OW}^{(k)}$
benzaldehyde	12	43
benzyl alcohol	0.54	12
benzoic acid	0.37	77
caffeine	0.04	0.74
2,4 dichlorophenoxyacetic acid	0.02	389
hexane	2577	8709
fluorobenzene	220	186

Table 5–4 Comparison of K_{CW} and K_{OW} for various compounds

Similarly, Karásek *et al.* [2002] also studied the partition coefficient of various substituted phenols, and found that K_{CW} was always smaller than K_{OW} . They postulated that the poor correlation between K_{CW} and K_{OW} could be attributed to the high H-bonding character of certain molecules allowing them to interact more strongly with octanol than with CO₂. This is understandable when considering the average hydrogen-bond enthalpies, which are –22 kJ mol^{–1} in 1–octanol [Palombo *et al.*, 2006], and –10.5 kJ mol^{–1} in CO₂–carbonyl interactions [Blatchford *et al.*, 2003]. Table 5–4 shows that compounds with strong hydrogen bonding capabilities (benzyl alcohol, benzoic acid and 2,4 dichlorophenoxyacetic acid) prefer octanol to CO₂, and consequently, have much higher

^(j)Obtained from [Timko *et al.*, 2004] at 30 °C/80 bar.

^(k)Obtained from <http://www.chemspider.com/> at 20 °C/1 bar.

K_{OW} (with the exception of caffeine). The trend is only reversed for fluorobenzene, due to the non-existent hydrogen bonding, but high CO_2 -philic character of fluorinated organic compounds [DeSimone *et al.*, 1992]. The unique pattern of hydrophilicity and hydrophobicity observed in $\text{CO}_2/\text{H}_2\text{O}$ systems may help in the design and fore thinking of applications that could benefit from such properties. Secondary products for example may be separated from wanted products and catalysts on the basis of structural differences.

5.4 Benzaldehyde Mass Transfer in CO₂/H₂O

Mass transfer experiments were conducted in order to assess the mass transfer coefficients using benzaldehyde as the model organic hydrophobic compound transferring from the CO₂ to the water phase. This would allow separation from kinetic effects in future studies involving mass transfer with reaction models. Under ultrasound irradiation, evaluation of the mass transfer coefficient could also shed valuable information regarding the mixing capacity of ultrasound for the vessel geometry and volume (1 dm³) used in the present study, and to compare this to other systems found in the literature. Detailed procedures relating to mass transfer experiments are provided in Section 3.3.3. In order to account for all the benzaldehyde present in the reactor and allow closure of the mass balance, the amount of benzaldehyde injected in the CO₂ phase was at least one order of magnitude below the solubility limit predicted by the Chrastil method in Section 5.2. Benzaldehyde was loaded in the vessel via the 6-port valve through a 1 mL standard loop. The concentration of benzaldehyde appearing in the water phase over time was measured by GC under either circulation or sonication at 30 °C/80 bar (Figure 5–9).

The results are of relevance as in combination with volume fraction experiments from Section 4.5, they shed some light on the effects of ultrasound. Even during sonication, two distinct environments emerged and existed simultaneously inside the vessel: the top CO₂-continuous phase and the lower water-continuous phase. The top section always remained highly enriched in benzaldehyde compared to the lower section. This trend would be extended to most organic hydrophobic compounds, which would concentrate in the low-density fluid fraction, allowing separation in real time. The equilibrium for benzaldehyde mass transport was reached in approximately 2 hours during only circulation conditions, whereas it was reached in under 1 minute following the start of sonication. This is

understandable considering the lack of mixing in conditions of no sonication, which may be assumed to only involve momentum transfer from the circulation pump.

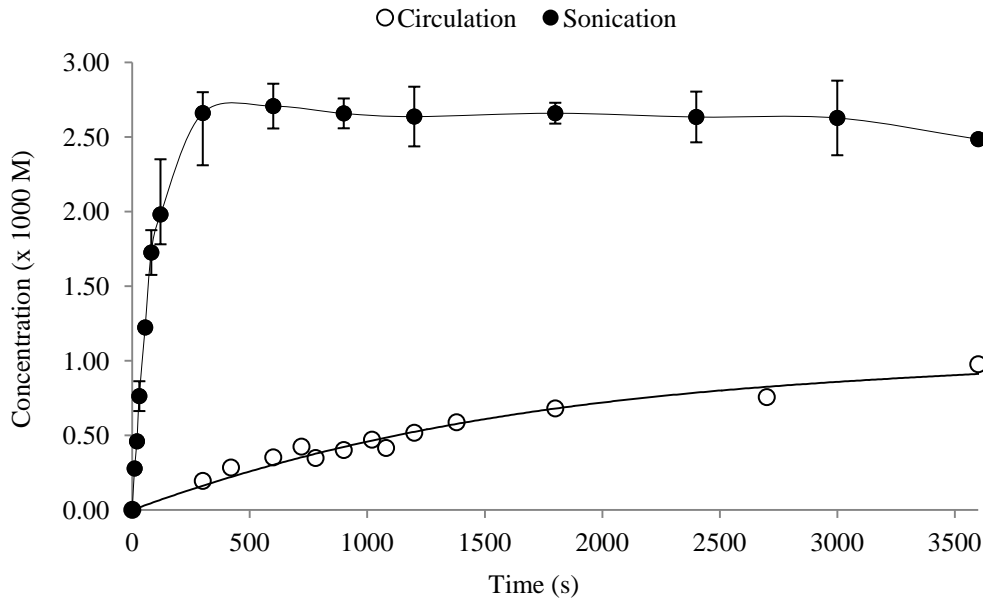


Figure 5–9 Concentration profiles for benzaldehyde appearing in the water phase following 1 mL injection into the CO₂ phase, in the presence of only circulation or under acoustic agitation. Conditions: 30 °C/80 bar, pulsed ultrasound at 70% amplitude, CO₂/H₂O (35% v/v), see Appendix A3

The concentration values for benzaldehyde mass transfer were inserted into the left-hand term (α) of Eq. 5.9, obtained from integration of Eq. 5.8 (see Appendix A3) for evaluation of the overall mass transfer coefficient on the CO₂ side, K_{mtCO_2} :

$$\frac{dC_c}{dt} = -\frac{1}{\frac{1}{k_c} + \frac{K_{CW}}{k_w}} \frac{a}{V_c} (C_c - K_{CW}C_w) \quad (5.8)$$

$$\ln \left| \frac{C_{c0} - \left(\frac{V_w}{V_c} + K_{CW} \right) C_w}{C_{c0}} \right| = -K_{mtCO_2} \frac{a}{V_c} \left(\frac{V_w}{V_c} + K_{cw} \right) t \quad (5.9)$$

The log-time plots for the mass transfer of benzaldehyde under circulation conditions (Figure 5–10) fits a straight line passing through the origin. The slope could then be utilised for evaluation of the mass transfer coefficient.

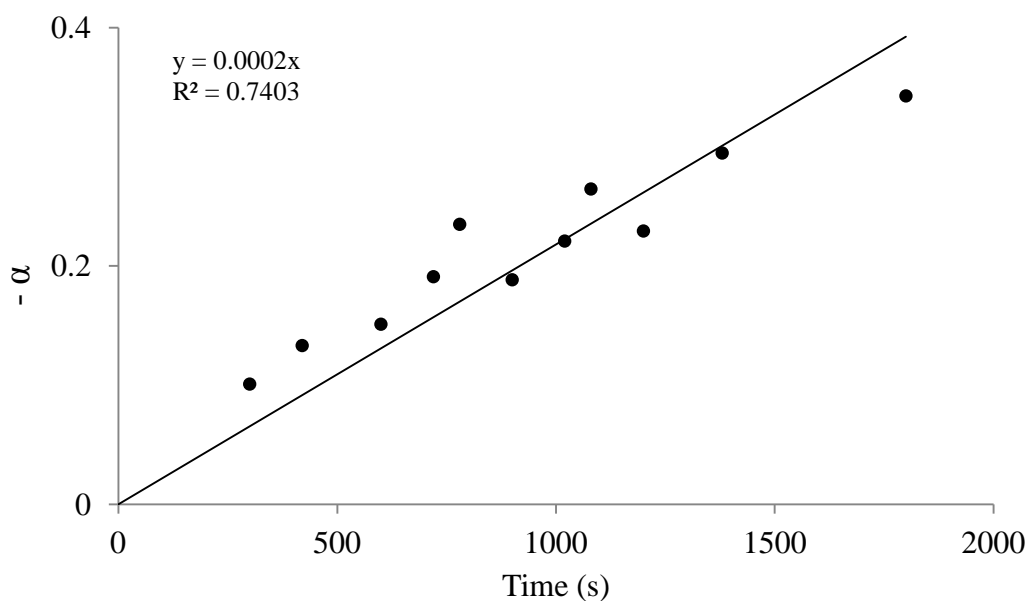


Figure 5–10 Plot of the left-hand term in Eq. 5.9, α , against time for benzaldehyde mass transfer for silent conditions (based on mean values shown in Figure 5–9)

The poor fit to the data could be due to localised thermal differences arising in the reactor in the absence of agitation and mixing, which would not be detected by a global temperature recording. This could alter momentum transfer and diffusion between experiments.

5.4.1 Mass Transfer Coefficients for the Silent Case

The logarithmic relationship for the mass transfer of benzaldehyde yielded a slope of $2.28 \times 10^{-4} \text{ s}^{-1}$ for the silent case, which was inserted with the other known parameters for extraction of the mass transfer coefficient, from Eq. 5.10:

$$\text{slope} = -K_{\text{mtCO}_2} \frac{a}{V_c} \left(\frac{V_w}{V_c} + K_{\text{CW}} \right) \quad (5.10)$$

For the silent case, insertion of known parameters ($a = 71 \text{ cm}^2$, $V_w = 650 \text{ cm}^3$, $V_c = 350 \text{ cm}^3$ and $K_{\text{CW}} = 12$) yielded an overall mass transfer coefficient K_{mtCO_2} of $\sim 8.1 \times 10^{-5} \text{ cm s}^{-1}$. Due to the impossibility of knowing a (in the case of ultrasound), it is often customary to express the mass transfer coefficient as an effective mass transfer coefficient:

$$K_{\text{mtCO}_2} \underline{a} = K_{\text{mtCO}_2} \frac{a}{V_c} \quad (5.11)$$

Calculation therefore yielded $K_{\text{mtCO}_2} \underline{a} = 0.0164 \times 10^{-3} \text{ s}^{-1}$ for the silent case. Separation of K_{mtCO_2} into its water and CO₂ components (k_w and k_c respectively) for the silent case requires hydrodynamic analysis of each phase via the Frossling correlation, according to Eq. 5.12:

$$Sh = \frac{kL}{D_A} = \text{constant}(Re)^{1/2}(Sc)^{1/3} \quad (5.12)$$

with the Reynolds number (Re) being:

$$Re = \frac{\rho LU}{\mu} \quad (5.13)$$

and the Schmidt number (Sc) being:

$$Sc = \frac{\mu}{\rho D_A} \quad (5.14)$$

where k is the mass transfer coefficient to be evaluated (cm s⁻¹), L is a characteristic length (here the length of the CO₂ phase through which the solute is assumed to travel, from the inlet point to the biphasic line, ≈ 8 cm), U is the linear velocity (with a circulation rate of 20 cm³ min⁻¹ and a cross section of 71 cm² based on the vessel diameter, U was 4.6×10^{-3} cm s⁻¹), D_A is the diffusivity ($D_{AW} = 1 \times 10^{-5}$ [Delgado, 2007], and $D_{AC} = 1 \times 10^{-4}$ [Fu *et al.*, 2000] cm² s⁻¹ for most organic compounds in water and dense CO₂, respectively), ρ is the fluid density (0.999 and 0.7 g cm⁻³ for water and CO₂ respectively), and μ is the fluid viscosity (9×10^{-3} and 6×10^{-4} g cm⁻¹ s⁻¹ for water and CO₂ at 30 °C/80 bar, respectively). Insertion of the values generates $Re \approx 43$ and $Re \approx 4$ for CO₂ and water respectively.

Eq. 5.12 simplifies to Eq. 5.15:

$$k = \text{constant} \left(\frac{\rho}{\mu} \right)^{1/6} \left(\frac{U}{L} \right)^{1/2} (D_A)^{2/3} \quad (5.15)$$

Since agitation through the CO₂/H₂O interface by momentum transfer would result in both velocities being almost equal at the interface, it is also true that:

$$\frac{k_c}{k_w} = \left(\frac{\rho_c \mu_w}{\mu_c \rho_w} \right)^{1/6} \left(\frac{D_{AC}}{D_{AW}} \right)^{2/3} \quad (5.16)$$

Substitution with the characteristic values results in $k_c/k_w \approx 7$. By Eq. 5.17 the overall mass transfer coefficient is equal to:

$$K_{mtCO_2} = \frac{1}{\frac{1}{k_c} + \frac{K_{cw}}{k_w}} \quad (5.17)$$

Substituting k_w for $k_c/7$, leads to $k_c = 7 \times 10^{-3}$ cm s⁻¹ and $k_w = 9 \times 10^{-4}$ cm s⁻¹ with an error of $\pm 25\%$ (associated with the line regression value from Figure 5–10). The values of k_w and k_c provided a first indication that the majority of the mass transfer resistance for benzaldehyde occurred in the water film.

5.4.2 Mass Transfer Coefficients for the Sonication Case

Several physical [Ghaini *et al.*, 2010] and chemical [Dehkordi and Savari, 2011] techniques have been developed for evaluation of mass transfer properties in agitated biphasic systems in recent years, although depending on the reactor geometry and the type of measurement technique employed, several sources of error could arise including, for example, the response time of sensors which are used to evaluate mass transfer rates in gas-liquid systems. Physical methods in which the concentration of the solute is monitored directly represent the most reliable method for evaluating mass transfer rates.

In emulsion systems, the transfer of the solute between the droplets and the continuous phase must be assessed, as in the present case, where the concentration of benzaldehyde was measured in the water-continuous phase. However, the emulsion model is complicated by the ability of droplets to act as carriers of the solute, potentially leading to overestimation of the concentration in the continuous phase if the phases are not separated at the time of sample collection. In the present high-pressure system, there was a possibility that the rate of benzaldehyde appearance in the water-continuous phase could be overestimated due to its release from CO_2 droplets during depressurisation. The average time required for the droplets to become depleted of benzaldehyde was defined as the droplet depletion time, which will be discussed in further detail later in this Section. Therefore, the depletion time was evaluated as ~ 0.2 s, which, given the large volume of the vessel, would be a much shorter time than the expected mean residence time of droplets in the vessel prior to reaching the sampling point. The residence time of droplets was not assessed in the present study, although it should form the scope of future investigations. Nonetheless, it would be reasonably safe to assume that the measured concentrations of benzaldehyde were directly related to its transport across the $\text{CO}_2/\text{H}_2\text{O}$ interface, and not to

benzaldehyde being released into the continuous phase following CO₂ droplet breakdown during depressurisation.

In biphasic systems, it is common practice to describe mass transfer effects in terms of the effective mass transfer coefficient on the liquid side (usually water). The overall mass transfer coefficient on the water and CO₂ side are interrelated through Eq. 5.17 and 5.18:

$$K_{mtCO_2} = \frac{K_{mtH_2O}}{K_{CW}} \quad (5.18)$$

If the overall mass transfer coefficient is taken on the water side, the mass balance may be written as:

$$\frac{dC_c}{dt} = -K_{mtH_2O}a \left(\frac{C_c}{K_{CW}} - C_w \right) \quad (5.19)$$

which in integrated form becomes:

$$\ln \left| \frac{C_{c0} - (K_{CW} + \frac{V_w}{V_c})C_w}{C_{c0}} \right| = -K_{mtH_2O}a \left(1 + \frac{V_w}{K_{CW}V_c} \right) t \quad (5.20)$$

It is also common practice to solve the mass balance by the Laplace transform technique, with the mass balance:

$$V_c \frac{dC_c}{dt} = -V_w K_{mtH_2O}a (C_c - C_w) \quad (5.21)$$

Integration yields:

$$\ln\left(\frac{C_c - C_{c\infty}}{C_{c0} - C_{c\infty}}\right) = -K_{mtH_2O} \underline{a} \frac{V_w}{V_c} * t \quad (5.22)$$

where $C_{c\infty}$ is the concentration of benzaldehyde at $t = \infty$. In order to obtain $K_{mtCO_2} \underline{a}$ and $K_{mtH_2O} \underline{a}$, the mean benzaldehyde concentration values determined during sonication (Figure 5–9) were inserted into Eq. 5.9, Eq. 5.20 and Eq. 5.22, generating slopes of $3.24 \times 10^{-2} \text{ s}^{-1}$, $3.29 \times 10^{-2} \text{ s}^{-1}$ and $2.25 \times 10^{-2} \text{ s}^{-1}$, respectively (Figure 5–11).

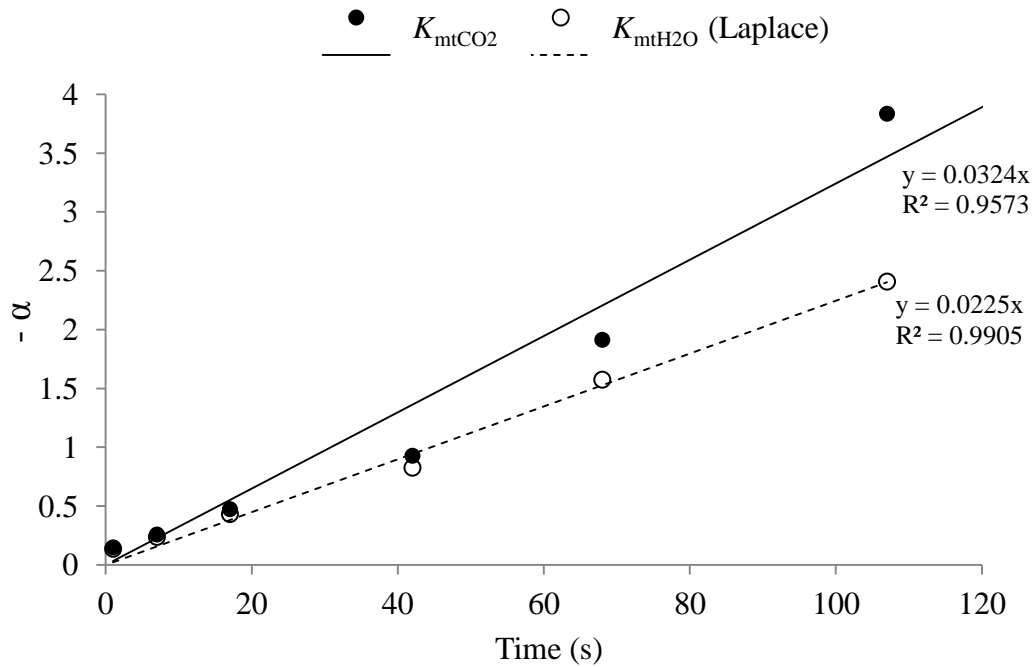


Figure 5–11 Plot of the logarithmic mass transfer term 'α' from Eq. 5.9 (K_{mtCO_2}) and Eq. 5.22 (K_{mtH_2O}) against time for benzaldehyde in the presence of ultrasound; concentrations and conditions were based on those presented in Figure 5–10; lines are best-fit to the data points. See Appendix A3

In theory, both sets of data from Figure 5–11 should fit straight lines passing through the origin, since it is expected that at $t = 0$, mass transfer should be zero. Therefore, the error associated with the line for obtaining K_{mtCO_2} is most probably associated with the type of analysis performed, as both sets represent the concentration values from Figure 5–9, excluding the presence of an induction period. The effective mass transfer coefficient thus

obtained on the CO₂ side was $2.3 \times 10^{-3} \text{ s}^{-1}$, over two orders of magnitude higher than in the silent case observed in Section 5.4.1. The effective mass transfer coefficient on the water side was 0.028 s^{-1} for the method from Eq.5.20 and 0.012 s^{-1} using the Laplace transform technique from Eq. 5.22. Taking the mean value generated $0.02 \pm 0.008 \text{ s}^{-1}$.

For the sonication case, the effective mass transfer coefficient, $K_{\text{mtCO}_2 a} (\text{s}^{-1})$, is defined by the overall mass transfer coefficient, $K_{\text{mtCO}_2} (\text{cm s}^{-1})$, and the specific interfacial area, $a (\text{cm}^{-1})$, which are both dependent on the emulsion droplet diameter. In addition, K_{mtCO_2} also depends on the dynamic nature of the emulsion, which must be taken into consideration. Although during continuous ultrasound operation, convective forces are expected to be significant due to the turbulent flow arising as a consequence of acoustic streaming [Kumar *et al.*, 2006], during pulsed ultrasound the majority of the kinetic energy is dissipated during the *off* stage of the cycle, and is insignificant during pulsed intervals of one every four seconds, as in the present study. Therefore, the most important convective forces may be assumed to originate as a consequence of droplets rising in the vessel (valid for CO₂ droplets) or settling (valid for water droplets) in the vessel, and the terminal velocity U_t for dilute emulsion systems with low droplet Re , may be determined by Eq.

5.23:

$$U_t = \frac{2gr^2(\rho_d - \rho)}{9\mu} \quad (5.23)$$

where g is the gravitational acceleration, r is the droplet radius, ρ_d and ρ are the densities of CO₂ and water, respectively, and μ is the viscosity of the continuous phase. Although droplets were visualised following sonication of the CO₂/H₂O mixture, and more specifically these appeared to be of diameter $\sim 10 \mu\text{m}$, an in-depth characterisation was not possible due to the lack of suitable equipment. Therefore, for the purpose of modelling the mass transfer and hydrodynamic properties of CO₂/H₂O emulsions, a Sauter mean diameter

for CO₂ droplets, d_{32} , of 15 μm will be used throughout the rest of this study, based on the values reported by Timko *et al.* [2006b]. Insertion of the parameters for a droplet of $r = 7.5$ μm yields $U_t = 4 \times 10^{-3} \text{ cm s}^{-1}$. Table 55 presents a summary of the physical properties used for evaluation of the hydrodynamic factors in CO₂ and water.

Property	CO ₂	H ₂ O
$D_A (\text{cm}^2 \text{ s}^{-1})$	1×10^{-4}	1×10^{-5}
$\mu (\text{g cm}^{-1} \text{ s}^{-1})$	6×10^{-4}	9×10^{-3}
$\rho (\text{g cm}^{-3})$	0.7	0.999
$U_t (\text{cm s}^{-1})$	0.061	0.004

Table 5–5 Main physical properties of CO₂ and water at 30 °C/80 bar

The Reynolds number is much lower than unity ($Re = 2\rho_d r U_t / \mu$) for a CO₂ droplet rising, allowing calculation of k_w and k_c for sonication conditions using an appropriate expression to take into account convective transfer. The numerical solution for the mass transfer from a liquid drop into the water-continuous phase in Stokes-type flow was found by Kumar and Hartland [1999] to be approximated by:

$$k_w = \frac{2D_{AW}}{d_{32}} 0.991 \left(\frac{U_t d_{32}}{D_{AW}} \right)^{1/3} \quad (5.24)$$

where $U_t d_{32} / D_{AW}$ is also referred to as the Peclet number, and d_{32} is the droplet Sauter mean diameter. The corresponding expression for obtaining k_c using characteristic values for CO₂ from Table 5–5 is:

$$k_c = \frac{2D_{AC}}{d_{32}} 0.991 \left(\frac{U_t d_{32}}{D_{AC}} \right)^{1/3} \quad (5.25)$$

The resulting values for k_w and k_c were evaluated as 0.011 cm s^{-1} and 0.13 cm s^{-1} , an order of magnitude higher than their respective values under silent conditions. Calculation of K_{mtCO_2} based on the local mass transfer coefficients and Eq. 5.17 led to a value of $9.1 \times 10^{-4} \text{ cm s}^{-1}$. The specific interfacial area arising from dispersions may be calculated from knowledge of the droplet diameter and volume fraction of the dispersed phase (ϕ), according to Eq. 5.26:

$$\underline{a} = \frac{6\phi}{d_{32}} \quad (5.26)$$

Defining K_{mtCO_2} and $K_{\text{mtCO}_2}\underline{a}$ for agitated multiphase systems is complicated by the dynamic nature of the dispersion [Clarke and Correia, 2008], and may significantly differ from the theoretical values predicted by Eqs. 5.17, 5.24 and 5.25. In their study, Timko *et al.* [2006b] calculated a total specific interfacial area of approximately 860 cm^{-1} for ultrasound-induced CO₂/H₂O emulsions. However, a specific interfacial area of this magnitude would result in a $K_{\text{mtCO}_2}\underline{a}$ in the order of 1 s^{-1} , or a water side coefficient $> 10 \text{ s}^{-1}$, which would be unexpectedly high considering that most contactors operate in the range of 10^{-2} s^{-1} [Ghaini *et al.*, 2010]. Similarly, in the study by Jasinska *et al.* [2013], the effective mass transfer coefficient determined by droplet size measurements and hydrodynamic parameters correlations was overestimated with respect to that observed experimentally using a rotor-stator mixer for emulsions with $d_{32} = 5 \text{ }\mu\text{m}$.

A model for the rate of mass transfer during sonication must therefore take into account the dynamic aspects of the emulsion, which, similar to many gas-liquid mechanically-agitated systems, considers the effective mass transfer rate to be determined by factors such as the position within the reactor and the bubble coalescence rate [Chatzi *et al.*, 1989; Linek *et al.*, 1996]. Since the ability of the droplets to act as effective solute carriers will only be possible during flow in the non-coalesced state, and for a given solvent system droplet

depletion depends on the solute structure, two time constants are introduced, namely the droplet lifetime τ_{LT} , and the droplet depletion time τ_{DEP} . Studies have shown that τ_{LT} strongly depends on droplet size and for μm -sized emulsions is approximately 20 s [Ivanov *et al.*, 1999], whereas Timko *et al.* [2006b] defined τ_{DEP} as:

$$\tau_{DEP} = \frac{d_{32}^2 K_{CW}}{12 D_{AW}} \quad (5.27)$$

According to Eq. 5.27, the depletion time for benzaldehyde was 0.225 s. As defined by Timko *et al.* [2006b], if a microscopic mass balance is carried out on a single droplet, a time-averaged solution may be obtained over the interval $0 < t < \tau_{LT}$, which may then be used for approximation of the diffusion-dependent transport in the presence of the emulsion:

$$\text{Diffusive Mass Transfer } (s^{-1}) = \frac{2 D_{AW} a}{d_{32} K_{CW}} \frac{\tau_{DEP}}{\tau_{LT}} \left[1 - e^{\left(-\frac{\tau_{LT}}{\tau_{DEP}} \right)} \right] \quad (5.28)$$

Two observations may be inferred from this model. Firstly, the exponential term normalises the mass transfer coefficient and interfacial area terms as τ_{LT} becomes greater than τ_{DEP} , signifying conditions in which mass transfer reaches a limit due to the inability by existing droplets to return to their respective phases to act as carriers, and instead acting as empty barriers to mass transfer. Conversely, shorter droplet life-times signify conditions in which the droplets can flux back and forth to their respective phases to become replenished of solute, and constantly maintaining a high driving force for diffusion. Short droplet life-times could also coincide with situations in which the droplet breaks before its depletion time has been reached, such as during the high acoustic pressure stage of ultrasound, or during the non-steady state phase of emulsion formation, when droplets carrying solute break and release their contents into the surrounding continuous phase, thus

constituting a form of convective transport. Additional terms should therefore be added to Eq. 5.28 to account for this form of convective transport.

Secondly, Eq. 5.28 highlights a marginal dependence of the effective mass transfer coefficient on K_{CW} , as K_{mtCO_2a} decreases by only 10% when K_{CW} increases from 12 (for benzaldehyde) to ~ 500 (*i.e.* for highly hydrophobic compounds such as chlorobenzene and toluene). Support of the possible small effect of K_{CW} is offered by Dumont *et al.* [2013], who observed only a two-fold increase in the effective mass transfer rate when the toluene partition coefficient was increased by two orders of magnitude by changing the oil fraction in water/silicone oil mixtures [Dumont *et al.*, 2013]. Furthermore, in the study by Guo and Roache [2003], the overall liquid-side mass transfer coefficient of several compounds varied by only one order of magnitude when the Henry constants varied by a factor of 10^4 . Comparison of characteristic mass transfer parameters under silent and sonication conditions (Table 5–6), revealed that the sonic enhancement increased the mass transfer by at least two orders of magnitude compared to the silent case due to hydrodynamic effects and higher interfacial areas.

Mass Transfer Parameter	Silent	Sonic	Sonic Enhancement
k_w (cm s ⁻¹)	9×10^{-4}	0.011 ⁽¹⁾	12
k_c (cm s ⁻¹)	7×10^{-3}	0.13 ⁽¹⁾	19
K_{mtCO_2a} (s ⁻¹)	1.64×10^{-5}	2.3×10^{-3}	~ 140

Table 5–6 Mass transfer coefficients for benzaldehyde under silent conditions and acoustic agitation at 30 °C/80 bar

⁽¹⁾Predicted with $d_{32} = 15 \mu\text{m}$.

Since hydrophobic compounds such as benzaldehyde are always expected to transfer through CO₂ faster than through water, mass transfer is limited by the presence of the water film around the droplet. Table 5–7 presents the values for the effective mass transfer coefficient on the water side obtained for a range of two-phase reactor systems. The value of $K_{\text{mtH}_2\text{O}}\underline{a}$ allows an approximate evaluation of the system mixing time, defined as $\tau_{\text{SM}} = (K_{\text{mtH}_2\text{O}}\underline{a})^{-1}$, which is 50 s. Mixing efficiency is an important parameter for selection of the appropriate reactor design. In the study by Jasinska *et al.* [2013], six-blade paddle impeller mixing was compared to rotor-stator mixing for the mass transfer of benzoic acid in a 1 dm³ toluene/water biphasic system.

Reactor	$k_{\text{L}}\underline{a}^{(\text{m})}$ (s ⁻¹)	\underline{a} (cm ⁻¹)	Reference
Microchannel contactor	0.77–30.6	-	[Su <i>et al.</i> , 2009]
Capillary microreactor	0.90–1.67	16–32	[Ghaini <i>et al.</i> , 2010]
Two-impinging jets reactor	0.28	10–34	[Dehkordi, 2002]
Packed extraction column	0.0034–0.005	0.8–4.5	[Verma and Sharma, 1975]
Agitated contactor	0.048–0.083	0.32–3.11	[Fernandes and Sharma, 1967]
Stirred contactor	0.35–1.3	8.35–34.2	[Koetsier and Thoenes, 1973]
6-blade impeller liquid-liquid	0.01	6–12	[Jasinska <i>et al.</i> , 2013]
Rotor-stator emulsifier liquid-liquid	0.005	100	[Jasinska <i>et al.</i> , 2013]
Ultrasound gas-liquid with stirring	0.02	-	[Laugier <i>et al.</i> , 2008]
Ultrasound liquid-liquid with stirring	0.045	-	[Wilhelm <i>et al.</i> , 2010]
Pulsed ultrasound	0.02	-	<i>present work</i>

Table 5–7 Comparison of the effective mass transfer coefficient and specific interfacial area obtained with a range of contacting devices

^(m) $k_{\text{L}}\underline{a}$ denotes the effective mass transfer coefficient on the liquid side (s⁻¹), expressed in the present study as $K_{\text{mtH}_2\text{O}}\underline{a}$.

The rotor-stator mixer operated at 6000 *rpm* with a maximum power draw of 250 W, similar to the power draw for the pulsed ultrasound utilised in the present system, and is conventionally employed as an emulsifier for the generation of μm -sized droplets. However, it was found that the six-blade impeller offered faster mass transfer rates at 500 *rpm* with a power draw that was two orders of magnitude lower. In order to generate smaller droplets ($d_{32} \approx 10 \mu\text{m}$), the emulsifier focuses the dissipated energy on a small portion of the fluid, with only a limited amount of energy being directed towards bulk mixing. The six-blade impeller, on the other hand, directs a significant portion of energy towards bulk mixing albeit generating in comparison larger droplets ($d_{32} \approx 100 \mu\text{m}$). The mixing effect obtained with pulsed ultrasound may offer both types of mixing by generating small droplets and providing bulk mixing due to the effects of acoustic streaming. The effective mass transfer coefficient achieved by pulsed ultrasound was approximately four times higher than the rotor-stator mixer with a similar power draw, and two-fold higher than that obtained with the six-blade impeller, albeit with a power consumption which was approximately two orders of magnitude higher. Mechanically-agitated systems have been previously used to increase the mass transfer rates in CO₂/H₂O systems. For example, Tai *et al.* [2000] studied the impeller-induced mass transfer of zinc(II) ions in a 1.3 dm³ vessel in a dense CO₂/H₂O biphasic system, achieving K_{mtCO_2} values of $0.2\text{--}2.6 \times 10^{-3} \text{ s}^{-1}$ at impeller speeds of 7.2–17.7 s⁻¹ at 40 °C/83 bar, similar to the present system. However, mass transfer parameters should only be used as a general guide when comparing different reactor methodologies. Some enhancements may be overshadowed due to the unequal dependence on bulk phase mixing and interfacial mixing. Therefore, mixing efficiency will be explored further in the proceeding Sections, where mass transfer will be discussed in relation to reaction kinetics.

5.5 Benzoyl Chloride Hydrolysis Rates in CO₂/H₂O

Since the mass transfer properties had been evaluated for the CO₂/H₂O system in the presence of ultrasound, the hydrolysis of benzoyl chloride was used as a model fast reaction for separation of the mass transfer and kinetic effects, and identification of the beneficial effects of ultrasound for enhancing the rate of chemical reactions. Similarly to benzaldehyde, benzoyl chloride is an organic hydrophobic compound, which may be used to study the transport from the CO₂ to the water phase, where it reacts. Hydrolysis represents an important reaction and is frequently encountered in the preparation of many pharmaceutical compounds. The hydrolysis rates of benzoyl chloride were assessed in the presence of silent conditions and under the effect of acoustic agitation.

As expected, the reaction proceeded faster under sonication compared to silent conditions. Maximum yields were reached within 30 minutes at 70% amplitude, while the conversion under silent conditions was relatively much slower ($7 \times 10^{-6} \text{ s}^{-1}$), Figure 5–12.

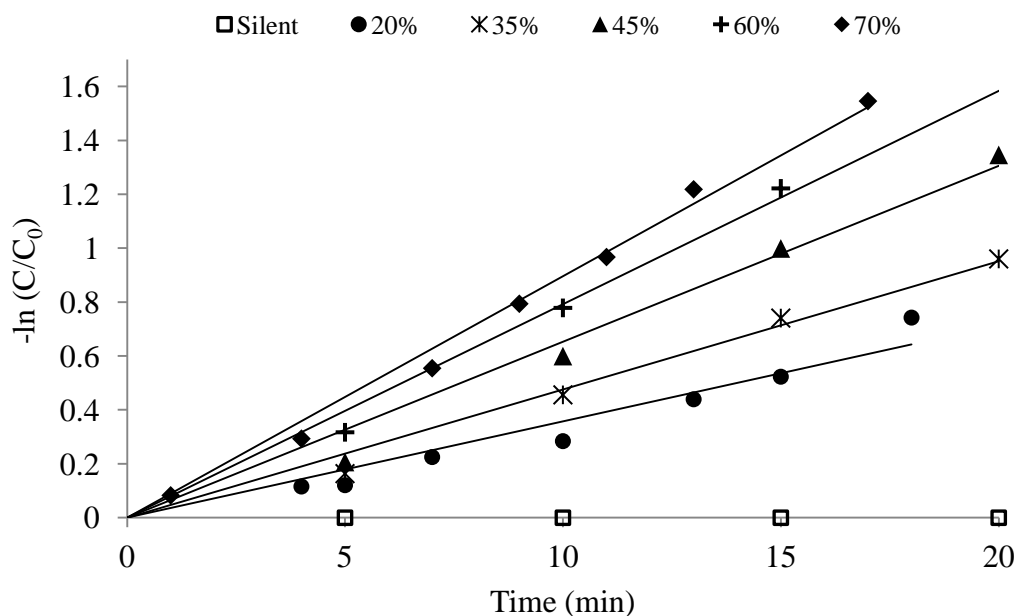


Figure 5–12 Pseudo first-order plots for the hydrolysis of benzoyl chloride in CO₂/H₂O, under silent conditions or in the presence of acoustic agitation at different amplitude settings; each value in the legend represents the amplitude setting; the lines are best-fit to the data ($r^2 \geq 0.96$) and the slopes are numerically equal to the observed reaction rate constant, k_{obs} ; see Appendix A4.1. Conditions: 30 °C/80 bar, CO₂/H₂O (35% v/v)

Comparison of the reaction rate constants for the sonicated and the silent case, revealed a sonic enhancement of approximately 180 at 70% amplitude. On the other hand, the rate increase observed between amplitude settings of 20% and 70% resulted in only a ~3-fold rate enhancement, from 0.56 to $1.6 \pm 0.2 \times 10^{-3} \text{ s}^{-1}$, Figure 5–13. The mixing effects of ultrasound may be due to large-scale mixing phenomena such as interfacial waves and acoustic streaming, and micromixing induced by emulsions. Separation of these different effects may be difficult when trying to interpret the observed mass transfer effects induced at various power amplitudes, as they may overlap. The energy required for emulsification is $< 0.1\%$ of the total input energy (the net increase in interfacial energy, in J cm^{-3} , is $\underline{a}\gamma = 6\phi\gamma/d_{32}$, where γ is the interfacial tension) [Tadros *et al.*, 2004]. Therefore, it is possible that emulsification may be achieved with reasonably high interfacial areas even at the lowest power setting specified by the ultrasound processor (here 20%), excluding the possibility that for power settings of 20%, the mass transfer enhancement relative to the silent case was controlled exclusively by large-scale mixing.

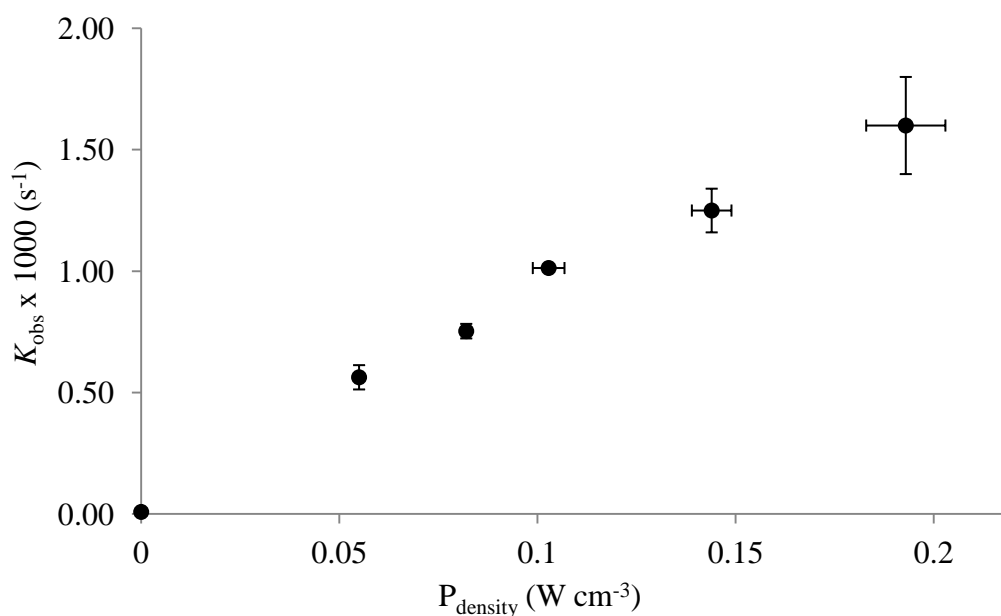


Figure 5–13 Effect of acoustic power on the apparent rate constant for the hydrolysis of benzoyl chloride, using the data and conditions from Figure 5–12

The rate constant for the hydrolysis of benzoyl chloride measured in pure water (k_{rxn}) is 1.2 s⁻¹ [Song and Jencks, 1989], which is approximately 1000-fold higher than the rate constant measured in CO₂/H₂O (k_{obs}), which was indicative of the preferential partitioning of benzoyl chloride in CO₂. The observed kinetic rate was therefore dependent on the rate of mass transfer of benzoyl chloride across the CO₂/H₂O interface. The degree of interdependence between mass transfer and kinetic effects is a function of the particular reaction being analysed. In order to understand the relationship between mass transfer effects and the reaction rate, both must be taken into account.

The physical properties of the solvent have a strong effect on the kinetics of the reaction. The dependence of the solvent on the kinetics is highlighted by examining the rate of hydrolysis of t-butyl chloride, which decreases 600-fold when the solvent is switched from pure water to a dioxane/water miscible mixture [Fainberg and Winstein, 1956]. Given its low relative permittivity, $\epsilon_r = 1\text{--}1.5$ [Beckman, 2004], dense CO₂ should also be a poor solvent for carrying out the hydrolysis of organic chlorides. The presence of water in CO₂ may contribute towards the observed hydrolysis rate, potentially leading to misinterpretation of the results for the transport-dependent reaction. The solubility of water in CO₂ at 30 °C/80 bar is $\sim 0.05 \text{ mol L}^{-1}$ [King *et al.*, 1992], approximately two-fold higher than the initial benzoyl chloride concentration in the CO₂ phase, so that the pseudo first-order rate of hydrolysis was at least 1000 times higher in the water phase (where the concentration of water is 55.55 mol L⁻¹). The pseudo first-order rate constant for benzoyl chloride hydrolysis in the CO₂ phase may then be estimated as $\sim 0.001 \text{ s}^{-1(n)}$, which is twenty times lower than the effective mass transfer rate measured in the absence of

⁽ⁿ⁾If $k_{\text{obs}} = k'[\text{W}] = 1.2 \text{ s}^{-1}$ in pure water ($[\text{W}] = 55.55 \text{ mol L}^{-1}$), k_{obs} may be calculated with the water concentration, $[\text{W}]$, present in the CO₂ phase (0.05 mol L^{-1}).

reaction under sonication determined in Section 5.4.2. Furthermore, the rate of hydrolysis occurring in the water phase leads to mass transfer rate enhancements, as described by the enhancement factor, E :

$$E = \frac{Ha}{\tanh(Ha)} \quad (5.29)$$

where Ha is commonly referred to as the Hatta number, and defined as the ratio of the maximum transfer rate due to reaction to that resulting from diffusion [Schultes, 1998]:

$$Ha = \frac{\sqrt{D_{AW} \times k_{rxn}}}{k_w} \quad (5.30)$$

For $Ha > 3$ fast kinetics dominate and the reaction is mass transfer-controlled, whereas for $Ha < 0.02$ the kinetics are slow compared to mass transfer. If E is calculated for silent conditions with $Ha = 3.8$, using $D_{AW} = 1 \times 10^{-5} \text{ cm}^2 \text{ s}^{-1}$, $k_{rxn} = 1.2 \text{ s}^{-1}$, and $k_w = 0.0009 \text{ cm s}^{-1}$ (from Section 5.4.1), then $E = 3.8$, signifying a considerable mass transfer enhancement of benzoyl chloride across the CO₂/H₂O interface due to reaction. These observations suggested that the hydrolysis in the CO₂ phase was comparably slower relative to that occurring in the water phase, and that the benzoic acid detected in the water phase was generated following benzoyl chloride transport across the CO₂/H₂O interface. Next it was important to assess whether the hydrolysis of benzoyl chloride was taking place in the interfacial region or in the bulk water phase.

For small organic compounds undergoing hydrolysis, the main determining factor for controlling the reaction rate is the flux from the interface through the water film. The reaction zone may thus be defined as a region occupied by the reacting species, with its volume depending on the species' relative rates of mass transfer and reaction (Figure 5–14).

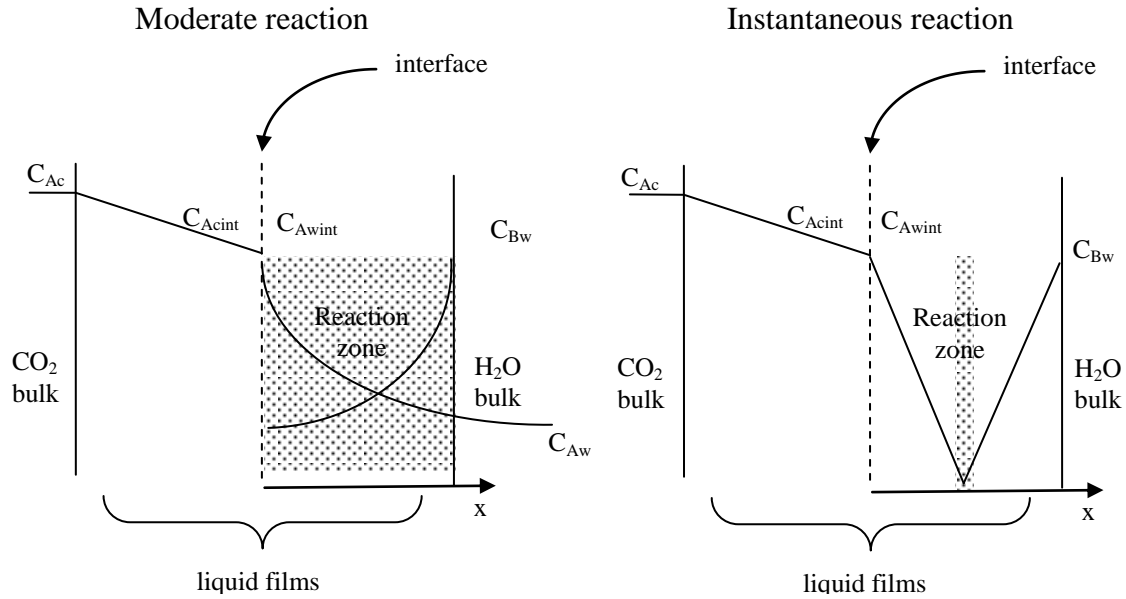


Figure 5–14 Scheme showing two hypothetical scenarios for the concentration profile of solutes travelling through two films with simultaneous mass transfer and reaction^(o). C_{Ac} = concentration of species A in the bulk CO₂ phase, C_{Acint} = concentration of species A at the interface on the CO₂ side, C_{Awint} = concentration of species A at the interface on the water side, C_{Bw} = concentration of species B in the bulk water phase, C_{Aw} = concentration of species A in the bulk water phase

In order to estimate the degree of reaction taking place in the interfacial region, the concentration profile must be determined within two boundaries. Bulk conditions require that the reaction zone is many times larger than the interfacial region.

In the absence of emulsions the rate of change of the reactant is related to the flux as follows:

$$-\frac{\partial N_{cx}}{\partial x} + r_c = \frac{\partial C_c}{\partial t} \quad (5.31)$$

where N_{cx} is the molar flux (mol m⁻² s⁻¹) of species C_c across distance x , and r_c is the first-order reaction rate of species C_c .

^(o)In the moderate reaction case, the reaction is moderately fast, and species C_B has enough time to diffuse across the water film and co-exist with species C_A which has diffused from the CO₂ film across the interface. The reaction is taking place across the water film and bulk regions. In the instantaneous reaction case, C_A is completely depleted in the water film region, and a more compressed reaction zone exists. Therefore, for instantaneous reactions, the transfer of C_A into the water film may be the rate-limiting factor (mass transfer-limited reaction).

Since Fick's First Law of Diffusion states that:

$$N_{cx} = -D_{AW} \frac{dC_c}{dx} \quad (5.32)$$

substitution of Eq. 5.32 into Eq. 5.31 leads to the PDE for C_c over an infinitesimal volume of $x + dx$:

$$-r_c = D_{AW} \frac{\partial^2 C_c}{\partial x^2} \quad (5.33)$$

Taking only one-dimensional component of x , and with the boundary conditions:

$$\text{when } x=0, C=C_{wint}$$

$$\text{when } x=x_c, C=C_w$$

the solution (see Appendix A4.1) for the concentration profile (C), becomes:

$$C = \frac{C_{wint} \sinh \left[Ha \left(1 - \frac{x}{x_c} \right) \right] + C_w \sinh Ha \frac{x}{x_c}}{\sinh Ha} \quad (5.34)$$

where x and x_c are respectively the interfacial region thickness (reported in most textbooks as being in the order of 10 nm) and the reaction zone thickness. Eq. 5.34 may be simplified by assuming that $C_w = 0$. Solving for a hypothetical value of $Ha = 100$ (*i.e.* for instantaneous reactions) and $x/x_c = 0.1$ (*i.e.* where the reaction zone is 10 times the interfacial region thickness), the concentration of reactant will still be 99.9% of that at the interface (*i.e.* virtually unchanged). Only when $x/x_c = 0.001$, the concentration will be ~10% of that at the interface. At this distance from the interface with $Ha = 3.8$ (evaluated for the silent case when $k_w = 0.0009 \text{ cm s}^{-1}$) the concentration of benzoyl chloride would be 100% of that at the interface. During sonication, $Ha \approx 0.3$ (evaluated with $k_w = 0.011 \text{ cm s}^{-1}$), and

transport is faster than reaction, indicating that benzoyl chloride may exist in the bulk water region.

These observations demonstrated that the interfacial contributions would be insignificant for benzoyl chloride hydrolysis, and that bulk water conditions would be satisfied. More specifically, k_{rxn} did not deviate from its measured value in pure water.

5.5.1 Hydrolysis in the $\text{CO}_2/\text{H}_2\text{O}$ /Tween 80 System

The presence of surfactants may either have a positive or negative effect on mass transfer, depending on the type of surfactant and system considered. Aside from diffusion-dependent effects, the mass transfer in quiescent liquid-liquid systems may be aided by Marangoni convection at the interface, a phenomenon known to occur due to interfacial tension gradients produced by the temperature differences that originate from the heats of solution. Non-ionic surfactants have been found to create a dampening of the Marangoni effect by forming a rigid interfacial film, and by creating a barrier to mass transfer of solutes across the interface [Agble and Mendes-Tatsis, 2000]. Barrier effects may be enhanced by solute-surfactant interactions, as highlighted by the work of Poteshnova and Zadymova [2006], who demonstrated that considerable partitioning of aromatic compounds occurred in the hydrophobic core of Tween 80-stabilised microemulsions and in the proximity of the outer ethylene oxide groups of the surfactant (donor-acceptor interactions with π -electrons of the aromatic ring), and by Yong Nam *et al.* [2011], who showed that the mass transfer resistance of hydrophobic solutes increased with increasing density of the surfactant head group region.

The mass transfer across Stokesian droplets may also be affected due to a reduction in the terminal velocity [Levan and Newman, 1976] and a reduction in the mass transfer

coefficient due to decreased circulation around the droplet [Raymond and Zieminski, 1971]. In the case of a bubble column reactor, gas-liquid mass transfer was lower in the presence of surfactants, as shown by a four-fold decrease in the water side mass transfer coefficient from 0.04 to 0.01 cm s⁻¹, and a decrease in the effective mass transfer coefficient from 0.0027 to 0.0015 s⁻¹ [Painmanakul *et al.*, 2005]. However, the effect of surfactant on interfacial area is expected to be minimal in gas-liquid bubble column reactors, where the interfacial area is primarily controlled by the efficiency of the sparger at the gas inlet, and by the gas flow rate. On the other hand, inclusion of a surfactant in agitated liquid-liquid systems is expected to have a significant effect on the volume of the dispersed phase. In the present study, inclusion of Tween 80 resulted in an increase of the dispersed CO₂ phase from 6.5% to 35% (see Section 4.5). Such increases in the volume fraction compensate for the small negative effects on the mass transfer coefficient usually observed in the presence of surfactants. Indeed, in their study on the mass transfer of heptanoic acid from water to limonene, Srivastava *et al.* [2000] showed that although the presence of Tween 80 led to a decrease in the liquid-side mass transfer coefficient from 0.0145 to 0.012 cm s⁻¹, the effective mass transfer coefficient increased from 0.0063 s⁻¹ to 0.07 s⁻¹ due to a 14-fold increase in the specific interfacial area compared to conditions in the absence of Tween 80. The use of surfactants has also been shown to increase reaction rates through an effect on the mass transfer for CO₂/H₂O systems. The half life for the hydrogenation of styrene to ethylbenzene in a 50% v/v CO₂/H₂O mixture was decreased by approximately one order of magnitude when anionic, cationic, or non-ionic surfactants were included [Jacobson *et al.*, 1999c]. This effect was independent of the type of emulsion formed, either C/W or W/C, which was controlled by the class of the surfactant employed.

Similarly, in the present system, the rate of benzoyl chloride hydrolysis was found to proceed with higher initial rates when 1% Tween 80 was included in the $\text{CO}_2/\text{H}_2\text{O}$ mixture (Figure 5–15, solid lines). Further confirmation of the C/W nature of the emulsion was obtained by injecting benzoyl chloride into the pre-formed emulsion, without further sonication, and analysing samples from both the upper and lower sections of the reactor. If the emulsion proved to be CO_2 -continuous (W/C), substantial dissolution of either benzoyl chloride, benzoic acid or both would have occurred. The samples, however, contained neither species implying that following injection, benzoyl chloride encountered a water-continuous phase, and due to its density (1.21 g cm^{-3}), resided at the bottom of the reactor.

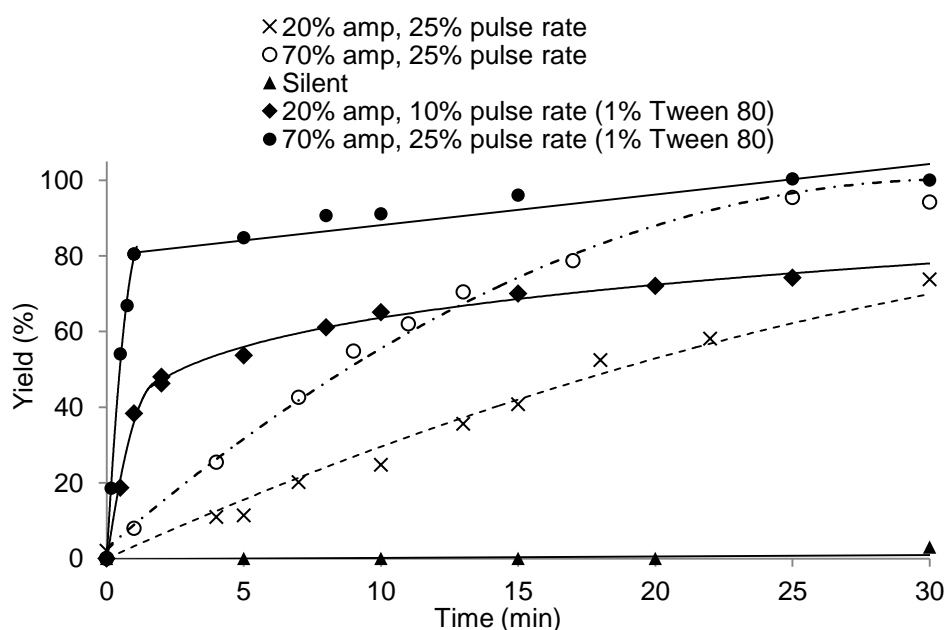


Figure 5–15 Hydrolysis rates of benzoyl chloride in $\text{CO}_2/\text{H}_2\text{O}$ at $30\text{ }^\circ\text{C}/80\text{ bar}$, in the presence and absence of Tween 80 and under various operating conditions; the lines are best-fit to the data, see Appendix A4.1 and A4.2

5.5.1.1 Effect of Pulse Rate

The rate of benzoyl chloride hydrolysis in the presence of Tween 80 could be controlled by manipulating the pulse rate, as only changing the amplitude setting had no significant effect. With 10% pulse rate and 20% amplitude, quantitative hydrolysis to benzoic acid was reached in ~120 minutes. Under these conditions, observation through the view cell revealed that upon starting sonication the emulsion initially appeared hazy, darkening the view cell progressively until reaching a maximum opacity after approximately six minutes. This maximum opacity, on the other hand, appeared almost instantly under conditions of 25% pulse rate and 70% amplitude. From Chapter 4, increased opacity through the view cell coincided with an increase in the volume fraction of the dispersed phase. The effects observed for the increase in opacity and the hydrolysis rates, implied that the lower hydrolysis rate observed with 10% pulse rate compared to 25% pulse rate was due to a decreased contact between the phases. Furthermore, Figure 5–15 also highlights that in the presence of Tween 80, some benzoyl chloride may react in the absence of an emulsion. This may be explained by the fact that prior to commencing sonication, Tween 80 is confined to the water phase in the form of micelles (see Section 3.2.3.2.1). Therefore, the micelle system could contribute to increasing the solubility of benzoyl chloride in water, and serve as an interface over which the reaction may take place. Indeed, the ability of non-ionic surfactants to increase the solubilisation of hydrophobic compounds in water due to interactions of the solute with the surfactant micelle core has been previously reported [Tehrani-Bagha and Holmberg, 2013].

At steady-state, the maximum interfacial area is achieved. Assuming a highest mean CO_2 droplet diameter of 5 μm as reported under conditions of shearing [Torino *et al.*, 2010] and a volume fraction of 0.35 (from Section 4.5), the maximum attainable specific interfacial

area in the presence of Tween 80 may be calculated using Eq. 5.26, and this would be 4200 cm⁻¹ compared to ~ 800 cm⁻¹ for ultrasound-induced emulsions obtained in the absence of Tween 80.

5.5.2 Comparison to the Literature

The hydrolysis of benzoyl chloride is a standard test for the study of reactions in biphasic systems. The rate constant obtained in the present study was similar to that reported for a smaller, 87.2 cm³ reactor (Table 5–8), with a deviation of approximately 12% under comparable electrical power intensities (107 W cm⁻² for the present system comprising the 1500 W sonifier and a probe-tip surface area of 2.8 cm², compared to the smaller vessel with a power intensity of 104 W cm⁻² from a 400 W sonifier and a probe-tip surface area of 0.5 cm²).

Emulsion System	Agitation Method	$k_{\text{obs}} (\times 10^3 \text{ s}^{-1})$	Reference
C/W and W/C	Ultrasound	1.6 ± 0.2	<i>Present work</i>
	Silent	0.007	
C/W and W/C	Ultrasound	1.8 ± 0.2	[Timko <i>et al.</i> , 2006b]
C/W/Tween 80	Ultrasound	6–16	<i>Present work</i>
W/C/PFPE ^(p)	Stirring	0.064	[Jacobson <i>et al.</i> , 1999b]
W/O/EO ^(q)	Stirring	0.25	[Campos-Rey <i>et al.</i> , 2009]
CO ₂ -expanded W/O/EO ^(r)	Stirring	0.1	[Zhang <i>et al.</i> , 2003]

Table 5–8 Benzoyl chloride hydrolysis rates in various emulsion systems

^(p) H₂O/CO₂/ PFPE (perfluoropolyether ammonium carboxylate) microemulsion, 35 °C/276 bar.

^(q) H₂O/isooctane/poly(oxyethylene) dodecyl ether microemulsion, 25 °C.

^(r) CO₂-expanded H₂O/*p*-xylene/polyethylene oxide-propylene oxide microemulsion, 40 °C/60 bar.

This close agreement highlights the possibility of scaling up processes that are dependent on the physical effects of ultrasound without compromising a specific outcome. Unlike for sonochemical applications, in which the vessel geometry is an important factor in determining the efficiency of the distribution of cavitation activity, and the effect that it produces on chemical reactions, in the present study ultrasound mediated rate enhancements through an effect on the interfacial area and mass transfer properties, which are factors that are much less dependent on the energy density distribution and therefore on the vessel volume.

Most examples present in the literature describe water in oil (W/O) or water in CO_2 (W/C) microemulsions stabilised with structurally-diverse surfactants. The water fraction in these systems is considerably small compared to the continuous hydrophobic fraction, and the water/surfactant molar ratios range from < 1 , signifying reactions occurring at the interface of micelles, to $\gg 1$, signifying conditions in which reactions take place in the bulk phase of water droplets. In the study by Zhang *et al.* [2003], k_{obs} was shown to increase by one order of magnitude when the water/surfactant molar ratio was increased from 1 to 3, indicating that although the water droplet size increased and the interfacial area decreased, the hydrolysis of benzoyl chloride was favoured as it moved to the bulk water region. This effect was attributed to an increase in the rate of the dissociative pathway of the hydrolysis reaction, which was more pronounced in the bulk water region, therefore further demonstrating that benzoyl chloride hydrolysis was occurring much faster in the bulk water region than at the interface.

5.6 Damköhler Analysis for Mass Transport with Reaction

In this Section, the model developed by Timko *et al.* [2006b] will be adopted to describe the results here obtained, and to draw important conclusions regarding the efficiency of ultrasound for removing the CO₂/H₂O interfacial resistance in chemical reactions. In order to determine the efficiency of acoustic agitation for removing the mass transfer effects in the hydrolysis reaction, the Damköhler number, Da , is introduced:

$$Da = \frac{\text{transport time}}{\text{reaction time}} \quad (5.35)$$

It follows that for $Da \gg 1$ the reaction is occurring much faster than diffusion, and the concentration of reactant in the bulk phase approximates zero. On the other hand, when $Da \ll 1$, the rate of transport of the reactant reaches equilibrium and the concentration of reactant in the water phase will be $C_w = C_o/K_{CW}$. The Damköhler number may be expressed for silent conditions as:

$$Da = \frac{k_{\text{rxn}}}{k_w \underline{a}} \quad (5.36)$$

or modified to take into account the emulsion droplet diameter and resulting interfacial area:

$$Da = \frac{k_{\text{rxn}} d_{32}}{2D_{AW} \underline{a}} \quad (5.37)$$

The Damköhler number, being a dimensionless property, only provides a general indication of the transport and kinetic processes under which a particular system may be operating. Another useful parameter which may be used for assessing the efficiency of a reactor in removing the mass transfer resistance is provided by $k_{\text{obs}}/k_{\text{rxn}}$, or the ratio of observed reaction rate to intrinsic reaction rate. Table 5–9 compiles the results obtained for the hydrolysis of various benzoyl halides reported in the literature, and those obtained for benzoyl chloride in the present study.

Benzoyl Halide	K_{CW}	k_{rxn}	k_{obs}^{sil}	k_{obs}^{us}	$k_{obs}^{us}/k_{obs}^{sil}$
Benzoyl fluoride	120	1.9×10^{-3}	1.7×10^{-6}	7.7×10^{-6}	4.6
<i>p</i> -Nitrobenzoyl chloride	130	0.055	1.7×10^{-5}	4.6×10^{-4}	30
<i>m</i> -Anisoyl chloride	220	0.6	3.3×10^{-6}	7.0×10^{-4}	210
Benzoyl chloride	140	1.3	1.1×10^{-5}	1.8×10^{-3}	160
Benzoyl chloride <i>Present work</i>	140	1.3	7×10^{-6}	1.6×10^{-3}	228
<i>p</i> -Anisoyl chloride	220	11	6.5×10^{-5}	3.6×10^{-3}	60
Benzoyl bromide	160	fast	1.7×10^{-4}	3.3×10^{-3}	20
<i>o</i> -Anisoyl chloride	220	fast	1.1×10^{-3}	0.027	30

Table 5–9 Various parameters used for the separation of kinetic and mass transfer properties for the hydrolysis of benzoyl halides in the CO₂/H₂O/ultrasound system reported by Timko *et al.* [2006b]

The data from Table 5–9 presents valuable information regarding the CO₂/H₂O/ultrasound system. Compounds with a fast intrinsic reaction rate, possessing a k_{rxn} from $\sim 1 \text{ s}^{-1}$ to $> 11 \text{ s}^{-1}$, experienced a maximum observed reaction rate in CO₂/H₂O, k_{obs} , in the order of 10^{-3} s^{-1} . The only exception was for *o*-anisoyl chloride, although the authors attributed this higher observed reaction rate to hydrolysis in the water-saturated CO₂ phase becoming more important (due to the solubility of water in CO₂), and therefore leading to pronounced transport-independent reaction and masking the true transport-dependent reaction occurring in the water phase. The value of k_{obs} obtained for the hydrolysis of benzoyl chloride in the present system closely paralleled k_{obs} for fast hydrolysis reactions in CO₂/H₂O reported by the authors for a smaller vessel. These results confirmed that irrespective of the reactor geometry (at least up to 1 dm^3 for the present system), reactions in which the organic solute must diffuse through the CO₂/H₂O interface, have a predicted observed rate constant which falls within the order of 10^{-3} s^{-1} when ultrasound is employed

as the method of agitation. This value reflected on the maximum possible rate of transfer of reagent across the CO₂/H₂O interface in the presence of ultrasonic energy.

The sonic enhancement $k_{\text{obs}}^{\text{us}}/k_{\text{obs}}^{\text{sil}}$ provides an initial indication to which reactions may benefit the most from acoustic agitation relative to silent conditions. Reactions that are intrinsically slow would not benefit from improved interfacial mixing, as they are limited by the kinetic rate. Evaluation of the idealised conditions under which ultrasound would remove all the mass transfer resistance in the hydrolysis of benzoyl chloride (the well-mixed limit) requires modification of k_{rxn} , since this value represents the reaction rate in pure water, and in order to serve as a reliable control measure it must take into account aspects such as the partition coefficient and bulk volumes of liquid being processed. In order for these conditions to be met, it must be that $k_{\text{obs}}/k_{\text{rxn}}$ approaches unity (well-mixed limit):

$$1 = \frac{k_{\text{obs}}}{k_{\text{rxn}}} \text{constant} \quad (5.38)$$

where the constant may be simply used to normalise k_{rxn} under the conditions in which k_{obs} is measured, and may be represented by $K_{\text{CW}}V_{\text{c}}/V_{\text{w}}$. The resulting well-mixed line (idealised by $k_{\text{obs}}/k_{\text{rxn}}$) for the benzoyl halides was in the order of 10^{-2} (with benzoyl chloride $K_{\text{CW}} = 140 \pm 20^{(\text{s})}$), signifying that when $k_{\text{obs}}/k_{\text{rxn}}$ was above this value, most of the mass transfer resistance would be removed (Figure 5–16). In theory, above this limit, k_{obs} may not show a further increase, as the maximum diffusive effects for the system have been reached.

^(s)From Timko *et al.* [2006b].

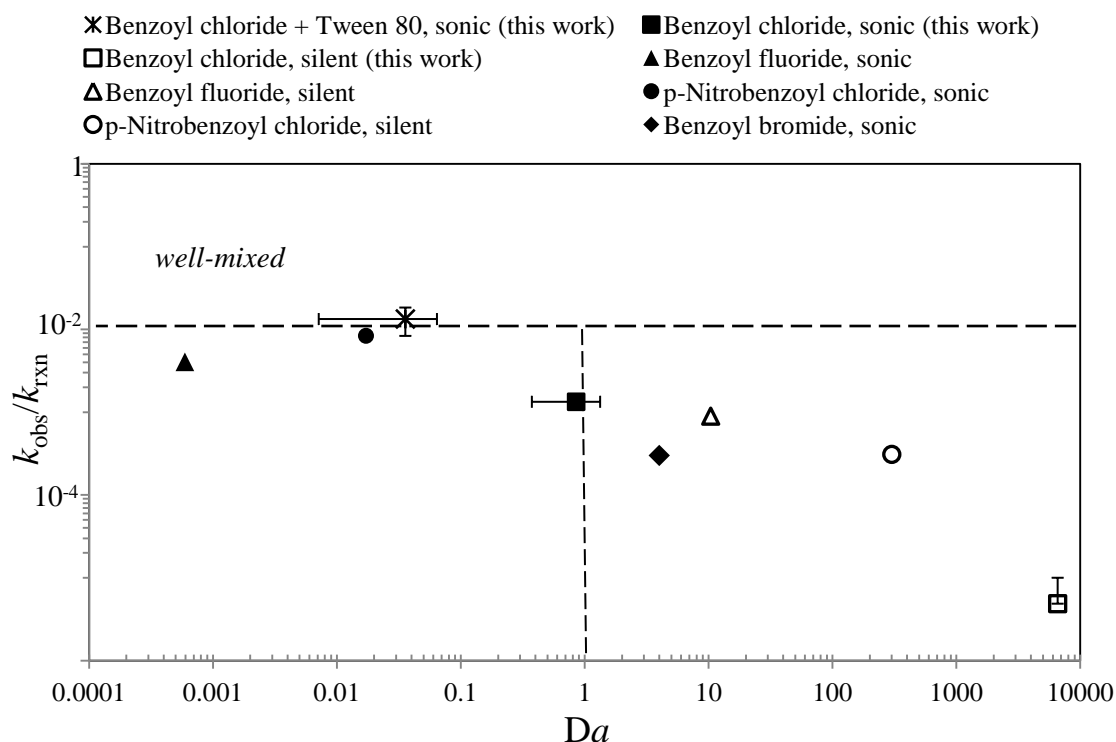


Figure 5–16 Observed rate constants (k_{obs})/intrinsic rate constants (k_{rxn}) as a function of the Damköhler number (Da) for the hydrolysis of several benzoyl halides in $\text{CO}_2/\text{H}_2\text{O}$ from the present work and from the results of Timko et al. [2006b]. For silent conditions $2D_{\text{AW}}/d_{32}$ was replaced by k_{w} . Vertical error bars are experimental uncertainties (not shown for literature data). Vertical line represents point when $Da = 1$; horizontal line represents the predicted well-mixed limit. See Appendix A5

Ultrasound moved the points upwards and to the left of the graph irrespective of the compounds tested, denoting conditions where k_{obs} tends to approach k_{rxn} and ultrasound decreased the interfacial resistances. The sonic enhancement was more pronounced for benzoyl chloride than for *p*-nitrobenzoyl chloride or benzoyl fluoride, as expected, as k_{rxn} for these latter compounds was much lower than for benzoyl chloride, and increasing the rate of mass transfer would not significantly affect the observed reaction rate. A different case was presented for the hydrolysis of benzoyl chloride in the presence of Tween 80, as Da decreased by over 10 times, signifying that much more efficient dispersion was taking place thus allowing well-mixed conditions to be reached.

5.7 Mixing Efficiency and Choice of Reactor in Biphasic Chemical Reactions

Figure 5–16 also presents two possible scenarios related to bulk water mixing. For fast reactions, the rate of reaction may be so fast compared to diffusion of reactant that the reaction occurs close to the film, and the concentration of reagent in the bulk water phase approximates zero. On the contrary, for slow reactions, the kinetic rate is slow compared to the diffusion rate, allowing the reagent to enter the bulk water phase, where significant reaction takes place and $C_w = C_c/K_{CW}$. Prediction of which reactions may benefit from the effects of ultrasound, and experience the highest sonic enhancements in order to approximate conditions of mass transfer equilibrium, requires the system mixing time, τ_{SM} , introduced in Section 5.4.2. The system mixing time identifies the time required for the bulk water phase to be completely mixed. The effective water side coefficient was 0.02 s^{-1} , resulting in a system mixing time, $\tau_{SM} = (K_{mtH_2O}a)^{-1}$ of 50 s. Therefore, in general terms, it may be said that for reactions with $k_{rxn} \ll 0.02 \text{ s}^{-1}$, the reaction is always expected to operate within the well-mixed regime. This value should however be taken as an order-of-magnitude approximation. In the study by Timko *et al.* [2006b] the well-mixed limit was extended to reactions with $k_{rxn} \approx 0.055 \text{ s}^{-1}$ (Table 5–9), almost three times the value estimated from τ_{SM} . For reactions with $0.02 \text{ s}^{-1} < k_{rxn} < 1 \text{ s}^{-1}$ the effects of ultrasound are expected to provide the highest sonic enhancement with respect to mechanical agitation, due to the positive effects of increased interfacial areas. For these reactions, the total bulk water volume is utilised. On the other hand, extremely fast reactions with $k_{rxn} \gg 1 \text{ s}^{-1}$ would leave the bulk phase unutilised, as they occur closer to the interface, and should therefore be carried out in smaller contactors that maximise interfacial mixing. For reactions with $k_{rxn} \ll 0.02 \text{ s}^{-1}$, as k_{rxn} decreases, mass transfer reaches equilibrium, although processing time and energy expenditure increase, as the reaction enters the

kinetically-controlled regime and ultrasound would not present any distinct advantages over mechanical agitation. The hydrolysis reactions were operated at a power input of 250–300 W, and if scaling-up was required this value would rise to several kW (with most of the energy being lost through heat dissipation). Therefore, large stirred tanks should constitute the primary choice of reactor for these slow reactions.

Now that the fundamental mass transfer and kinetic properties in the $\text{CO}_2/\text{H}_2\text{O}$ /ultrasound system had been identified using appropriate models, the ability of the system to mediate synthetically-useful chemical reactions and separations could next be explored.

5.8 Conclusions

The Chrastil method was a suitable model for evaluation of the solubility of benzaldehyde in dense CO_2 at 30 °C/80 bar, thus identifying the maximum quantity of benzaldehyde that would freely diffuse in the CO_2 phase following loading in the reactor under these conditions. Benzaldehyde was employed as the hydrophobic organic compound for evaluating the mass transfer properties in the $\text{CO}_2/\text{H}_2\text{O}$ system during acoustic agitation. The effective mass transfer coefficient on the water side was thus experimentally determined and evaluated as 0.02 s^{-1} , resulting in a system mixing time of 50 s. The hydrolysis of benzoyl chloride provided a model for the study of mass transfer in the presence of a fast reaction in $\text{CO}_2/\text{H}_2\text{O}$. The observed reaction rate constant in the presence of pulsed ultrasound was 750- and 75 times lower than in pure water, for the $\text{CO}_2/\text{H}_2\text{O}$ and the $\text{CO}_2/\text{H}_2\text{O}$ /Tween 80 system, respectively, highlighting both the presence of a significant barrier to mass transfer exerted by the biphasic system, and the better dispersive capacity of Tween 80 compared to ultrasound alone.

Notation

\underline{a}	Specific interfacial area	cm ⁻¹
a	Interfacial area	cm ²
C_c	Solute concentration in CO ₂	mol L ⁻¹
C_{c0}	Initial solute concentration in CO ₂	mol L ⁻¹
$C_{c\infty}$	Solute concentration in CO ₂ at time ∞	mol L ⁻¹
C_w	Solute concentration in water	mol L ⁻¹
C/W	CO ₂ in water emulsion	-
d_{32}	Sauter mean diameter of droplet	cm
Da	Damköhler number	-
D_{AC}	Diffusivity in CO ₂	cm ² s ⁻¹
D_{AW}	Diffusivity in water	cm ² s ⁻¹
E	Enhancement factor	-
g	Gravitational acceleration	cm s ⁻²
Ha	Hatta number	-
H_v	Enthalpy of vaporisation	J mol ⁻¹
K_{CW}	CO ₂ /H ₂ O partition coefficient (molar concentration)	-
K_{CW}^x	CO ₂ /H ₂ O partition coefficient (mole fraction)	-
K_{OW}	Octanol/H ₂ O partition coefficient (molar concentration)	-
K_{mtCO_2}	Overall CO ₂ -side mass transfer coefficient	cm s ⁻¹
K_{mtH_2O}	Overall water-side mass transfer coefficient	cm s ⁻¹
$K_{mtCO_2\bar{a}}$	Overall effective CO ₂ -side mass transfer coefficient	s ⁻¹
$K_{mtH_2O\bar{a}}$	Overall effective water-side mass transfer coefficient	s ⁻¹
k_c	CO ₂ film mass transfer coefficient	cm s ⁻¹
k_w	Water film mass transfer coefficient	cm s ⁻¹
k_{obs}	Observed reaction rate constant	s ⁻¹
k_{rxn}	Intrinsic reaction rate constant	s ⁻¹
MW	Molecular weight	g mol ⁻¹
N_{cx}	Molar flux of C across distance x	mol m ⁻² s ⁻¹
n_{c0}	Initial moles of solute in CO ₂	mol
n_c	Moles of solute at sampling time	mol
$P_{density}$	Power density	W cm ⁻³

R	Gas constant	$\text{J K}^{-1} \text{mol}^{-1}$
r	Droplet radius	cm
r_c	First-order reaction rate	$\text{mol L}^{-1} \text{s}^{-1}$
Re	Reynolds number	-
S	Solute solubility in CO ₂	g L^{-1}
Sc	Schmidt number	-
Sh	Sherwood number	-
Sil	Silent	-
t	Time	s
US	Ultrasound	-
U_t	Terminal velocity of droplet	cm s^{-1}
V_c	CO ₂ phase volume	cm^3
V_m	Molar volume	$\text{cm}^3 \text{mol}^{-1}$
V_w	Water phase volume	cm^3
W/C	Water in CO ₂ emulsion	-
y	Mole fraction of solute dissolved in CO ₂	-
x	Diffusive path of analyte	cm
<i>Greek letters</i>		
α	Logarithmic LHS term, Eqs. 5–9, 5–20, 5–22	-
δ_d	Dispersive Hansen solubility parameter	$\text{MPa}^{0.5}$
δ_p	Dipole-dipole Hansen solubility parameter	$\text{MPa}^{0.5}$
δ_h	H-bonding Hansen solubility parameter	$\text{MPa}^{0.5}$
ϵ_r	Relative permittivity	-
ϕ	Volume fraction of dispersed phase	-
γ	Interfacial tension	N m^{-1}
μ_c	CO ₂ viscosity	$\text{g cm}^{-1} \text{s}^{-1}$
μ_D	Permanent dipole	D
μ_w	Water viscosity	$\text{g cm}^{-1} \text{s}^{-1}$
ρ	Fluid density	g cm^{-3}
ρ_c	CO ₂ density	g cm^{-3}
ρ_w	Water density	g cm^{-3}
τ_{DEP}	Droplet depletion time	s
τ_{LT}	Droplet life time	s
τ_{SM}	System mixing time	s

Chapter 6

SYNTHETIC APPLICATIONS IN CO₂/H₂O: THE BARBIER REACTION

6.1 Introduction

The development of novel sustainable methodologies for the synthesis of organic compounds is an ongoing challenge within the chemical and pharmaceutical industry. Therefore, efforts should be directed at identifying potential new synthetic strategies that lead to facilitated reactions and separations. The findings from the previous chapters, namely that ultrasound leads to emulsification of CO₂/H₂O mixtures, and that reaction rates may be enhanced by effects on the mass transfer across the CO₂/H₂O interface, set the ground for exploration of the synthetically important Barbier reaction. The reaction progresses through interception of a metal mediator with allyl halide to form the organometallic reagent, followed by nucleophilic addition to the carbonyl compound [Dam *et al.*, 2008], Figure 6–1.

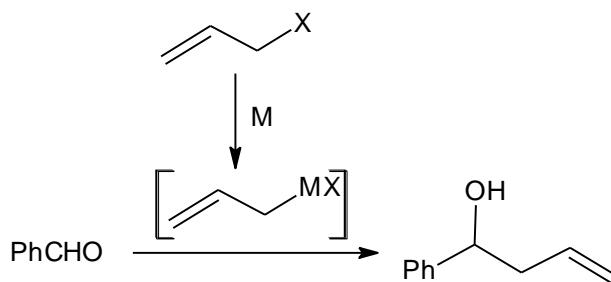


Figure 6.1 Reaction scheme for the Barbier synthesis, forming homoallylic alcohol

In the report by Guimaraes *et al.* [2007] the reaction time for the Barbier synthesis was dramatically decreased to 5 minutes in the presence of an acidic aqueous phase as the solvent. Therefore, the initial stage of the study presented in this Chapter was to evaluate the time course of the allylation reaction between benzaldehyde and allyl bromide in the CO₂/H₂O/ultrasound system and to assess any potential intrinsic catalysis mediated by

carbonic acid presence. The yield of the homoallylic alcohol product will be assessed and methods for its optimisation will be investigated. Finally, the possibility to separate the product by exploiting the CO₂/H₂O biphasic system will be studied. Details describing the experimental procedures for the Barbier synthesis are given in Section 3.6.

6.2 Zinc-Mediated Barbier Synthesis in CO₂/H₂O

Due to the reactive, cheap and non-toxic nature of zinc, preliminary investigations were carried out using this metal. Most zinc-mediated allylations use zinc in its powder-form (size not specified, but generally >100 µm), which is reported as being fairly inactive towards Barbier-type allylations in water, achieving only 20% yield in 24 hours [Zhou *et al.*, 2004]. In order to increase the efficiency of the powder, a method of prior activation is usually employed, such as the use of ultrasound [Petrier *et al.*, 1985a], inclusion of organic proton donors such as acetic acid [Oda *et al.*, 1992], the inclusion of salts (commonly NH₄Cl) [Zha *et al.*, 2003], and the use of sonoelectrochemistry techniques [Durant *et al.*, 1999]. Zinc in the form of particulates of size <10 µm (commonly also referred to as zinc dust), presents a more reactive form of the metal, typically requiring no prior activation. The dependency of zinc particle size was demonstrated in the zinc-mediated, palladium(0)-catalysed C–C coupling reaction studied by Mukhopadhyay *et al.* [2000], who found that zinc particles in the 40–60 µm range were much more active than zinc particles with diameters of 1000 µm. The use of zinc is also rapidly emerging as a mediator for transformations employed in the synthesis of a number of biologically active novel compounds [Hodgson *et al.*, 2011].

The Barbier reaction between benzaldehyde and allyl bromide in the presence of zinc dust (<10 µm) proceeded well in CO₂/H₂O under acoustic agitation, affording moderate yields of the desired homoallylic alcohol product **1** within 2 hours (Table 6–1, entry 1).

Entry	Zinc/allyl bromide/PhCHO (stoichiometry) ^(a)	Conditions	Homoallylic alcohol yield% (selectivity) ^(b)
1	2:2:1	30 °C/80 bar	67 (74)
2	2:2:1	30 °C/80 bar <i>No ultrasound</i>	traces
3	2:2:1	30 °C/80 bar <i>20% amplitude</i>	17 (60)
4	2:2:1	30 °C/80 bar <i>CO₂ only</i>	26 (100)
5	2:2:1	60 °C/120 bar	78 (87)
6	2:1.5:1	30 °C/80 bar	55 (64)
7	1.3:1.2:1	30 °C/80 bar	52 (75)
8	1:1:1	30 °C/80 bar	29 (61)

Table 6–1 Zinc-promoted allylation of benzaldehyde by allyl bromide. Conditions: 2 hours pulsed ultrasound at 80% amplitude, and CO₂/H₂O (42% v/v) unless stated otherwise

This reaction time was used as a guide for broadly categorising the initial findings. A more detailed discussion regarding the overall time-course of the Barbier synthesis will be provided later in this Section. The metal-mediated reduction of the benzaldehyde electrophile to benzyl alcohol **2** (Figure 6–2) was a significant side-reaction. A detailed mechanism of the classical Barbier reaction is not currently fully understood, although it may involve the formation of several radical species arising from single electron transfer

^(a)Typical reagent ratios: benzaldehyde (61 mmol), allyl bromide (120 mmol), zinc dust (120 mmol).

^(b)% yields determined by GC; the other major product was benzyl alcohol. See Appendix A6.1 for GC data.

pathways, which may account for the formation of the reduction product [Li and Zhang, 1998]. Indeed, the reaction of the reduced aldehyde radical anion with water could be an important pathway (Figure 6–3). Benzaldehyde reduction by zinc in scCO₂ has also been reported as a side reaction occurring in the alkylation of aldehydes with dialkylzinc following a quenching step with salt-saturated water, although no benzaldehyde reduction product was observed if the supercritical fluid was replaced with fluoroform or ethane [Jessop *et al.*, 2002]. Furthermore, the reducing capacity of zinc has been previously employed to exclusively obtain reduction products from nitroarenes in CO₂/H₂O mixtures [Liu *et al.*, 2009].

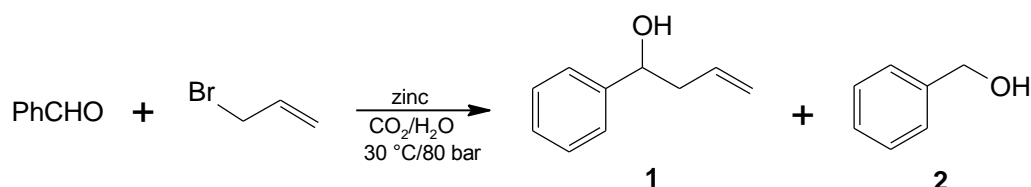


Figure 6–2 Formation of homoallylic alcohol (**1**) and benzyl alcohol (**2**)

In aqueous media, competing protodemetalation of the *in situ*-generated allyl metal species may also be an issue [Petrier and Luche, 1985]. This competing reaction presumably accounts for the observation that when the allyl bromide/zinc mixture was sonicated for 1 hour before the addition of benzaldehyde, neither the homoallylic alcohol product nor the benzaldehyde reduction product was observed, despite observing the disappearance of the allyl bromide (by GC analysis).

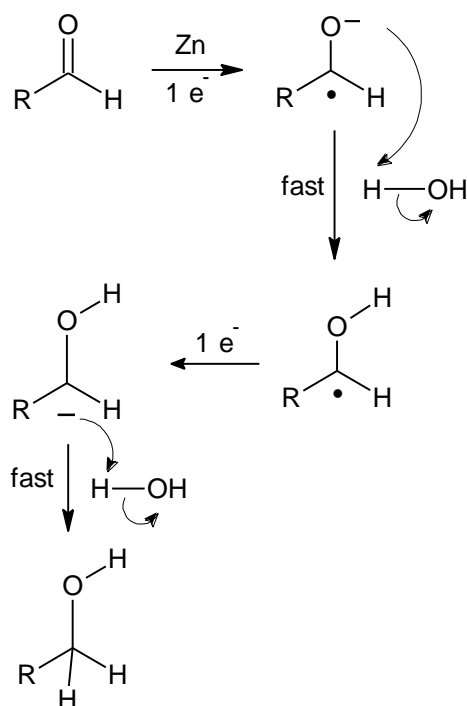


Figure 6–3 Possible electron-transfer pathway leading to the reduction of aldehyde

Fortunately, protodemetalation did not compete with the desired allylation when the reaction was performed under typical Barbier conditions (one-step addition of both reagents to the vessel containing the metal). Failure of the reaction to progress satisfactorily without ultrasound or at low amplitude setting (Table 6–1, entries 2–3) highlighted the beneficial role of acoustic agitation. The relevance of ultrasound will be discussed in more detail in later Sections, when the phase distribution of the reagents and solid mediator will be addressed in relation to mass transfer effects. The ability of the system to achieve moderate yields of the homoallylic alcohol product in relatively short times provided the incentive to investigate the reaction further.

6.2.1 Investigation of Reaction Conditions on the Barbier Synthesis

Given that the yield and selectivity had been established under a particular set of conditions (presence of the CO₂/H₂O biphasic system, 30 °C/80 bar, and 2:2:1 molar ratio of zinc and allyl bromide with respect to benzaldehyde), each condition was next assessed separately in order to evaluate its effect on the outcome of the reaction.

The effect of the presence of biphasic conditions was investigated by carrying out the reaction in only CO₂. Early reports have shown that the reaction is greatly accelerated when water is included as a counter-phase to a hydrophobic organic solvent such as diethyl ether [Nokami *et al.*, 1983]. Moreover, if only an organic phase is employed, quenching is usually carried out with water as a final step [Ranu *et al.*, 1995]. Although the exact role of water is not known, it is likely that it serves to liberate the product through the transfer of protons and hydroxyl ions. In the present case, evidence for the beneficial role of water was provided by observation of a much lower yield when only CO₂ was employed as the solvent (26% yield, Table 6–1, entry 4). On the other hand, no benzyl alcohol formation was observed in the absence of water, further implying that water was responsible for mediating the reduction pathway, as suggested in Figure 6–3.

The reaction was next assessed at the higher temperature and pressure of 60 °C/120 bar. Although pressure may have an effect on reaction rates via effects on the activation volume, the pressure change in the present case may be considered to be insufficient to influence the rate of reaction to any significant extent, and was merely employed to provide dissolution of the species in CO₂ phase. No previous in-depth quantitative studies have been undertaken on the effect of temperature on the rate of allylation, although it is generally accepted that for inactive metals such as indium, tin, and bismuth, increasing the temperature has a positive effect on the rate of allylation [Dam *et al.*, 2008]. With respect

to the original conditions, increasing the temperature and pressure had the effect of increasing the yield and selectivity of the homoallylic alcohol product from 67 to 78%, and from 74 to 87%, respectively (Table 6–1, entry 5). The reaction was also investigated in the presence of different molar ratios of zinc and allyl bromide (Table 6–1, entries 6–8). However, no improvement was observed, as lowering the quantities of zinc and/or reagent led to lower yields and selectivities.

The influence of water has been briefly addressed in relation to the zinc-mediated Barbier synthesis using CO₂ as the hydrophobic solvent. The nature of the solvent also significantly affects the course of the reaction. In the study by Gao *et al.* [2012], the zinc-mediated allylation of benzaldehyde occurred much faster (a reduction in reaction time from 12–6 hours) when THF was added as a co-solvent to water, whereas the reaction was slower when DMF was used as the co-solvent, reaching comparable yields in 15 hours [Hodgson *et al.*, 2011]. These observations may be indicative of a potential effect mediated by the physical properties of the solvent, such as for example the relative permittivity, which decreases by approximately 5 times when DMF is replaced with THF.

The time-course of the Barbier reaction may also be affected by varying the pH. Traditionally, Barbier reactions in aqueous media are slow and without activation of the metal may take up to 24 hours [Wang *et al.*, 2002; Zha *et al.*, 2003]. As reported by Guimaraes *et al.* [2007], the allylation of various substituted benzaldehydes by allyl bromide mediated by tin only required 5–15 minutes to reach quantitative yields if a hydrochloric acid solution was employed as the solvent. Although the authors did not provide an explanation for the faster rates observed, the effect of acid in these systems may be assumed to be mediated by two factors:

- Increased protonation of the aldehyde leading to a greater concentration of this more electrophilic species. Indeed, activation of the aldehyde by proton sources such as phosphoric acid has been postulated as a possible mechanism affecting zinc-mediated allylations [Fuchs *et al.*, 2013].
- The presence of acid may also activate the metal, facilitating the formation of the organozinc reagent. Most of the literature is centred on the effect of hydrochloric acid on the corrosion of aluminium. It is thought that conditions of low pH increase the rate of corrosion, due to chemisorption of chloride ions on the passive oxide film, followed by dissolution via the formation of oxide-chloride complexes [Garrigues *et al.*, 1996; Van Gheem *et al.*, 2002].

Carbonic acid originating from the reaction between CO₂ and water results in an aqueous phase pH of ~3 [Holmes *et al.*, 1999; Beckman, 2004], and therefore could constitute an intrinsic proton source for acceleration of the allylation reaction via activation of the aldehyde or of the metal. Evaluation of the time-course of the allylation reaction would be instrumental for identification of the observed rate constant and separation of the mass transfer and kinetic effects. A combination of high amplitude ultrasound and an excess of zinc and allyl bromide were key to effective formation of the homoallylic alcohol in CO₂/H₂O (Figure 6–4).

The formation of benzyl alcohol (dashed lines) followed a similar time-course of formation to the homoallylic alcohol product (solid lines), showing a gradual rise in the rate of formation over 2 hours. The zinc-mediated allylation of benzaldehyde with allyl bromide was also carried out in the ultrasound reactor under water pressurised by N₂ rather than by CO₂, and in sealed bottles at ambient conditions under magnetic stirring. These preliminary

investigations were conducted so as to potentially highlight a beneficial effect induced by the $\text{CO}_2/\text{H}_2\text{O}$ /ultrasound system.

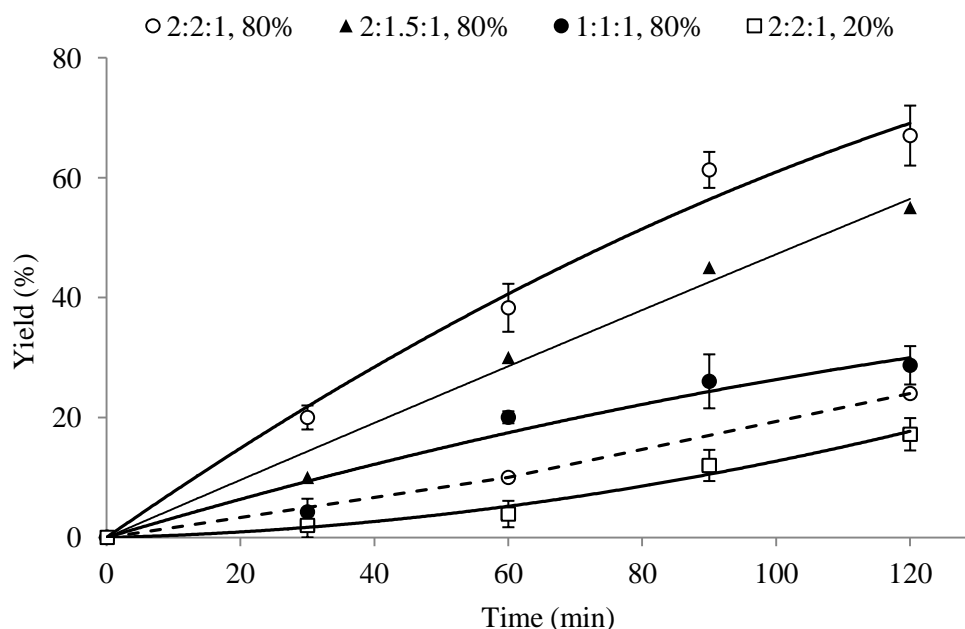


Figure 6-4 Time course of the allylation reaction in $\text{CO}_2/\text{H}_2\text{O}$. $x:y:z$ represent initial molar ratios (zinc/allyl bromide/aldehyde), while “%” values represent the ultrasound amplitude setting. (---) Benzyl alcohol product; (—) homoallylic alcohol product; lines are best-fit to the data. Conditions: $\text{CO}_2/\text{H}_2\text{O} = 42\%$ v/v, $30^\circ\text{C}/80$ bar, 25% pulse rate

The yield of the allylation product was similar whether reactions were carried out in the presence or absence of CO_2 (Table 6-2). On the other hand, benzyl alcohol formation was higher when the reaction was performed in $\text{CO}_2/\text{H}_2\text{O}$ mixtures. The higher selectivity observed in reactions where CO_2 was not present render these methodologies more attractive, as would for example a procedure involving reaction in only water as the first step, followed by subsequent pressurisation with CO_2 for separation.

Entry	Solvent system/conditions	Homoallylic alcohol	Benzyl alcohol
		(%)	(%)
1	CO ₂ /H ₂ O, 30 °C/80 bar ultrasound, 2 h	67	23
2	N ₂ /H ₂ O, 30 °C /70 bar ultrasound, 1 h	72	<5
3	H ₂ O, 30 °C /ambient stirring, 1 h [†]	68	trace

Table 6–2 Comparison of the zinc-mediated allylation in the presence of ultrasound and pressurised water (by either CO₂ or N₂), or under stirring at ambient conditions in a sealed bottle. [†]Yield/selectivity after 4 hours was unchanged

The results presented above indicated that the CO₂/H₂O biphasic system did not have the desired effect of increasing the rate of homoallylic alcohol product formation (through a possible intrinsic catalytic role of carbonic acid) with respect to ambient conditions. It was therefore anticipated that the effects mediated by the CO₂/H₂O/ultrasound system such as physical activation of the metal by ultrasound would be more subtle and required further investigation.

6.2.2 Determination of Zinc Particle Size

Both chemical and physical phenomena are expected to influence the size of zinc particles. The effects arising as a result of a decrease in the zinc particle radius due to zinc depletion by the allylation reaction will be dealt with in Section 6.8. The present Section aims at highlighting possible changes in the size of zinc particles resulting as a consequence of ultrasound treatment.

In Section 4.3.1 ultrasound was shown to induce aluminium erosion, which was proposed to be due to the presence of cavitation streams appearing in the region beneath the ultrasound probe. Ultrasound may therefore induce similar physical effects on zinc particle size through erosion, leading to preferential activation of the metal surface. Structural

changes in the form of surface roughness have been demonstrated on zinc plates following ultrasound treatment (see Section 4.3.1). Depending on the liquid/solid composition, the effects of ultrasound may vary. Doktycz and Suslick [1990] revealed that metal particles in zinc- and tin-hydrocarbon slurries increased in size, which they attributed to high-velocity-induced particle fusion, although this explanation has been refuted by Margulis [1992], who postulated that particle velocities would need to be much higher than the speed of ultrasound ($\sim 1500 \text{ m s}^{-1}$) for metal particles to fuse together.

In the present study, the zinc particle size was assessed before and after sonication in CO₂/H₂O and N₂/H₂O mixtures. A suspension of zinc dust in water was prepared by ambient stirring, and subsequently examined with the mastersizer. The particle size calculated in this manner was 13.5 μm (Figure 6–5), slightly higher than that stated by the manufacturer ($< 10 \mu\text{m}$).

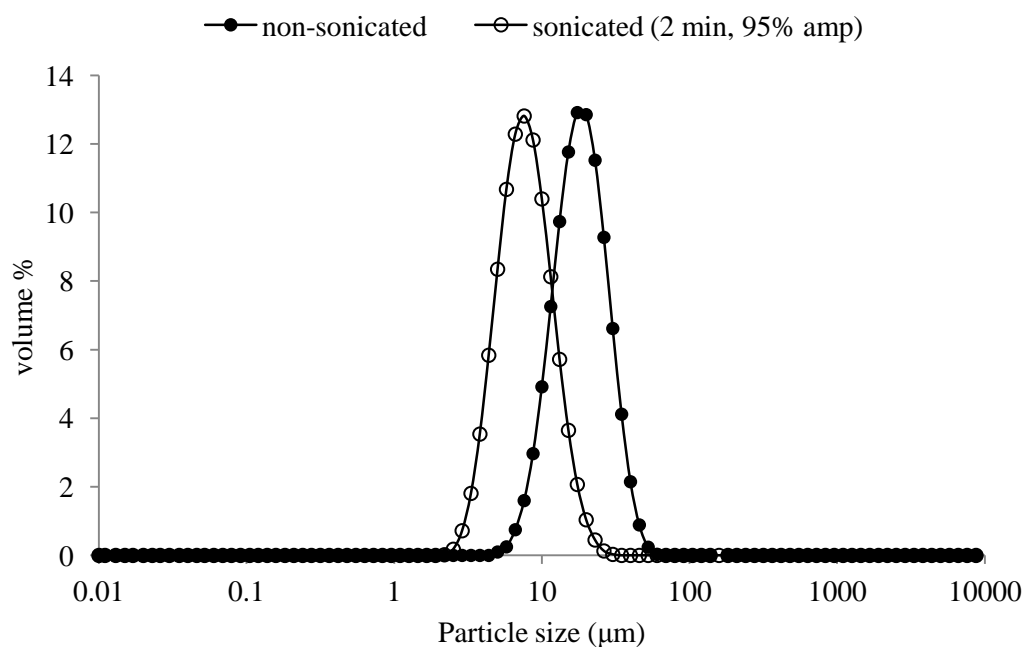


Figure 6–5 Particle size of untreated zinc, before and after ambient sonication with a 500 W sonifier at ambient conditions (described in Section 3.6.4)

This was expected, since aggregation may occur due to the presence of attractive electrostatic inter-particle forces. In colloid science operations, this aggregation is usually reverted by sonication of solid particle-containing dispersions [Mandzy *et al.*, 2005]. Indeed, treatment of the zinc suspension using the 500 W sonifier at ambient pressure generated a mean particle size of $7.5\ \mu\text{m}$, signifying that zinc dust is in the form of agglomerates which are held together by electrostatic forces, and which may be overcome by the effect of ambient ultrasound.

Sonication of a $0.2\ \text{mol L}^{-1}$ zinc/water mixture for 1 hour in the ultrasound vessel pressurised with N_2 at 70 bar produced an unexpected additional population, specifically an agglomeration of approximate mean particle size $100\ \mu\text{m}$. If samples from this suspension were further treated with ambient sonication for 2 minutes, the $100\ \mu\text{m}$ population disappeared, and only the $10\ \mu\text{m}$ population could be observed (Figure 6–6).

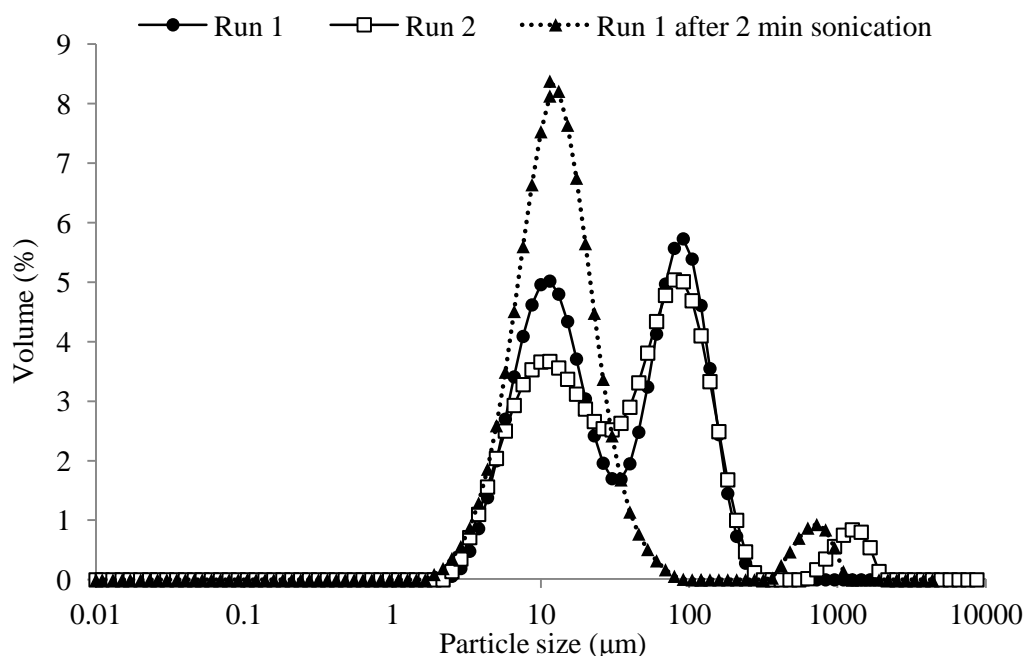


Figure 6–6 Zinc particle size following sonication of zinc ($0.2\ \text{mol L}^{-1}$) in $\text{N}_2/\text{H}_2\text{O}$ for 1 hour at $30\ ^\circ\text{C}/70$ bar. Run 1 and run 2 signify repeats of the same experiment (solid lines); samples from runs 1 and 2 after ambient sonication for 2 minutes (dashed line)

The effects of ambient sonication are expected to differ significantly from those of high-pressure sonication in that the occurrence of cavitation is less pronounced under high hydrostatic pressures due to the Blake threshold (Section 4.3.1). Sonication of zinc in $\text{CO}_2/\text{H}_2\text{O}$ for 1 hour produced an increase in the mean particle size of zinc relative to untreated zinc (45 μm for the first experiment and 90 μm for the second experiment, Figure 6–7). Ambient sonication was not carried out on samples that underwent sonication in $\text{CO}_2/\text{H}_2\text{O}$, as the visual appearance of the suspension became gel-like, showing an increasing presence of bubbles following collection. The data by the mastersizer seemed to mirror these changes as the samples from the $\text{CO}_2/\text{H}_2\text{O}$ experiments showed the least reproducibility of all the conditions used.

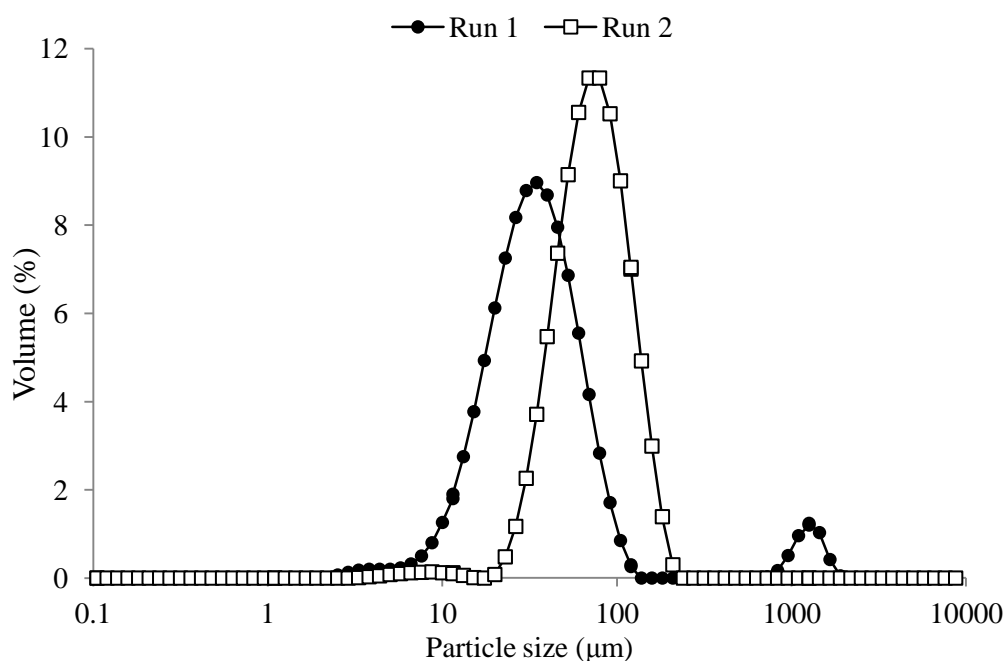


Figure 6–7 Zinc particle size following sonication in $\text{CO}_2/\text{H}_2\text{O}$ for 1 hour at 30 °C/80 bar; the two data series represent repeats of the same experiment

The presence of bubbles may be associated with the production of H_2 following the reaction of zinc with carbonic acid and formation of ZnCO_3 . In relation to the Barbier synthesis, the presence of a parallel reaction involving zinc and carbonic acid would not constitute an advantage, as it would provide a source of competition with the allylation, and a form of zinc depletion prior to its interception with allyl bromide.

The above observations may be summarised as follows:

- Prolonged exposure of a zinc/water suspension to high-pressure pulsed ultrasound has the effect of increasing the mean particle size of zinc, an effect which may be reverted by a short burst of ambient sonication, at least for samples collected following high-pressure sonication using nitrogen as the pressurising gas.
- Following exposure of zinc to high-pressure ultrasound in a $\text{CO}_2/\text{H}_2\text{O}$ environment, the visual appearance changed from a grey suspension to a gel-like fluid, in combination with significant evolution of a large number of bubbles, suggesting that zinc may be taking part in the reduction of protons.

The increase in the size of metal particles as a result of ultrasonic exposure is a well-known phenomenon and has been intensely investigated. For example, in their study, Suslick and Casadonte [1987] showed that nickel particles (original size 5 μm) increased in agglomeration following 1 hour ultrasonic irradiation under an argon atmosphere. Furthermore, the nickel exposed to ultrasound showed enhanced activity towards hydrogenation reactions due to a five-fold decrease in the passive oxide layer thickness (determined by Auger electron microscopy), an effect which was not observed under mechanical stirring. The gradual degradation of the passive oxide layer could indeed be a consequence of cavitation-induced plastic deformations which would occur in the presence of ultrasonic irradiation (excluding other phenomena such as chemical corrosion), leading

to increased inter-particle attraction. This would also provide a possible explanation for the decreased particle size observed following ambient sonication (Figure 5–4), as the presence of air would be expected to replenish the oxide film^(c) thus restoring the original particle size.

The results from the zinc particle size analysis are in agreement with the results obtained from aluminium erosion tests presented in Section 4.3.1, and further support the hypothesis that under conditions of high-pressure, pulsed ultrasound induces structural changes on soft metal surfaces. The gel-like appearance of the suspension following irradiation of zinc in CO₂/H₂O hints at the presence of amorphous structures which could be inspected by using a polarized light microscope. Efforts were next directed towards the optimisation of product partitioning and efficiency of the allylation reaction.

6.2.3 Partitioning of Reagents and Products

Knowledge regarding the partitioning of reagents and products is important firstly due to the intrinsic advantage posed by using a biphasic system for separation and recovery, and secondly for evaluating mass transfer rates in multiphase systems. Analysis of the CO₂ and aqueous fractions revealed that benzyl alcohol was present in only trace amounts in the CO₂ phase compared with the homoallylic alcohol product, which was found almost entirely in the CO₂ phase. This observation is in accordance with the reported CO₂/H₂O partition coefficient, K_{CW} , of benzyl alcohol [Timko *et al.*, 2004], which is much lower than its octanol/water equivalent ($K_{CW} = 0.5$, whereas $K_{OW} = 12.6$, based on molar concentrations). As discussed in Section 5.3.2, the partitioning in CO₂/H₂O may differ

^(c)In the experiments by Suslick and Casadonte [1987] the oxide film was completely restored following 15 minutes of air exposure.

significantly from that in octanol/water depending on the hydrogen-bonding character of the solute.

Experimental determination of the concentration of the homoallylic alcohol product in the CO₂ and aqueous fractions allowed evaluation of the *apparent* $K_{CW} = 9 \pm 0.8$. Together with its higher yield, this led to an advantageous enrichment of the desired allylation product in the CO₂ phase. Due to the high volatility of allyl bromide experimental determination of K_{CW} was impractical and this was therefore calculated using the LSER approach described in Section 5.3.2. Since Kamlet-Taft parameters were not available for allyl bromide, a search was undertaken for chemical structures with similar properties to allyl bromide. More specifically, the selection criteria were based on similarities in the octanol/water partition coefficient, K_{OW} , the molar volume and polarisability, and absence of H-bond donor/acceptor sites. The search led to trans-1,2 dichloroethene as the most suitable candidate for which Kamlet-Taft parameters were readily available. Insertion of $\alpha = 0$, $\beta = 0$, and $\pi_2 = 0.44^{(d)}$, and $V_2 = 0.635$, $R_2 = 0.416^{(e)}$ into Eq. 5.7 yielded $K_{CW} \approx 40 \pm 10$. In the study by Timko *et al.* [2004], the correlation between K_{CW} predicted by the seven-parameter LSER relationship from Eq. 5.7 was found to agree well with K_{CW} measured experimentally for halogenated compounds with no H-bond donors.

^(d)Obtained online from <http://www.stenutz.eu/chem/solv26.php>.

^(e)Obtained from Timko *et al.* [2004] based on 1,2 dichloroethane due to equal refractive index and molar volume to trans-1,2 dichloroethene.

6.2.4 Effect of Salts on the Allylation Reaction

Since salts are frequently employed in organic synthesis due to their beneficial effects on the outcome of many chemical reactions, and indeed, allylation procedures often include them as mediators [Petrier and Luche, 1985; Smith *et al.*, 2004], the effect of salts on the Barbier synthesis was investigated. In addition to their use as mediators for chemical reactions, studies of ternary systems of CO₂/H₂O/salt have attracted recent interest due to their applications in, for example, geologic sequestration of CO₂ and enhanced oil recovery of petroleum fractions from deep oil wells by CO₂ injection [Kovscek and Cakici, 2005; Springer *et al.*, 2012].

6.2.4.1 Effect on the Chemoselectivity

To date, the role of salts in the Barbier reaction remains unclear, although their use has been shown in some cases to lead to a dramatic improvement in the yield, depending on the nature of the cation or halide anion used [Sun *et al.*, 2008]. As was previously discussed in Section 6.2.1 for inorganic acids, the salt may activate the metal by interaction of the halide anion with the oxide film. The effect of salt may also be the result of a change in the solvent properties. Salt solutions show a concentration-dependent decrease in the relative permittivity (ϵ) of the aqueous phase (from $\epsilon \approx 80$ in pure water to $\epsilon \approx 40$ in saturated salt solutions) [Liszi *et al.*, 1988]. The reduction in ϵ in the presence of increasing salt concentration is related to the formation of a hydration shell around the ion, which serves to lower water's response to an external electric field [Zasetsky and Svishchev, 2001]. Salts have been employed to modify the solvent properties in reactions such as the hydrolysis of guaiacol in supercritical water [Huppert *et al.*, 1989]. The Barbier reaction does not progress well in solvents with low ϵ [Marton *et al.*, 1996; Ito *et al.*, 2000], and

CO₂ has a low ε ($\varepsilon = 1.0\text{--}1.6$), comparable with the most hydrophobic organic solvents [Beckman, 2004], which may account for the much lower rate of allylation that was observed in the absence of water (Table 6–1, entry 4). Inclusion of an aqueous phase saturated with either NaCl or NH₄Cl, led to increased chemoselectivities in favour of the homoallylic alcohol product (Table 6–3).

Entry	Zinc/allyl bromide/PhCHO (molar ratio)	Salt (mol eq.)	Homoallylic alcohol yield% (selectivity)
1	2:2:1	NaCl (satd.)	90 (95)
2	2:2:1	NH ₄ Cl (satd.)	93 (99)
3	1:1:1	NH ₄ Cl (6)	41 (91)

Table 6–3 Effect of salt on the chemoselectivity of the allylation reaction. Conditions: 30 °C/ 80 bar, 2 hours pulsed ultrasound, 80% amplitude, CO₂/H₂O (42% v/v)

As previously stated, the salt may function as a chloride source for metal activation through dissolution of the oxide layer, and not by a different mechanism such as for example phase transfer catalysis. This is demonstrated by equally high yields and chemoselectivities obtained when the cation is switched from Na⁺ to NH₄⁺. Furthermore, the reaction between CO₂, H₂O and NH₄⁺ may lead to the formation of species such as ammonium bicarbonate and carbamic acid, effectively removing the capacity by ammonium to ‘shuttle’ other ions across the interphase, as is required for phase transfer catalysis. The effect of salts on the rate of allylation was therefore investigated by varying the countercation, counteranion and salt concentration (Figure 6–8).

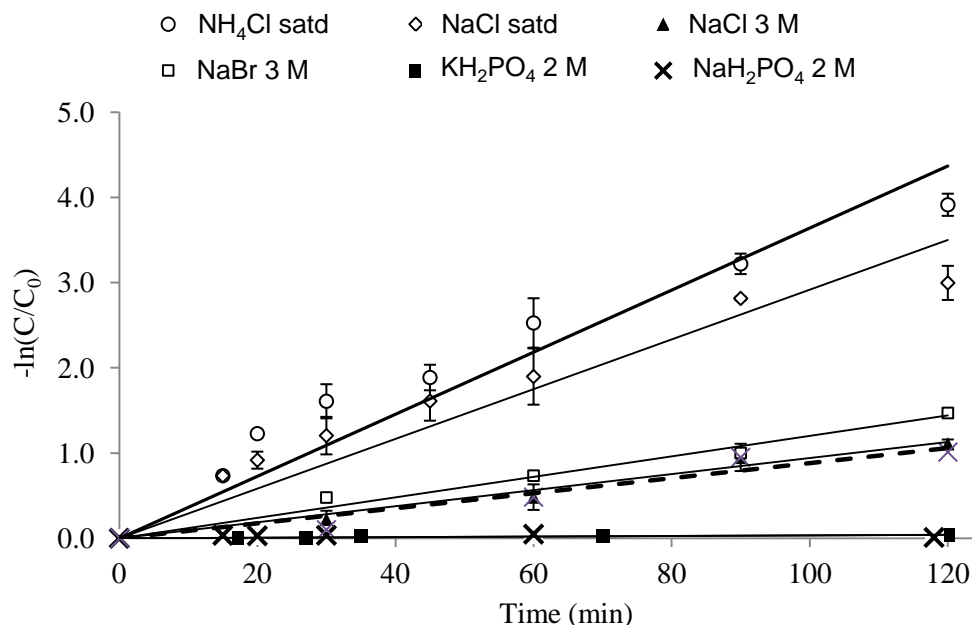


Figure 6–8 Effect of various salts on allylation kinetics (dashed line represents reaction without salt).
Conditions: $\text{CO}_2/\text{aq.} = 40 \text{ v/v\%}$, $30^\circ\text{C}/80 \text{ bar}$, ultrasound amplitude 80%

The kinetics of the Barbier synthesis are extremely complicated due to the interaction of various parallel and sequential mechanistic pathways, and the unclear role played by water and the dependency on the metal particle size, which varies during progress of the reaction. However, according to Dam *et al.* [2008], for the purpose of comparative reasons the kinetics may be simplified by assuming the reactions in first-order to benzaldehyde. Inclusion of saturated solutions of NaCl and NH_4Cl resulted in improved chemoselectivity, with the allylation rate being between 2 and 4 times higher than when just water was employed as the aqueous phase. When the aqueous phase was 3 M NaCl the rate of allylation rate was lower, while the reduction rate was similar to that observed in experiments performed in the absence of salt. In order to rule out any specific mechanistic involvement by the chloride counteranion, 3 M NaBr was also tested as the aqueous phase, as any non concentration-dependent effect would be observed by the different halide

species; however, a similar result was observed as with NaCl. Interestingly, when the counteranion was dihydrogenphosphate, the chemoselectivity was reversed in favour of the reduction product. In this case, the allylation product was formed in only traces amounts, while benzaldehyde conversion also decreased, indicating that the zinc may be inactive under these conditions. This particular effect could be related to the pH of the reaction mixture, which was significantly lower in collected samples following depressurisation (pH 4.0–4.4 with the dihydrogenphosphates compared to 5.6–6.9 with the halides). Since the presence of carbonic acid alone ensures a low pH, however, the pH should not be expected to directly influence the outcome of the reaction. A more plausible explanation may be offered by the effect of phosphate anions on the oxide film of the metal. Refaey [2005] demonstrated that the corrosive effect of hydrochloric acid solutions on steel could be inhibited by inclusion of a phosphate solution. It was suggested that interaction of phosphates with the oxide may form a protective layer against aggressive chloride ions. Indeed, to date, phosphate coatings form one of the most important groups for corrosion prevention chemistry.

6.2.4.2 Effect of Salt on Homoallylic Alcohol K_{CW}

The inclusion of salts is expected to affect the partitioning of non-electrolyte solutes in CO₂/H₂O/salt mixtures. Indeed, the presence of salts was found to have a salting-out effect on the homoallylic alcohol product, producing a decrease in its concentration in the aqueous phase and an increase in the CO₂ phase (Figure 6–9). Literature describing quaternary systems of CO₂/water/salt/solute is scarce. Wagner *et al.* [2003] reported a 2.7-fold increase in the K_{CW} of phenol when NaCl was included at ~3 M. Sieder and Maurer [2004] observed a salting-out effect and a two-fold increase in the K_{CW} of acetic acid when

NaCl was included at 1.5 M. Similarly, the K_{CW} of the homoallylic alcohol product showed a 1.6-fold increase with the inclusion of NaCl up to 6 M. The slightly lower effect observed compared to that reported for phenol and acetic acid may be due to the homoallylic alcohol being more hydrophobic than these compounds, and therefore experiencing a less marked change in the solubilities in both phases.

The above results demonstrate that although the inclusion of salt may lead to a beneficial role on both the chemoselectivity of the reaction and the partitioning of homoallylic alcohol product in the CO₂ phase, these effects would not justify the use of a saturated salt phase. The rate of reaction only increased by up to four times with the inclusion of a saturated salt phase, and in terms of the overall process this would not constitute a significant advantage since the presence of salt at high concentrations in the aqueous phase (in the absence of recycle) is expected to reduce the environmental performance considerably and increase waste treatment costs.

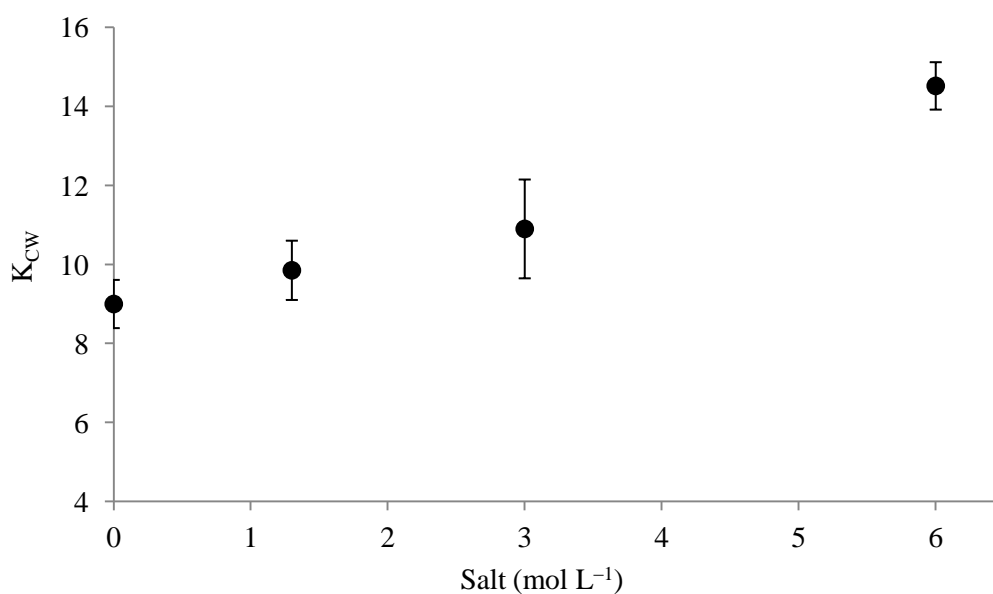


Figure 6–9 Effect of salt concentration on homoallylic alcohol K_{CW}

Nonetheless, salts provided a good investigative tool for the Barbier synthesis and will be discussed throughout the remainder of this Chapter in relation to their effect on the chemoselectivity.

6.4 Allylations Using Other Metals

In order to investigate whether or not the reduction side-reaction was influenced by the choice of metal, the Barbier reaction was next assessed with tin metal. Tin is a useful mediator for several synthetic transformations [Roy and Roy, 2010]. Whilst it possesses a lower first ionisation energy than zinc, its use in allylation reactions has been shown to require prior activation by inorganic acids [Mandai *et al.*, 1984; Guimaraes *et al.*, 2007] or ultrasound [Petrier *et al.*, 1985b; Einhorn and Luche, 1987], through the use of tin nanoparticles [Wang *et al.*, 2002; Zha *et al.*, 2003], or its use in combination with salts such as NaBF₄ [Houllemare *et al.*, 1997]. In the present system, allylation using tin powder was only observed when the reaction was carried out at 60 °C/120 bar (Table 6–4).

Entry	M	Salt (mol eq.)	Conditions	Homoallylic alcohol yield% (selectivity)
1	Sn	-	30 °C/ 80 bar	-
2	Sn	-	60 °C/ 120 bar	34 (100)
3	Sn	NaCl (18)	60 °C/ 120 bar	73 (100)
4	Bi	-	60 °C/ 120 bar	-

Table 6–4 Effect of changing the metal mediator on allylations; M/allyl bromide/benzaldehyde 1:1:1 (based on 61 mmol of benzaldehyde); Conditions: CO₂/H₂O (42% v/v), 2 hours pulsed ultrasound 80% amplitude

The addition of NaCl significantly improved the yield of the homoallylic alcohol product at this temperature and pressure, indicating that these two factors may be working in synergy. Thus, in the presence of NaCl at 60 °C/120 bar, tin metal was used with the other

two reagents in equimolar ratios to achieve moderate yields of the homoallylic alcohol. Bismuth has recently attracted attention as a safer alternative to tin for mediating Barbier reactions [Smith *et al.*, 2004]; however, even at 60 °C/120 bar, bismuth powder did not lead to any product formation, and was not investigated any further.

6.5 Effect of Allylic Reagent Leaving Group

The Barbier synthesis was next performed with allylic reagents possessing different leaving groups (Table 6–5).

Entry	X	Mediator ^(f)	Conditions	Homoallylic alcohol yield% (selectivity)
1	Br	Zn Zn/NaCl	30 °C/120 bar	67 (74) 90 (95)
2	Cl	SnCl ₂ /KI	60 °C/120 bar	47 (100)
3	OH	SnCl ₂ /KI	60 °C/120 bar	-

Table 6–5 Allylation reactions with various allylic compounds. Allylic reagent/benzaldehyde 2:1 (based on 61 mmol of benzaldehyde). Conditions: CO₂/H₂O (42% v/v), 2 hours pulsed ultrasound 80% amplitude; X = leaving group in allylic reagent

In order to improve the cost efficiency of the reaction, cheaper allyl chloride would be preferable to allyl bromide, even if this were at the expense of longer reaction times [Houllemare *et al.*, 1997]. Unfortunately, in the present case, the reaction did not proceed satisfactorily with allyl chloride and most of the benzaldehyde underwent preferential reduction. The inclusion of sodium or potassium iodide can be used to improve the conversion of allyl chloride in the Barbier reaction, with iodide participating in a

^(f)Entries 2–3 performed with SnCl₂ (60 mmol), KI (0.5 M). Entry 1 zinc 120 mmol, satd NaCl.

Finkelstein reaction with the allyl chloride, generating the more reactive allyl iodide *in situ*; indeed, allyl chloride was able to form the homoallylic alcohol product, albeit in moderate amounts, when SnCl₂/KI was employed at 60 °C/ 120 bar; however, this offers no synthetic advantage over the use of allyl bromide. The use of allyl alcohol did not lead to any product formation even under forcing conditions.

6.6 Effect of Aromatic Aldehyde Structure

In order to extend the scope of the Barbier synthesis, the effect of aldehyde structure was investigated. Substituted aromatic aldehydes were chosen as examples as aromatic compounds are the most structurally-relevant substrates for many applications, forming over 90% of all substances entering the R&D programs of major pharmaceutical companies [Carey *et al.*, 2006]. The allylation reaction proceeded efficiently with various other aldehydes (Table 6–6).

Under the optimised conditions, 4-methylbenzaldehyde showed lower reactivities for the allylation and reduction reactions (Table 6–6, entry 1), while 4-methoxybenzaldehyde also exhibited lower chemoselectivity (Table 6–6, entry 2). With both substrates, the yield and selectivity could again be improved by including NaCl in the aqueous phase. The reaction with the more electrophilic 2-chlorobenzaldehyde generated a high yield of the corresponding homoallylic alcohol product, even in the absence of NaCl (Table 6–6, entry 3). Finally, the reaction with (*E*)-cinnamaldehyde (Table 6–6, entry 4) occurred regioselectively, affording the 1,2-addition compound as the major product.

Entry	Aldehyde	Homoallylic alcohol product ^g	Conditions [‡]	Homoallylic alcohol conversion% (selectivity)	Benzyl alcohol product%
1		2a	Zn Zn/NaCl	62 (95) 69 (95)	3.3 3.6
2		3a	Zn Zn/NaCl	52 (61) 85 (94)	33 5.4
3		4a	Zn Zn/NaCl	86 (95) 77 (72)	4.5 22
4		5a	Zn Zn/NaCl	74 (80) 86 (93)	18.5 6.5

Table 6–6 Allylation reactions with substituted aromatic aldehydes. Conditions: 30 °C/80 bar, CO₂/H₂O (42% v/v), 2 hours pulsed ultrasound 80% amplitude, zinc/allyl bromide/aldehyde 2:2:1, satd. NaCl where applicable

6.7 The Barbier Synthesis in the CO₂/H₂O/Tween 80 System

In Section 5.5.1 the presence of Tween 80 was shown to induce a positive effect on the rate of hydrolysis of benzoyl chloride, by enhancing the observed rate constant, k_{obs} , by one order of magnitude. The effects were attributed to removal of the mass transfer resistance by increasing the volume fraction of the CO₂ dispersed phase, and an increase in the total interfacial area. Therefore, in order to assess whether the Barbier synthesis was under any mass transfer limitations, reactions were also performed in the presence of Tween 80.

With regards to C–C bond-forming reactions, various authors have reported the use of surfactants for facilitated product synthesis. For example, Lu *et al.* [2013] employed a non-ionic surfactant as a replacement for the organic phase in Stille

^(g)The numbers refer to each respective homoallylic alcohol synthesised as defined in the Appendix A6.4.

coupling reactions [Lu *et al.*, 2013]. Tween 80 has also been previously employed for its ability to act as an efficient ionophore [Thoman, 1999], and as a phase-transfer catalyst in several reactions [Thoman *et al.*, 1989; Kapdi *et al.*, 2013].

A CO₂/H₂O/1% Tween 80 system showed a similar improvement in the rate of homoallylic alcohol product formation, reaching quantitative yields of the desired product (Figure 6–10).

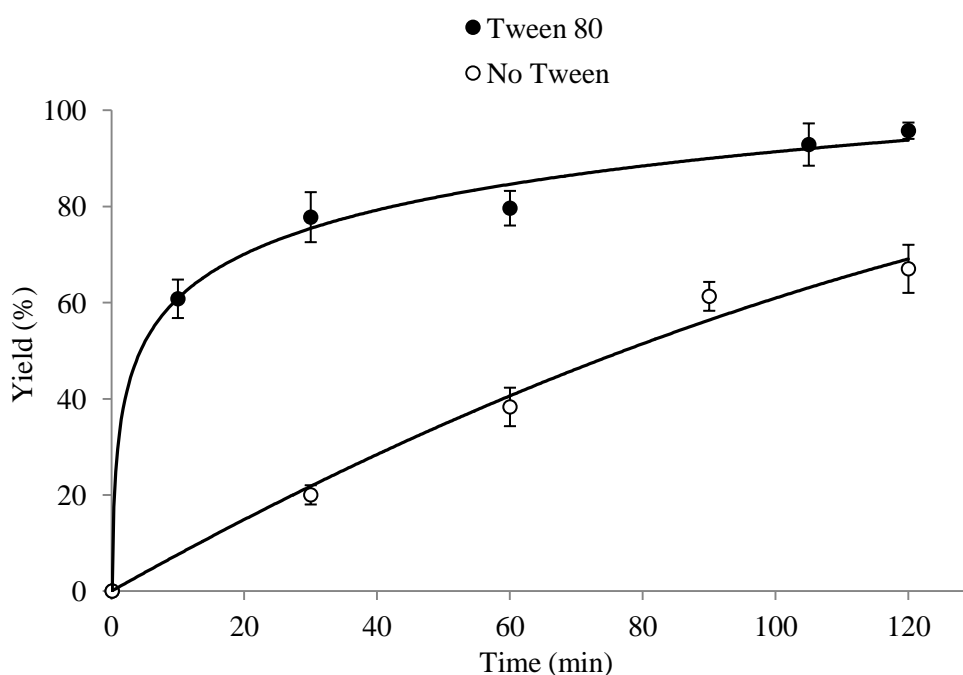


Figure 6–10 Time course for the formation of the homoallylic alcohol product in the presence and absence of 1% Tween 80. Conditions: 30 °C/ 80 bar, CO₂/H₂O = 42%, v/v, pulsed ultrasound at 80% amplitude, zinc/allyl bromide/benzaldehyde 2:2:1

Most noticeably, in the presence of Tween 80, the chemoselectivity of the reaction was dramatically improved, with the homoallylic alcohol product now being formed in > 95% selectivity. The resulting enhancement in the observed rate of reaction of benzaldehyde, k_{obs} , due to the presence of Tween 80 was three-fold, from $1.45 \times 10^{-4} \text{ s}^{-1}$ to $4.43 \times 10^{-4} \text{ s}^{-1}$ (see Appendix A6.2). These results provide a first indication that the allylation reaction

may be kinetically-controlled, as here k_{obs} is over one order of magnitude lower than that for the hydrolysis of benzoyl chloride. In order to better understand the effects induced by ultrasound on the Barbier reaction, the mass transfer and kinetic effects were next considered.

6.8 Mass Transfer with Reaction in Liquid-Liquid-Solid Systems

Unlike for the hydrolysis of benzoyl chloride explored in Section 5.5, where the reaction is homogeneous, the Barbier synthesis occurs in two steps: formation of the organometallic reagent on the metal particle surface, followed by reaction between benzaldehyde and the organometallic reagent. The three-phase mass transfer with reaction model for the Barbier synthesis in $\text{CO}_2/\text{H}_2\text{O}$ therefore resembles that of hydrogenation reactions, where the reagent must travel from the gas to the liquid phase and from the liquid phase to the solid catalyst surface. However, compared to hydrogenation reactions (i.e. shrinking core model) the allylation model does not include a solid reacted layer on the particles as the metal is gradually removed from the surface during the reaction (potentially forming other aggregates of reacted metal salts), and also includes the compressed CO_2 phase which serves as an additional sink for organic species to diffuse into. The primary event for both steps is transfer of the hydrophobic reagents across the $\text{CO}_2/\text{H}_2\text{O}$ interface into the water phase, where metallic zinc resides. The transport of allyl bromide encounters more resistances in its path compared to benzaldehyde, due to the requirement to cross a water-solid film for adsorption and reaction on the metal particle surface (Figure 6–11).

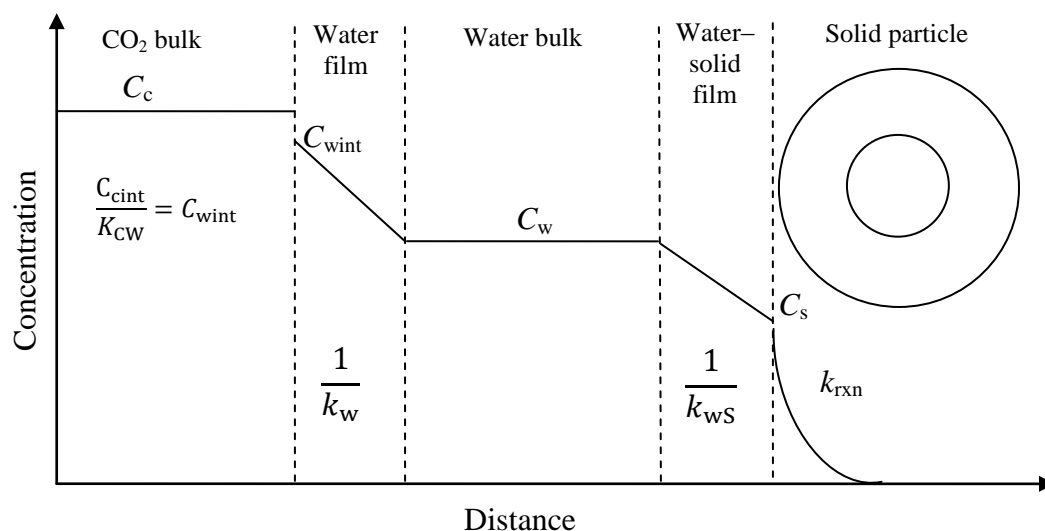


Figure 6-11 Simplified model for the mass transfer of allyl bromide with reaction on the metal particle

Here C_c , C_{wint} , C_w and C_s are the respective concentrations of reactant in the bulk CO₂, at the CO₂/H₂O interface on the water side, in the bulk water and on the solid surface; K_{CW} , k_w and k_{ws} are the CO₂/H₂O partition coefficient, the water film coefficient, and the water-solid film coefficient for the reactant, respectively. The relation between particle size and the rate of reaction is difficult to demonstrate in the present case, especially due to the fact that at the end of the reaction zinc is still present in the form of inactive aggregates of zinc salts (possibly a combination of hydroxides, carbonates, and halides) which are present as a fine white precipitate. However, an indication may be obtained from the work of Olson *et al.*, [2011], who measured the reaction rates for allylindium formation using allyl halides and indium particles. The authors found that the reaction rate increased linearly with time as the radius of the spheres decreased from 500 μm to 200 μm over 30 hours. Particles of smaller radius were then tested (5–20 μm) showing faster reaction rates than the spheres (the final size of the particles was not given). Analysis of the experimental data confirmed

that the step of allyl halide adsorption and reaction on the metal surface was under mass transfer control. However, in reaction systems where the allylmethyl formation step is followed by a C–C coupling step (as in the present case) any rate enhancements due to shrinking of the particles would be masked, due to the slower kinetics of the rate-determining C–C bond-forming step [Dam *et al.*, 2008]. However, shrinking of zinc particles to the nm range may not be excluded, nor faster kinetics of allylzinc formation with decreasing particle size.

Barbier reactions are facilitated by the presence of water (see Table 6–1, entry 4), and since water is thought to drive the final step by liberating the homoallylic alcohol product from the metal salt, this water-dependent step would occur much faster in the aqueous phase, where the concentration of water (55.55 mol L^{–1}) is higher than in the CO₂ phase (0.05 mol L^{–1}, see Section 5.5). Therefore, in this case C–C bond formation would take place in the water phase, followed by transfer of the homoallylic alcohol product to the CO₂ phase under the control of its CO₂/H₂O partition coefficient (Figure 6–12).

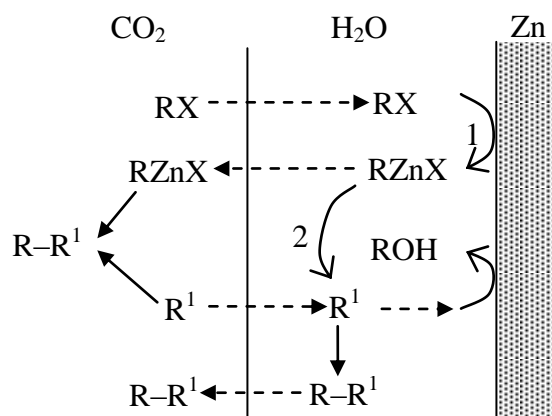


Figure 6–12 Possible transport/reaction pathways experienced by various species during the zinc-mediated Barbier synthesis in CO₂/H₂O mixtures; RX = allyl bromide, R^I = benzaldehyde, ROH = benzyl alcohol, RZnX = organozinc intermediate, R–R^I = homoallylic alcohol product, shown are successive reaction steps of allylzinc formation (1), and homoallylic alcohol formation (2), dashed arrows = mass transfer, solid arrows = reaction

A second possibility may be presented by the transfer of the organozinc reagent across the CO₂/H₂O interface into the CO₂ phase, prior to its interception of benzaldehyde. This scenario would require the mass transfer rate of the organozinc species to be faster than its rate of reaction with benzaldehyde in the water phase. As reported by Dam *et al.* [2008], the rate-limiting (slowest) step in the Barbier reaction for most transition metals is indeed C–C bond formation [Dam *et al.*, 2008], and therefore transfer of the organozinc reagent to the CO₂ phase may be possible, and occur in parallel with other mass transfer and reaction processes as depicted in Figure 6–12. Absolute rate measurements for the allylation reaction are thus impractical, as heterogeneous reagents may introduce important but unknown mass transfer factors that preclude the formulation of accurate rate equations. Nonetheless, for simplicity, the C–C bond-forming step may be used as the source for estimation of k_{rxn} , the intrinsic reaction rate constant measured in pure solvent, which may be obtained from the literature. Kalkan and Erdik [2013] carried out a kinetics analysis for the allylation of mixed organozinc reagents with allyl bromide in THF at 25 °C. Under the conditions studied, the reaction was homogeneous and a cyclic transition state was proposed by the authors, reconcilable with that experienced for zinc-mediated allylations, making the study a suitable example for approximation of k_{rxn} . The resulting pseudo first-order rate constant was $0.21\text{--}1.26 \times 10^{-3} \text{ s}^{-1}$. The second example was provided by Denmark and Fu [2000], who investigated the allylation of benzaldehyde with chlorosilanes (also proposed to progress through a cyclic transition state) [Denmark and Fu, 2000]. The resulting pseudo first-order rate constant with respect to benzaldehyde was $\sim 0.3\text{--}1.5 \times 10^{-3} \text{ s}^{-1}$.

Evaluation of the Hatta number, Ha , defined by Eq. 5.30 as the ratio of the maximum transfer rate due to reaction to that resulting from diffusion, necessitates insertion of k_{rxn}

and k_w , the water film mass transfer coefficient. For the Barbier reaction in the presence of pulsed ultrasound, k_{obs} was measured as $1.45 \times 10^{-4} \text{ s}^{-1}$, therefore the highest value of k_{rxn} ($1.5 \times 10^{-3} \text{ s}^{-1}$) reported by Denmark and Fu [2000] should be used, since it is not expected that k_{rxn} would be equal to or lower than k_{obs} due to the presence of the interfacial CO₂/H₂O resistance. Insertion of k_{rxn} , k_w for silent (0.0009 cm s^{-1} , from Section 5.4.1) and ultrasound conditions (0.011 cm s^{-1} from Section 5.4.2), and diffusivity in water, D_{AW} , of $1 \times 10^{-5} \text{ cm}^2 \text{ s}^{-1}$ generates $Ha = 0.13$ – 0.011 , indicative of slow reactions. Under acoustic agitation, Ha for the Barbier reaction ($Ha = 0.011$) was much lower than for the hydrolysis of benzoyl chloride explored in Section 5.5 ($Ha = 0.3$).

6.8.1 Damköhler Analysis for the Barbier Reaction in CO₂/H₂O

Following an analysis analogous to that used for the hydrolysis of benzoyl halides presented in Section 5.6, the Damköhler number, Da , was calculated for the Barbier reaction in CO₂/H₂O mixtures, and used to identify the conditions under which the reaction would operate in the well-mixed regime of mass transfer equilibrium. Based on the predictions for the CO₂/H₂O partition coefficient of allyl bromide from Section 6.2.3 ($K_{\text{CW}} = 40 \pm 10$), the well-mixed limit was approximated by $k_{\text{obs}}/k_{\text{rxn}}$, calculated from:

$$1 = \frac{k_{\text{obs}} K_{\text{CW}} V_{\text{c}}}{k_{\text{rxn}} V_{\text{w}}} \quad (6.1)$$

where V_{c} and V_{w} are respectively, the volumes of the CO₂ (0.42 L) and water phase (0.58 L). As observed for the hydrolysis of benzoyl halides, conditions of increasingly efficient mixing, represented by ultrasonic irradiation of the reaction mixture either in the absence or in the presence of 1% Tween 80, resulted in a reduction in the transport time (symbolised by lower Da values), and an increase in k_{obs} (Figure 6–13), compared to silent

conditions. The position of the well-mixed line indicated that in the presence of Tween 80 the reaction operated in conditions in which diffusive mass transport reached equilibrium. For conditions in which ultrasound was employed in the absence of Tween 80 a clear interpretation may be obscured by the uncertainties in k_{rxn} .

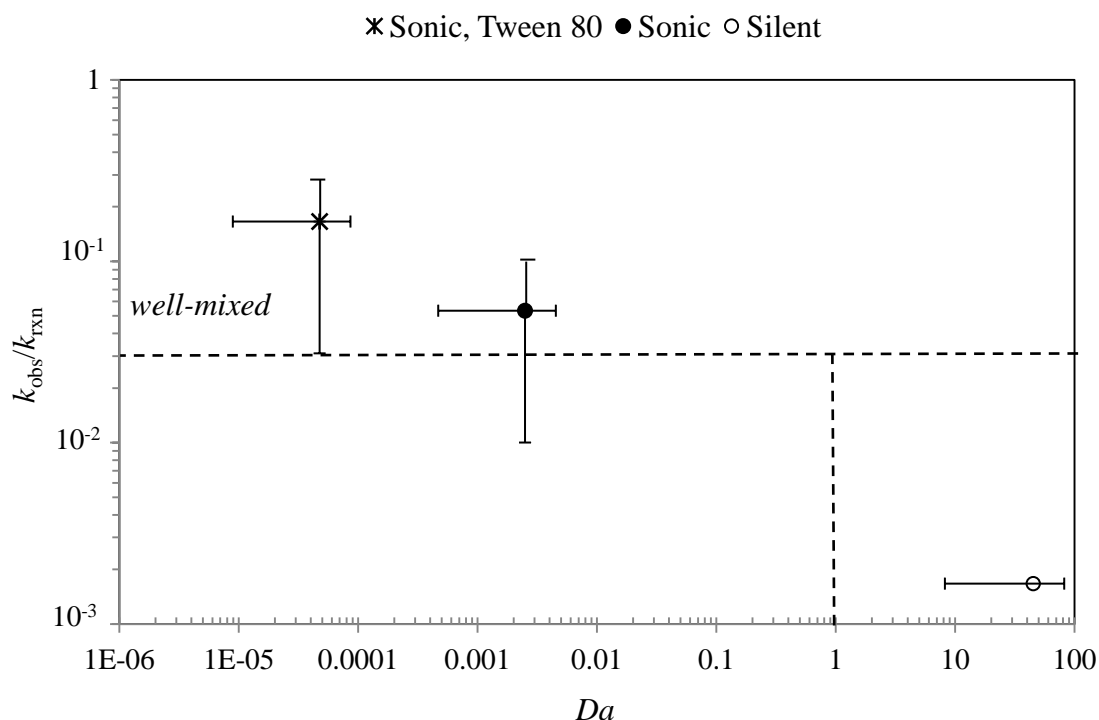


Figure 6–13 Comparison of observed rate constants k_{obs} and intrinsic rate constants k_{rxn} as a function of the Damköhler number Da , for the zinc-mediated Barbier reaction. The vertical error bars are associated with the uncertainties in k_{rxn} ; the horizontal error bars are associated with uncertainties in droplet diameters. Conditions: 30 °C/ 80 bar, CO₂/H₂O (42% v/v), zinc/allyl bromide/benzaldehyde 2:2:1 (based on 0.061 mol of benzaldehyde), 2 hours pulsed ultrasound at 80% amplitude^(h)

Since the inclusion of Tween 80 induced a three-fold enhancement in k_{obs} , and assuming that this effect was exclusively mediated by an increase in mass transfer rates, then it would be reasonable to suggest that the Barbier reaction would be operating below the well-mixed limit when only acoustic agitation was employed without the addition of Tween 80. In reality, for Barbier reactions, k_{rxn} may be higher in aqueous media than in

^(h)See Appendix A6 for details.

organic solvents as reported by Denmark and Fu [2000]. Further support for this hypothesis derives from the observation that for the range of hydrolysis reactions studied by Timko *et al.* [2006b], $k_{\text{rxn}}/k_{\text{obs}}$ in CO₂/H₂O systems was never below ~100 (Table 5–9). This is exemplified by the hydrolysis of *p*-nitrobenzoyl chloride, which showed a ~100-fold decrease in the reaction rate when the solvent was switched from pure water to CO₂/H₂O ($k_{\text{rxn}} = 0.055 \text{ s}^{-1}$ in pure water and $k_{\text{obs}} = 4.6 \times 10^{-4} \text{ s}^{-1}$ in CO₂/H₂O). The vertical error bars in Figure 6–13 highlighted how the position of the data points would vary if k_{rxn} for the Barbier reaction was indeed in the order of 10^{-2} s^{-1} . If this was the case, k_{rxn} would approximate the value of the effective mass transfer coefficient (0.02 s^{-1}) described in Chapter 5, implying that during ultrasound the Barbier reaction was operating close to the well-mixed region. This was supported by:

- The observed low *Da* values.
- A three-fold increase in k_{obs} when Tween 80 was included (compared to a ten-fold increase in the hydrolysis of benzoyl chloride).
- A 58-fold sonic enhancement in k_{obs} relative to silent conditions, compared to the hydrolysis of benzoyl chloride which showed a sonic enhancement of 268, Table 5–8).

These observations suggested that the Barbier reaction was less affected by the high surface areas generated by ultrasound compared to the hydrolysis of benzoyl chloride explored in Chapter 5, and that the reaction was close to the kinetically-controlled regime. Therefore, although ultrasound provided adequate mixing of the liquid/liquid/solid phases, it may not comprise the most suitable methodology, as the intrinsic rate constant of the Barbier reaction fell outside the range for which the high surface areas generated by ultrasound would be most beneficial ($0.02 \text{ s}^{-1} < k_{\text{rxn}} < 1 \text{ s}^{-1}$), and for which sonic enhancements would be most pronounced.

As a final measure of the capabilities of the CO₂/H₂O system, the recovery of the homoallylic alcohol product was next assessed by exploiting its favourable partitioning in the top CO₂ fraction.

6.9 Homoallylic Alcohol Product Separation

The ability to recover products from dense CO₂ as an immiscible counter phase is of significant interest in reaction or extraction procedures [Blanchard and Brennecke, 2001]. Separation procedures are highly flexible in CO₂/H₂O biphasic systems, as in theory, either the water phase or the CO₂ phase may be separated and any soluble fractions preferentially recovered. The low solubility of water in CO₂, coupled to the ability to easily separate the CO₂ fraction by depressurisation, make the CO₂/H₂O biphasic system an ideal solvent environment for carrying out sequential reaction and separation procedures. A preferred separation strategy would involve complete discharge of the aqueous phase at constant pressure through an opening in the bottom of the vessel, followed by isolation of the product by depressurization. Compression and recirculation of the vented CO₂ may also be possible for minimising waste. The reactor in the present study possessed a rectangular base, while the aqueous phase could only be collected through a dip tube, and therefore following discharge of the aqueous phase some water remained in the bottom of the reactor. The product was therefore isolated by passing the CO₂ fraction into the 30 cm³ view cell.

By employing this separation strategy, the yield of homoallylic alcohol product recovered following the zinc-mediated allylation of benzaldehyde by allyl bromide was $76 \pm 6\%$ in the presence of salt and $55 \pm 4\%$ in the absence of salt (after two experiments for each condition). Following experiments in which salt was included, the top CO₂ fraction contained roughly 10 wt.% of water, possibly arising as a result of enhanced stability of the

CO₂/H₂O/salt emulsion. Further studies would be required to assess the stability of these salt-containing dispersions and improve their breakdown for more efficient recovery of the product. Nonetheless, in these samples the salt-containing water fraction slowly separated from the transparent top product phase if stored overnight at 4 °C. Due to the H-bonding character of the homoallylic alcohol there could be a possibility that small amounts of water would still be present in the enriched product, however these were not assessed due to time limitations. GC analysis of aliquots taken from the enriched product fraction revealed that this comprised > 95% homoallylic alcohol. GC analysis of the aqueous phase remaining in the vessel following separation of the product-containing CO₂ fraction showed presence of 5–12 mol% of homoallylic alcohol, closing the mass balance to within 5% and demonstrating close agreement between the yields calculated by the internal standard method and isolated yields. Finally, it may be anticipated that the solubility of the homoallylic alcohol product may increase by tuning the CO₂ solvent properties. As reported by Walther and Maurer [1992], the solubility of benzaldehyde in CO₂ increased ~300 times, from 0.29 g L⁻¹ to 88.0 g L⁻¹ in the range 40 °C/60 bar to 100 °C/203.2 bar. Similarly, an increase in the solubility of homoallylic alcohol in the CO₂ fraction would minimise the amount of product lost to the aqueous phase, and avoid further extraction procedures.

6.10 Conclusions

The results presented in this Chapter demonstrate the capabilities of acoustic agitation for carrying out the zinc-mediated Barbier allylation in CO₂/H₂O. The inability of the reaction to progress effectively in only CO₂ justified the use of a CO₂/H₂O biphasic mixture. The CO₂ phase offered an environment for solubilisation of the organic hydrophobic reagents and critically also allowed preferential partitioning of the homoallylic alcohol product, facilitating its recovery from the solvent. Experiments using the non-ionic surfactant Tween 80, saturated salt solutions as the aqueous phase, and higher temperatures suggested that the improved yields and chemoselectivities for the homoallylic alcohol product were the result of rate enhancements over the competing zinc-mediated reduction. Separation of mass transfer and kinetic effects by identification of the Damköhler number and the sonic enhancement relative to silent conditions, revealed that the Barbier synthesis was operating close to the kinetically-controlled regime, potentially ruling out the use of ultrasound as the primary choice for achieving multiphase mixing in these reactions, due to their less dependency on high surface areas for reaching mass transfer equilibrium. Separation of the mixture following the reaction afforded moderate to high isolated yields of solvent-free homoallylic alcohol product.

Chapter 7

GENERAL CONCLUSIONS AND FUTURE RECOMMENDATIONS

7.1 General Conclusions

➤ Chapter 4 discussed the results obtained for the general characterisation of the CO₂/H₂O/ultrasound system. Calibration of the acoustic power using a calorimetric technique showed the energy efficiency to be approximately 70% when amplitude settings were > 70%. Cavitation activity was demonstrated to occur below the ultrasound probe during sonication by observation of considerable erosion of aluminium foil. However, this cavitation was inconsistent with that generally responsible for the *true* sonochemical effects of ultrasound that lead to extremely high localised temperatures and pressures and enhanced reaction kinetics through free-radical sonolytic reactions. This was demonstrated by sonolytic formation of iodide species during sonication at 1 bar but not at 70 bar, indicating that sonolysis of water is not possible at elevated pressures. The stability of CO₂/H₂O emulsions generated by ultrasound was quantified by analysis of time-lapse recordings of the emulsion through a high-pressure view cell positioned in-line with the ultrasound. The majority of the emulsions broke down in the first few minutes, and the emulsion completely reverted back to biphasic conditions in approximately 20 minutes. On the other hand, ultrasound-generated CO₂/H₂O emulsions stabilised by 1% Tween 80 lasted for over 1 hour, demonstrating the higher stability of these droplets in the presence of this non-ionic surfactant. Water collection and experiments using octane as the CO₂-soluble tracer revealed that two simultaneous environments were present during acoustic agitation, namely a water-continuous phase appearing below the ultrasound probe where the CO₂ dispersed phase occupied a volume fraction of ~6%, and a CO₂-continuous phase where water occupied a volume fraction of ~6.5%. The volume of the dispersed phase depended on the position of the CO₂/H₂O biphasic line below the ultrasound probe.

Inclusion of Tween 80 resulted in only the water-continuous emulsion being formed, leading to a higher volume fraction of the CO₂ dispersed phase.

➤ Chapter 5 described the study of the mass transfer of benzaldehyde and the kinetics of benzoyl chloride hydrolysis in CO₂/H₂O. The solubility of benzaldehyde in water-saturated CO₂ was predicted using the Chrastil method. The mass transfer of benzaldehyde served as a model for the transport of hydrophobic organic compounds from CO₂ to water. Therefore, the mass transfer parameters were assessed using the two-film theory. Based on the hydrodynamic properties of CO₂ and water, the majority of the resistance to benzaldehyde mass transfer was placed in the water film, so that for silent conditions the mass transfer of hydrophobic organic compounds across the CO₂/H₂O interface would always be controlled by their diffusivity in water and the film thickness. In the presence of ultrasound, increased interfacial areas and changes in hydrodynamic factors, led to a higher effective mass transfer coefficient. Thus, sonic enhancement compared to silent conditions was ~140 for the effective mass transfer coefficient, which was 0.02 s⁻¹ on the water-side. More importantly, an approximation for the system mixing time, τ_{SM} , defined as the time required for the diffusive mass transfer to reach equilibrium, could be derived and was determined to be 50 s. The model for mass transfer in the presence of a fast chemical reaction was represented by the hydrolysis of benzoyl chloride. This was used for separating mass transfer and kinetic effects and identification of the reactions for which ultrasound would be most beneficial. More specifically, it helped to identify which class of reactions would fall under the well-mixed regime of diffusive equilibrium, and for which sonic enhancements would be most significant. In the case of benzoyl chloride hydrolysis, acoustic agitation led to a 230-fold sonic enhancement of the rate constant relative to the

silent case. Benzoyl chloride hydrolysis was close to the mass transfer-controlled regime, which may be identified as the limit beyond which ultrasound may not remove the $\text{CO}_2/\text{H}_2\text{O}$ resistance any further. Further removal of the mass transfer resistance was only possible by inclusion of 1% Tween 80, which resulted in higher interfacial areas and a rate constant for benzoyl chloride hydrolysis which was up to an order of magnitude higher. For reactions with increasingly shorter half-lives below the system mixing time ($< \sim 1$ s), ultrasound may not accelerate reaction rates any further, leaving the bulk water phase largely unutilised due to a limitation in the system capacity for removing the interfacial resistance. Therefore, for these reactions smaller contacting devices able to maximise the interfacial areas should be employed. For reactions with half-lives in the range of 1-50 s (the system mixing time), the maximum sonic enhancement is achieved. The ultrasound reactor in these cases provides combined increased interfacial areas and efficient bulk phase mixing, while the fast kinetics also contributes to enhancing the transport of the reactant. For reactions with intrinsic rate constants $\ll 0.02 \text{ s}^{-1}$, diffusive mass transfer reaches equilibrium, sonic enhancement becomes minimal, and the presence of the ultrasound-induced emulsion does not provide any distinct advantages over mechanical agitation as the reaction is in the kinetically-controlled regime.

➤ Chapter 6 described the study of the synthetically important metal-mediated Barbier allylation between allyl bromide and benzaldehyde in the $\text{CO}_2/\text{H}_2\text{O}$ /ultrasound system. For the first time, this reaction was carried out in a $\text{CO}_2/\text{H}_2\text{O}$ solvent and provided the desired homoallylic alcohol product in moderate to high yields. Commercially available zinc dust proved to be a cheap and safe mediator for the reaction. The presence of the polar aqueous medium was necessary for an effective reaction since lower yields were obtained with only

CO₂ as the solvent. The reactants were injected in the CO₂ phase, which served as the hydrophobic solvent, and also provided a suitable fraction for enrichment of the homoallylic alcohol product, due to its favourable CO₂/H₂O partition coefficient ($K_{CW} = 9 \pm 0.8$). On the other hand, the benzyl alcohol product of the competing reduction of benzaldehyde was mostly confined to the water phase due to its lower partition coefficient. A range of mediators and conditions were examined in order to assess the effects on yields and chemoselectivity. Experiments using Tween 80, saturated salt solutions as the aqueous phase, and higher temperatures afforded improved yields and chemoselectivities for the homoallylic alcohol product as a result of a rate enhancement over the competing zinc-mediated reduction. Reaction was complete within two hours and the observed first-order rate constant with respect to benzaldehyde was approximately one order of magnitude lower than that observed for benzoyl chloride hydrolysis, signifying that the slower Barbier allylation was likely to operate in the kinetically-controlled regime. This study highlighted that although ultrasound provided an efficient method for achieving multiphase dispersion and conditions of diffusion equilibrium, it may not prove to be beneficial over mechanical agitation for these types of allylation reactions. Nevertheless, the CO₂/H₂O biphasic system offered the possibility for separation of solvent-free homoallylic alcohol product following depressurisation.

7.2 Future Recommendations

Improving our understanding of the effects of ultrasound on fluid flow and micro-mixing in CO₂/H₂O systems will be invaluable for predicting those classes of reactions that will find the most benefit compared to conditions under mechanical agitation.

For low-frequency ultrasound, acoustic agitation of the CO₂/H₂O biphasic system resulted in both types of CO₂ in water and water in CO₂ emulsions. The presence of the emulsion has been previously shown to lead to an increase in the selectivity of a Diels-Alder reaction compared to silent agitation [Timko *et al.*, 2006a]. Other reactions that could benefit from acoustic agitation of CO₂/H₂O mixtures are hydrogenation reactions, which have been shown to be facilitated by the presence of CO₂ due to its greater miscibility with hydrogen, and furthermore have been shown to progress well in a CO₂/H₂O environment [Bourne *et al.*, 2007]. In certain cases, the volume of water present has also been shown to affect the product selectivity [Chatterjee *et al.*, 2014]. Therefore, these systems could constitute ideal candidates for future exploration in the field of ultrasound-induced processing.

Appropriate studies should also be undertaken to identify the effects of ultrasound frequency in high-pressure systems. With regards to turbulent mixing, high-frequency ultrasound (in the MHz region and with power intensities $< 1 \text{ W cm}^{-2}$) differs significantly from low-frequency ultrasound. Unlike for low-frequency ultrasound, which is known to induce the high-pressure fluctuations that generate cavitations and vortex-like Rayleigh streaming, high-frequency ultrasound has been shown to produce Eckart streaming. On the other hand, the emulsification capacity of ultrasound may decrease at higher ultrasound frequencies, and therefore compensatory effects should exist in order to justify operation at higher frequencies. For example, it has been demonstrated that when high-frequency ultrasound is applied to streams in mixing-layer flow, more efficient turbulent mixing may

be achieved on large and small scales compared to mean fluid shear, enhancing the rate of transport and reaction of species at the interface [Ito *et al.*, 2002]. High-frequency ultrasound is particularly efficient at generating mixing on the small scale by an effect on buoyancy forces. In relation to this, natural convection transport is more prominent in supercritical fluids due to the inverse proportionality between kinematic viscosity and buoyant effects [Debenedetti and Reid, 1986]. Furthermore, the low surface tension and low liquid density of high-pressure CO₂ may lead to local density differences in a CO₂/H₂O biphasic, leading to more pronounced interfacial disruption [Van Iersel *et al.*, 2010] and buoyancy forces that drive the mixing process. Therefore, a reactor design that optimises the effects of turbulent mixing at both the small and large scale would be highly desirable for exploiting the distinct physical properties of supercritical fluids.

Since most scale-up problems are usually associated with heterogeneities in the sonochemical effect, arising as a consequence of changes in the spatial distribution of cavitation streams in larger reactors, the scale-up of cavitation-independent high-frequency processes should be less problematic than for low-frequency applications. Also, since cavitation is mostly associated with low-frequency ultrasound and is not expected to lead to any significant sonochemical activity in pressurised fluids, low-frequency ultrasound should not comprise the primary mixing method in these systems. With increasing ultrasound frequencies ultrasound-induced sonochemical effects decrease [Beckett and Hua, 2001] while energy efficiency increases [Asakura *et al.*, 2008], making high-frequency ultrasound a more suitable choice as a method for agitation of fluid mixtures containing dense CO₂ and water. In this respect, the use of variable frequency transducers would offer the possibility to investigate the full range of conditions under which mixing of high-pressure biphasic mixtures would be optimal.

For fast reactions that do not require long mixing times, the turbulent mixing occurring in proximity of the ultrasound probe may be exploited by employing flow ultrasound reactors. In such systems, the average time spent by the fluid in proximity of the probe is much longer than in cylindrical vessels of large dimensions, where the turbulent zone only represents a small fraction of the vessel volume. A number of applications have been developed using tube-flow ultrasound reactors, with the scope of improving process time and efficiency [Gondrexon *et al.*, 1999; Cintas *et al.*, 2010; Alexandru *et al.*, 2013].

Fluid flow was not assessed in the present reactor, although the different fluid behaviour of CO₂/H₂O mixtures under pulsed and continuous acoustic irradiation, and their relation to mass transfer effects should form the scope of future studies. For this purpose, non-invasive particle tracking techniques such as PEPT have been developed and previously employed for the study of fluid flow in high-pressure multiphase systems [Leadbeater *et al.*, 2012].

Further work should also be undertaken for the characterisation of the ultrasound-generated CO₂/H₂O emulsions. In the present work, only limited microscopic evidence was gained of the droplets due to the difficulties associated with fabrication of the required devices for visualisation of the droplets. A future study should therefore address the droplet size in relation to stability and possibly flow. Ultrasound was also used to generate Tween 80-stabilised emulsions. Since this method has never been previously reported, a study should also aim to characterise these novel systems, potentially highlighting any beneficial roles compared to surfactant-free CO₂/H₂O emulsions.

Chapter 8

REFERENCES

- Abraham, M. H., Chadha, H. S., Whiting, G. S. and Mitchell, R. C. (1994). Hydrogen-bonding 32. An analysis of water-octanol and water-alkane partitioning and the delta-log-P parameter of Seiler. *J. Pharm. Sci.*, **83**, (8) 1085-1100.
- Abraham, M. H. and McGowan, J. C. (1987). The use of characteristic volumes to measure cavity terms in reversed phase liquid-chromatography. *Chromatographia*, **23**, (4) 243-246.
- Agble, D. and Mendes-Tatsis, M. A. (2000). The effect of surfactants on interfacial mass transfer in binary liquid-liquid systems. *Int. J. Heat Mass Tran.*, **43**, (6) 1025-1034.
- Alargova, R. G., Deguchi, S. and Tsujii, K. (2001). Dynamic light scattering study of polystyrene latex suspended in water at high temperatures and high pressures. *Colloid. Surface. A*, **183**, 303-312.
- Alexander, M. and Dalgleish, D. G. (2006). Dynamic light scattering techniques and their applications in food science. *Food Biophys.*, **1**, (1) 2-13.
- Alexandru, L., Cravotto, G., Giordana, L., Binello, A. and Chemat, F. (2013). Ultrasound-assisted extraction of clove buds using batch- and flow-reactors: a comparative study on a pilot scale. *Innov. Food Sci. Emerg.*, **20**, 167-172.
- Ando, T., Sumi, S., Kawate, T., Ichihara, J. and Hanafusa, T. (1984). Sonochemical switching of reaction pathways in solid liquid 2-phase reactions. *J. Chem. Soc. Chem. Comm.*, (7) 439-440.
- Andrews, P. C., Peatt, A. C. and Raston, C. L. (2001). Metal mediated solvent free synthesis of homoallylic alcohols. *Green Chem.*, **3**, (6) 313-315.
- Asakura, Y., Nishida, T., Matsuoka, T. and Koda, S. (2008). Effects of ultrasonic frequency and liquid height on sonochemical efficiency of large-scale sonochemical reactors. *Ultrason. Sonochem.*, **15**, (3) 244-250.
- Aspinall, H. C., Bissett, J. S., Greeves, N. and Levin, D. (2002). Lanthanum triflate-catalysed allylation of aldehydes: crucial activation by benzoic acid. *Tetrahedron Letters*, **43**, (2) 319-321.
- Balachandran, S., Kentish, S. E., Mawson, R. and Ashokkumar, M. (2006). Ultrasonic enhancement of the supercritical extraction from ginger. *Ultrason. Sonochem.*, **13**, (6) 471-479.
- Bang, J. H. and Suslick, K. S. (2010). Applications of Ultrasound to the Synthesis of Nanostructured Materials. *Adv. Mater.*, **22**, (10) 1039-1059.
- Banerjee, S., Hassenklover, E., Kleijn, J. M., Stuart, M. A. C. and Leermakers, F. A. M. (2013). Interfacial tension and wettability in water-carbon dioxide systems: experiments and self-consistent field modeling. *J. Phys. Chem. B*, **117**, (28) 8524-8535.
- Barigou, M. (2004). Particle tracking in opaque mixing systems: an overview of the capabilities of PET and PEPT. *Chem. Eng. Res. Des.*, **82**, (A9) 1258-1267.
- Beckett, M. A. and Hua, I. (2001). Impact of ultrasonic frequency on aqueous sonoluminescence and sonochemistry. *J. Phys. Chem. A*, **105**, (15) 3796-3802.
- Beckman, E. J. (2004). Supercritical and near-critical CO₂ in green chemical synthesis and processing. *J. Supercrit. Fluid*, **28**, (2-3) 121-191.

- Bhanage, B. M., Ikushima, Y., Shirai, M. and Arai, M. (1999). Heck reactions using water-soluble metal complexes in supercritical carbon dioxide. *Tetrahedron Letters*, **40**, (35) 6427-6430.
- Blanchard, L. A. and Brennecke, J. F. (2001). Recovery of organic products from ionic liquids using supercritical carbon dioxide. *Ind. Eng. Chem. Res.*, **40**, (1) 287-292.
- Blatchford, M. A., Raveendran, P. and Wallen, S. L. (2002). Raman spectroscopic evidence for cooperative C-H...O interactions in the acetaldehyde-CO₂ complex. *J. Am. Chem. Soc.*, **124**, (50) 14818-14819.
- Blatchford, M. A., Raveendran, P. and Wallen, S. L. (2003). Spectroscopic studies of model carbonyl compounds in CO₂: evidence for cooperative C-H...O interactions. *J. Phys. Chem. A*, **107**, (48) 10311-10323.
- Blom, M. T., Tas, N. R., Pandraud, G., Chmela, E., Gardeniers, J. G. E., Tijssen, R., Elwenspoek, M. and van den Berg, A. (2001). Failure mechanisms of pressurized microchannels: model and experiments. *J. Microelectromech. S.*, **10**, (1) 158-164.
- Boldrini, G. P., Lodi, L., Tagliavini, E., Tarasco, C., Trombini, C. and Umanironchi, A. (1987). Synthesis of enantiomerically enriched homoallylic alcohols and of 1,2-dien-4-ols using chiral tin(IV) complexes containing diethyl tartrate as an auxiliary ligand. *J. Org. Chem.*, **52**, (24) 5447-5452.
- Bourne, R. A., Stevens, J. G., Ke, J. and Poliakoff, M. (2007). Maximising opportunities in supercritical chemistry: the continuous conversion of levulinic acid to γ -valerolactone in CO₂. *Chem. Commun.*, (44) 4632-4634.
- Brudi, K., Dahmen, N. and Schmieder, H. (1996). Partition coefficients of organic substances in two-phase mixtures of water and carbon dioxide at pressures of 8 to 30 MPa and temperatures of 313 to 333 K. *J. Supercrit. Fluid*, **9**, (3) 146-151.
- Cains, P. W., Martin, P. D. and Price, C. J. (1998). The use of ultrasound in industrial chemical synthesis and crystallization. 1. Applications to synthetic chemistry. *Org. Process Res. Dev.*, **2**, (1) 34-48.
- Campos-Pozuelo, C., Granger, C., Vanhille, C., Moussatov, A. and Dubus, B. (2005). Experimental and theoretical investigation of the mean acoustic pressure in the cavitation field. *Ultrason. Sonochem.*, **12**, (1-2) 79-84.
- Campos-Rey, P., Cabaleiro-Lago, C. and Herves, P. (2009). Promoting mechanistic changes: solvolysis of benzoyl halides in nonionic microemulsions. *J. Phys. Chem. B*, **113**, (35) 11921-11927.
- Carey, J. S., Laffan, D., Thomson, C. and Williams, M. T. (2006). Analysis of the reactions used for the preparation of drug candidate molecules. *Org. Biomol. Chem.*, **4**, (12) 2337-2347.
- Chatterjee, M., Ishizaka, T. and Kawanami, H. (2014). Hydrogenation of 5-hydroxymethylfurfural in supercritical carbon dioxide–water: a tunable approach to dimethylfuran selectivity *Green Chem.*, **16**, 1543-1551.
- Chatzi, E. G., Gavrielides, A. D. and Kiparissides, C. (1989). Generalized-model for prediction of the steady-state drop size distributions in batch stirred vessels. *Ind. Eng. Chem. Res.*, **28**, (11) 1704-1711.

- Chen, D., Sharma, S. K. and Mudhoo, A. (eds.) 2012. Handbook on applications of ultrasound: sonochemistry for sustainability, London: *CRC Press*.
- Chrastil, J. (1982). Solubility of solids and liquids in supercritical gases. *J. Phys. Chem.*, **86**, (15) 3016-3021.
- Cintas, P., Mantegna, S., Gaudino, E. C. and Cravotto, G. (2010). A new pilot flow reactor for high-intensity ultrasound irradiation. Application to the synthesis of biodiesel. *Ultrason. Sonochem.*, **17**, (6) 985-989.
- Clarke, K. G. and Correia, L. D. C. (2008). Oxygen transfer in hydrocarbon-aqueous dispersions and its applicability to alkane bioprocesses: a review. *Biochem. Eng. J.*, **39**, (3) 405-429.
- Consani, K. A. and Smith, R. D. (1990). Observations on the solubility of surfactants and related molecules in carbon dioxide at 50°C. *J. Supercrit. Fluid.*, **3**, 51-65.
- Cooper, T. W. J., Campbell, I. B. and Macdonald, S. J. F. (2010). Factors determining the selection of organic reactions by medicinal chemists and the use of these reactions in arrays (small focused libraries). *Angew. Chem. Int. Edit.*, **49**, (44) 8082-8091.
- Cornils, B. (1999). Bulk and fine chemicals via aqueous biphasic catalysis. *J. Mol. Catal. A-Chem.*, **143**, (1-3) 1-10.
- Cornils, B., Herrmann, W. A. and Eckl, R. W. (1997). Industrial aspects of aqueous catalysis. *J. Mol. Catal. A-Chem.*, **116**, (1-2) 27-33.
- Cravotto, G. and Cintas, P. (2007). Forcing and controlling chemical reactions with ultrasound. *Angew. Chem.-Int. Edit.*, **46**, (29) 5476-5478.
- Cravotto, G. and Cintas, P. (2012). Harnessing mechanochemical effects with ultrasound-induced reactions. *Chem. Sci.*, **3**, (2) 295-307.
- Cravotto, G., Gaudino, E. C. and Cintas, P. (2013). On the mechanochemical activation by ultrasound. *Chem. Soc. Rev.*, **42**, (18) 7521-7534.
- Crum, L. A. (1995). Comments on the evolving field of sonochemistry by a cavitation physicist. *Ultrason. Sonochem.*, **2**, (2) S147-S152.
- D'Auzay, S. d. L. R., Blais, J.-F. and Naffrechoux, E. (2010). Comparison of characterization methods in high frequency sonochemical reactors of differing configurations. *Ultrason. Sonochem.*, **17**, (3) 547-554.
- Da Rocha, S. R. P., Harrison, K. L. and Johnston, K. P. (1999). Effect of surfactants on the interfacial tension and emulsion formation between water and carbon dioxide. *Langmuir*, **15**, (2) 419-428.
- Da Rocha, S. R. P., Psathas, P. A., Klein, E. and Johnston, K. P. (2001). Concentrated CO₂-in-water emulsions with nonionic polymeric surfactants. *J. Colloid Interf. Sci.*, **239**, (1) 241-253.
- Dahlem, O., Risse, J. and Halloin, V. (1999). The radially vibrating horn: a scaling-up possibility for sonochemical reactions. *Chem. Eng. Sci.*, **54**, (13-14) 2829-2838.
- Dam, J. H., Fristrup, P. and Madsen, R. (2008). Combined experimental and theoretical mechanistic investigation of the Barbier allylation in aqueous media. *J. Org. Chem.*, **73**, (8) 3228-3235.

- Danckwerts, P. V. (1951). Significance of liquid-film coefficients in gas absorption. *Ind. Eng. Chem.*, **43**, (6) 1460-1467.
- Dardin, A., DeSimone, J. M. and Samulski, E. T. (1998). Fluorocarbons dissolved in supercritical carbon dioxide. NMR evidence for specific solute-solvent interactions. *J. Phys. Chem. B*, **102**, (10) 1775-1780.
- Darr, J. A. and Poliakoff, M. (1999). New directions in inorganic and metal-organic coordination chemistry in supercritical fluids. *Chem. Rev.*, **99**, (2) 495-541.
- Davies, I. W. and Welch, C. J. (2009). Looking forward in pharmaceutical process chemistry. *Science*, **325**, (5941) 701-704.
- Debenedetti, P. G. and Reid, R. C. (1986). Diffusion and mass-transfer in supercritical fluids. *AIChE J.*, **32**, (12) 2034-2046.
- Dehkordi, A. M. (2002). Liquid-liquid extraction with an interphase chemical reaction in an air-driven two-impinging-streams reactor: effective interfacial area and overall mass-transfer coefficient. *Ind. Eng. Chem. Res.*, **41**, (16) 4085-4093.
- Dehkordi, A. M. and Savari, C. (2011). Determination of interfacial area and overall volumetric mass-transfer coefficient in a novel type of two impinging streams reactor by chemical method. *Ind. Eng. Chem. Res.*, **50**, (10) 6426-6435.
- Deleersnyder, K., Shi, D., Binnemans, K. and Parac-Vogt, T. N. (2008). Lanthanide-surfactant-combined catalysts for the allylation of benzaldehyde with tetraallyltin in aqueous solutions. *J. Alloy. Compd.*, **451**, (1-2) 418-421.
- Delgado, J. (2007). Molecular diffusion coefficients of organic compounds in water at different temperatures. *J. Phase Equilib. Diff.*, **28**, (5) 427-432.
- Denmark, S. E. and Fu, J. P. (2000). On the mechanism of catalytic, enantioselective allylation of aldehydes with chlorosilanes and chiral Lewis bases. *J. Am. Chem. Soc.*, **122**, (48) 12021-12022.
- Denmark, S. E. and Fu, J. P. (2003). Catalytic enantioselective addition of allylic organometallic reagents to aldehydes and ketones. *Chem. Rev.*, **103**, (8) 2763-2793.
- Derjaguin, B. V., Titijevskaia, A. S., Abrikosova, I. I. and Malkina, A. D. (1954). Investigations of the forces of interaction of surfaces in different media and their application to the problem of colloid stability. *Discuss. Faraday Soc.*, (18) 24-41.
- DeSimone, J. M., Guan, Z. and Elsbernd, C. S. (1992). Synthesis of fluoropolymers in supercritical carbon-dioxide. *Science*, **257**, (5072) 945-947.
- Desyatnyk, O., Pszczolkowski, L., Thorwirth, S., Krygowski, T. M. and Kisiel, Z. (2005). The rotational spectra, electric dipole moments and molecular structures of anisole and benzaldehyde. *Phys. Chem. Chem. Phys.*, **7**, (9) 2080-2080.
- Dezhkunov, N., Iernetti, G., Francescutto, A., Reali, M. and Ciuti, P. (1997). Cavitation erosion and sonoluminescence at high hydrostatic pressures. *Acustica*, **83**, (1) 19-24.
- Dharmarathne, L., Ashokkumar, M. and Grieser, F. (2012). Reaction of ferricyanide and methyl viologen with free radicals produced by ultrasound in aqueous solutions. *J. Phys. Chem. A*, **116**, (30) 7775-7782.

- Dickson, J. L., Adkins, S. S., Cao, T., Webber, S. E. and Johnston, K. P. (2006). Interactions of core-shell silica nanoparticles in liquid carbon dioxide measured by dynamic light scattering. *Ind. Eng. Chem. Res.*, **45**, (16) 5603-5613.
- Dickson, J. L., Psathas, P. A., Salinas, B., Ortiz-Estrada, C., Luna-Barcenas, G., Hwang, H. S., Lim, K. T. and Johnston, K. P. (2003). Formation and growth of water-in-CO₂ miniemulsions. *Langmuir*, **19**, (12) 4895-4904.
- Doktycz, S. J. and Suslick, K. S. (1990). Interparticle collisions driven by ultrasound. *Science*, **247**, (4946) 1067-1069.
- Dumont, E., Darracq, G., Couvert, A., Couriol, C., Amrane, A., Thomas, D., Andres, Y. and Le Cloirec, P. (2013). Volumetric mass transfer coefficients characterising VOC absorption in water/silicone oil mixtures. *Chem. Eng. J.*, **221**, 308-314.
- Durant, A., Delplancke, J. L., Libert, V. and Reisse, J. (1999). Sonoelectroreduction of metallic salts: a new method for the production of reactive metallic powders for organometallic reactions and its application in organozinc chemistry. *Eur. J. Inorg. Chem.*, (11) 2845-2851.
- Durant, A., Delplancke, J. L., Winand, R. and Reisse, J. (1995). A new procedure for the production of highly reactive metal powders by pulsed sonoelectrochemical reduction. *Tetrahedron Letters*, **36**, (24) 4257-4260.
- Eckert, C. A. and Chandler, K. (1998). Tuning fluid solvents for chemical reactions. *J. Supercrit. Fluid*, **13**, (1-3) 187-195.
- Eckert, C. A. and Knutson, B. L. (1993). Molecular charisma in supercritical fluids. *Fluid Phase Equilib.*, **83**, 93-100.
- Eckert, C. A., Ziger, D. H., Johnston, K. P. and Kim, S. (1986). Solute partial molal volumes in supercritical fluids. *J. Phys. Chem.*, **90**, (12) 2738-2746.
- Einhorn, C. and Luche, J. L. (1987). Selective allylation of carbonyl-compounds in aqueous-media. *J. Organomet. Chem*, **322**, (2) 177-183.
- Eren, Z. and Ince, N. H. (2010). Sonolytic and sonocatalytic degradation of azo dyes by low and high frequency ultrasound. *J. Hazard. Mater.*, **177**, (1-3) 1019-1024.
- Fainberg, A. H. and Winstein, S. (1956). Correlation of solvolysis rates 3. Tert-butyl chloride in a wide range of solvent mixtures. *J. Am. Chem. Soc.*, **78**, (12) 2770-2777.
- Federsel, H. J. (2009). Chemical process research and development in the 21st century: challenges, strategies, and solutions from a pharmaceutical industry perspective. *Accounts Chem. Res.*, **42**, (5) 671-680.
- Feng, R., Zhao, Y. Y., Zhu, C. P. and Mason, T. J. (2002). Enhancement of ultrasonic cavitation yield by multi-frequency sonication. *Ultrason. Sonochem.*, **9**, (5) 231-236.
- Fernandes, J. B. and Sharma, M. M. (1967). Effective interfacial area in agitated liquid-liquid contactors. *Chem. Eng. Sci.*, **22**, (10) 1267-1282.
- Flannigan, D. J. and Suslick, K. S. (2005). Plasma formation and temperature measurement during single-bubble cavitation. *Nature*, **434**, (7029) 52-55.

- Foster, N. R., Macnaughton, S. J., Chaplin, R. P. and Wells, P. T. (1989). Critical locus and partial molar volume studies of the benzaldehyde carbon-dioxide binary-system. *Ind. Eng. Chem. Res.*, **28**, (12) 1903-1907.
- Friberg, S. E., Larsson, K. and Sjoblom, J. (eds.) 2004. Food Emulsions, New York: *Marcel Dekker Inc.*
- Fryer, P. J. and Robbins, P. T. (2005). Heat transfer in food processing: ensuring product quality and safety. *Appl. Therm. Eng.*, **25**, (16) 2499-2510.
- Fu, H., Coelho, L. A. F. and Matthews, M. A. (2000). Diffusion coefficients of model contaminants in dense CO₂. *J. Supercrit. Fluid*, **18**, (2) 141-155.
- Fuchs, M., Schober, M., Orthaber, A. and Faber, K. (2013). Asymmetric synthesis of beta-substituted alpha-methylenebutyrolactones via TRIP-catalyzed allylation: mechanistic studies and application to the synthesis of (S)-(-)-hydroxymatairesinol. *Adv. Synth. Catal.*, **355**, (13) 2499-2505.
- Gao, Y., Wang, X., Sun, L., Xie, L. and Xu, X. (2012). Zinc or indium-mediated Barbier-type allylation of aldehydes with 3-bromomethyl-5H-furan-2-one in aqueous media: an efficient synthesis method for alpha-methylene-gamma-butyrolactone. *Org. Biomol. Chem.*, **10**, (20) 3991-3998.
- Garrigues, L., Pebere, N. and Dabosi, F. (1996). An investigation of the corrosion inhibition of pure aluminum in neutral and acidic chloride solutions. *Electrochim. Acta*, **41**, (7-8) 1209-1215.
- Ghaini, A., Kashid, M. N. and Agar, D. W. (2010). Effective interfacial area for mass transfer in the liquid-liquid slug flow capillary microreactors. *Chem. Eng. Process.*, **49**, (4) 358-366.
- Glezakou, V.-A., Rousseau, R., Dang, L. X. and McGrail, B. P. (2010). Structure, dynamics and vibrational spectrum of supercritical CO₂/H₂O mixtures from *ab initio* molecular dynamics as a function of water cluster formation. *Phys. Chem. Chem. Phys.*, **12**, (31) 8759-8771.
- Gogate, P. R., Sutkar, V. S. and Pandit, A. B. (2011). Sonochemical reactors: important design and scale up considerations with a special emphasis on heterogeneous systems. *Chem. Eng. J.*, **166**, (3) 1066-1082.
- Goldfarb, D. L., Corti, H. R., Marken, F. and Compton, R. G. (1998). High-pressure sonoelectrochemistry in aqueous solution: soft cavitation under CO₂. *J. Phys. Chem. A*, **102**, (45) 8888-8893.
- Gondrexon, N., Renaudin, V., Petrier, C., Boldo, P., Bernis, A. and Gonthier, Y. (1999). Degradation of pentachlorophenol aqueous solutions using a continuous flow ultrasonic reactor: experimental performance and modelling. *Ultrason. Sonochem.*, **5**, (4) 125-131.
- Gonzalez, L. A., Kracke, P., Green, W. H., Tester, J. W., Shafer, L. M. and Timko, M. T. (2012). Oxidative desulfurization of middle-distillate fuels using activated carbon and power ultrasound. *Energy & Fuels*, **26**, (8) 5164-5176.
- Gordon, C. M. and Ritchie, C. (2002). Indium and tin-mediated allylation in ionic liquids. *Green Chem.*, **4**, (2) 124-128.

- Gore, P. H., Hopkins, P. A., Lefevre, R. J. W., Radom, L. and Ritchie, G. L. D. (1971). Molecular polarisability - dipole moments and molar Kerr constants of benzaldehyde, acetophenone, 1,4-diformylbenzene, and 1,4-diacetylbenzene. *J. Chem. Soc. B*, (1) 120-123.
- Guida, A., Nienow, A. W. and Barigou, M. (2010). Shannon entropy for local and global description of mixing by Lagrangian particle tracking. *Chem. Eng. Sci.*, **65**, (10) 2865-2883.
- Guida, A., Nienow, A. W. and Barigou, M. (2012). Lagrangian tools for the analysis of mixing in single-phase and multiphase flow systems. *AIChE J.*, **58**, (1) 31-45.
- Guimaraes, R. L., Lima, D. J. P., Barros, M. E. S. B., Cavalcanti, L. N., Hallwass, F., Navarro, M., Bieber, L. W. and Malvestiti, I. (2007). Aqueous Barbier allylation of aldehydes mediated by tin. *Molecules*, **12**, (9) 2089-2105.
- Guo, Z. and Roache, N. F. (2003). Overall mass transfer coefficient for pollutant emissions from small water pools under simulated indoor environmental conditions. *Ann. Occup. Hyg.*, **47**, (4) 279-286.
- Gupta, R. B., Panayiotou, C. G., Sanchez, I. C. and Johnston, K. P. (1992). Theory of hydrogen-bonding in supercritical fluids. *AIChE J.*, **38**, (8) 1243-1253.
- Gurdial, G. S., Macnaughton, S. J., Tomasko, D. L. and Foster, N. R. (1993). Influence of chemical modifiers on the solubility of *o*-hydroxybenzoic and *m*-hydroxybenzoic acid in supercritical CO₂. *Ind. Eng. Chem. Res.*, **32**, (7) 1488-1497.
- Haberman, J. X., Irvin, G. C., John, V. T. and Li, C. J. (1999). Aldehyde allylation in liquid carbon dioxide. *Green Chem.*, **1**, (6) 265-267.
- Hagenson, L. C. and Doraiswamy, L. K. (1998). Comparison of the effects of ultrasound and mechanical agitation on a reacting solid-liquid system. *Chem. Eng. Sci.*, **53**, (1) 131-148.
- Hallett, J. P., Ford, J. W., Jones, R. S., Pollet, P., Thomas, C. A., Liotta, C. L. and Eckert, C. A. (2008). Hydroformylation catalyst recycle with gas-expanded liquids. *Ind. Eng. Chem. Res.*, **47**, (8) 2585-2589.
- Hansen, C. M. (2007). Hansen solubility parameters: a user's handbook, Boca Raton: CRC Press.
- Hansson, I. and Morch, K. A. (1980). The dynamics of cavity clusters in ultrasonic (vibratory) cavitation erosion. *J. Appl. Phys.*, **51**, (9) 4651-4658.
- Harrison, K., Goveas, J., Johnston, K. P. and Orear, E. A. (1994). Water-in-carbon dioxide microemulsions with a fluorocarbon-hydrocarbon hybrid surfactant. *Langmuir*, **10**, (10) 3536-3541.
- Hart, E. J. and Henglein, A. (1985). Free-radical and free atom reactions in the sonolysis of aqueous iodide and formate solutions. *J. Phys. Chem.*, **89**, (20) 4342-4347.
- Hebach, A., Oberhof, A. and Dahmen, N. (2004). Density of water plus carbon dioxide at elevated pressures: measurements and correlation. *J. Chem. Eng. Data*, **49**, (4) 950-953.
- Henderson, R. K., Jimenez-Gonzalez, C., Constable, D. J. C., Alston, S. R., Inglis, G. G. A., Fisher, G., Sherwood, J., Binks, S. P. and Curzons, A. D. (2011). Expanding GSK's

- solvent selection guide - embedding sustainability into solvent selection starting at medicinal chemistry. *Green Chem.*, **13**, (4) 854-862.
- Henglein, A. and Gutierrez, M. (1988). Sonolysis of polymers in aqueous-solution - new observations on pyrolysis and mechanical degradation. *J. Phys. Chem.*, **92**, (13) 3705-3707.
- Herrmann, W. A., Kohlpaintner, C. W., Manetsberger, R. B., Bahrmann, H. and Kottmann, H. (1995). Water-soluble metal-complexes and catalysts 7. New efficient water-soluble catalysts for 2-phase olefin hydroformylation - BINAS-Na, a superlative in propene hydroformylation. *J. Mol. Catal. A-Chem.*, **97**, (2) 65-72.
- Hintermair, U., Franciò, G. and Leitner, W. (2011). Continuous flow organometallic catalysis: new wind in old sails. *Chem. Commun.*, **47**, (13) 3691-3701.
- Hodgson, D. M., Talbot, E. P. A. and Clark, B. P. (2011). Stereoselective synthesis of beta-(hydroxymethylaryl/alkyl)-alpha-methylene-gamma-butyrolactones. *Org. Lett.*, **13**, (10) 2594-2597.
- Hoefling, T. A., Enick, R. M. and Beckman, E. J. (1991). Microemulsions in near-critical and supercritical CO₂. *J. Phys. Chem.*, **95**, (19) 7127-7129.
- Hollingsworth, K. G., Sederman, A. J., Buckley, C., Gladden, L. F. and Johns, M. L. (2004). Fast emulsion droplet sizing using NMR self-diffusion measurements. *J. Colloid Interf. Sci.*, **274**, (1) 244-250.
- Holmes, J. D., Ziegler, K. J., Audriani, M., Lee, C. T., Bhargava, P. A., Steytler, D. C. and Johnston, K. P. (1999). Buffering the aqueous phase pH in water-in-CO₂ microemulsions. *J. Phys. Chem. B*, **103**, (27) 5703-5711.
- Horst, C., Kunz, U., Rosenplanter, A. and Hoffmann, U. (1999). Activated solid-fluid reactions in ultrasound reactors. *Chem. Eng. Sci.*, **54**, (13-14) 2849-2858.
- Houllemare, D., Outurquin, F. and Paulmier, C. (1997). Synthesis of homoallylic (but-3-enylic) alcohols from aldehydes with allylic chlorides, tin(II) chloride and potassium iodide in water. *J. Chem Soc. Perk. T. I*, (11) 1629-1632.
- Huppert, G. L., Wu, B. C., Townsend, S. H., Klein, M. T. and Paspek, S. C. (1989). Hydrolysis in supercritical water - identification and implications of a polar transition-state. *Ind. Eng. Chem. Res.*, **28**, (2) 161-165.
- Hutli, E. A. F., Nedeljkovic, M. S. and Radovic, N. A. (2008). Mechanics of submerged jet cavitating action: material properties, exposure time and temperature effects on erosion. *Arch. Appl. Mech.*, **78**, (5) 329-341.
- Issenmann, B., Wunenburger, R., Chraïbi, H., Gandil, M. and Delville, J. P. (2011). Unsteady deformations of a free liquid surface caused by radiation pressure. *J. Fluid Mech.*, **682**, 460-490.
- Ito, A., Kishida, M., Kurusu, Y. and Masuyama, Y. (2000). Regio- and diastereocontrol in carbonyl allylation by 1-halobut-2-enes with tin(II) halides. *J. Org. Chem.*, **65**, (2) 494-498.
- Ito, Y., Nagata, K. and Komori, S. (2002). The effects of high-frequency ultrasound on turbulent liquid mixing with a rapid chemical reaction. *Phys. Fluids*, **14**, (12) 4362-4371.

- Ivanov, I. B., Danov, K. D. and Kralchevsky, P. A. (1999). Flocculation and coalescence of micron-size emulsion droplets. *Colloid. Surface. A*, **152**, (1-2) 161-182.
- Iwai, Y. and Li, S. C. (2003). Cavitation erosion in waters having different surface tensions. *Wear*, **254**, (1-2) 1-9.
- Iwai, Y., Nagano, H., Lee, G. S., Uno, M. and Arai, Y. (2006). Measurement of entrainer effects of water and ethanol on solubility of caffeine in supercritical carbon dioxide by FT-IR spectroscopy. *J. Supercrit. Fluid*, **38**, (3) 312-318.
- Iwai, Y., Tanabe, D., Yamamoto, M., Nakajima, T., Uno, M. and Arai, Y. (2002). FT-IR study on interactions between solutes and entrainers in supercritical carbon dioxide. *Fluid Phase Equilib.*, **193**, (1-2) 203-216.
- Iwai, Y., Uno, M., Nagano, H. and Arai, Y. (2004). Measurement of solubilities of palmitic acid in supercritical carbon dioxide and entrainer effect of water by FTIR spectroscopy. *J. Supercrit. Fluid*, **28**, (2-3) 193-200.
- Jacobson, G. B., Lee, C. T., da Rocha, R. P. and Johnston, K. P. (1999a). Organic synthesis in water carbon dioxide emulsions. *J. Org. Chem.*, **64**, (4) 1207-1210.
- Jacobson, G. B., Lee, C. T. and Johnston, K. P. (1999b). Organic synthesis in water carbon dioxide microemulsions. *J. Org. Chem.*, **64**, (4) 1201-1206.
- Jacobson, G. B., Lee, C. T., Johnston, K. P. and Tumas, W. (1999c). Enhanced catalyst reactivity and separations using water/carbon dioxide emulsions. *J. Am. Chem. Soc.*, **121**, (50) 11902-11903.
- Jasinska, M., Baldyga, J., Cooke, M. and Kowalski, A. (2013). Investigations of mass transfer with chemical reactions in two-phase liquid-liquid systems. *Chem. Eng. Res. Des.*, **91**, (11) 2169-2178.
- Jessop, P. G. (2006). Homogeneous catalysis using supercritical fluids: recent trends and systems studied. *J. Supercrit. Fluid*, **38**, (2) 211-231.
- Jessop, P. G., Brown, R. A., Yamakawa, M., Xiao, J. L., Ikariya, T., Kitamura, M., Tucker, S. C. and Noyori, R. (2002). Pressure-dependent enantio-selectivity in the organozinc addition to aldehydes in supercritical fluids. *J. Supercrit. Fluid*, **24**, (2) 161-172.
- Jessop, P. G., Hsiao, Y., Ikariya, T. and Noyori, R. (1996). Homogeneous catalysis in supercritical fluids: hydrogenation of supercritical carbon dioxide to formic acid, alkyl formates, and formamides. *J. Am. Chem. Soc.*, **118**, (2) 344-355.
- Jessop, P. G., Ikariya, T. and Noyori, R. (1994). Homogeneous catalytic hydrogenation of supercritical carbon-dioxide. *Nature*, **368**, (6468) 231-233.
- Jessop, P. G., Ikariya, T. and Noyori, R. (1995). Homogeneous catalysis in supercritical fluids. *Science*, **269**, (5227) 1065-1069.
- Jessop, P. G., Jessop, D. A., Fu, D. and Lam, P. (2012). Solvatochromic parameters for solvents of interest in green chemistry. *Green Chem.*, **14**, (5) 1245-1259.
- Johnston, K. P., Harrison, K. L., Clarke, M. J., Howdle, S. M., Heitz, M. P., Bright, F. V., Carlier, C. and Randolph, T. W. (1996). Water in carbon dioxide microemulsions: an environment for hydrophiles including proteins. *Science*, **271**, (5249) 624-626.

- Johnston, K. P. and Haynes, C. (1987). Extreme solvent effects on reaction rate constants at supercritical fluid conditions. *AIChE J.*, **33**, (12) 2017-2026.
- Kainz, S., Koch, D., Baumann, W. and Leitner, W. (1997). Perfluoroalkyl-substituted arylphosphanes as ligands for homogeneous catalysis in supercritical carbon dioxide. *Angew. Chem.-Int. Edit. Engl.*, **36**, (15) 1628-1630.
- Kalkan, M. and Erdik, E. (2013). Reactivities of mixed organozinc and mixed organocopper reagents. Part 7. Comparison of the transfer rate of the same group in allylation of mixed and homo diorganozinc reagents. *J. Phys. Org. Chem.*, **26**, (3) 256-260.
- Kapdi, A. R., Jain, C., Padte, T., Shevde, U., Pednekar, S., Fischer, C. and Schulzke, C. (2013). Tween-80: a bio-degradable and recyclable phase transfer catalyst for microwave assisted synthesis of highly substituted dicoumarols. *Int. J. Green Chem. Bioproc.*, **3**, 17-23.
- Karásek, P., Pol, J., Planeta, J., Roth, M., Vejrosta, J. and Wicar, S. (2002). Partition coefficients of environmentally important phenols in a supercritical carbon dioxide-water system from cocurrent extraction without analysis of the compressible phase. *Anal. Chem.*, **74**, (16) 4294-4299.
- Kardos, N. and Luche, J. L. (2001). Sonochemistry of carbohydrate compounds. *Carbohydr. Res.*, **332**, (2) 115-131.
- Kazarian, S. G., Vincent, M. F., Bright, F. V., Liotta, C. L. and Eckert, C. A. (1996). Specific intermolecular interaction of carbon dioxide with polymers. *J. Am. Chem. Soc.*, **118**, (7) 1729-1736.
- Kerwin, B. A. (2008). Polysorbates 20 and 80 used in the formulation of protein biotherapeutics: structure and degradation pathways. *J. Pharm. Sci.*, **97**, (8) 2924-2935.
- Keswani, M., Raghavan, S. and Deymier, P. (2013). Effect of non-ionic surfactants on transient cavitation in a megasonic field. *Ultrason. Sonochem.*, **20**, (1) 603-609.
- King, M. B., Mubarak, A., Kim, J. D. and Bott, T. R. (1992). The mutual solubilities of water with supercritical and liquid carbon dioxide. *J. Supercrit. Fluid.*, **5**, (4) 296-302.
- Koda, S., Kimura, T., Kondo, T. and Mitome, H. (2003). A standard method to calibrate sonochemical efficiency of an individual reaction system. *Ultrason. Sonochem.*, **10**, (3) 149-156.
- Koetsier, W. and Thoenes, D. (1973). Mass transfer in a closed stirred gas/liquid contactor: Part 2: the liquid phase mass transfer coefficient k_L . *Chem. Eng. J.*, **5**, (1) 71-75.
- Kopach, M. E., Roberts, D. J., Johnson, M. D., Groh, J. M., Adler, J. J., Schafer, J. P., Kobierski, M. E. and Trankle, W. G. (2012). The continuous flow Barbier reaction: an improved environmental alternative to the Grignard reaction? *Green Chem.*, **14**, (5) 1524-1536.
- Kordikowski, A., Robertson, D. G., Aguiar-Ricardo, A. I., Popov, V. K., Howdle, S. M. and Poliakov, M. (1996). Probing vapor/liquid equilibria of near-critical binary gas mixtures by acoustic measurements. *J. Phys. Chem.*, **100**, (22) 9522-9526.

- Kovscek, A. R. and Cakici, M. D. (2005). Geologic storage of carbon dioxide and enhanced oil recovery II. Cooptimization of storage and recovery. *Energ. Convers. Manage.*, **46**, (11-12) 1941-1956.
- Kruus, P., O'Neill, M. and Robertson, D. (1990). Ultrasonic initiation of polymerization. *Ultrasonics*, **28**, (5) 304-309.
- Kuijpers, M. W. A., Iedema, P. D., Kemmere, M. F. and Keurentjes, J. T. F. (2004). The mechanism of cavitation-induced polymer scission; experimental and computational verification. *Polymer*, **45**, (19) 6461-6467.
- Kuijpers, M. W. A., Jacobs, L. J. M., Kemmere, M. F. and Keurentjes, J. T. F. (2005). Influence of CO₂ on ultrasound-induced polymerizations in high-pressure fluids. *AIChE J.*, **51**, (6) 1726-1732.
- Kuijpers, M. W. A., van Eck, D., Kemmere, M. F. and Keurentjes, J. T. F. (2002). Cavitation-induced reactions in high-pressure carbon dioxide. *Science*, **298**, (5600) 1969-1971.
- Kumar, A., Gogate, P. R. and Pandit, A. B. (2007). Mapping the efficacy of new designs for large scale sonochemical reactors. *Ultrason. Sonochem.*, **14**, (5) 538-544.
- Kumar, A. and Hartland, S. (1999). Correlations for prediction of mass transfer coefficients in single drop systems and liquid-liquid extraction columns. *Chem. Eng. Res. Des.*, **77**, (A5) 372-384.
- Kumar, A., Kumaresan, T., Pandit, A. B. and Joshi, J. B. (2006). Characterization of flow phenomena induced by ultrasonic horn. *Chem. Eng. Sci.*, **61**, (22) 7410-7420.
- Lagalante, A. F. and Bruno, T. J. (1998). Modeling the water-supercritical CO₂ partition coefficients of organic solutes using a linear solvation energy relationship. *J. Phys. Chem. B*, **102**, (6) 907-909.
- Laugier, F., Andriantsiferana, C., Wilhelm, A. M. and Delmas, H. (2008). Ultrasound in gas-liquid systems: effects on solubility and mass transfer. *Ultrason. Sonochem.*, **15**, (6) 965-972.
- Leadbeater, T. W., Parker, D. J. and Gargiuli, J. (2012). Positron imaging systems for studying particulate, granular and multiphase flows. *Particuology*, **10**, (2) 146-153.
- Lee, C. K. Y., Holmes, A. B., Ley, S. V., McConvey, I. F., Al-Duri, B., Leeke, G. A., Santos, R. C. D. and Seville, J. P. K. (2005). Efficient batch and continuous flow Suzuki cross-coupling reactions under mild conditions, catalysed by polyurea-encapsulated palladium(II) acetate and tetra-*n*-butylammonium salts. *Chem. Commun.*, (16) 2175-2177.
- Lee, C. T., Psathas, P. A., Johnston, K. P., deGrazia, J. and Randolph, T. W. (1999). Water-in-carbon dioxide emulsions: formation and stability. *Langmuir*, **15**, (20) 6781-6791.
- Lee, J.-K., Fuchter, M. J., Williamson, R. M., Leeke, G. A., Bush, E. J., McConvey, I. F., Saubern, S., Ryan, J. H. and Holmes, A. B. (2008). Diaryl ether synthesis in supercritical carbon dioxide in batch and continuous flow modes. *Chem. Commun.*, (39) 4780-4782.
- Leeke, G. A. (2000). The influence of water on the phase behaviour and extraction of organic compounds using carbon dioxide as solvent. PhD Thesis, University of Birmingham.

- Leeke, G. A., Santos, R. C., Seville, J., Al-Duri, B., Lee, C. K. Y. and Holmes, A. B. (2004). Solubilities of *p*-tolylboronic acid, bromobenzene, and 4-phenyltoluene in carbon dioxide at elevated pressures. *J. Chem. Eng. Data*, **49**, (1) 48-52.
- Leeke, G. A., Santos, R. C. D., Al-Duri, B., Seville, J. P. K., Smith, C. J., Lee, C. K. Y., Holmes, A. B. and McConvey, I. F. (2007). Continuous-flow Suzuki-Miyaura reaction in supercritical carbon dioxide. *Org. Process Res. Dev.*, **11**, (1) 144-148.
- Leitner, W. and Jessop, P. G. (1999). Chemical synthesis in supercritical fluids, New York: Wiley-VCH.
- Lenderink, H. J. W., Vanderlinden, M. and Dewit, J. H. W. (1993). Corrosion of aluminium in acidic and neutral solutions. *Electrochim. Acta*, **38**, (14) 1989-1992.
- Leong, T., Collis, J., Manasseh, R., Ooi, A., Novell, A., Bouakaz, A., Ashokkumar, M. and Kentish, S. (2011). The role of surfactant headgroup, chain length, and cavitation microstreaming on the growth of bubbles by rectified diffusion. *J. Phys. Chem. C*, **115**, (49) 24310-24316.
- Levan, M. D. and Newman, J. (1976). Effect of surfactant on terminal and interfacial velocities of a bubble or drop. *AIChE J.*, **22**, (4) 695-701.
- Lewis, W. K. and Whitman, W. G. (1924). Principles of gas absorption. *Ind. Eng. Chem.*, **16**, 1215-1220.
- Li, C. J. (1996). Aqueous Barbier-Grignard type reaction: scope, mechanism, and synthetic applications. *Tetrahedron*, **52**, (16) 5643-5668.
- Li, C. J. (2005). Organic reactions in aqueous media with a focus on carbon-carbon bond formations: a decade update. *Chem. Rev.*, **105**, (8) 3095-3165.
- Li, C. J. and Zhang, W. C. (1998). Unexpected Barbier-Grignard allylation of aldehydes with magnesium in water. *J. Am. Chem. Soc.*, **120**, (35) 9102-9103.
- Li, G. L. and Zhao, G. (2005). Efficient allylation of aldehydes promoted by carboxylic acids. *J. Org. Chem.*, **70**, (11) 4272-4278.
- Licence, P., Ke, J., Sokolova, M., Ross, S. K. and Poliakoff, M. (2003). Chemical reactions in supercritical carbon dioxide: from laboratory to commercial plant. *Green Chem.*, **5**, (2) 99-104.
- Lindley, J. (1992). Sonochemical effects on syntheses involving solid and supported catalysts. *Ultrasonics*, **30**, (3) 163-167.
- Linek, V., Moucha, T. and Sinkule, J. (1996). Gas-liquid mass transfer in vessels stirred with multiple impellers 1. Gas-liquid mass transfer characteristics in individual stages. *Chem. Eng. Sci.*, **51**, (12) 3203-3212.
- Liszi, J., Felinger, A. and Kristof, E. H. (1988). Static relative permittivity of electrolyte solutions. *Electrochim. Acta*, **33**, (9) 1191-1194.
- Liu, S., Wang, Y., Jiang, J. and Jin, Z. (2009). The selective reduction of nitroarenes to *N*-arylhydroxylamines using Zn in a CO₂/H₂O system. *Green Chem.*, **11**, (9) 1397-1400.
- Loh, T. P. and Xu, J. (1999). Trifluoromethane sulphonic acid: a Brønsted acid catalyst for the addition of allyltributylstannanes to carbonyl compounds in water. *Tetrahedron Letters*, **40**, (12) 2431-2434.

- Lu, G.-P., Cai, C. and Lipshutz, B. H. (2013). Stille couplings in water at room temperature. *Green Chem.*, **15**, (1) 105-109.
- Luche, J. L. (1994). Effect of ultrasound on heterogeneous systems. *Ultrason. Sonochem.*, **1**, (2) S111-S118.
- Luche, J. L. and Damiano, J. C. (1980). Ultrasounds in organic synthesis 1. Effect on the formation of lithium organometallic reagents. *J. Am. Chem. Soc.*, **102**, (27) 7926-7927.
- Luche, J. L., Einhorn, C., Einhorn, J. and Sinisterragago, J. V. (1990). Organic sonochemistry - a new interpretation and its consequences. *Tetrahedron Letters*, **31**, (29) 4125-4128.
- Macnaughton, S. J. and Foster, N. R. (1994). Solubility of DDT and 2,4-D in supercritical carbon-dioxide and supercritical carbon-dioxide saturated with water. *Ind. Eng. Chem. Res.*, **33**, (11) 2757-2763.
- Mandai, T., Nokami, J., Yano, T., Yoshinaga, Y. and Otera, J. (1984). Facile one-pot synthesis of bromo homoallyl alcohols and 1,3-keto acetates via allyl tin intermediates. *J. Org. Chem.*, **49**, (1) 172-174.
- Mandroyan, A., Doche, M. L., Hihn, J. Y., Viennet, R., Bailly, Y. and Simonin, L. (2009). Modification of the ultrasound induced activity by the presence of an electrode in a sono-reactor working at two low frequencies (20 and 40 kHz). Part II: mapping flow velocities by particle image velocimetry (PIV). *Ultrason. Sonochem.*, **16**, (1) 97-104.
- Mandzy, N., Grulke, E. and Druffel, T. (2005). Breakage of TiO₂ agglomerates in electrostatically stabilized aqueous dispersions. *Powder Technol.*, **160**, (2) 121-126.
- Margulis, M. A. (1992). Fundamental aspects of sonochemistry. *Ultrasonics*, **30**, (3) 152-155.
- Marre, S., Roig, Y. and Aymonier, C. (2012). Supercritical microfluidics: opportunities in flow-through chemistry and materials science. *J. Supercrit. Fluid*, **66**, 251-264.
- Marton, D., Stivanello, D. and Tagliavini, G. (1996). Stereochemical study of the allylation of aldehydes with allyl halides in cosolvent/water(salt)/Zn and in cosolvent/water(salt)/Zn/haloorganotin media. *J. Org. Chem.*, **61**, (8) 2731-2737.
- Mason, T. J. (1991). Practical sonochemistry: user's guide to applications in chemistry and chemical engineering, Chichester: *Ellis Horwood*.
- Mason, T. J. and Lorimer, J. P. (2002). Applied sonochemistry: the uses of power ultrasound in chemistry and processing, Weinheim: *Wiley-VCH*.
- Mason, T. J., Lorimer, J. P., Bates, D. M. and Zhao, Y. (1994). Dosimetry in sonochemistry - the use of aqueous terephthalate ion as a fluorescence monitor. *Ultrason. Sonochem.*, **1**, (2) S91-S95.
- Matsuyama, K. and Mishima, K. (2010). Particle coating of talc with TiO₂ nanoparticles using ultrasonic irradiation in liquid CO₂. *Ind. Eng. Chem. Res.*, **49**, (3) 1289-1296.
- Matsuyama, K., Mishima, K., Kato, T. and Ohara, K. (2011). Formation of porous glass via core/shell-structured poly(methyl methacrylate)/powder glass prepared by ultrasonic irradiation in liquid CO₂. *J. Supercrit. Fluid*, **57**, (2) 198-206.
- McClements, D. J. (1999). Food emulsions: principles, practices, and techniques, Boca Raton: *CRC Press*.

- McClements, D. J. (2011). Edible nanoemulsions: fabrication, properties, and functional performance. *Soft Matter*, **7**, (6) 2297-2316.
- McClements, D. J. (2012). Nanoemulsions versus microemulsions: terminology, differences, and similarities. *Soft Matter*, **8**, (6) 1719-1729.
- McClements, D. J. and Povey, M. J. W. (1989). Scattering of ultrasound by emulsions. *J. Phys. D Appl. Phys.*, **22**, (1) 38-47.
- McHugh, M. A. and Krukonis, V. J. (1994). Supercritical fluid extraction: principles and practice, London: *Butterworth-Heinemann*.
- Mei, H., Mei, B. W. and Yen, T. F. (2003). A new method for obtaining ultra-low sulfur diesel fuel via ultrasound assisted oxidative desulfurization. *Fuel*, **82**, (4) 405-414.
- Mezheritsky, A. V. (2004). Elastic, dielectric, and piezoelectric losses in piezoceramics: how it works all together. *IEEE T. Ultrason. Ferr.*, **51**, (6) 695-707.
- Monk, D. J., Soane, D. S. and Howe, R. T. (1993). A review of the chemical-reaction mechanism and kinetics for hydrofluoric-acid etching of silicon dioxide for surface micromaching applications. *Thin Solid Films*, **232**, (1) 1-12.
- Morison, K. R. and Hutchinson, C. A. (2009). Limitations of the Weissler reaction as a model reaction for measuring the efficiency of hydrodynamic cavitation. *Ultrason. Sonochem.*, **16**, (1) 176-183.
- Mukhopadhyay, S., Rothenberg, G., Gitis, D. and Sasson, Y. (2000). On the mechanism of palladium-catalyzed coupling of haloaryls to biaryls in water with zinc. *Org. Lett.*, **2**, (2) 211-214.
- Murphy, E. R., Inoue, T., Sahoo, H. R., Zaborenko, N. and Jensen, K. F. (2007). Solder-based chip-to-tube and chip-to-chip packaging for microfluidic devices. *Lab Chip*, **7**, (10) 1309-1314.
- Nishikido, N., Shinozaki, M., Sugihara, G. and Tanaka, M. (1981). A study on the micelle formation of surfactants in aqueous-solutions under high-pressure by laser light-scattering technique 2. *J. Colloid Interf. Sci.*, **82**, (2) 352-361.
- Nishikido, N., Shinozaki, M., Sugihara, G., Tanaka, M. and Kaneshina, S. (1980). A study on the micelle formation of surfactants in aqueous-solutions under high-pressure by laser light-scattering technique 1. *J. Colloid Interf. Sci.*, **74**, (2) 474-482.
- Nokami, J., Otera, J., Sudo, T. and Okawara, R. (1983). Allylation of aldehydes and ketones in the presence of water by allylic bromides, metallic tin, and aluminum. *Organometallics*, **2**, (1) 191-193.
- Nomura, H., Koda, S., Yasuda, K. and Kojima, Y. (1996). Quantification of ultrasonic intensity based on the decomposition reaction of porphyrin. *Ultrason. Sonochem.*, **3**, (3) S153-S156.
- Noyori, R. (2005). Pursuing practical elegance in chemical synthesis. *Chem. Commun.*, (14) 1807-1811.
- O'Neill, M. L., Yates, M. Z., Harrison, K. L., Johnston, K. P., Canelas, D. A., Betts, D. E., DeSimone, J. M. and Wilkinson, S. P. (1997). Emulsion stabilization and flocculation in CO₂ 1. Turbidimetry and tensiometry. *Macromolecules*, **30**, (17) 5050-5059.

- Oakes, R. S., Heppenstall, T. J., Shezad, N., Clifford, A. A. and Rayner, C. M. (1999). Use of scandium tris(trifluoromethanesulfonate) as a Lewis acid catalyst in supercritical carbon dioxide: efficient Diels-Alder reactions and pressure dependent enhancement of endo : exo stereoselectivity. *Chem. Commun.*, (16) 1459-1460.
- Oda, Y., Matsuo, S. and Saito, K. (1992). An efficient synthesis of 3-chlorohomoallyl alcohols - zinc-promoted 2-chloroallylation of carbonyl-compounds with 2,3-dichloropropene in an aqueous solvent system. *Tetrahedron Letters*, **33**, (1) 97-100.
- Olson, I. A., Bacon, W. A., Sosa, Y. Y. B., Delaney, K. M., Forte, S. A., Guglielmo, M. A., Hill, A. N., Kiesow, K. H., Langenbacher, R. E., Xun, Y., Young, R. O. and Bowyer, W. J. (2011). Measurement of heterogeneous reaction rates: three strategies for controlling mass transport and their application to indium-mediated allylations. *J. Phys. Chem. A*, **115**, (40) 11001-11007.
- Ottino, J. M. (1989). The kinematics of mixing: stretching, chaos, and transport, Cambridge: *Cambridge University Press*.
- Painmanakul, P., Loubiere, K., Hebrard, G., Mietton-Peuchot, M. and Roustan, M. (2005). Effect of surfactants on liquid-side mass transfer coefficients. *Chem. Eng. Sci.*, **60**, (22) 6480-6491.
- Palombo, F., Sassi, P., Paolantoni, M., Morresi, A. and Cataliotti, R. S. (2006). Comparison of hydrogen bonding in 1-octanol and 2-octanol as probed by spectroscopic techniques. *J. Phys. Chem. B*, **110**, (36) 18017-18025.
- Pando, C., Renuncio, J. A. R., McFall, T. A., Izatt, R. M. and Christensen, J. J. (1983). The excess-enthalpies of (carbon-dioxide + decane) from 283.15 to 323.15-K at 7.58 MPa. *J. Chem. Thermodyn.*, **15**, (2) 173-180.
- Pappa, G. D., Perakis, C., Tsimpanogiannis, I. N. and Voutsas, E. C. (2009). Thermodynamic modeling of the vapor-liquid equilibrium of the CO₂/H₂O mixture. *Fluid Phase Equilib.*, **284**, (1) 56-63.
- Park, S. H., Yoon, H. K. and Lee, H. W. (2008). Metal-mediated diastereoselective allylation reaction of chiral α,β -epoxy aldehyde. Part 2. *B. Kor. Chem. Soc.*, **29**, (9) 1663-1664.
- Pasha, M. A. and Jayashankara, V. P. (2005). Reduction of aryl nitro compounds to azoarenes and/or arylamines by Al/NaOH in methanol under ultrasonic conditions. *Ultrason. Sonochem.*, **12**, (6) 433-435.
- Pashley, R. M. (1981). DLVO and hydration forces between mica surfaces in Li⁺, Na⁺, K⁺, and Cs⁺ electrolyte-solutions - a correlation of double-layer and hydration forces with surface cation-exchange properties. *J. Colloid Interf. Sci.*, **83**, (2) 531-546.
- Paulaitis, M. E. and Alexander, G. C. (1987). Reactions in supercritical fluids - a case-study of the thermodynamic solvent effects on a Diels-Alder reaction in supercritical carbon-dioxide. *Pure Appl. Chem.*, **59**, (1) 61-68.
- Pearce, K. N. and Kinsella, J. E. (1978). Emulsifying properties of proteins - evaluation of a turbidimetric technique. *J. Agr. Food Chem.*, **26**, (3) 716-723.
- Peres, C., Da Silva, D. R. G. and Barreiros, S. (2003). Water activity effects on geranyl acetate synthesis catalyzed by novozym in supercritical ethane and in supercritical carbon dioxide. *J. Agr. Food Chem.*, **51**, (7) 1884-1888.

- Petrier, C., Barbosa, J. C. D., Dupuy, C. and Luche, J. L. (1985a). Ultrasound in organic-synthesis 7. Preparation of organozinc reagents and their nickel-catalyzed reactions with α,β -unsaturated carbonyl-compounds. *J. Org. Chem.*, **50**, (26) 5761-5765.
- Petrier, C., Einhorn, J. and Luche, J. L. (1985b). Selective tin and zinc mediated allylations of carbonyl-compounds in aqueous-media. *Tetrahedron Letters*, **26**, (11) 1449-1452.
- Petrier, C. and Luche, J. L. (1985). Allylzinc reagent additions in aqueous-media. *J. Org. Chem.*, **50**, (6) 910-912.
- Petrier, C. and Francony, A. (1997). Ultrasonic waste-water treatment: incidence of ultrasonic frequency on the rate of phenol and carbon tetrachloride degradation. *Ultrason. Sonochem.*, **4**, (4) 295-300.
- Petsev, D. N. (2004). Emulsions: structure stability and interactions, Amsterdam: Elsevier.
- Pflieger, R., Brau, H.-P. and Nikitenko, S. I. (2010). Sonoluminescence from $\text{OH}(\text{C}^2\Sigma^+)$ and $\text{OH}(\text{A}^2\Sigma^+)$ radicals in water: evidence for plasma formation during multibubble cavitation. *Chem.-Eur. J.*, **16**, (39) 11801-11803.
- Poliakoff, M., Howdle, S. M. and Kazarian, S. G. (1995). Vibrational spectroscopy in supercritical fluids - from analysis and hydrogen-bonding to polymers and synthesis. *Angew. Chem.-Int. Edit. Engl.*, **34**, (12) 1275-1295.
- Poteshnova, M. V. and Zadymova, N. M. (2006). Normal micelles and oil-in-water microemulsions in a water-toluene-Tween 80 ternary system. *Colloid J.*, **68**, (2) 201-210.
- Price, G. J., Harris, N. K. and Stewart, A. J. (2010). Direct observation of cavitation fields at 23 and 515 kHz. *Ultrason. Sonochem.*, **17**, (1) 30-33.
- Price, G. J. and Smith, P. F. (1993). Ultrasonic degradation of polymer-solutions 2. The effect of temperature, ultrasound intensity and dissolved-gases on polystyrene in toluene. *Polymer*, **34**, (19) 4111-4117.
- Psathas, P., Sander, E., Lee, M. Y., Lim, K. T. and Johnston, K. (2002). Mapping the stability and curvature of emulsions of H_2O and supercritical CO_2 with interfacial tension measurements. *J. Disper. Sci. Technol.*, **23**, (1) 65-80.
- Psathas, P. A., da Rocha, S. R. P., Lee, C. T., Johnston, K. P., Lim, K. T. and Webber, S. (2000). Water-in-carbon dioxide emulsions with poly(dimethylsiloxane)-based block copolymer ionomers. *Ind. Eng. Chem. Res.*, **39**, (8) 2655-2664.
- Qian, J., Timko, M. T., Allen, A. J., Russell, C. J., Winnik, B., Buckley, B., Steinfeld, J. I. and Tester, J. W. (2004). Solvophobic acceleration of Diels-Alder reactions in supercritical carbon dioxide. *J. Am. Chem. Soc.*, **126**, (17) 5465-5474.
- Raber, E. C., Dudley, J. A., Salerno, M. and Urayama, P. (2006). Capillary-based, high-pressure chamber for fluorescence microscopy imaging. *Rev. Sci. Instrum.*, **77**, (9) 1-3.
- Rajagopal, R., Jarikote, D. V. and Srinivasan, K. V. (2002). Ultrasound promoted Suzuki cross-coupling reactions in ionic liquid at ambient conditions. *Chem. Commun.*, (6) 616-617.
- Randolph, T. W., Blanch, H. W. and Prausnitz, J. M. (1988). Enzyme-catalyzed oxidation of cholesterol in supercritical carbon-dioxide. *AIChE J.*, **34**, (8) 1354-1360.

- Ranu, B. C., Majee, A. and Das, A. R. (1995). Facile and efficient synthesis of homoallylic alcohols using allyl bromide and commercial zinc dust. *Tetrahedron Letters*, **36**, (27) 4885-4888.
- Rathke, J. W., Klingler, R. J. and Krause, T. R. (1991). Propylene hydroformylation in supercritical carbon-dioxide. *Organometallics*, **10**, (5) 1350-1355.
- Raveendran, P., Ikushima, Y. and Wallen, S. L. (2005). Polar attributes of supercritical carbon dioxide. *Accounts Chem. Res.*, **38**, (6) 478-485.
- Raveendran, P. and Wallen, S. L. (2003). Exploring CO₂-philicity: effects of stepwise fluorination. *J. Phys. Chem. B*, **107**, (6) 1473-1477.
- Raymond, D. R. and Zieminski, S. A. (1971). Mass transfer and drag coefficients of bubbles rising in dilute aqueous solutions. *AIChE J.*, **17**, (1) 57-65.
- Reamer, H. H. and Sage, B. H. (1965). Partial volumetric behavior in hydrocarbon systems: *n*-decane and carbon dioxide in liquid phase of *n*-decane-carbon dioxide system. *J. Chem. Eng. Data*, **10**, (1) 49-57.
- Reddy, M. B. M., Jayashankara, V. P. and Pasha, M. A. (2013). Aluminum-catalyzed efficient synthesis of anilides by the acylation of aryl amines under ultrasonic conditions. *Green Chem. Letters Rev.*, **6**, (1) 107-112.
- Refaey, S. A. M. (2005). Inhibition of steel pitting corrosion in HCl by some inorganic anions. *Appl. Surf. Sci.*, **240**, (1-4) 396-404.
- Riesz, P. and Kondo, T. (1992). Free-radical formation induced by ultrasound and its biological implications. *Free Radical Bio. Med.*, **13**, (3) 247-270.
- Rong, L., Kojima, Y., Koda, S. and Nomura, H. (2001). Simple quantification of ultrasonic intensity using aqueous solution of phenolphthalein. *Ultrason. Sonochem.*, **8**, (1) 11-15.
- Roosen, C., Ansorge-Schumacher, M., Mang, T., Leitner, W. and Greiner, L. (2007). Gaining pH-control in water/carbon dioxide biphasic systems. *Green Chem.*, **9**, (5) 455-458.
- Rooze, J., Rebrov, E. V., Schouten, J. C. and Keurentjes, J. T. F. (2013). Dissolved gas and ultrasonic cavitation - a review. *Ultrason. Sonochem.*, **20**, (1) 1-11.
- Roy, U. K. and Roy, S. (2010). Making and breaking of Sn-C and In-C bonds in situ: the cases of allyltins and allylindiums. *Chem. Rev.*, **110**, (4) 2472-2535.
- Saez, V., Frias-Ferrer, A., Iniesta, J., Gonzalez-Garcia, J., Aldaz, A. and Riera, E. (2005). Characterization of a 20 kHz sonoreactor. Part I: analysis of mechanical effects by classical and numerical methods. *Ultrason. Sonochem.*, **12**, (1-2) 59-65.
- Saito, S. (ed.) 1996. Science and technology of supercritical fluids, Tokyo: *Sankyo Business Co. Ltd.*
- Sanganwar, G. P. and Gupta, R. B. (2009). Nano-mixing of dipyridamole drug and excipient nanoparticles by sonication in liquid CO₂. *Powder Technol.*, **196**, (1) 36-49.
- Schneide, G., Alwani, Z., Heim, W., Horvath, E. and Franck, E. U. (1967). Phase equilibria and critical phenomena in binary mixtures (CO₂ with *n*-octane *n*-undecane *n*-tridecane and *n*-hexadecane up to 1500 bar). *Chem. Ing. tech.*, **39**, (11) 649-656.

- Schultes, M. (1998). Absorption of sulphur dioxide with sodium hydroxide solution in packed columns. *Chem. Eng. Technol.*, **21**, (2) 201-209.
- Seymour, J. D., Wallace, H. C. and Gupta, R. B. (1997). Sonochemical reactions at 640 kHz using an efficient reactor. Oxidation of potassium iodide. *Ultrason. Sonochem.*, **4**, (4) 289-293.
- Shchukin, D. G., Skorb, E., Belova, V. and Möhwald, H. (2011). Ultrasonic cavitation at solid surfaces. *Adv. Mater.*, **23**, (17) 1922-1934.
- Sheldon, R. A. (1997). Catalysis: the key to waste minimization. *J. Chem. Technol. Biotechnol.*, **68**, (4) 381-388.
- Shezad, N., Clifford, A. A. and Rayner, C. T. (2002). Pd-catalysed coupling reactions in supercritical carbon dioxide and under solventless conditions. *Green Chem.*, **4**, (1) 64-67.
- Sieder, G. and Maurer, G. (2004). Experimental investigation of the influence of the single salts sodium chloride and sodium acetate on the high-pressure phase equilibrium of the system carbon dioxide plus water plus acetic acid. *J. Chem. Eng. Data*, **49**, (5) 1303-1310.
- Smith, K., Lock, S., El-Hiti, G. A., Wada, M. and Miyoshi, N. (2004). A convenient procedure for bismuth-mediated Barbier-type allylation of aldehydes in water containing fluoride ions. *Org. Biomol. Chem.*, **2**, (6) 935-938.
- Smith, R. D., Frye, S. L., Yonker, C. R. and Gale, R. W. (1987). Solvent properties of supercritical Xe and SF₆. *J. Phys. Chem.*, **91**, (11) 3059-3062.
- Song, B. D. and Jencks, W. P. (1989). Mechanism of solvolysis of substituted benzoyl halides. *J. Am. Chem. Soc.*, **111**, (22) 8470-8479.
- Sparks, D., Hernandez, R. and Estevez, L. (2008). Evaluation of density-based models for the solubility of solids in supercritical carbon dioxide and formulation of a new model. *Chem. Eng. Sci.*, **63**, (17) 4292-4301.
- Springer, R. D., Wang, Z., Anderko, A., Wang, P. and Felmy, A. R. (2012). A thermodynamic model for predicting mineral reactivity in supercritical carbon dioxide: I. Phase behavior of carbon dioxide-water-chloride salt systems across the H₂O-rich to the CO₂-rich regions. *Chem. Geol.*, **322**, 151-171.
- Srivastava, P., Hahr, O., Buchholz, R. and Worden, R. M. (2000). Enhancement of mass transfer using colloidal liquid aphrons: measurement of mass transfer coefficients in liquid-liquid extraction. *Biotechnol. Bioeng.*, **70**, (5) 525-532.
- Su, Y., Chen, G., Zhao, Y. and Yuan, Q. (2009). Intensification of liquid-liquid two-phase mass transfer by gas agitation in a microchannel. *AIChE J.*, **55**, (8) 1948-1958.
- Sun, X.-W., Liu, M., Xu, M.-H. and Lin, G.-Q. (2008). Remarkable salt effect on In-mediated allylation of *N*-tert-butanefulfinyl imines in aqueous media: highly practical asymmetric synthesis of chiral homoallylic amines and isoindolinones. *Org. Lett.*, **10**, (6) 1259-1262.
- Suslick, K. S. (1990). Sonochemistry. *Science*, **247**, (4949) 1439-1445.
- Suslick, K. S. and Casadonte, D. J. (1987). Heterogeneous sonocatalysis with nickel powder. *J. Am. Chem. Soc.*, **109**, (11) 3459-3461.

- Suslick, K. S., Doktycz, S. J. and Flint, E. B. (1990). On the origin of sonoluminescence and sonochemistry. *Ultrasonics*, **28**, (5) 280-290.
- Suslick, K. S. and Flannigan, D. J. (2008). Inside a collapsing bubble: sonoluminescence and the conditions during cavitation. *Annu. Rev. Phys. Chem.*, **59**, 659-683.
- Suslick, K. S., Mdleleni, M. M. and Ries, J. T. (1997). Chemistry induced by hydrodynamic cavitation. *J. Am. Chem. Soc.*, **119**, (39) 9303-9304.
- Sutkar, V. S. and Gogate, P. R. (2009). Design aspects of sonochemical reactors: techniques for understanding cavitation activity distribution and effect of operating parameters. *Chem. Eng. J.*, **155**, (1-2) 26-36.
- Tabata, K., Ito, W., Kojima, T., Kawabata, S. and Misaki, A. (1981). Ultrasonic degradation of Schizophyllan, an anti-tumor polysaccharide produced by *Schizophyllum-commune* fries. *Carbohydr. Res.*, **89**, (1) 121-135.
- Tadros, T., Izquierdo, R., Esquena, J. and Solans, C. (2004). Formation and stability of nano-emulsions. *Adv. Colloid Interfac.*, **108**, 303-318.
- Tai, C. Y., You, G. S. and Chen, S. L. (2000). Kinetics study on supercritical fluid extraction of zinc(II) ion from aqueous solutions. *J. Supercrit. Fluid*, **18**, (3) 201-212.
- Tassaing, T., Oparin, R., Danten, Y. and Besnard, A. (2005). Water-CO₂ interaction in supercritical CO₂ as studied by infrared spectroscopy and vibrational frequency shift calculations. *J. Supercrit. Fluid*, **33**, (1) 85-92.
- Taylor, P. (1998). Ostwald ripening in emulsions. *Adv. Colloid Interfac.*, **75**, (2) 107-163.
- Tehrani-Bagha, A. R. and Holmberg, K. (2013). Solubilization of hydrophobic dyes in surfactant solutions. *Materials*, **6**, (2) 580-608.
- Tennyson, A. G., Wiggins, K. M. and Bielawski, C. W. (2010). Mechanical activation of catalysts for C-C bond forming and anionic polymerization reactions from a single macromolecular reagent. *J. Am. Chem. Soc.*, **132**, (46) 16631-16636.
- Thanthiriwatte, K. S., Duke, J. R., Jackson, V. E., Felmy, A. R. and Dixon, D. A. (2012). High-level *ab initio* predictions of the energetics of mCO₂---(H₂O)_n (n=1-3, m=1-12) clusters. *J. Phys. Chem. A*, **116**, (39) 9718-9729.
- Thoman, C. J. (1999). The versatility of Polysorbate 80 (Tween 80) as an ionophore. *J. Pharm. Sci.*, **88**, (2) 258-260.
- Thoman, C. J., Habeeb, T. D., Huhn, M., Korpusik, M. and Sligh, D. F. (1989). Use of Polysorbate-80 (Tween-80) as a phase-transfer catalyst. *J. Org. Chem.*, **54**, (18) 4476-4478.
- Thompson, L. H. and Doraiswamy, L. K. (1999). Sonochemistry: science and engineering. *Ind. Eng. Chem. Res.*, **38**, (4) 1215-1249.
- Timko, M. T., Diffendal, J. M., Tester, J. W., Smith, K. A., Peters, W. A., Danheiser, R. L. and Steinfeld, J. I. (2003). Ultrasonic emulsification of liquid, near-critical carbon dioxide-water biphasic mixtures for acceleration of a hydrolysis reaction. *J. Phys. Chem. A*, **107**, (29) 5503-5507.

- Timko, M. T. (2004). Acoustic emulsions of liquid, near-critical carbon dioxide and water : application to synthetic chemistry through reaction engineering. PhD Thesis, Massachusetts Institute of Technology.
- Timko, M. T., Nicholson, B. F., Steinfeld, J. I., Smith, K. A. and Tester, J. W. (2004). Partition coefficients of organic solutes between supercritical carbon dioxide and water: experimental measurements and empirical correlations. *J. Chem. Eng. Data*, **49**, (4) 768-778.
- Timko, M. T., Allen, A. J., Danheiser, R. L., Steinfeld, J. I., Smith, K. A. and Tester, J. W. (2006a). Improved conversion and selectivity of a Diels-Alder cycloaddition by use of emulsions of carbon dioxide and water. *Ind. Eng. Chem. Res.*, **45**, (5) 1594-1603.
- Timko, M. T., Smith, K. A., Danheiser, R. L., Steinfeld, J. I. and Tester, J. W. (2006b). Reaction rates in ultrasonic emulsions of dense carbon dioxide and water. *AIChE J.*, **52**, (3) 1127-1141.
- Toor, H. L. and Marchello, J. M. (1958). Film-penetration model for mass and heat transfer. *AIChE J.*, **4**, (1) 97-101.
- Torino, E., Reverchon, E. and Johnston, K. P. (2010). Carbon dioxide/water, water/carbon dioxide emulsions and double emulsions stabilized with a nonionic biocompatible surfactant. *J. Colloid Interf. Sci.*, **348**, (2) 469-478.
- Torr, G. R. (1984). The acoustic radiation force. *Am. J. Phys.*, **52**, (5) 402-408.
- Trachsel, F. (2008). Design of a microreactor for reactions using supercritical fluids as the reaction solvent. PhD Thesis, Swiss Federal Institute of Technology.
- Trachsel, F., Hutter, C. and von Rohr, P. R. (2008). Transparent silicon/glass microreactor for high-pressure and high-temperature reactions. *Chem. Eng. J.*, **135**, S309-S316.
- Trachsel, F., Tidona, B., Desportes, S. and von Rohr, P. R. (2009). Solid catalyzed hydrogenation in a Si/glass microreactor using supercritical CO₂ as the reaction solvent. *J. Supercrit. Fluid*, **48**, (2) 146-153.
- Trujillo, F. J. and Knoerzer, K. (2011). A computational modeling approach of the jet-like acoustic streaming and heat generation induced by low frequency high power ultrasonic horn reactors. *Ultrason. Sonochem.*, **18**, (6) 1263-1273.
- Tucker, J. L. (2006). Green chemistry, a pharmaceutical perspective. *Org. Process Res. Dev.*, **10**, (2) 315-319.
- Tucker, S. C. (1999). Solvent density inhomogeneities in supercritical fluids. *Chem. Rev.*, **99**, (2) 391-418.
- Tuziuti, T., Yasui, K., Lee, J., Kozuka, T., Towata, A. and Iida, Y. (2008). Mechanism of enhancement of sonochemical-reaction efficiency by pulsed ultrasound. *J. Phys. Chem. A*, **112**, (22) 4875-4878.
- Tzanakis, I., Hadfield, M. and Henshaw, I. (2011). Observations of acoustically generated cavitation bubbles within typical fluids applied to a scroll expander lubrication system. *Exp. Therm. Fluid Sci.*, **35**, (8) 1544-1554.
- Van Gheem, E., Vereecken, J. and Le Pen, C. (2002). Influence of different anions on the behaviour of aluminium in aqueous solutions. *J. Appl. Electrochem.*, **32**, (11) 1193-1200.

- Van Iersel, M. M., Cornel, J., Benes, N. E. and Keurentjes, J. T. F. (2007). Inhibition of nonlinear acoustic cavitation dynamics in liquid CO₂. *J. Chem. Phys.*, **126**, (6) 064508.
- Van Iersel, M. M., Mettin, R., Benes, N. E., Schwarzer, D. and Keurentjes, J. T. F. (2010). Sound-driven fluid dynamics in pressurized carbon dioxide. *J. Chem. Phys.*, **133**, (4) 044304.
- Verdan, S., Burato, G., Comet, M., Reinert, L. and Fuzellier, H. (2003). Structural changes of metallic surfaces induced by ultrasound. *Ultrason. Sonochem.*, **10**, (4-5) 291-295.
- Verma, R. P. and Sharma, M. M. (1975). Mass-transfer in packed liquid-liquid-extraction columns. *Chem. Eng. Sci.*, **30**, (3) 279-292.
- Verwey, E. and Overbeek, J. (1948). Theory of the stability of lyophobic colloids, New York: Elsevier.
- Vyas, B. and Preece, C. M. (1977). Cavitation erosion of face-centered cubic metals. *Metall. Trans. A*, **8**, (6) 915-923.
- Wada, M. and Akiba, K. (1985). Metallic bismuth mediated allylation of aldehydes to homoallylic alcohols. *Tetrahedron Letters*, **26**, (35) 4211-4212.
- Wagner, K.-D., Dahmen, N. and Griesheimer, P. (2003). Salt effects on the partition coefficients of phenol in two-phase mixtures of water and carbon dioxide at pressures from (8 to 30) MPa at a temperature of 313 K. *J. Chem. Thermodyn.*, **35**, (4) 677-687.
- Wagner, K. D., Brudi, K., Dahmen, N. and Schmieder, H. (1999). Partition coefficients of aromatic organic substances in two-phase mixtures of water and carbon dioxide at pressures from 8 to 30 MPa and at temperatures of 313 to 333 K. Part II. *J. Supercrit. Fluid*, **15**, (2) 109-116.
- Walther, D. and Maurer, G. (1992). High-pressure vapor-liquid-equilibria in binary-mixtures of carbon-dioxide and benzaldehyde, bromobenzene, chlorobenzene, 1,2-dichlorobenzene and 2-chloro-1-methylbenzene at temperatures between 313-K and 393-K and pressures up to 22-MPa. *Ber. Bunsen Phys. Chem.*, **96**, (8) 981-988.
- Wang, Z. Y., Zha, Z. G. and Zhou, C. L. (2002). Application of tin and nanometer tin in allylation of carbonyl compounds in tap water. *Org. Lett.*, **4**, (10) 1683-1685.
- Watahiki, T. and Oriyama, T. (2002). Iron(III) chloride-catalyzed effective allylation reactions of aldehydes with allyltrimethylsilane. *Tetrahedron Letters*, **43**, (49) 8959-8962.
- Wilhelm, A.-M., Laugier, F., Kidak, R., Ratsimba, B. and Delmas, H. (2010). Ultrasound to enhance a liquid-liquid reaction. *J. Chem. Eng. Jpn.*, **43**, (9) 751-756.
- Williams, L. L., Rubin, J. B. and Edwards, H. W. (2004). Calculation of Hansen solubility parameter values for a range of pressure and temperature conditions, including the supercritical fluid region. *Ind. Eng. Chem. Res.*, **43**, (16) 4967-4972.
- Worsley, D. and Mills, A. (1996). The effects of power ultrasound on the oxidation of water by Ce-IV ions mediated by thermally activated ruthenium dioxide hydrate. *Ultrason. Sonochem.*, **3**, (2) S119-S123.
- Wu, Z. and Ondruschka, B. (2010). Ultrasound-assisted oxidative desulfurization of liquid fuels and its industrial application. *Ultrason. Sonochem.*, **17**, (6) 1027-1032.

- Xiao, J. L., Nefkens, S. C. A., Jessop, P. G., Ikariya, T. and Noyori, R. (1996). Asymmetric hydrogenation of α,β -unsaturated carboxylic acids in supercritical carbon dioxide. *Tetrahedron Letters*, **37**, (16) 2813-2816.
- Yamamoto, H. 2013. Hansen Solubility Parameters [Online]. Available: <http://pirika.com/NewHP/PirikaE/Endocrine.html> [Accessed 20/11/2013].
- Yamamoto, Y. and Asao, N. (1993). Selective reactions using allylic metals. *Chem. Rev.*, **93**, (6) 2207-2293.
- Yanagida, H. (2008). The effect of dissolved gas concentration in the initial growth stage of multi cavitation bubbles - differences between vacuum degassing and ultrasound degassing. *Ultrason. Sonochem.*, **15**, (4) 492-496.
- Yanagisawa, A., Inoue, H., Morodome, M. and Yamamoto, H. (1993). Highly chemoselective allylation of carbonyl compounds with tetraallyltin in acidic aqueous-media. *J. Am. Chem. Soc.*, **115**, (22) 10356-10357.
- Yanagisawa, A., Morodome, M., Nakashima, H. and Yamamoto, H. (1997). Allylation of aldehydes with allyltin compounds in acidic aqueous media - a catalytic version. *Synlett*, (11) 1309-1311.
- Yates, M. Z., O'Neill, M. L., Johnston, K. P., Webber, S., Canelas, D. A., Betts, D. E. and DeSimone, J. M. (1997). Emulsion stabilization and flocculation in CO₂ 2. Dynamic light scattering. *Macromolecules*, **30**, (17) 5060-5067.
- Yong Nam, A., Gupta, A., Chauhan, A. and Kopelevich, D. I. (2011). Molecular transport through surfactant-covered oil-water interfaces: role of physical properties of solutes and surfactants in creating energy barriers for transport. *Langmuir*, **27**, (6) 2420-2436.
- Yoshida, J. and Itami, K. (2002). Tag strategy for separation and recovery. *Chem. Rev.*, **102**, (10) 3693-3716.
- Zasetsky, A. Y. and Svishchev, I. M. (2001). Dielectric response of concentrated NaCl aqueous solutions: molecular dynamics simulations. *J. Chem. Phys.*, **115**, (3) 1448-1454.
- Zha, Z. G., Xie, Z., Zhou, C. L., Chang, M. X. and Wang, Z. Y. (2003). High regio- and stereoselective Barbier reaction of carbonyl compounds mediated by NaBF₄/Zn (Sn) in water. *New J. Chem.*, **27**, (9) 1297-1300.
- Zhang, J., Yang, F., Ren, G., Mak, T. C. W., Song, M. and Wu, Y. (2008). Ultrasonic irradiation accelerated cyclopalladated ferrocenylimines catalyzed Suzuki reaction in neat water. *Ultrason. Sonochem.*, **15**, (2) 115-118.
- Zhang, R., Liu, J., He, J., Han, B. X., Wu, W. Z., Jiang, T., Liu, Z. M. and Du, J. M. (2003). Organic reactions and nanoparticle preparation in CO₂-induced water/P104/p-xylene microemulsions. *Chem.-Eur. J.*, **9**, (10) 2167-2172.
- Zhou, C. L., Zhou, Y. Q., Jiang, J. Y., Xie, Z., Wang, Z. Y., Zhang, J. H., Wu, J. H. and Yin, H. (2004). Organometallic reactions in aqueous media: the allylations of carbonyl compounds mediated in Zn/CdSO₄ and Zn/SnCl₂ bimetal systems. *Tetrahedron Letters*, **45**, (28) 5537-5540.

APPENDIX

A1.1 UV Absorbance of Sonochemically-Generated Iodine

Evaluation of sonochemical activity was undertaken in the 1 dm³ reactor. To this end, the effect of type of pressurizing fluid and pressure were investigated for a commonly employed test of sonolytic reactions, the free radical-mediated generation of iodine from potassium iodide. Table A1–1 presents the data for iodine generation by ultrasound in N₂/H₂O mixtures at 30 °C/1 bar.

Time (min)	Abs				I ₂ (μM)				
	1	2	3	Average Abs	1	2	3	Average (μM)	Error %
15	0.024	0.027	0.024	0.025	6.03681	6.220859	6.03681	6.09816	2.012072
30	0.067	0.065	0.063	0.065	8.674847	8.552147	8.429448	8.552147	1.43472
60	0.134	0.133	0.132	0.133	12.78528	12.72393	12.66258	12.72393	0.48216
90	0.21	0.2	0.19	0.2	17.44785	16.83436	16.22086	16.83436	3.644315
120	0.262	0.263	0.261	0.262	20.63804	20.69939	20.57669	20.63804	0.297265

Table A1–1 Sonolytic iodine formation^(a)

A1.2 Stability of Ultrasound-Generated CO₂/H₂O Emulsions

The Integrated Density values calculated by ImageJ following analysis of time-lapse recordings of CO₂/H₂O dispersions are shown in Table A1–2.

Time (min)	I _D	I _D /I _D MAX* %
3	15513894	27
5	23833828	41
7	34674128	60
12	45781636	79
15	50178808	87
20	51771760	89
30	57429272	99

*I_DMAX = 57881016 = maximum integrated density calculated in the absence of turbidity. I_D = integrated density calculated by ImageJ

Table A1–2 Integrated density values calculated by ImageJ for stability of CO₂/H₂O emulsions

^(a) Abs = UV absorbance at 354 nm; no iodine (I₂) was detected at 30 °C/70 bar N₂.
UV calibration for I₂: y = 0.0163x – 0.0744.
12 wt.% initial KI solution (0.8 L of water).

A1.3 Volume fractions of Emulsions Generated by Ultrasound

A1.3.1 Water Collection Experiments

The water collection experiments were carried out in order to establish the amount of water present in CO₂/H₂O dispersions generated by ultrasound, as described in Section 3.2.3.4.1. The 20 mL capped glass vial was used for weighing the water collected. Table A1–3.1 shows water collection experiments on dispersions originating from the top section of the ultrasound vessel.

System	Experiment	Vial (g)	Vial + Sample (g)	Sample (g)
CO ₂ /H ₂ O	1	26.671	26.842	0.171
	2	26.715	26.876	0.161
	3	26.665	26.824	0.159
	4	26.684	26.852	0.168
	5	26.664	26.822	0.158
Mean				0.1634
Error %				4.6
V _{wc} ϕ %				6.5
System	Experiment	Vial (g)	Vial + Sample (g)	Sample (g)
CO ₂ /H ₂ O/Tween 80	1	26.671	28.351	1.68
	2	26.675	28.165	1.49
	3	26.697	28.217	1.52
Mean				1.56
Error %				7.4
V _{wc} ϕ %				62.4

Table A1–3 Water volume fractions (V_wϕ) in dispersions generated by ultrasound^(b)

^(b) Conditions: 30 °C/80 bar, ultrasound = 25% pulse rate, 70% amp, CO₂/H₂O 40 v/v%; sampling section L1 (2.5 mL) was used for sample collection.

A1.3.1.1 Estimation of Evaporative Water Loss by Sampling

The expanded CO₂ stream leaving the sampling section will act as a carrier for a small quantity of water vapour, which will be lost to the atmosphere. Estimation of the loss due to flushing gas over the sample may be evaluated by Eq. A1.3.1, as described by Leeke^(c):

$$Loss (g) = \frac{Vol\ Gas\ Passed_{STP} (dm^3)}{Molar\ Vol\ of\ Gas_{STP} (dm^3\ mol^{-1})} \times \frac{P_{20^\circ C}^*}{P_{atm}} \times M_s (g\ mol^{-1}) \quad (A1.3.1)$$

STP = 0 °C/100 kPa

For a typical experiment at 30 °C/80 bar the mols of CO₂ in the sample tube may be quantified as
 $= 2.5\ mL \times 0.7\ g\ mL^{-1} / 44\ g\ mol^{-1} = 0.039\ mols$

Molar Vol of CO₂ at STP (from NIST) = 22.56 dm³ mol⁻¹

P^* = vapour pressure of water at 20 °C = 2.3 kPa

P_{atm} = atmospheric pressure = 101.325 kPa

M_s = molecular mass of water = 18 g mol⁻¹

Therefore, by passing 0.87 dm³ of gas by expansion of CO₂ during sample collection, the theoretic loss of water would be 1.6×10^{-2} g. This would constitute approximately a maximum error of 10%.

^(c)From Leeke [2000].

A1.3.2 CO₂ Volume Fraction Experiments

The volume fractions of CO₂ droplets dispersed in water was assessed for samples collected from the lower section of the ultrasound vessel via sample line L2 following sonication (Table A1–3.2). The tracer technique was employed as described in Section 3.2.3.4.3. Octane (6.1 mmol) was injected as the CO₂-soluble tracer and GC peak areas from collected samples were converted to CO₂ volume fractions according to Eq. A.1.3.2:

$$\text{Volume fraction (\%)} = \frac{C_c}{C_{c0}} \times \frac{V_{dil}}{V_s} \times 100 \quad (\text{A1.3.2})$$

C_c = octane concentration in dispersion

C_{c0} = initial octane concentration in CO₂ phase (octane mols /CO₂ phase volume)

V_{dil}/V_s = dilution factor (1:6 v/v)

GC Settings

Sample injection = 0.5 µL

Injector split ratio = 30

Injector T = 300 °C

FID T = 300 °C

FID gain= 100 × (maximum sensitivity)

Gas pressure = 100 kPa

Carrier gas = (He Air mixture)

Oven program: heat isothermally at 120 °C for 5 min, stop. Octane retention time = 2.2 min.

GC Calibration for Octane

$$y = 9769.4 \times 10^4 x + 2750$$

The effect of the position of the biphasic line with respect to the ultrasound probe was also assessed. No octane was detected in the water phase after 3 hours in the absence of ultrasound.

SD (cm)	H ₂ O Phase (L)	C _D Peak Area	Diluted C _D (mmol L ⁻¹)	Undiluted C _D (mmol L ⁻¹)	C _C (mmol L ⁻¹)	V _{CΦ} % ^(d)	Mean V _{CΦ} % ^(e)	Error %
-1.2	0.8	5166	0.025	0.148	30.77	0.48	0.98	63
0.2	0.7	8884	0.063	0.377	20.51	1.84	2.81	74
0.9	0.65	18517	0.161	0.968	17.58	5.51	4.3	35
1.1	0.63	19355	0.170	1.020	16.63	6.13	4.96	33
1.6	0.6	22727	0.204	1.227	15.39	7.97	6.22	35
2	0.58	27768	0.256	1.536	14.65	9.99	6.75	48
2 ^(f)	0.58	82354	0.815	4.888	14.65	33.36	35.17	5

Table A1–4 CO₂ volume fractions (V_{CΦ}) from emulsions generated by ultrasound^(g)

^(d) representative values of V_{CΦ}

^(e) mean values of V_{CΦ} with respective errors

^(f) Experiment carried out with 1 wt.% Tween 80.

^(g) SD = standoff distance of biphasic line from ultrasound probe; V_{CΦ} = volume fraction of CO₂ droplets in water; the number of experimental points for each standoff distance was between 3 and 7. Conditions: 30 °C/80 bar, 25% pulse rate, 70% amplitude, CO₂/H₂O 40 v/v%.

A2.1 Prediction of Benzaldehyde Solubility in CO₂: The Chrastil Method

The solubility of benzaldehyde in CO₂ at 30 °C (303 K)/80 bar was extrapolated from existing data reported by Walther and Maurer [1992] using the Chrastil method as described in Section 3.3.1 and shown in Eq. A2.1:

$$\ln S = k \ln(\rho) + \frac{a}{T} + b \quad (\text{A2.1})$$

Table A2–1 compiles the data used for evaluation of the solubility of benzaldehyde relating to the results in Section 5.2.

Temp. (K)	Pressure (bar)	Solubility <i>S</i> (g L ⁻¹) ^(h)	<i>lnS</i>	<i>ln(ρ)</i> ⁽ⁱ⁾	<i>k</i> * <i>ln(ρ)</i>	<i>lnS</i> – (<i>k</i> * <i>lnρ</i>)	<i>lnS</i> –(<i>k</i> * <i>lnρ</i>) Isothermal Average
313	66	0.298	-1.211	5.173	16.857	-18.069	-18.096
	71	0.443	-0.814	5.318	17.333	-18.147	
	76.1	0.810	-0.210	5.481	17.861	-18.072	
333	91.9	1.300	0.262	5.501	17.929	-17.666	-17.458
	102.1	2.923	1.073	5.714	18.621	-17.548	
	112.2	8.576	2.149	5.925	19.310	-17.161	
353	81.8	0.599	-0.513	5.109	16.650	-17.163	-17.052
	102.1	1.490	0.399	5.433	17.706	-17.307	
	122.5	5.711	1.742	5.728	18.669	-16.927	
	142.6	14.481	2.673	5.979	19.485	-16.812	
373	102.1	1.681	0.520	5.266	17.162	-16.642	-16.378
	122.5	4.384	1.478	5.517	17.981	-16.503	
	142.6	10.359	2.338	5.733	18.685	-16.347	
	162.8	18.005	2.891	5.917	19.284	-16.394	
	183	44.130	3.787	6.072	19.789	-16.002	
393	122.4	3.695	1.307	5.374	17.515	-16.208	-15.916
	141.2	7.636	2.033	5.559	18.116	-16.083	
	162.8	15.701	2.754	5.737	18.695	-15.942	
	183	26.904	3.292	5.889	19.192	-15.900	
	203.2	45.672	3.821	6.014	19.599	-15.777	
	223.4	76.865	4.342	6.115	19.930	-15.587	

Table A2–1 Calculated Chrastil parameters for the prediction of the solubility of benzaldehyde in CO₂ using *k* = 3.259

^(h)From Walther and Maurer [1992].

⁽ⁱ⁾Benzaldehyde density (g L⁻¹) at the specified temperature and pressure.

A2.2 Experimental Evaluation of Benzaldehyde Concentration in CO₂

GC Settings for determination of benzaldehyde and decane concentrations in CO₂

Sample injection = 0.5 µL

Injector split ratio = 30

Injector T = 300 °C

FID T = 300 °C

FID gain = 100 × (maximum sensitivity)

Gas pressure = 100 kPa

Carrier gas = (He/Air mixture)

Oven program: heat isothermally at 60 °C for 5 min, ramp at 38 °C min⁻¹ for 5 min, ramp at 6 °C min⁻¹ for 5 min, hold at 280 °C for 5 min, stop.

GC Calibration Values:

benzaldehyde

$$y = 6570 * 10^4 x + 54804$$

decane

$$y = 9702.7 * 10^4 x - 7630$$

The concentration of benzaldehyde appearing in the CO₂ phase over time was evaluated during sonication (Table A2–2).

Experiment ^(j)	Time (min)	Benzaldehyde Peak Area	Decane Peak Area	Benzaldehyde (mol L ⁻¹)	Mean Benzaldehyde (mol L ⁻¹)	Error %
1	20	390282	90696	0.044	0.038	16.3
	40	2872850	213243	0.137	0.138	0.7
	60	3315091	223204	0.151	0.152	0.4
	90	1673162	111327	0.153	0.153	0.3
2	20	374621	121021	0.032		
	40	2116893	154862	0.139		
	60	3464958	231469	0.152		
	90	15114416	998748	0.154		

Table A2–2 GC Data for evaluation of benzaldehyde concentration in CO₂

^(j) Sonication time at 75% amplitude; 2.6 mmol of decane (internal standard) and 0.06 mol of benzaldehyde were placed in the vessel before pressurisation.

Evaluation of Benzaldehyde Concentrations:

For CO₂ samples the concentration of unknown compound (homoallylic alcohol or benzaldehyde) was obtained by using the formula $= \frac{A_{BZDi} \times C_{Di}}{RRF \times A_{Di}}$, where A_{BZDi} and A_{Di} are the respective GC areas of benzaldehyde and decane in samples collected from the CO₂ phase, RRF is the relative response factor, and C_{Di} is the concentration of decane in the CO₂ phase.

$RRF = \frac{RF_{BZD}}{RF_D} = \frac{A_{BZD}/C_{BZD}}{A_D/C_D}$ where RF_{BZD} and RF_D are the response factors for benzaldehyde and decane, respectively; A_{BZD} and A_D are the peak areas of benzaldehyde, and C_{BZD} and C_D are the concentrations of benzaldehyde and decane obtained from standard calibrations.

$RRF \text{ benzaldehyde/decane} = 0.72$.

A3 Benzaldehyde Mass Transfer from CO₂ to Water

The appearance of benzaldehyde in the water phase was measured by GC following injection of 1 mL benzaldehyde in the CO₂ phase, under different mixing methods (momentum transfer by the circulation pump or sonication) (Table A3–1).

The Two-Film Model for Benzaldehyde Mass Transfer

The two-film model was applied to describe benzaldehyde mass transfer from CO₂ to water^(k).

Notations

C_{c0} = initial concentration in CO₂ (mol L⁻¹)

C_c = concentration in CO₂ at $t > 0$ (mol L⁻¹)

C_{cint} = concentration at the interface on CO₂ side

C_w = concentration in H₂O at time ' t ' (mol L⁻¹)

C_{wint} = concentration at the interface on H₂O side

k_c = mass transport coefficient in CO₂ (cm s⁻¹)

k_w = mass transport coefficient in H₂O (cm s⁻¹)

K_{CW} = partition coefficient CO₂/H₂O

K_{mCO_2} = overall mass transport coefficient on CO₂ side (cm s⁻¹)

t = time (s)

a = interfacial area (cm²)

V_c = volume of CO₂ phase (cm³)

V_w = volume of H₂O phase (cm³)

N_c = flux of benzaldehyde (mol cm⁻²·s⁻¹)

The two-film theory takes into consideration a small region or boundary layer on either side of the interface, where flow becomes stagnant and where most resistance to mass transport is thought to occur. In the absence of convective flow the molecular flux is assumed to be completely diffusive. At steady state the flux on both sides is equal:

$$N_c = k_c(C_c - C_{cint}) = -k_w(C_w - C_{wint}) \quad (A3.1)$$

at the interface the main driving force is the partition coefficient

$$K_{CW} = \frac{C_{cint}}{C_{wint}} \quad (A3.2)$$

rearranging in terms of C_{wint} two equations may be obtained

$$N_c = k_c(C_c - K_{CW}C_{wint}) \quad (A3.3)$$

and

$$C_{wint} = \left(\frac{N_c}{k_w} + C_w \right) \quad (A3.4)$$

^(k)The analysis was similar to that followed by Timko [2004] and Tai *et al.* [2000].

substitution of C_{wint} , leads to:

$$N_c = k_c \left(C_c - K_{CW} \left(\frac{N_c}{k_w} + C_w \right) \right) \quad (A3.5)$$

which is also equal to:

$$\frac{N_c}{k_c} + \frac{K_{CW} N_c}{k_w} = C_c - K_{CW} C_w \quad (A3.6)$$

rearranging in terms of the flux then generates:

$$N_c = \frac{1}{\frac{1}{k_c} + \frac{K_{CW}}{k_w}} (C_c - K_{CW} C_w) \quad (A3.7)$$

the concentration in the CO_2 phase over time may be obtained by a mass balance:

$$C_c = C_{c0} - \frac{V_w}{V_c} C_w \quad (A3.8)$$

the overall resistance may then be simplified as:

$$K_{mtCO_2} = \frac{1}{\frac{1}{k_c} + \frac{K_{cw}}{k_w}} \quad (A3.9)$$

the relationship may therefore be expressed in terms of measurable quantities:

$$\frac{dC_c}{dt} = -K_{mtCO_2} \frac{a}{V_c} (C_{c0} - \left(\frac{V_w}{V_c} + K_{CW} \right) C_w) \quad (A3.10)$$

finally, integration yields:

$$\ln \left| \frac{C_{c0} - \left(\frac{V_w}{V_c} + K_{CW} \right) C_w}{C_{c0}} \right| = -K_{mtCO_2} \frac{a}{V_c} \left(\frac{V_w}{V_c} + K_{CW} \right) t \quad (A3.11)$$

A plot of the left-hand term (for simplicity ' α ') against time yielded a straight line (see Section 5.4.1) passing through the origin, and a slope containing the mass transport coefficient.

GC settings

Sample injection = 0.5 μ L

Injector split ratio = 30

Injector T = 300 °C

FID T = 300 °C

FID gain = 100 \times (maximum sensitivity)

Gas pressure = 100 kPa

Carrier gas = (He/Air mixture)

Oven program: heat isothermally at 120 °C for 5 minutes, increase to 250 °C at 13 °C min⁻¹, continue at 250 °C for 5 minutes, stop.

GC Calibration for Benzaldehyde in water

$$y = 4272500x - 380$$

Circulation ^(l)			Pulsed Ultrasound (70% amp.) ^(m)			
Time (s)	Peak Area	C_w (mmol L ⁻¹)	Time (s)	Peak Area	C_w (mmol L ⁻¹)	Error %
300	451	0.19	10	806	0.28	
420	835	0.28	20	1585	0.46	
600	1126	0.35	30	2882	0.76	3
720	1433	0.42	55	4851	1.22	0.5
780	1107	0.35	80	7000	1.72	21
900	1336	0.40	120	8092	1.98	18
1020	1633	0.47	300	11000	2.66	8
1080	1395	0.41	600	11200	2.71	4
1200	1831	0.52	900	10991	2.66	6
1380	2133	0.59	1200	10900	2.64	4
1800	2530	0.68	1800	10996	2.66	8
2700	2854	0.76	2400	10888	2.63	3
3600	3796	0.98	3000	10860	2.63	6
5400	4370	1.11	3600	10251	2.48	10

Table A3–1 Concentration of benzaldehyde appearing in the water phase following injection in the CO₂ phase

^(l) Aggregated data for three experiments over different time points.

^(m) Each time point represents a repetition of three experiments.

The concentration profiles presented in Table A3–1 were inserted into Eq. A3.11 for construction of the log-time plot and evaluation of the mass transfer coefficient under circulation (Table A3–2) and ultrasound (Table A3–3) conditions.

$$\ln \left| \frac{C_{c0} - \left(\frac{V_w}{V_c} + K_{CW} \right) C_w}{C_{c0}} \right| = \alpha$$

$$C_{c0} = 28 \text{ mM}$$

$$V_c = 0.35 \text{ L}$$

$$V_w = 0.65 \text{ L}$$

$$K_{CW} = 12$$

C_w = benzaldehyde concentration in water

Circulation		
C_w (mmol L ⁻¹)	$-\alpha$ (K_{mtCO_2})	Time (s)
0.19	0.10	300
0.25	0.13	420
0.28	0.15	600
0.35	0.19	720
0.42	0.23	780
0.34	0.19	900
0.4	0.22	1020
0.47	0.26	1080
0.41	0.23	1200
0.51	0.29	1380
0.53	0.34	1800

Table A3–2 Log-time values for benzaldehyde mass transfer with circulation

C_w (mmol L ⁻¹)	$-\alpha$ (K_{mtCO_2})	$-\alpha$ (K_{mtH_2O})	Time ⁽ⁿ⁾ (s)
0.27	0.15	0.13	10
0.45	0.26	0.23	20
0.76	0.47	0.43	30
1.2	0.93	0.82	55
1.7	1.91	1.57	80
1.9	3.83	2.40	120

Table A3–3 Log-time values for evaluation of the mass transfer coefficients on the CO₂ K_{mtCO_2} and on the water side (by the Laplace method, K_{mtH_2O}) during sonication

⁽ⁿ⁾The time delay of 13 s described in Section 3.2.3.1 was subtracted from the sampling time for correction of the concentration-time relationship, resulting in a maximum 20% error in the effective mass transfer coefficient, although this remained within the same order of magnitude.

A4.1 Benzoyl Chloride Hydrolysis Rates in CO₂/H₂O

The effect of ultrasound on the rate of hydrolysis of benzoyl chloride was evaluated by measuring its rate of disappearance over time under different ultrasound amplitudes, with the pseudo first-order kinetics represented by:

$$\ln \frac{C_c}{C_{c0}} = -k_{obs}t \quad (A4.1)$$

C_c = benzoyl chloride concentration in CO₂ (mol L⁻¹)

C_{c0} = initial benzoyl chloride concentration in CO₂ (8.6 mmol, 2.45×10^{-2} mol L⁻¹)

k_{obs} = observed reaction rate constant for benzoyl chloride hydrolysis (s⁻¹)

Since the reaction is 100% selective towards benzoic acid, which is highly soluble in water, C_c may be evaluated by a mass balance on the benzoic acid measured in the water phase:

$$C_c = C_{c0} - \left(\frac{V_w}{V_c}\right)C_w \quad (A4.2)$$

C_w = benzoic acid (BZ_{AC}) concentration in the water phase measured by GC (mol L⁻¹)

V_w = 0.65 L

V_c = 0.35 L

Sonic Amplitude %	Time (min)	GC Peak Area	C_w (mmol L ⁻¹)	BZ _{AC} in H ₂ O (mmol)	C_c (mmol L ⁻¹)	$\ln(C_c/C_{c0})$	Yield %	k_{obs} (s ⁻¹) × 1000 ^(o)	Errors %
Silent	10	–	–	–	–	–	–	–	–
	20	–	–	–	–	–	–	–	–
	300	3070	0.92	0.6	22.88	-0.07	7	0.007	5
20	5	4881	1.30	0.85	22.17	-0.10	10		
	10	13712	3.18	2.07	18.69	-0.27	24		
	15	25375	5.65	3.67	14.10	-0.56	43		
35	30	28115	6.23	4.05	13.02	-0.64	47	0.6	4
	5	8158	2.00	1.30	20.88	-0.16	15		
	10	21598	4.85	3.15	15.59	-0.46	37		
45	15	31410	6.93	4.51	11.72	-0.74	52		
	20	37278	8.18	5.31	9.41	-0.96	62	0.8	9
	5	10395	2.47	1.61	20.00	-0.21	19		
60	10	24354	5.43	3.53	14.50	-0.60	41		
	15	38189	8.37	5.44	9.05	-1.00	63		
	20	44931	9.80	6.37	6.40	-1.35	74	1.1	9
70	5	15702	3.60	2.34	17.91	-0.32	27		
	10	32515	7.17	4.66	11.29	-0.78	54		
	15	42781	9.34	6.07	7.24	-1.22	71	1.3	10
70	4	14611	3.37	2.19	18.34	-0.29	25		
	7	25323	5.64	3.67	14.12	-0.55	43		
	9	32952	7.26	4.72	11.11	-0.79	55		
	13	42716	9.33	6.06	7.27	-1.22	70		
	17	47870	10.42	6.77	5.24	-1.55	79	1.6	12.5

Table A4–I Benzoyl chloride hydrolysis rates in CO₂/H₂O

GC Calibration for Benzoic Acid $y = 471.51 \times 10^4 x - 1270$

^(o)The mean values for the rate constants are shown from the best of three experiments with their respective errors; conditions: 30 °C/80 bar.

Solution to 2nd Order ODE (from Fick's Second Law with Chemical Reaction)

From Eq. 5.33, taking only one variable with respect to C (in the x direction), Fick's second law of diffusion in the presence of chemical reaction becomes the linear homogeneous ODE of the type:

$$D \frac{d^2 C}{dx^2} = kC \quad (\text{A4.3})$$

Second order linear equations usually find complementary solutions of the form:

$$y_c = Ae^{rx} \quad (\text{A4.4})$$

where A is the integration constant and r represents a characteristic root.

The roots may be represented in the form of a quadratic equation, which finds the following solution:

$$r_{1,2} = \frac{-b \pm \sqrt{b^2 - 4ac}}{2a} \quad (\text{A4.5})$$

In A4.3, the roots are $\pm\sqrt{r\lambda}$, real and unequal. If two possible roots exist, the theorem of superposition states that two linearly independent solutions exist for the complementary solution:

$$y_c = Ae^{r_1 x} + Be^{r_2 x} \quad (\text{A4.6})$$

the general solution for the differential equation is therefore:

$$C = C_1 e^{\lambda x} + C_2 e^{-\lambda x} \quad (\text{A4.7})$$

for the boundary condition when $x=0$, $C=C_{wint}$ we see that

$$C_1 = C_{wint} - C_2 \quad (\text{A4.8})$$

substituting this into Eq. A4.7 and rearranging, the following is also true

$$C_2 = \frac{C_{wint} e^{\lambda x} - C_{wint}}{e^{\lambda x} - e^{-\lambda x}} \quad (\text{A4.9})$$

If we introduce the dimensionless Hatta number in the form

$$Ha = \lambda x_c = \frac{\sqrt{k_{irr}}}{\sqrt{D_{AW}}} = \frac{\sqrt{k_{irr} D_{AW}}}{k_w} \quad (\text{A4.10})$$

then

$$C_2 = \frac{C_{wint} e^{Ha} - C_{wint}}{e^{Ha} - e^{-Ha}} \quad (\text{A4.11})$$

and the complementary solution becomes

$$C = C_{wint} - \left(\frac{C_{wint} e^{Ha} - C_{wint}}{e^{Ha} - e^{-Ha}} \right) e^{\lambda x} + \left(\frac{C_{wint} e^{Ha} - C_{wint}}{e^{Ha} - e^{-Ha}} \right) e^{-\lambda x} \quad (\text{A4.12})$$

rearranging:

$$C = C_{wint} - \left(\frac{C_{wint} e^{Ha+\lambda x} - C_{wint} e^{\lambda x}}{e^{Ha} - e^{-Ha}} \right) + \left(\frac{C_{wint} e^{Ha-\lambda x} - C_{wint} e^{-\lambda x}}{e^{Ha} - e^{-Ha}} \right) \quad (\text{A4.13})$$

It is usually convenient to express this type of solution using hyperbolic functions, therefore since

$$\sinh(x) = \frac{e^x - e^{-x}}{2} \quad (\text{A4.14})$$

we finally obtain:

$$C = \frac{C_{wint} \sinh \left[Ha - Ha \frac{x}{x_c} \right] + C_w \sinh \left[Ha \frac{x}{x_c} \right]}{\sinh Ha} \quad (\text{A4.15})$$

A4.2 Benzoyl Chloride Hydrolysis in the CO₂/H₂O/Tween 80 System

Benzoyl chloride hydrolysis was assessed in the presence of 1 wt.% Tween 80, under different power conditions (Table A4–2).

Sonic Conditions Pulse Rate/Amplitude	Time (min)	GC Peak Area	Diluted C_D (mmol L ⁻¹) ^(p)	Undiluted C_D (mmol L ⁻¹)	Yield ^(q) %	Errors %
25%/70%	0.5	38205	0.90	5.40	54	
	1	59920	1.34	8.04	80	
	5	63469	1.41	8.48	85	4.5
	8	68283	1.51	9.06	91	
	10	68659	1.52	9.12	91	4.7
	15	72721	1.60	9.60	96	
	25	76258	1.67	10.02	100	
	30	81052	1.77	10.62	100	8.9
10%/20%	2	35041	0.84	5.04	48	
	5	37890	0.89	5.34	54	3.2
	10	47275	1.08	6.48	65	
	15	51321	1.17	7.00	70	
	20	52994	1.20	7.20	72	7.4
	25	54780	1.24	7.44	74	
	35	60034	1.34	8.04	80	

Table A4–2 Benzoyl chloride hydrolysis in the presence of Tween 80

Initial rates for the different power conditions were obtained using the following logarithmic values:

Time (s)	$\ln(C_c/C_{c0})$ 25%/70%	$\ln(C_c/C_{c0})$ 10%/20%
10	0.15	-
30	0.52	0.16
45	0.7	0.27
60	0.93	0.37
k_{obs} (s ⁻¹)	0.016	0.006

Table A4–3 Rate constant for benzoyl chloride hydrolysis in the presence of Tween 80

GC Calibration for Benzoic Acid

$$y = 4934.5 \cdot 10^4 x - 6258.3$$

^(p) C_D = benzoic acid concentration in the dispersion (1:6 v/v sample dilution).

^(q) Theoretic Yield = 10 mmol L⁻¹ (see Section 3.4.2).

A5 Damköhler Analysis for Hydrolysis of Benzoyl Halides in CO₂/H₂O

The mixing efficiency of ultrasound was evaluated with respect to the hydrolysis of benzoyl chloride by taking into account a Damköhler number appropriate for emulsions, as discussed in Section 5.6:

$$Da = \frac{k_{rxn}d_{32}}{2D_{AW}\underline{a}} \quad (\text{A5.1})$$

k_{rxn} = intrinsic reaction rate constant (s⁻¹)

k_{obs} = overall reaction rate constant (s⁻¹)

d_{32} = droplet Sauter mean diameter (cm)

D_{AW} = diffusivity in water (1×10^{-5} cm² s⁻¹)

\underline{a} = specific surface area (cm⁻¹); calculated for emulsion by $6\phi/d_{32}$

ϕ = volume fraction of CO₂ dispersed in H₂O (here 0.35).

A Damköhler analysis was undertaken on the hydrolysis of benzoyl chloride, as presented in Table A5–1 and shown in Figure 5.16. Two extreme cases for d_{32} and \underline{a} are given using predictions from Timko *et al.* [2006b], who also provide parameters for the hydrolysis of other benzoyl halides in CO₂/H₂O, which are included for comparison. Information regarding CO₂/H₂O/Tween 80 emulsions was obtained from Torino *et al.* [2010].

System	d_{32} (cm)	\underline{a} (cm ⁻¹)	Da	Da (mean) ^(r)	Error ^(s) %	k_{rxn} (s ⁻¹)	k_{obs} (s ⁻¹)
Benzoyl Chloride ^(t)	0.002	90	1.3				
	0.0015	240	0.4	0.85	56	1.2	1.8×10^{-3}
Benzoyl Chloride (with Tween 80)	0.0015	1400	0.12				
	0.0005	4200	0.007	0.06	89	1.2	0.016
p-Nitrobenzoyl Chloride Timko <i>et al.</i> [2006b]	0.0015	240		0.02		0.055	4.6×10^{-4}
Benzoyl Fluoride Timko <i>et al.</i> [2006b]	0.0015	240		0.0006		0.0019	7.7×10^{-6}

Table A5 Parameters for the Damköhler analysis of the hydrolysis of benzoyl halides

Values for Da in silent conditions were evaluated by:

$$Da = \frac{k_{rxn}}{k_w \underline{a}} \quad (\text{A5.2})$$

k_w = mass transfer coefficient on the water side, which was 9×10^{-4} cm s⁻¹

$\underline{a} = a/V_c = 71 \text{ cm}^2/350 \text{ cm}^3 = 0.2 \text{ cm}^{-1}$

k_{obs} = for silent conditions was evaluated experimentally as 7×10^{-4} s⁻¹

^(r)Mean Da values are shown for experimental rate constants of benzoyl chloride hydrolysis.

^(s)Errors were associated with smallest and largest estimated values of d_{32} .

^(t)For simplicity, only CO₂ in water droplets were considered.

A6.1 Representative Data for the Barbier Synthesis in CO₂/H₂O at 30 °C/80 bar

Phase	Time† (min)	BZD Peak Area	HA Peak Area	BZA Peak Area	DA Peak Area	HA (mol L ⁻¹)	HA (mol)	HA Tot Mols	HA yield %	BZD (mol L ⁻¹)	BZD mol	BZD Tot Mols	BZD conv%
CO ₂	30	1620454	584950		153285	0.023	0.010	0.013	21	0.088	0.0371	0.0378	37
A	60	1271528	1336805		188611	0.042	0.018	0.022	36	0.056	0.0237	0.0243	60
	90	372660	1710498		142920	0.072	0.030	0.036	58	0.022	0.0092	0.0096	84
	120	238678	1952119		141822	0.082	0.035	0.040	65	0.014	0.0059	0.0061	90
H ₂ O	30	70521	471696	193927		0.005	0.003				0.0006		
	60	63706	679833	383589		0.007	0.004				0.0006		
	90	47442	910344	518197		0.009	0.005				0.0004		
	120	20000	866231	791856		0.009	0.005				0.0002		
CO ₂	30	1560840	136601		126371	0.006	0.003	0.004	7	0.103	0.0434	0.0445	26
B	60	1411760	394149		146723	0.016	0.007	0.009	15	0.080	0.0338	0.0353	41
	90	1295250	725773		164944	0.026	0.011	0.014	23	0.065	0.0276	0.0293	51
	120	1124017	727685		141543	0.031	0.013	0.016	26	0.066	0.0279	0.0295	51
H ₂ O	30	119152	189207	150547		0.002	0.001				0.0011		
	60	163050	339408	339407		0.004	0.002				0.0014		
	90	194117	455408	481723		0.005	0.003				0.0017		
	120	179432	452170	559620		0.005	0.003				0.0016		
CO ₂	30	1045153	127565		103964	0.007	0.003	0.006	10	0.084	0.0353	0.0353	41
C	60	1545153	916352		195481	0.028	0.012	0.016	26	0.066	0.0278	0.0278	54
	90	1045153	1467081		172538	0.051	0.021	0.026	43	0.050	0.0213	0.0228	62
	120	1208367	2555759		277044	0.055	0.023	0.028	46	0.036	0.0153	0.0172	71
H ₂ O	30		435604	113509		0.005	0.003						
	60		701869	355097		0.007	0.004						
	90	175936	778702	434353		0.008	0.005				0.0016		
	120	217327	855624	518485		0.009	0.005				0.0019		

Phase	Time [†] (min)	BZD Peak Area	HA Peak Area	BZA Peak Area	DA Peak Area	HA (mol L ⁻¹)	HA (mol)	HA Tot Mols	HA yield %	BZD (mol L ⁻¹)	BZD mol	BZD Tot Mols	BZD conv%
CO ₂	30	105702	8981		9897	0.005	0.002	0.006	10	0.089	0.0375	0.0390	35
D	60	1032908	986170		152868	0.039	0.016	0.021	34	0.056	0.0237	0.0245	59
	90	386258	1289834		139151	0.056	0.023	0.028	46	0.023	0.0098	0.0103	83
	120	284931	2711019		233813	0.069	0.029	0.033	55	0.010	0.0043	0.0048	92
H ₂ O	30	161001	624773	596502		0.007	0.004				0.0014		
	60	82633	729484	811506		0.008	0.004				0.0007		
	90	63755	781089	862956		0.008	0.005				0.0006		
	120	60000	677298	773395		0.007	0.004				0.0005		
CO ₂	10	513864	1824265		105129	0.104	0.044		72	0.041	0.0172	0.0172	71
E	30	522688	2337173		124892	0.112	0.047		77	0.035	0.0147	0.0147	75
	60	720738	5094423		247521	0.123	0.052		85	0.024	0.0102	0.0102	83
	105	326686	5519543		252789	0.131	0.055		90	0.011	0.0045	0.0045	92
	120	339582	5729113		249756	0.137	0.058		95	0.011	0.0048	0.0048	92
CO ₂	30		1054793		61048	0.096	0.040	0.043	71				
F	60		1156478		59147	0.107	0.045	0.049	80				
	90		1425598		66728	0.119	0.050	0.054	89				
	120	27359	1082642		61957	0.126	0.053	0.058	95	0.004	0.0018	0.0085	86
H ₂ O	30		195214			0.005	0.003						
	60		225786			0.007	0.004						
	90		325874			0.008	0.004						
	120	39378	382743			0.008	0.005				0.0068	0.0068	
CO ₂	120	797153	265691		72589	0.015	0.015		25	0.043	0.0434	0.0427	28
G													

[†]Sample collection time from either the CO₂ or the water fraction.

Table A6–1 Data for the zinc-mediated Barbier reaction between benzaldehyde and allyl bromide in CO₂/H₂O

Notes to Table A6–1

BZD = benzaldehyde; BZA = benzyl alcohol reduction product; HA = homoallylic alcohol adduct product; DA = decane internal standard

➤ A–D represent the mole ratios of zinc/allyl bromide/benzaldehyde; A (2:2:1); B (1:1:1); C (1.3:1.2:1); D (2:1.5:1); based on 0.061 mol of benzaldehyde, 0.0025 mol of *n*-decane; E (inclusion of 1 wt.% Tween 80); F (aq. satd. NH₄Cl); G (sonication in only CO₂).

All carried out at 30 °C/80 bar, CO₂ = 0.42 L, H₂O = 0.58 L.

➤ For CO₂ samples the concentration of unknown compound (homoallylic alcohol or benzaldehyde) was obtained by using the formula:

$$\frac{A_{Hi} \times C_{Di}}{RRF \times A_{Di}} \quad (\text{A6.1})$$

where A_{Hi} and A_{Di} are the respective GC areas of homoallylic alcohol (or benzaldehyde) and decane in samples collected from the CO₂ phase, RRF is the relative response factor, and C_{Di} is the concentration of decane in the CO₂ phase.

$$RRF = \frac{RF_H}{RF_D} = \frac{A_H/C_H}{A_D/C_D} \quad (\text{A6.2})$$

where RF_H and RF_D are the response factors for homoallylic alcohol (or benzaldehyde) and decane; A_H and A_D are the peak areas of homoallylic alcohol (or benzaldehyde), and C_H and C_D are the concentrations of homoallylic alcohol (or benzaldehyde) and decane obtained from standard calibrations.

➤ For H₂O samples the concentration was determined directly from the dissolved product in water by using the GC calibration. For reaction with satd. salt solutions, the aqueous phase was extracted with Et₂O (1:2 final dilution). The total number of moles of remaining reagent or product was calculated by combining the number of moles measured in the CO₂ and H₂O phases (with the exception of experiments using Tween 80, due to only CO₂ in H₂O emulsions being formed).

RRF homoallylic alcohol/decane = 1.02

RRF benzaldehyde/decane = 0.73

GC Calibration Values:

benzaldehyde

$$y = 6570 * 10^4 x + 54804$$

homoallylic alcohol

$$y = 10485 * 10^4 x - 71907$$

decane

$$y = 9702.7 * 10^4 x - 7630$$

A6.2 Barbier Synthesis in the CO₂/H₂O/Tween 80 System

First-order kinetic plots were generated for evaluation of the observed rate constant (k_{obs}) in the presence and absence of Tween 80 (Figure A6). The method was analogous to that described for the hydrolysis of benzoyl chloride (see Appendix A4.1) apart from the fact that the internal standard was used for quantification of homoallylic product formed; the first-order rate constant in was numerically equivalent to the slope in plots of $\ln(C/C_0)$ against time, where C_c is the concentration of benzaldehyde in CO₂ (calculated by a mole balance of homoallylic alcohol formed), and C_{c0} is the initial benzaldehyde concentration in CO₂ (0.145 mol L⁻¹).

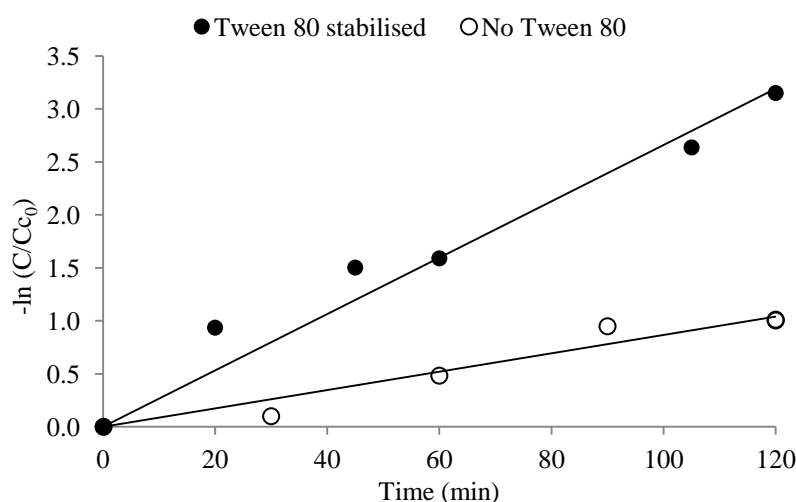


Figure A6 First-order plots for the reaction of benzaldehyde in the Barbier synthesis; k_{obs} (Tween 80) = $4.43 \times 10^{-4} \text{ s}^{-1}$; k_{obs} (without Tween 80) = $1.45 \times 10^{-4} \text{ s}^{-1}$; ($r^2 \geq 0.94$). Conditions: CO₂/H₂O 42% v/v, 30 °C/80 bar, pulsed ultrasound at 80% amplitude

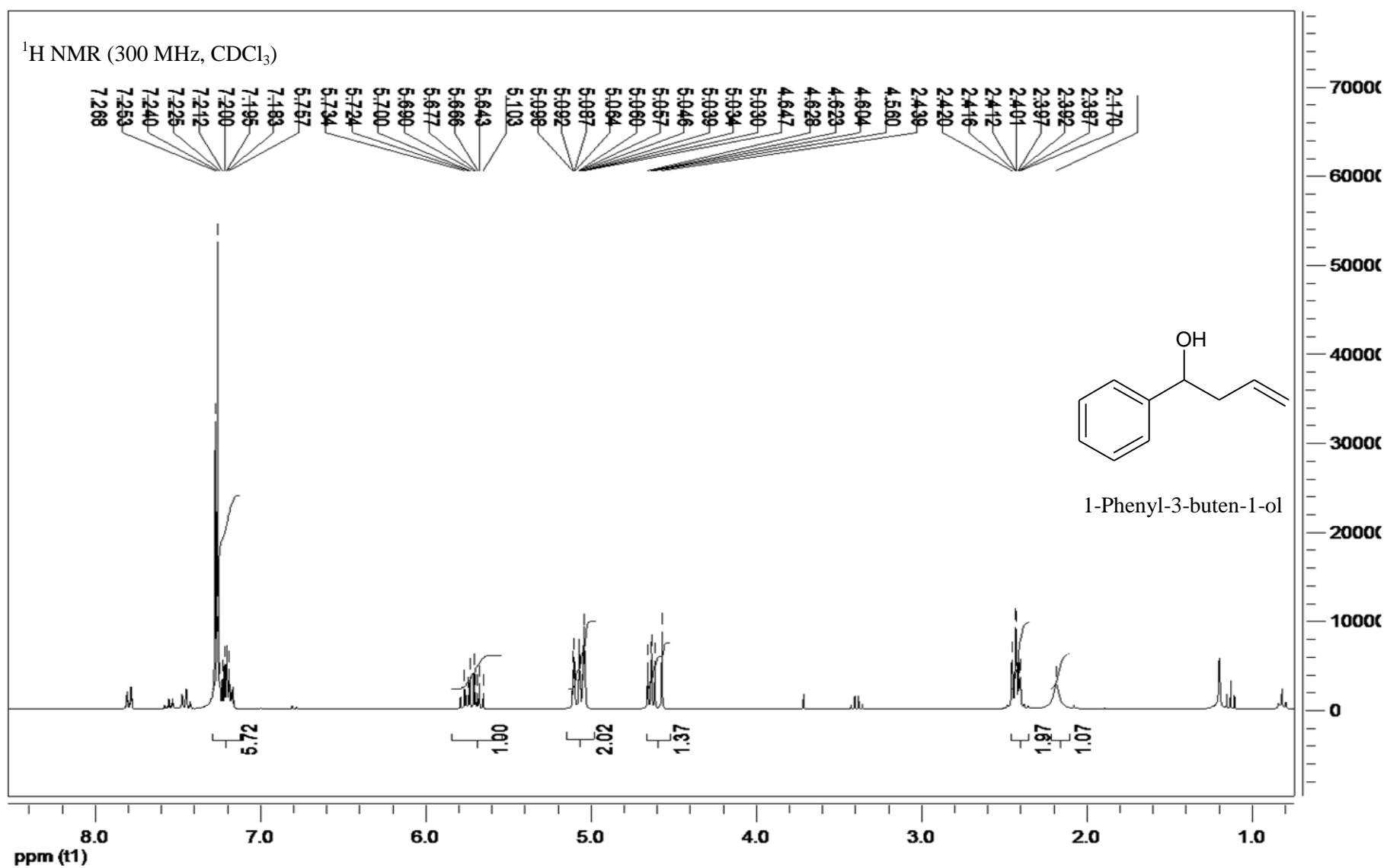
A6.3 Barbier Synthesis in CO₂/H₂O with Substituted Aromatic Aldehydes

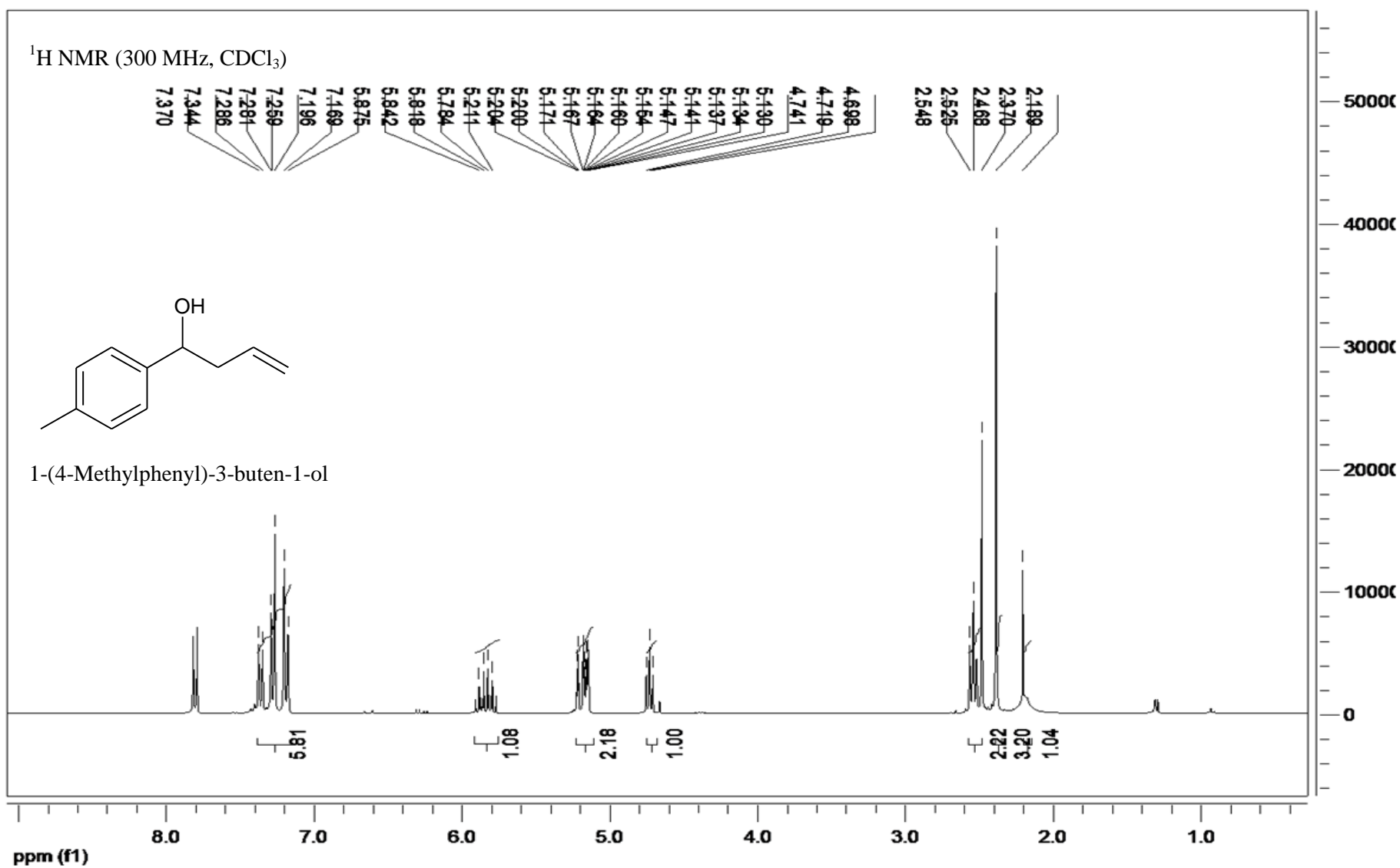
Aldehyde	RT (min)	Homoallylic Alcohol RT (min)	Reduction Product RT (min)
benzaldehyde	7.0	<i>1-Phenyl-3-buten-1-ol</i> (1a) 9.27	7.7
4-methylbenzaldehyde	8.3	<i>1-(4-Methylphenyl)-3-buten-1-ol</i> (2a) 9.8	-
4-methoxybenzaldehyde	9.5	<i>1-(4-Methoxyphenyl)-3-buten-1-ol</i> (3a) 10.5	10.2, 14.7
2-chlorobenzaldehyde	8.6	<i>1-(2-Chlorophenyl)-3-buten-1-ol</i> (4a) 10.1	9.1
(<i>E</i>)-3-phenylprop-2-enal	9.7	(<i>E</i>)- <i>1-Phenylhexa-1,5-dien-3-ol</i> (5a) 10.6	10.3

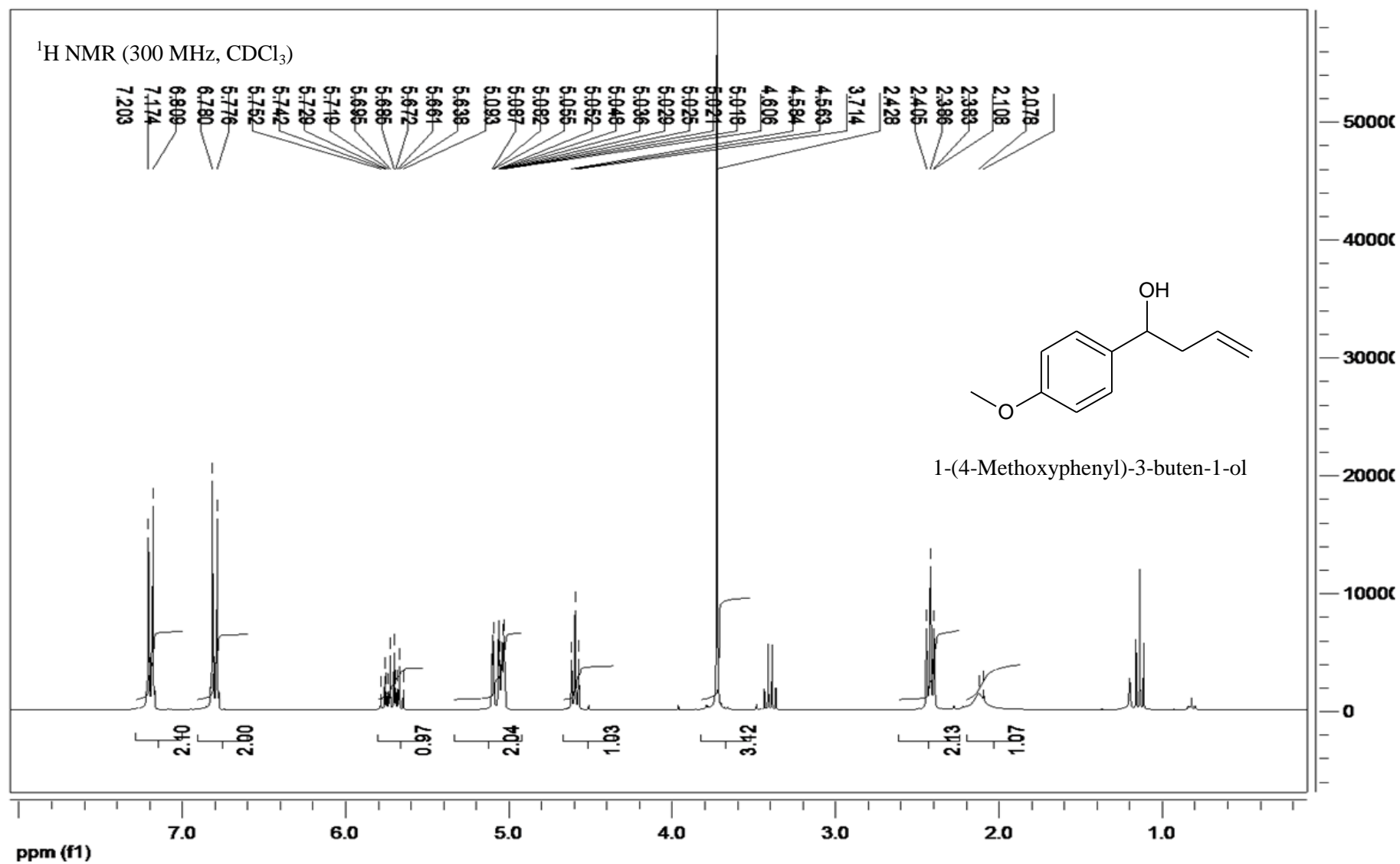
RT = retention time.

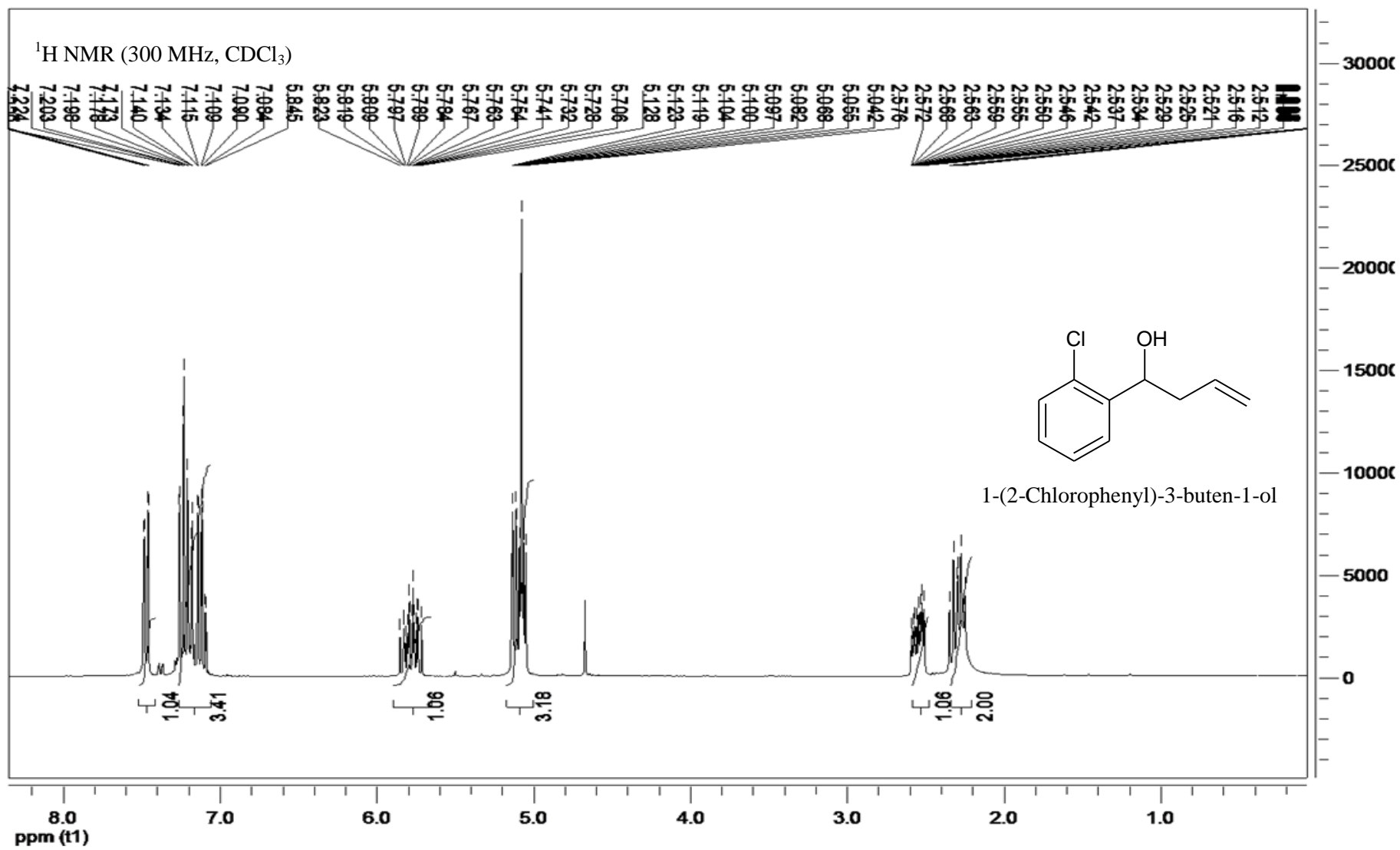
Table A6–2 GC retention times of reagents and products employed in the Barbier synthesis

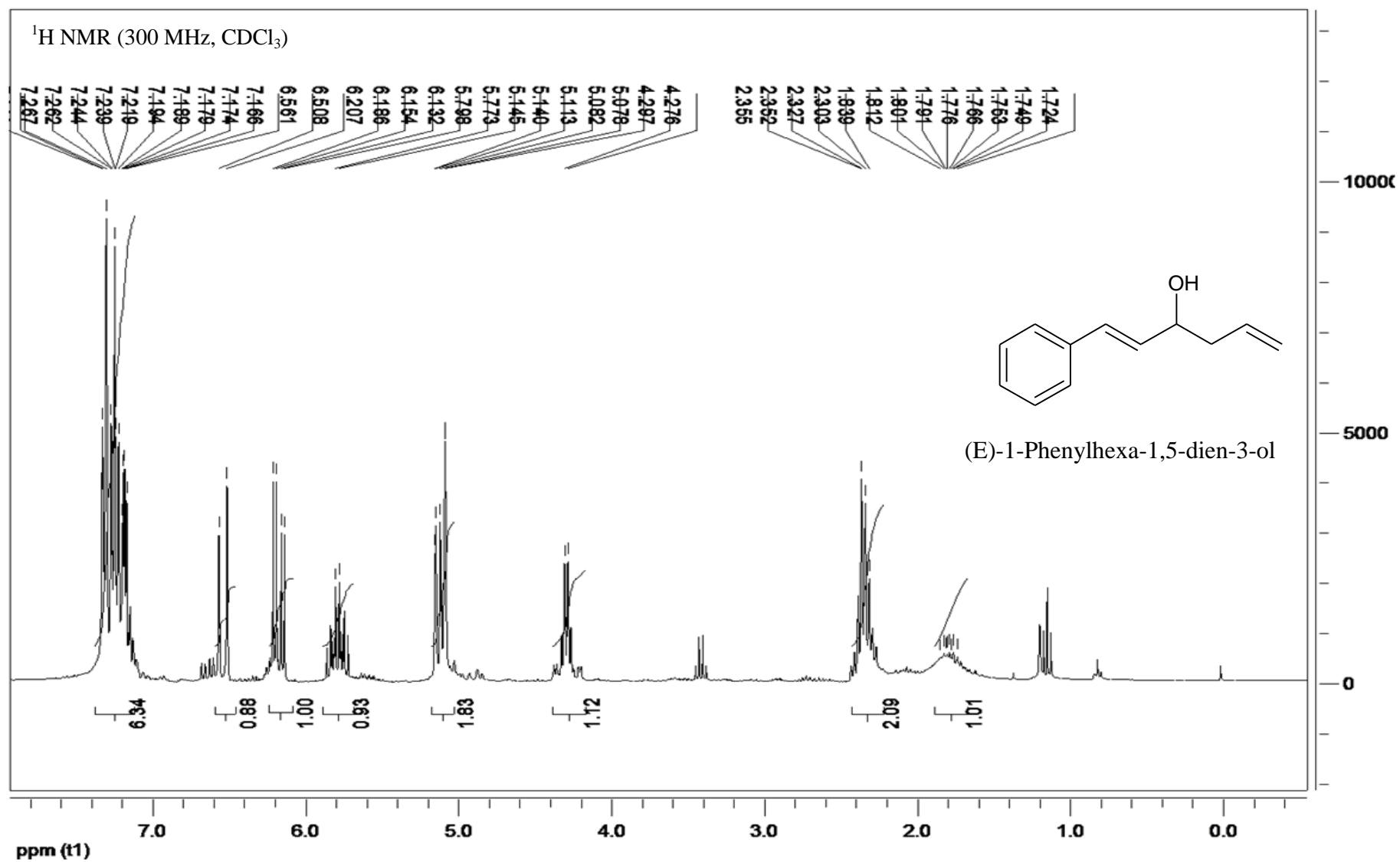
A6.4 NMR Spectral Data

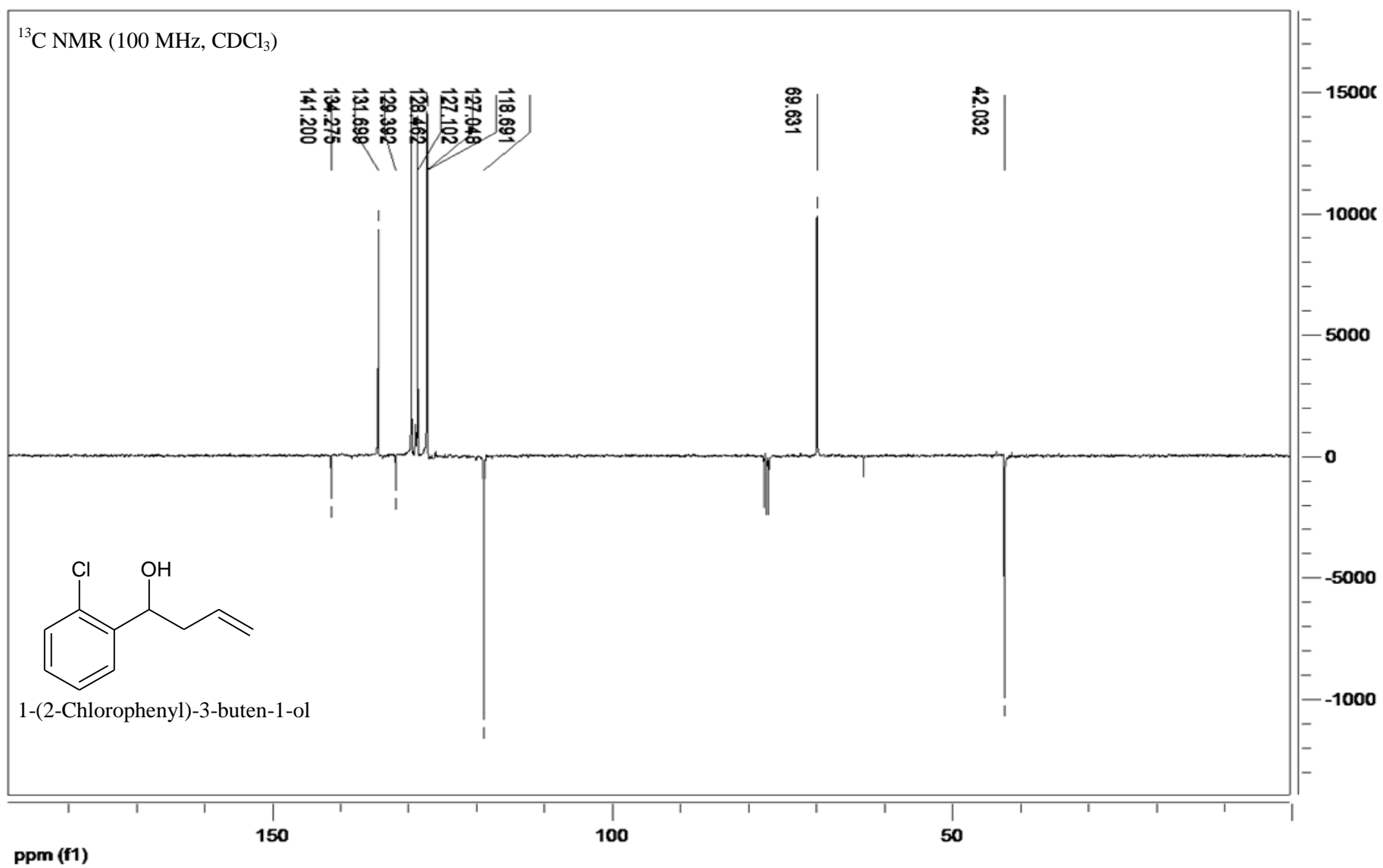












1-Phenyl-3-buten-1-ol (1a)

¹H NMR (300 MHz, CDCl₃): δ = 7.29–7.16 (m, 5H, ArH), 5.83 (dddd, *J* 17.2, 10.2, 7.2, 6.9, 1H, CH=CH₂), 5.10–5.02 (m, 2H, CH=CH₂), 4.63 (dd, *J* 7.2, 5.7, 1H, CHOH), 2.46–2.37 (m, 2H, CH₂), 2.17 (br s, 1H, OH).

¹³C NMR (100 MHz, CDCl₃): δ = 144.6, 134.5, 128.7, 128.0, 126.0, 118.5, 73.5, 44.1.

1-(4-Methylphenyl)-3-buten-1-ol (2a)

¹H NMR (300 MHz, CDCl₃): δ = 7.39–7.17 (m, 4H, ArH), 5.83 (dddd, *J* 17.2, 10.1, 7.2, 7.1, 1H, CH=CH₂), 5.22–5.13 (m, 2H, CH=CH₂), 4.72 (app. t, *J* 6.5, 1H, CHOH), 2.55–2.49 (m, 2H, CH₂), 2.37 (s, 3H, CH₃), 2.18 (s, 1H, OH).

¹³C NMR (100 MHz, CDCl₃): δ = 141.0, 137.2, 134.7, 129.7, 125.8, 118.2, 73.2, 43.8, 21.1.

1-(4-Methoxyphenyl)-3-buten-1-ol (3a)

¹H NMR (300 MHz, CDCl₃): δ = 7.21–7.17 (m, 2H, ArH), 6.82–6.77 (m, 2H, ArH), 5.71 (app. ddt, *J* 17.2, 10.2, 7.1, 1H, CH=CH₂), 5.09–5.01 (m, 2H, CH=CH₂), 4.58 (app. t, *J* 6.5, 1H, CHOH), 3.71 (s, 3H, CH₃), 2.43–2.38 (m, 2H, CH₂), 2.11 (s, 1H, OH).

¹³C NMR (100 MHz, CDCl₃): δ = 159.0, 136.1, 134.7, 127.1, 118.2, 113.8, 73.0, 55.3, 43.7.

1-(2-Chlorophenyl)-3-buten-1-ol (4a)

¹H NMR (300 MHz, CDCl₃): δ = 7.48–7.45 (m, 1H, ArH), 7.26–7.08 (m, 3H, ArH), 5.85–5.71 (stack, 1H, CH=CH₂), 5.13–5.04 (stack, 3H, CH=CH₂, CHOH), 2.58–2.49 (m, 1H), 2.34–2.23 (m, 2H)

¹³C NMR (100 MHz, CDCl₃): δ = 141.2, 134.3, 131.7, 129.4, 128.4, 127.1, 127.0, 118.7, 69.6, 42.0.

(E)-1-Phenylhexa-1,5-dien-3-ol (5a)

¹H NMR (300 MHz, CDCl₃): δ = 7.33–7.16 (m, 5H, ArH), 6.56 (d, *J* 15.9, 1H, ArCH=CH), 6.20 (dd, *J* 15.9, 6.3, 1H, ArCH=CH), 5.79 (app. ddt, *J* 17.1, 10.2, 7.2, 1H, CH=CH₂), 5.15–5.05 (m, 2H, CH=CH₂), 4.32–4.24 (m, 1H, CHOH), 2.38–2.26 (m, 2H, CH₂), 1.8 (br, 1H, OH).

¹³C NMR (100 MHz, CDCl₃): δ = 136.7, 134.1, 131.6, 130.4, 128.6, 127.9, 126.6, 118.5, 71.8, 42.0.

A6.5 Damköhler Analysis for the Barbier Synthesis in CO₂/H₂O

The mixing effects of ultrasound were evaluated for the Barbier reaction in CO₂/H₂O by taking into account the Damköhler number from Eq. A5.1. This section provides further support to the results discussed in Section 6.8.1.

k_{rxn} = intrinsic reaction rate constant (s⁻¹)

k_{obs} = overall reaction rate constant (s⁻¹)

d_{32} = droplet diameter (cm)

D_{AW} = diffusivity in water (1×10^{-5} cm² s⁻¹)

\underline{a} = specific surface area of emulsion (cm⁻¹), calculated by $6\phi/de$, where ϕ = volume fraction of CO₂ droplets dispersed in water.

Values for Da in silent conditions were obtained using Eq. A5.2.

For silent conditions k_{obs} was 2.5×10^{-6} s⁻¹, \underline{a} was 0.2 cm⁻¹, and k_w was 9×10^{-4} cm s⁻¹

System	Droplet diameter (cm)	Specific surface area (cm ⁻¹)	Mean Da	k_{rxn} (s ⁻¹)	k_{obs} (s ⁻¹)
CO ₂ /H ₂ O ultrasound	0.0015	240	2.5×10^{-3}	$0.145\text{--}1.5 \times 10^{-3}$	1.45×10^{-4}
CO ₂ /H ₂ O ultrasound Tween 80	0.0005	4200	4.7×10^{-5}	$0.145\text{--}1.5 \times 10^{-3}$	4.43×10^{-4}
CO ₂ /H ₂ O silent	-	0.2	45	$0.145\text{--}1.5 \times 10^{-3}$	2.5×10^{-6}

Table A6–3 Damköhler parameters for the Barbier synthesis

Errors were associated with uncertainties in k_{rxn} , therefore for clarity here the errors associated with droplet size uncertainties were neglected, although they were of the same magnitude as those in Appendix A5. The lowest value of k_{rxn} was obtained from Denmark and Fu [2000], whereas the highest value was estimated from the trends in $k_{\text{rxn}}/k_{\text{obs}}$ reported by Timko *et al.* [2006b]. The resulting error in Da was ~80%.